University of Alberta

An Analysis Framework to Study Steady State Friction Dominated Saint-Venant Equations

by

Mohammad Mostafa Ali

A thesis submitted to the Faculty of Graduate Studies and Research in partial fulfillment of the requirements for the degree of

Doctor of Philosophy

in

Water Resources Engineering

Department of Civil and Environmental Engineering

Fall 2011
Edmonton, Alberta

Abstract

An analysis framework to study the friction term dominated steady state 1D Saint-Venant equations is developed using a non-uniform flow test case and Fourier analysis. In the non-uniform flow test, a sudden bed perturbation is introduced, and in the Fourier analysis, a periodic bed perturbation is used. In both analyses, the effects of the bed perturbations on the solution variables in a steady state case are observed. Both the shock capturing and non-shock capturing numerical schemes have been studied in this research. From the non-uniform flow test results, it is found that the oscillations in the discharge and/or depth solutions are apparent when discretization, roughness, and slope are large, and the errors in the solution variables increase with an increase in these parameters. From the Fourier analysis, the main non-dimensional parameter groups identified are: the number of discretization intervals per wavelength, the average flow Froude number, and the numerical Friction number. The Fourier analysis results show that the errors in both depth and discharge solutions or only in the depth solutions are observed whenever there is any perturbation in the bed topography. These errors increase with an increasing Froude number and increasing numerical Friction number. A combined friction parameter is proposed for practical modeling purposes which captures the variations of the separate parameters. The proposed combined friction parameter is capable of locating the friction dominated region in open channel flow modeling. The proposed combined friction parameter is easy to calculate and to implement in any open channel flow model. The proposed combined friction parameter is applied and used in 1D and 2D flow

models as a mesh refinement indicator and as a minimum depth criterion. The results show that the proposed combined friction parameter is effective to identify and to eliminate or reduce spurious velocity vectors. The analysis presented in this study can be applicable to a wide range of numerical methods to study the friction dominated steady state Saint-Venant equations.

Acknowledgements

I would like to express heartfelt gratitude to my supervisor Dr. Peter Steffler for his unique supervision and excellent guidance throughout my PhD thesis work. His timely advice and inspiration enabled me to complete my research successfully and on time. Working with him was a learning experience that I thoroughly enjoyed.

I also thank the review committee for their valuable comments, which have helped to improve and polish my work at every stage of writing. I am gratefully indebted to the Faculty of Graduate Studies and Research (FGSR) and the Department of Civil and Environmental Engineering at the University of Alberta, as well as to the The Natural Sciences and Engineering Research Council of Canada (NSERC) for funding my PhD research.

A special thanks to Terry Waddle for providing me with the data and the photographs of the South Platte River and for allowing me to use his results.

Finally, my greatest thanks are to my parents, my wife, and to my family for their constant and loving support during this challenging undertaking. Without them, none of this would have been possible.

Contents

List of Tables

List of Figures

List of Symbols

A	Area of a cross-section
A_1	Cross-sectional area at x_1
A_2	Cross-sectional area at x_2
$\mathbf{A}$	Jacobian matrix
B	Channel width
C_*	Non-dimensional Chezy coefficient
Cr_0	Average flow Courant number
D_n	Numerical diffusion coefficient
f_j	Interpolation function in the FEM
F_g	Gravitational force
F_f	Frictional force
F_{P1}	Pressure force at x_1
F_{P2}	Pressure force at x_2
Fr_0	Average flow Froude number
$\mathbf{F}(\mathbf{U})$	Flux vectors
g	Gravitational acceleration
h	Depth
h_0	Average depth
h'	Small perturbation to h_0
h_{out}	Downstream boundary depth in the non-uniform test case
$\bar{h}$	Depth at the centroid
$\bar{h}_1$	Depth at the centroid at x_1
$\bar{h}_2$	Depth at the centroid at x_2
H	Water surface elevation
H_a	Non-dimensional analytical amplitude of the depth perturbation

H_n	Non-dimensional numerical amplitude of the depth perturbation
i	Imaginary number
L	Characteristic length scale
n	Manning's roughness coefficient
N	Number of nodes in a domain
N_λ	Number of discretization intervals per wavelength
P	Wetted perimeter
q	Unit discharge
q_x	Unit discharge in longitudinal direction
q_y	Unit discharge in lateral direction
q_0	Average unit discharge
q'	Small perturbation to q_0
q_{in}	Inflow boundary unit discharge in the non-uniform test case
Q	Discharge
Q_1	Discharge at x_1
Q_2	Discharge at x_2
R	Hydraulic radius
$\mathbf{R}$	Right eigenvectors
S_0	Average bed slope
S_b	Local bed slope
S_{bx}	Bed slope in longitudinal direction
S_{by}	Bed slope in lateral direction
S_{b1}	Smaller channel bed slope in the non-uniform test case
S_{b2}	Higher channel bed slope in the non-uniform test case
S_f	Local friction slope
S_{fx}	Friction slope in longitudinal direction
S_{fy}	Friction slope in lateral direction
S_w	Local water surface slope
$\mathbf{S}(\mathbf{U})$	Source vectors
t	Time coordinate
T	Characteristic time scale
u	Cross-sectional average velocity

u_0	Average velocity
u_1	Velocity at x_1
u_2	Velocity at x_2
$\mathbf{U}$	Conserved variable vectors
$\tilde{\mathbf{U}}$	Trial function in the FEM
v	Velocity in lateral direction
v_i	Weighting function in the FEM
w	Upwinding coefficient
$\mathbf{W}$	Upwinding Matrix
x	Space coordinate
x_1	Location of first control volume section
x_2	Location of second control volume section
z	Local Bed elevation
z_0	Bed elevations corresponding to S_0
z'	Small perturbation to z_0
Z	Non-dimensional amplitude of the bed elevation perturbation
β	Friction number
$\beta_{\Delta x}$	Numerical friction number
γ	Non-dimensional water surface elevation
ϵ	Mesh generation coefficient
ζ	Non-dimensional bed elevation perturbation
η	Non-dimensional depth perturbation
θ	Weighting coefficient
κ	Non-dimensional wave number of the bed elevation perturbation
λ	Dimensional wavelength of the bed elevation perturbation
ξ	Non-dimensional longitudinal coordinate
ρ	Density of fluid
τ	Non-dimensional time coordinate
ϕ	Angle between channel bed and horizontal
φ	Non-dimensional discharge perturbation
Δx	Discretization length
$\Delta\xi$	Non-dimensional discretization length

$\mathbf{\Lambda}$	Eigenvalue matrix
$\sum F$	Summation of forces
Φ_a	Non-dimensional analytical amplitude of the discharge perturbation
Φ_n	Non-dimensional numerical amplitude of the discharge perturbation

Chapter 1

Introduction

1.1 Introduction

The flow in an open channel or in a closed conduit with a free surface is referred to as free-surface or open channel flow (Chow 1959, Chanson 1999, Chaudhry 2008). Some examples of open channel flow are the flow in natural streams and rivers, and the flow in man-made channels, including irrigation and navigation canals, drainage pipes, culverts, and spillways. The study of the flow behavior in open channels is known as open channel hydraulics and this knowledge is essential in many water resources problems. For example, flood forecasting, hydraulic structures designing, morphological modeling, fish habitat modeling, ice process modeling, and contaminant transport modeling all require knowledge of the velocity and depth of an open channel flow.

Flow behaviors in open channel flows are normally studied using physical modeling and/or numerical modeling. A physical model is a scaled representation of the real flow situation, while a numerical model is a computer program that solves the governing equations of open channel flow. The Saint-Venant equations (Saint-Venant 1871) provide the fundamental mathematical description governing the depth and average velocity in one-dimensional (1D) and two-dimensional (2D) open channel flows (Chow 1959, Abott 1979, Cunge and Verway 1980, Chanson 1999, Chaudhry 2008). However, these equations consist of partial differential equations with non-linear terms, which makes it difficult to get any closed form analytical solutions, except for in some simplified cases. Though the simplified solutions are useful in many cases, they do not provide detailed solutions that are necessary for many practical water resources problems. Moreover, with advances in computing power, the numerical models usually have the advantage of quicker results and lower cost when compared to the physical models and therefore are now widely used in most practical cases.

The numerical solution of an open channel flow problem is known as Computational Hydraulics and has become an important subfield of open channel hydraulics. My research studies the friction-dominated flow, which is one particular issue that arises in Computational Hydraulics. The study is required for a robust model that is applicable to the full range of practical applications. The flow in open channels can either be gentle, like the flow in flood plains or in irrigation canals, or it can be rough, like in mountain streams or in spillways. Moreover, a variety of complex topographies may be present in a channel, for example wet/dry areas, small depth areas, steep areas, and large boulder areas. Modeling the flow in these cases can be challenging, as spurious velocities or stability problems may occur.

In this chapter, first a brief history of Computational Hydraulics will be presented and then the different numerical issues present in Computational Hydraulics will be discussed in depth. Finally, we will discuss why the friction dominated problem is chosen as the focus of this study, and how we address the problem.

1.2 A Brief History of Computational Hydraulics

The Computational Hydraulics field can be viewed as a subfield of Computational Fluid Dynamics (CFD). Many numerical schemes used in Computational Hydraulics originated in CFD, especially from the 1D mass transport problem and the compressible gas dynamics problem. While modern Computational Hydraulics and CFD became widespread with the advent of the digital computer in the early 1950s (Chung 2002, Szymkiewicz 2010), each of these fields started their own journeys independently.

The development of CFD began with Finite Difference Method (FDM) because of FDM's simplicity in formulation and computations. FDM uses finite difference equations to approximate partial derivatives in a differential equation. Some early applications of FDM in CFD are found in the works of Courant and

Lewy (1928), Courant and Rees (1952), Lax (1957), Lax and Wendroff (1960), and MacCormack (1969) (Chung 2002). However, FDM requires structured grids, which necessitates grid transformations in case of 2D flow problems.

Finite Element Method (FEM), which has the support of unstructured grids and can easily handle 2D geometry, was applied in CFD almost three decades after the first uses of FDM in CFD. In FEM, the solution domain is divided into small subdivisions, and the governing partial differential equations are transformed into a set of finite element equations using approximate trial functions. Some early applications of FEM in CFD can be found in Zeienkiewicz and Cheung (1965), Olson (1972), Oden (1972), and Baker (1973) (Norrie and de Vries 1978, Baker 1983).

Finite Volume Method (FVM), which combines the advantages of both FDM and FEM, was also applied in CFD during almost the same time as FEM. FVM supports unstructured grids, so it proves advantageous over FDM, which could only support structured grids, and its underlying formulation guarantees the conservation properties of the system. Some early applications of FVM in CFD can be found in Godunov (1959), Gentry and Daly (1966), Runchal (1972), Raithby and Torrence (1974), Van Leer (1974), and Roe (1981) (Patankar 1980, Toro 2009).

Computational Hydraulics had a slightly different process of development. Computational Hydraulics started its journey with Method of Characteristic (MOC) long before FDM had been applied in CFD. MOC was available to solve the shallow water equations since 1889 (Rouse and Ince 1957), and some notable early applications of MOC in Computational Hydraulics are found in the works of Massau (1905), Stoker (1957) and Abott and Verwey (1970) (Liggett and Cunge 1975). Though the method is not used much today for numerical solutions, it still provides the fundamental characteristics of the differential equations and the understanding of the boundary condition requirements (Abott 1979, Cunge and Verway 1980, Chaudhry 2008).

Use of FDM in Computational Hydraulics started almost three decades after its first use in CFD. Some early applications of FDM in Computational Hydraulics can be found in Morgali and Linsley (1965), Liggett and Woolhisher (1967), and

Koren and Kuchment (1967) (Liggett and Cunge 1975).

Applications of FEM in Computational Hydraulics came a few years after its first application in CFD. Some early notable applications of FEM in Computational Hydraulics are by Taylor and Davis (1972), Grotkop (1973), Norton and Orlob (1973) and Partridge and Brebbia (1976) (Gray 1980).

Applications of FVM in Computational Hydraulics started almost three decades later than its first application in CFD. Some early applications of FVM in Computational Hydraulics can be found in Glaister (1987), Alcrudo and Garcia-Navarro (1992), Glaister (1992), and Bermudez and Vazquez (1994) (Toro and Garcia-Navarro 2007).

Most of the aforementioned studies in both CFD and Computational Hydraulics were done by academic researchers. However, besides these, there were also contributions from different governmental and private institutions in both fields.

For example, FLOW-3D (Hirt and Nichols 1988) is a commercial CFD software package developed by Flow Science, Inc; ANSYS Fluent (ANSYS 2009a) and ANSYS CFX (ANSYS 2009b) are two popular commercial CFD software packages developed by ANSYS, Inc; OpenFOAM (OpenCFD 2009) is an open source CFD software package developed by OpenCFD Ltd.

In the development of Computational Hydraulics, the United States Army Corps of Engineers (USACE) was a pioneer. The Hydrologic Engineering Center (HEC) and the Coastal Hydraulics Laboratory (CHL) of USACE developed several hydrodynamic, contaminant transport and sediment models including HEC-RAS (Brunner 2008), RMA2 (Barbara 2006a), HIVEL2D (Berger 1997), RMA4 (Barbara 2008) and SED2D (Barbara 2006b).

Besides USACE, there were some other U.S. government agencies which also supported the development of hydrodynamic models such as FESWMS (FHA 2002), developed by the U.S. Department of Transportation, WASP (Wool and Comer 2004), developed by the U.S. Environmental Protection Agency, and CCHE1D (Wu and Vieira 2002) and CCHE2D (Jia and Wang 2001), developed by the U.S. Department of Agricultural Research Service.

Besides the U.S. agencies, there were contributions from one North American country, i.e., Canada, and from European countries, e.g., France, Denmark, and the Netherlands. River1D (Hicks 2005) and River2D (Steffler and Blackburn 2002) are two hydrodynamic models developed at the University of Alberta, Canada. SOBEK (Dhonida and Stelling 2004) and Delft3D (WL|Delft 2006) were developed at WL|Delft Hydraulics, the Netherlands. MIKE11 (DHI 2003), MIKE21 (DHI 2005) and MIKE3 (DHI 2005) were developed at Danish Hydraulic Institutes (DHI), Denmark. TELEMAC2D (Lang 2010) model was developed by *É*lectrecit*é* de France (EDF).

All of these Computational Hydraulics software packages are now widely used in many practical applications of water resources problems, and all of them are available in the public domain except DHI's softwares.

1.3 Numerical Issues in Computational Hydraulics

Irrespective of the specific numerical method, there are five main issues encountered in Computational Hydraulics. These are: transcritical flow, advection dominated flow, zero/negative depth, presence of bed slope term or source term, and friction dominated flow. The transcritical and advection dominated flow issues are also observed and handled in CFD, especially in the compressible inviscid flow problem, i.e., the Euler equations, and in the mass transport equation. The transcritical flow, advection dominated flow, zero/negative depth, and presence of bed slope term or source term issues are well recorded in the literatures, and hence are only briefly covered in this section. On the contrary, the friction dominated issue has not been studied that much; therefore, this issue is the main focus of this study.

1.3.1 Transcritical Flow Case

The first issue is the stability problem in any transcritical flow. Similar to the Euler equations, the Saint-Venant equations (as derived and presented in section 2.2) are a hyperbolic system of equations and can generate sharp discontinuity in the solution variables due to any variation of the flow geometry, and can produce transcritical flow with a hydraulic jump or bore (Abott 1979, Cunge and Verway 1980, Chaudhry 2008, Toro 2001). Therefore, the numerical scheme used to solve this type of equations should have the capability to capture and handle the shock.

There are two approaches to computing solutions containing discontinuity: the shock-fitting approach and the shock-capturing approach. In the shock-fitting approach, discontinuities are fitted or tracked explicitly, and the rest of the areas are solved by a numerical scheme which is suitable for smooth flows (Toro 2001). While the advantage of this approach is that the discontinuities can be computed as a true discontinuity, the approach becomes too complicated or impossible to apply for multiple dimensions (Toro 2001).

In the shock-capturing approach, a single numerical scheme is used for the complete domain, and shock waves emerge as part of the solution (Toro 2001). The disadvantage of this approach is that the discontinuities are not computed as a true discontinuity; instead, they are smeared or spread over a number of computing cells (Toro 2001). Regardless of its disadvantages, this type of approach is often used in practice due to its simplicity and applicability to any problem.

Both non-conservative and conservative shock-capturing numerical schemes can handle the transcritical flow. However, the conservative schemes are preferable because they produce the correct shock propagation speed (Cunge and Verway 1980, Chaudhry 2008, Toro 2001, Toro 2009). Shock-capturing numerical schemes can be classified into two categories: classical shock-capturing schemes, where linear dissipation is used, that is, equal dissipation is used for all grids (e.g., Lax-Wendroff scheme (Lax and Wendroff 1960) or MacCormack scheme (MacCormack 1969)), and modern shock-capturing schemes, where non-linear dissipation is used, that is, dissipation varies from grid to grid (e.g., Total Variation Diminishing (TVD) schemes and Essentially Non-Oscillatory (ENO) schemes) (Yee 1987).

1.3.2 Advection Dominated Flow Case

The next issue is the stability problem in any advection-diffusion problem. Many fundamental findings of CFD have been developed from the studies with the simple 1D mass transport equation. The 1D mass transport equation can be written as (Patankar 1980, Cunge and Verway 1980, LeVeque 2002):

$$\frac{\partial C}{\partial t} + u\frac{\partial C}{\partial x} = D\frac{\partial^2 C}{\partial x^2} \tag{1.1}$$

where C is the mass per unit volume, u is the average velocity of flow, and D is the mass diffusion coefficient. The Saint-Venant equations can be viewed as a system of advection-diffusion equations. For the 2D Saint-Venant equations, the diffusion terms come from the turbulent stress portion, and for the 1D Saint-Venant equations, the diffusion term is zero.

Eq. 1.1 is a mixed type of a partial differential equation. The equation can be a hyperbolic equation or parabolic equation depending on whether the advection or diffusion term dominates. A non-dimensional parameter called the Peclet number, i.e., $\frac{uL}{D}$, where L is a length scale, is used to define the problem. When $\frac{uL}{D} \geq 2$, the equation becomes advection dominated; otherwise, it is diffusion dominated (Patankar 1980).

Two major problems occur in the case of advection dominated flow. The first one is related to an unsteady flow problem. When a forward explicit time step numerical discretization is used, the time step should be such that the solution propagation over a time step does not exceed the space discretization in order to avoid any stability problem. In other words, for a Δt time step and a Δx space discretization, if the solution propagates with a speed of u, then the condition states that $\frac{u\Delta t}{\Delta x} \leq 1$. This condition is known as the famous CFL condition, named after Courant, Friedrichs, and Lewy (Courant and Lewy 1928). However, an implicit numerical scheme does not need to satisfy this condition in order to get a stable solution (Abott 1979, Cunge and Verway 1980).

The second problem with advection dominated flow is related to a steady state flow problem. When advection dominates, the use of central difference schemes will produce spurious oscillations due to the inability to resolve the boundary layer caused by a fixed value downstream boundary condition (Chung 2002, Brooks and Hughes 1982, Date 2005, Toro 2009). A non-dimensional parameter called the grid Peclet number, $\frac{u\Delta x}{D}$, is used to define the problem. When $\frac{u\Delta x}{D} \geq 2$, any central difference scheme will produce spurious wiggles (Chung 2002, Brooks and Hughes 1982, Date 2005, Toro 2009). As the Saint-Venant equations are a system of advection type equations, they are not free from this problem.

Reducing Δx is one way to eliminate the spurious oscillations, and applying artificial diffusion is the other way to suppress these oscillations. Artificial diffusion is normally applied by considering an upwind numerical scheme. For the 1D mass transport equation, i.e., Eq. 1.1, the upwinding is achieved by applying a one-sided upwinding based on the flow direction. For example, when flow direction is positive, the upwinding is done for FDM by taking the backward finite difference; for FVM it is done by taking the upstream cell value as a flux at the cell interface; for FEM it is done by putting more weight on the upstream node.

However, the simple one-sided upwind scheme based on the flow direction produces an unstable scheme for a system of hyperbolic equations, e.g., the Euler equations or the Saint-Venant equations (Ying and Wang 2004, Toro 2009). For a system of hyperbolic equations, different eigenvalues with different directions (signs) could be possible; therefore, a simple one-sided upwind numerical scheme based on the flow direction may not give upwinding for all the eigenvalues.

The remedy to this problem is to do the upwinding based on the wave propagation direction embodied in the eigenvalues of the system of hyperbolic equations, and this remedy is a key philosophy behind the Godunov upwind scheme (Godunov 1959). The Godunov scheme is a shock-capturing scheme as well, and it was in the center of focus in both CFD and Computational Hydraulics for the last forty years. Several numerical schemes were developed based on this philosophy in FDM, FEM, and FVM (e.g., Van Leer 1979, Roe 1981, Harten and Van Leer 1983, Steger and Warming 1981, Brooks and Hughes 1982, Hicks and Steffler 1992, Hubbard and Garcia-Navarro 2000).

The early schemes, e.g., Godunov's (1959) and Roe's (1981), are of first-order upwind schemes and thus over-diffusive; therefore, higher-order upwind schemes were sought. There are also some linear higher-order schemes (e.g., Lax-Wendroff scheme (Lax and Wendroff 1960) or MacCormack scheme (MacCormack 1969)) which are centered-difference in space but still dissipative because of the dissipation term present in the time discretization. However, these schemes produce spurious wiggles in the vicinity of the discontinuity or the sharp gradient (Cunge and Verway 1980, LeVeque 2002, Chung 2002, Toro 2009).

TVD (Total Variation Diminishing) schemes (e.g., Van Leer 1974, Harten and

Van Leer 1983, Osher 1984) are developed where higher-order schemes are used in the smooth regions and first-order upwind schemes are used in the discontinuous regions of a flow. The switch from a higher-order scheme to a first-order scheme is done using some sort of limiters, e.g., slope limiters or flux limiters. Essentially non-oscillatory (ENO) higher-order upwind schemes (e.g., Harten and Osher 1987) are also developed where higher-order polynomial data reconstruction is used.

The above-mentioned high resolution schemes are mainly of FDM and FVMs. However, there are also finite element high resolution schemes, e.g., Brooks and Hughes (1982), Katopodes (1984*a*), and Hicks and Steffler (1992), which are philosophically similar to the Godunov type scheme and produce better results than the linear higher-order schemes.

1.3.3 Zero/Negative Depth Flow Case

The third issue is the zero/negative depth case or the wetting/drying problem. The solution becomes indeterminate or imaginary when the depth becomes zero or negative. Flood plain modeling, tidal flow modeling, dam break flow modeling, and low flow fish habitat modeling all face this problem. Handling the wetting/drying problem properly is important as it can produce spurious velocities or can calculate an incorrect speed of the wetting/drying front (Bates and Hervouet 1999).

Two approaches are used to handle the wetting/drying problem: one is the Eulerian approach, where the computational domain is fixed, and the other is the Lagrangian approach, where the computational domain evolves with the position of a moving boundary (Tchamen and Kahawita 1998, Bates and Hervouet 1999, Defina 2000, Heniche and Leclerc 2002). For practical modeling, it appears that the Eulerian approach is easier to use than the Lagrangian approach, as the Lagrangian approach is harder to program and is complicated to apply, especially with complex topography (Tchamen and Kahawita 1998, Bates and Hervouet 1999, Defina 2000, Heniche and Leclerc 2002).

In either case, the common practice is to use a minimum depth to set the velocity to zero, to switch to an alternate equation, or to remove dry nodes from the computational domain. For example, Lynch and Gray (1980) used the Lagrangian approach; Tchamen and Kahawita (1998) and Dietrich (2006) used a reduced momentum equation, i.e., dropping inertia terms; Bates and Hervouet (1999), Defina (2000), and Heniche and Leclerc (2002) used modified Saint-Venant equations, i.e., adding porosity to the equations; and the River2D model (Steffler and Blackburn 2002) and Khan (2000) used a ground water equation for the dry nodes.

However, there is no definite criterion for setting a minimum depth. A wide range of minimum depths is suggested for applied modeling, e.g., 0.01 m in the River2D model (Steffler and Blackburn 2002), 0.02 m to 0.05 m in the CCHE2D model (Jia and Wang 2001), and 0.005 m to 0.1 m in the MIKE21 model (DHI 2005). This indicates that a criterion for setting up the minimum depth would be beneficial for practical modeling.

1.3.4 Presence of Bed Slope Term Case

The fourth issue is the handling of the bed slope term in the Saint-Venant equations. Most of the schemes used in the Computational Hydraulics were developed with a homogenous set of equations, i.e., the Euler equations, but are also applied to non-homogenous equations. The source terms in the Saint-Venant equations include the bed slope term and the friction term. However, most of the studies related to the source terms issue mainly deal with the bed slope term.

Evidently, the presence of the bed slope term is important in Computational Hydraulics, especially in non-level bed channels. Special numerical treatment is required to handle it correctly, especially for the finite volume schemes (Bradford and Sanders 2005, Toro and Garcia-Navarro 2007, Petaccia and Zech 2009). Hubbard and Garcia-Navarro (2000) showed that if the bed slope term or the source terms are not properly balanced with the flux terms, then for a steady state case, the discharge solutions at the cell centers may not be balanced, and spurious oscillations in the steady state discharge solutions may appear. Such oscillations in the steady state discharge solutions with non-balanced or point source Godunov schemes have been reported by several researchers (e.g., Bradford and Sanders 2005, Petaccia and Zech 2009, Hubbard and Garcia-Navarro 2000, Zhou and Ingram 2001).

Different techniques to handle the non-level bed in FVM have been proposed (Bermudez and Vazquez 1994, Nujic 1995, LeVeque 1998, Hubbard and Garcia-Navarro 2000, Zhou and Ingram 2001, Galloute and Sequin 2003). LeVeque (1998) used the fractional step method to handle the bed slope term, but this method provides relatively poor solutions for quasi-steady or steady problems (Bradford and Sanders 2005). More effective are the proposals of Bermudez and Vazquez (1994), who have proposed the upwinding of the bed slope term to be taken as consistent with the flux term, and Hubbard and Garcia-Navarro (2000), who extended their method to the higher-order accuracy method.

Nujic (1995) proposed the reconstruction of water surface elevation instead of primitive variable depth, and Zhou and Ingram (2001) extended the method to the higher-order accuracy method and named the method the Surface Gradient Method (SGM). Galloute and Sequin (2003) assumed the bathometry as a piece-wise constant and solved the Riemann problem for the difference in bed elevation at the cell boundaries. All of these schemes are mainly concerned with ensuring constant water level with non-level beds under a quiescent flow test condition, which is also known as a C-property test.

1.3.5 Friction Dominated Flow Case

The last and least discussed issue is the friction term dominated case. The above-mentioned studies dealing with source terms have not taken the friction term as a separate issue, and therefore, left the need for the friction term to be investigated in more depth. Balancing the source terms or ensuring the C-property solves one part of the source term problem, but does not solve the whole problem.

The friction term becomes more important when the depth is small, the discretization is large, the roughness is high, or the slope is steep. A typical problematic situation is a reach of rapids in a stream or river. Problem with the small depth was first explicitly mentioned by Cunge and Verway (1980) on page 175: "In certain situations, computational difficulties develop when physical flow depths are small, usually when flood waters first appear in dry channels or on the flood plain, and we refer to these difficulties when we speak of the 'small depth problem'."

This observation is also supported by various reports of spurious velocities at the flow boundaries in 2D models due to the small depths (e.g., Bates and Hawkes 1997, Tchamen and Kahawita 1998, Heniche and Leclerc 2002, Dietrich 2006). For example, Tchamen and Kahawita (1998) observed numerical instabilities in the form of negative depth and/or too large of a velocity within cells that are partially wet due to small depth. Dietrich (2006) also observed oscillations and instabilities in regions with steep bathymetry when a thin film of water was allowed to flow uninterrupted.

Similar spurious velocities have been experienced with the River2D model. Fig. 1.1 shows a typical velocity vector solution in the River2D model which shows spurious velocity vectors near the boundaries. We suspect that these spurious velocities are a result of small depths, i.e., the friction dominated case. This is the motivation for undertaking this study and for studying the friction dominated case in detail.

Most of the time, the small depth problems can trigger the zero/negative depth problems and can be taken care of by the wetting/drying algorithm using some minimum depths, and this makes it even more difficult to distinguish the friction dominated cases from the others. However, depending on the discretization size or the slope, the friction term dominated cases can occur at a higher depth than the practical minimum depths (e.g., 0.01 or 0.05 cm), when we may still see spurious velocities.

Among the available literatures, very few studies have focused on the friction dominated problem. The few studies that do exist can be classified into two broad categories. In the first category, the restriction over the time step due to the friction dominated case has been the focus. The very first work found in this category is by Liggett and Cunge (1975). They proposed an extra criterion for explicit schemes that helps to limit the time step in the case of friction domination in addition to the CFL conditions. Recently, Burguete and Murillo (2008) also presented another criterion on the time step discretization based on limiting the friction force, and this stability criterion is also used by Liang and Marche (2009) and Berthon and Turpault (2011). However, the additional restriction on the time step can be avoided by using an implicit discretization of the friction term (Liggett and Cunge 1975, Burguete and Gracia-Palacin 2007, Burguete and Murillo 2008).

The next category is the stability issue in any steady state flow due to the friction dominated case. The restriction over the time step is not necessary in this case. However, stability problems may arise when spatial discretization becomes large and the effect of the friction term becomes significant. One of the works that has been found in the existing literature is by Burguete and Gracia-Palacin (2007), who proposed a stability constraint on spatial discretization due to the friction dominated case, considering the flow on a simple adverse slope with a flat water surface. Their proposed criterion is:

$$\Delta x \leq \frac{2R^{4/3}}{gn^2} \tag{1.2}$$

where Δx is the spatial discretization, R is the hydraulic radius, g is the gravitational acceleration and n is the Manning's roughness coefficient. They showed with the numerical solutions of very small depth flows in an irrigation channel that Eq. 1.2 has to be satisfied in order to get an oscillation-free wet/dry front (Burguete and Gracia-Palacin 2007).

1.4 Objectives

The previously-mentioned high resolution schemes, i.e., TVD and ENO schemes, ensure non-oscillatory solutions for the advection dominated and transcritical flow cases, but they do not guarantee non-spurious solutions when the friction term dominates in the Saint-Venant equations (Cunge and Verway 1980, Toro and Garcia-Navarro 2007, Burguete and Murillo 2008). Moreover, it was found that all the studies that dealt with the source terms focused on the bed slope term only. In particular to the friction dominated issue, one study, i.e., Burguete and Gracia-Palacin (2007), looked at the steady state friction dominated case. However, their restriction over the spatial discretization, i.e. Eq. 1.2, was developed from a simplified test case with the simplified form of the Saint-Venant equations. The friction dominated problem has not been studied so far using the complete Saint-Venant equations. In addition to these, there is no straight method to define or distinguish the friction dominated case, which is also needed to be set up.

Therefore, in this research our main objective is to study and to understand the friction dominated issue with the full Saint-Venant equations. This will lead us to a stable numerical scheme that can be applicable to a wide range of practical water resources problems.

The following specific objectives will lead us to achieve our main objective. Our specific objectives are:

- To develop a framework analysis to study the friction dominated issue. Because there have not been any studies on this particular issue using the full Saint-Venant equations, a framework analysis which can be applicable to a wide range of numerical schemes is needed.

- To identify the different dimensional parameters that affect the friction dominated case and to understand their effect.

- To formulate the non-dimensional parameters that may affect the friction dominated case and to understand their effect. The friction dominated problem can be analogous to the advection dominated problem. Similar to the grid Peclet number, one or more non-dimensional parameters and their critical values could be found for the friction dominated problem.

- To find a suitable numerical scheme that will be stable and non-oscillatory for the friction dominated case. Analogous to the upwinding schemes for the advection dominated case, similar numerical schemes can be found for the friction dominated case.

- To understand the friction dominated problem in the 2D flow case. Similar or equivalent non-dimensional parameters found with the 1D Saint-Venant equations can be found for the 2D Saint-Venant equations. From the practical application point of consideration, this is the most important objective of this study.

1.5 Methodology

In this research we will study the 1D Saint-Venant equations in depth. While our ultimate goal is to apply the findings in 2D models, studying the 1D Saint-Venant equations can provide us with sufficient knowledge of the problem to do so.

We focus on the steady state solutions of the 1D Saint-Venant equations; the friction dominated flow can be seen in both transient and steady flow cases. To eliminate the effects of the transient issue, we have limited ourselves to steady state solutions. However, the transient model is still used to obtain the final steady state solutions.

We have also limited ourselves to the sub-critical flow regime. While topographic variations necessitate that some local areas in open channels can have super-critical flow, flow in most areas is in the sub-critical regime. Therefore, to avoid any trans-critical flow issue, we mainly focus on the sub-critical flow regime.

The friction term becomes dominant when the depth is small, the discretization is large, or the roughness is high. To see these parameters' effects on the solution variables, we do non-linear model analysis. In this analysis, final steady state solutions are solved for a simple non-uniform flow test case, where two abrupt slope changes are introduced to create a non-uniform sub-critical flow. We then run this test case using different discretizations, roughnesses, and slopes, and observe their effects on the solution variables.

To find the non-dimensional parameters and their effects, we do Fourier analysis of the linearized non-dimensional form of the Saint-Venant equations, which includes the bed slope and the friction term. The discrete form of the non-dimensional Saint-Venant equations give us the non-dimensional parameters. In the Fourier analysis, a periodic bed perturbation is introduced and the effects on the solution variables are observed.

As a side note, it is not feasible to cover all the numerical schemes available in the Computational Hydraulics field within the time period of this study. Therefore, we have limited our focus to two schemes from each numerical method, such that it covers both shock-capturing and non-shock-capturing schemes as well as balanced and non-balanced numerical schemes. While we have limited our study to just a few numerical schemes, the analysis can be applied to a wide range of numerical schemes.

From FDM, we have taken the box finite difference scheme (Preissmann 1961) and the MacCormack scheme (MacCormack 1969); from FEM, we have studied the Bubnov-Galerkin scheme (Baker 1983) and the Characteristic Dissipative Galerkin (CDG) scheme (Hicks and Steffler 1992); finally, from FVM, we have taken two first-order shock-capturing finite volume schemes: a balanced Godunov scheme (Hubbard and Garcia-Navarro 2000) and a one-sided upwind-downwind scheme (Ying and Wang 2004). The box finite difference scheme and the Bubnov-Galerkin finite element scheme are non-shock-capturing schemes, and the rest are shock-capturing schemes.

Once we understand the friction dominated problem with 1D Saint-Venant equations, we move forward to the 2D flow problem. Similar or equivalent parameters to the 1D non-dimensional parameters can be found for the 2D model. Subsequently, the non-dimensional parameters' effects can be investigated with 2D flow test case. In this research, two test cases (flow past a submerged groin and flow in a natural river) have been used for that purpose and we use the River2D (Steffler and Blackburn 2002) model for this stage.

1.6 Organization of the Thesis

The organization of this thesis is as follows. In chapter 2, the governing equations for the open channel flow, i.e. the 1D Saint-Venant equations, are derived, and different forms of the 1D Saint-Venant equations are presented. The linearized and the non-dimensionalized forms of the 1D Saint-Venant equations are also presented in this chapter.

Chapter 3 presents the framework analysis to study the 1D steady state friction dominated Saint-Venant equations. Both non-linear model analysis and Fourier analysis are presented in this chapter.

In the following six chapters, the six numerical schemes are investigated for the friction dominated case with the framework analysis, and the results are presented.

Chapter 10 outlines the general discussions on the friction dominated problem based on the results of the previous six chapters. Different utilities and the significance of the current study are also presented in this chapter.

In chapter 11, the non-dimensional parameter identified from the framework analysis of the 1D model is extended to the 2D model. The results from the 2D idealized test case and the natural river test case are presented in this chapter.

Chapter 12 presents conclusions and future recommendations for further research. Finally, the coefficients used in the Fourier analysis for different numerical schemes are presented in appendices.

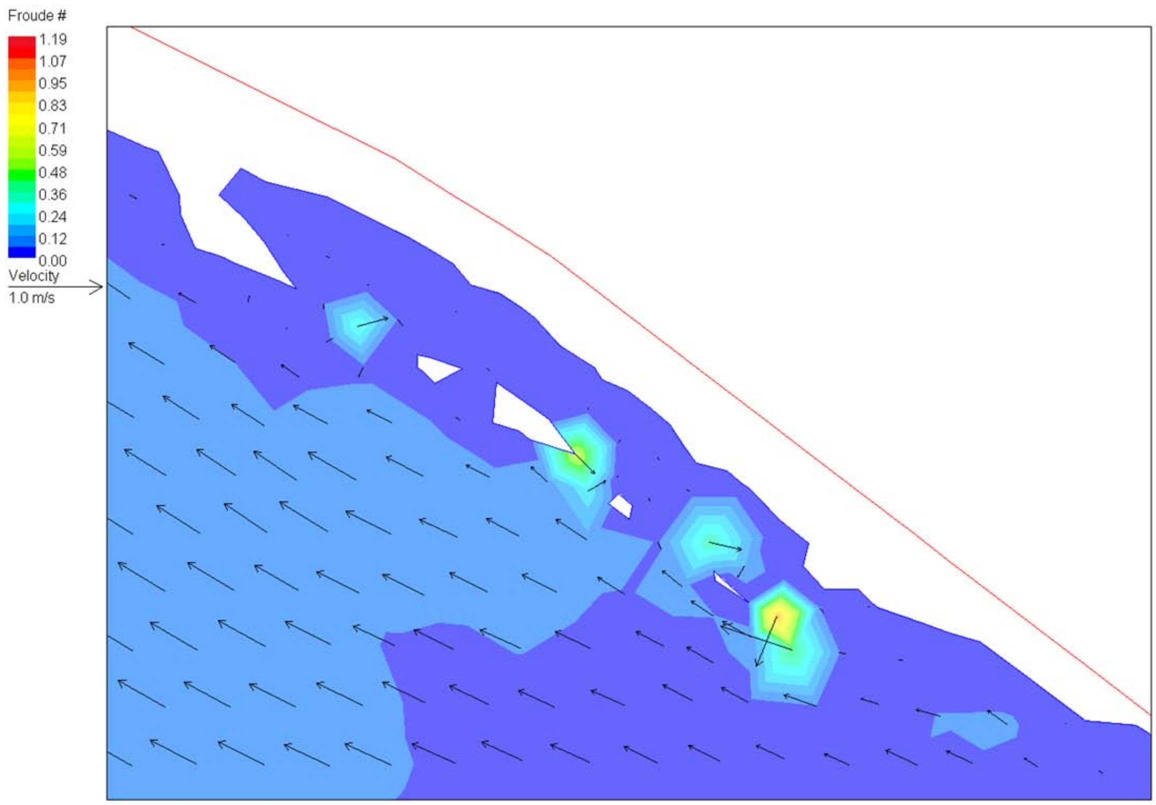

Figure 1.1: A typical Froude number contour and velocity vectors plot with the River2D open channel flow model.

Chapter 2

Governing Equations

2.1 Introduction

Three conservation laws - mass, momentum, and energy - are used to describe open channel flows (Abott 1979, Cunge and Verway 1980, Chaudhry 2008). In 1D open channel flows, two independent variables, such as the flow depth and velocity or the flow depth and discharge, are needed to describe the flow conditions. Therefore, two governing equations are required to express a 1D flow. The conservation of mass and momentum or the conservation of mass and energy laws can be used in this case.

The expression of a 1D flow can be either continuous or not continuous. If flow variables are not continuous, such as in the hydraulic jump or bore, the conservation of mass and momentum should be used, and if flow variables are continuous, either of the two sets of laws can be used (Cunge and Verway 1980, Chaudhry 2008). Since the conservation of mass and momentum laws are applicable to both continuous and discontinuous situations, this set of laws is the most often used in open channel hydraulics (Cunge and Verway 1980, Chaudhry 2008).

2.2 1D Saint-Venant Equations

The Saint-Venant equations (Saint-Venant 1871) comprise the fundamental mathematical description governing the depth and average velocity in both 1D and 2D open channel flows (Chow 1959, Cunge and Verway 1980, Chaudhry 2008, Chanson 1999). These equations have been studied extensively both analytically and numerically. The basic assumptions needed to derive the 1D Saint-

Venant equations as well as derivations of these equations are well presented in many books pertaining to open channel hydraulics and Computational Hydraulics (e.g., Chow 1959, Liggett 1975, Abott 1979, Cunge and Verway 1980, Chanson 1999, Chaudhry 2008, Szymkiewicz 2010). Since our main focus is on the 1D Saint-Venant equation, the assumptions and derivations for these equations are presented in this chapter. Moreover, different forms of the 1D Saint-Venant equations including the linearized and non-dimensionalized forms of the equations are also presented here.

2.2.1 Basic Assumptions

The basic assumptions in deriving the Saint-Venant equations are as follows (Cunge and Verway 1980, Hicks 1990, Chaudhry 2008):

- the flow is one-dimensional, i.e., velocity is in the direction of the channel;
- the streamline curvature is small and the vertical accelerations are negligible, hence the pressure distribution is hydrostatic;
- the velocity distribution is uniform over the cross-section;
- the channel bed slope is small enough that $\sin\phi$ may be replaced by $\tan\phi$ and $\cos\phi$ by unity, where, ϕ is the angle between the channel bed and the horizontal;
- frictional resistance formulae for steady uniform flow are applicable to unsteady non-uniform flow;
- the dependent variables are continuous differentiable functions;
- the channel is prismatic;
- no lateral flows occur;
- the fluid (water) is incompressible;
- shear stress on the surface due to wind is negligible.

2.2.2 Conservation of Mass

The conservation of mass states that the mass within a closed system remains constant with time. Therefore, for a control volume, as shown in Fig. 2.1, and for a system without any lateral inflows, the net rate of change in fluid mass within the control volume must equal the net rate of inflow of fluid mass into the control volume (Cunge and Verway 1980, Hicks 1990, Chaudhry 2008).

$$\frac{\partial}{\partial t}\int_{x1}^{x2} \rho A dx = \rho Q_1 - \rho Q_2 \tag{2.1}$$

where ρ is the density of the fluid, in this case water. A is the area of the cross-section and Q_1 and Q_2 are the discharges acting on the upstream (x_1) and the downstream (x_2) end, respectively. x and t are the space and time coordinates, respectively. Applying the mean value theorem of calculus (Chaudhry 2008), Eq. 2.1 becomes:

$$\frac{\partial}{\partial t}\int_{x1}^{x2} \rho A dx = -\int_{x1}^{x2} \frac{\partial}{\partial x}(\rho Q) dx \tag{2.2}$$

where Q is the discharge. As for most of the practical cases, the density of water is constant (Chaudhry 2008, Hicks 1990), and since x_1 and x_2 are two arbitrary locations, Eq. 2.2 becomes:

$$\frac{\partial A}{\partial t} + \frac{\partial Q}{\partial x} = 0 \tag{2.3}$$

which is generally known as the continuity equation.

2.2.3 Conservation of Momentum

The conservation of momentum states that for the control volume as shown in Fig. 2.2, the net rate of change of momentum in a control volume is equal to the summation of all forces ($\sum F$) acting on the control volume plus net momentum influx along the longitudinal direction (Liggett 1975, Cunge and Verway 1980, Chaudhry 2008). Thus we can write:

$$\sum F = \frac{\partial}{\partial t}\int_{x1}^{x2} \rho Q dx + \rho Q_2 u_2 - \rho Q_1 u_1 \tag{2.4}$$

where u_1 and u_2 are the cross-sectional average velocities acting on the upstream and downstream end of the control volume. As we can see in Fig. 2.2, there are four forces: two pressure forces (Fp_1 and Fp_2); one gravitational force (F_g); and one frictional force (F_f), acting on the control volume. So:

$$\sum F = Fp_1 - Fp_2 + F_g - F_f \tag{2.5}$$

The pressure forces are (Chaudhry 2008):

$$Fp_1 = \rho g A_1 \bar{h}_1 \tag{2.6}$$

and:

$$Fp_2 = \rho g A_2 \bar{h}_2 \tag{2.7}$$

where g is the gravitational acceleration, and $\bar{h}_1$ and $\bar{h}_2$ are the depths of the centroid of flow area A_1 and A_2, respectively. Furthermore, the gravitational force can be taken as the component of weight of the water in the control volume in the longitudinal direction:

$$F_g = \int_{x1}^{x2} \rho g A \sin\phi dx \tag{2.8}$$

As the channel bed slope is small, $\sin\phi$ can be replaced with $\tan\phi$ or the channel bed slope, S_b, itself. So,

$$\sin\phi = -\frac{dz}{dx} \approx \tan\phi = S_b \tag{2.9}$$

where z is the bed elevation. Therefore, Eq. 2.8 becomes:

$$F_g = \int_{x1}^{x2} \rho g A S_b dx \tag{2.10}$$

The frictional force due to the shear between water and channel sides and channel bottom may be expressed in terms of friction slope, S_f (Cunge and Verway 1980, Chaudhry 2008):

$$F_f = \int_{x1}^{x2} \rho g A S_f dx \tag{2.11}$$

In this study the frictional slope is evaluated using Chezy's equation:

$$u = C_* \sqrt{gRS_f} \tag{2.12}$$

where u is the cross-sectional average velocity, C_* is the non-dimensional Chezy coefficient and R is the hydraulic radius equal to $\frac{A}{P}$. P is the wetted perimeter of a cross-section. C_* can be calculated from Manning's roughness coefficient, n, as (Chow 1959, Chaudhry 2008)

$$C_* = \frac{R^{1/6}}{n\sqrt{g}} \tag{2.13}$$

where n is in SI units. After applying Eq. 2.5 to 2.11 to Eq. 2.4 we get:

$$\frac{\partial}{\partial t}\int_{x1}^{x2} \rho Q dx + \rho Q_2 u_2 - \rho Q_1 u_1 = \rho g A_1 \bar{h}_1 - \rho g A_2 \bar{h}_2 + \int_{x1}^{x2} \rho g A S_b dx - \int_{x1}^{x2} \rho g A S_f dx \tag{2.14}$$

Applying the mean value theorem of calculus (Chaudhry 2008), Eq. 2.14 becomes:

$$\frac{\partial}{\partial t}\int_{x1}^{x2} \rho Q dx + \int_{x1}^{x2} \frac{\partial(\rho Q u)}{\partial x} dx = -\int_{x1}^{x2} \frac{\partial(\rho g A \bar{h})}{\partial x} dx + \int_{x1}^{x2} \rho g A S_b dx - \int_{x1}^{x2} \rho g A S_f dx \tag{2.15}$$

As for most of the practical cases, the density of water is constant (Chaudhry 2008, Hicks 1990), and since x_1 and x_2 are two arbitrary locations, we find:

$$\frac{\partial Q}{\partial t} + \frac{\partial (Qu)}{\partial x} + \frac{\partial (g A \bar{h})}{\partial x} = gA(S_b - S_f) \tag{2.16}$$

Eq. 2.16 is commonly known as the momentum equation in longitudinal direction.

Eq. 2.3 and Eq. 2.16 together are known as the Saint-Venant (1871) equations for one-dimensional open channel flow in a prismatic channel without any lateral inflows.

2.2.4 For a Wide Rectangular Channel

In this study, we have assumed the channel to be a wide rectangular channel of a width B. So, for a wide rectangular channel, Eq. 2.3 and Eq. 2.16 can be written as (Cunge and Verway 1980, Chaudhry 2008):

$$\frac{\partial h}{\partial t} + \frac{\partial q}{\partial x} = 0 \tag{2.17}$$

and

$$\frac{\partial q}{\partial t} + \frac{\partial (\frac{q^2}{h})}{\partial x} + \frac{\partial (\frac{gh^2}{2})}{\partial x} = gh(S_b - S_f) \tag{2.18}$$

where q is the per unit width discharge equal to $\frac{Q}{B}$, and h is the depth.

2.3 Different Forms of the 1D Saint-Venant Equations

2.3.1 Conservative Form

Eq. 2.3 and Eq. 2.16, or Eq. 2.17 and Eq. 2.18, are known as the conservative form of the Saint-Venant equations, because the equations are written in terms of the conserved variables. The conservative form of the Saint-Venant equations is mainly used in Computational Hydraulics as this form gives the correct propagation speed of a shock (Cunge and Verway 1980, Chaudhry 2008, Toro 2001). In our study, this form of equations is used in most numerical schemes, except for one particular numerical scheme, i.e., the one-sided upwind-downwind finite volume scheme.

We can write Eq. 2.17 and Eq. 2.18 in a matrix form as:

$$\frac{\partial \mathbf{U}}{\partial t} + \frac{\partial \mathbf{F}(\mathbf{U})}{\partial x} = \mathbf{S}(\mathbf{U}) \tag{2.19}$$

where $\mathbf{U}$, $\mathbf{F}(\mathbf{U})$, $\mathbf{S}(\mathbf{U})$ are, respectively, the vectors of the conserved variables, fluxes, and sources, defined as follows: $\mathbf{U} = \begin{bmatrix} h \\ q \end{bmatrix}$, $\mathbf{F}(\mathbf{U}) = \begin{bmatrix} q \\ \frac{q^2}{h} + \frac{gh^2}{2} \end{bmatrix}$, $\mathbf{S}(\mathbf{U}) = \begin{bmatrix} 0 \\ gh(S_b - S_f) \end{bmatrix}$.

2.3.2 Non-conservative Form

When the derivatives in the Saint-Venant equations are written in terms of the solution variables, $\mathbf{U}$, rather than the fluxes, $\mathbf{F}$, the equations are called as the non-conservative form of the Saint-Venant equations (Cunge and Verway 1980, Chaudhry 2008). Though this form of equations does not produce the correct shock speed, this form is still used in certain cases, e.g., for obtaining the linearized form of the Saint-Venant equations, and for evaluating wave propagation directions and speeds for numerical upwinding purposes. The non-conservative form of Eq. 2.19 can be written as:

$$\frac{\partial \mathbf{U}}{\partial t} + \mathbf{A}\frac{\partial \mathbf{U}}{\partial x} = \mathbf{S}(\mathbf{U}) \tag{2.20}$$

where $\mathbf{A}$ is the Jacobian of the Saint-Venant equations which is equal to $\frac{\partial \mathbf{F}}{\partial \mathbf{U}}$. $\mathbf{U}$, $\mathbf{F}(\mathbf{U})$, and $\mathbf{S}(\mathbf{U})$ are the same as in Eq. 2.19. $\mathbf{A}$ For Eq. 2.19 can be written as:

$$\mathbf{A} = \begin{bmatrix} 0 & 1 \\ (gh - u^2) & 2u \end{bmatrix} \tag{2.21}$$

2.3.3 Partial-conservative Form

The partial derivative of the pressure force in Eq. 2.18, i.e., $\frac{\partial(\frac{gh^2}{2})}{\partial x}$, can be written in non-conservative form, i.e., $gh\frac{\partial h}{\partial x}$. This term can then be taken to the right hand side of the equation and added to the gravitational force term, i.e., $-gh\frac{\partial z}{\partial x}$. This alteration places the equation in terms of the derivative of the water surface elevation, i.e., $-gh\frac{\partial H}{\partial x}$, where H is the water surface elevation equal to $h + z$.

Several researchers, such as Nujic (1995), Zhou and Ingram (2001), and Ying and Wang (2004), found that this form of the Saint-Venant equations is suitable to use with non-level beds. As this form of equations does not use the full non-conservative form, i.e., Eq. 2.20, nor the full conservative form, i.e., Eq. 2.19, we call this form of equations the partial-conservative form of the 1D Saint-Venant equations. In our study, the partial-conservative form of equations is used for one particular numerical scheme, i.e., the one-sided upwind-downwind finite volume scheme. The partial-conservative form of the 1D Saint-Venant equations can be written in matrix form as:

$$\frac{\partial \mathbf{U}}{\partial t} + \frac{\partial \mathbf{F}(\mathbf{U})}{\partial x} = \mathbf{S}(\mathbf{U}) \tag{2.22}$$

where $\mathbf{U}$, $\mathbf{F}(\mathbf{U})$, and $\mathbf{S}(\mathbf{U})$ can be defined as follows: $\mathbf{U} = \begin{bmatrix} h \\ q \end{bmatrix}$, $\mathbf{F}(\mathbf{U}) = \begin{bmatrix} q \\ \frac{q^2}{h} \end{bmatrix}$, $\mathbf{S}(\mathbf{U}) = \begin{bmatrix} 0 \\ -gh\frac{\partial H}{\partial x} - ghS_f \end{bmatrix}$.

2.3.4 Linearized Form

The linearized form of the 1D Saint-Venant equations is often used in Computational Hydraulics. This form simplifies the Saint-Venant equations, which allows us to do theoretical analysis on the equations, such as Fourier analysis (e.g., Ponce 1977, Abott 1979, Cunge and Verway 1980, Katopodes 1984*b*, Hicks and Steffler 1992). The non-conservative form of the Saint-Venant equations, i.e., Eq. 2.20, is used for the linearization process.

The linearized form of the 1D Saint-Venant equations are derived by taking $h = h_0 + h'$ and $q = q_0 + q'$, where h_0 and q_0 are the average quantities and h' and q' are the small amplitude perturbations to them, respectively. Similarly we can take $z = z_0 + z'$, where z_0 is the bed elevation corresponding to the average bed slope S_0, where $S_0 = -\frac{dz_0}{dx}$ and z' represents the small perturbation to z_0. Neglecting the products of the small perturbations, Eq. 2.20 becomes:

$$\frac{\partial h'}{\partial t} + \frac{\partial q'}{\partial x} = 0 \tag{2.23}$$

for the continuity equation, and:

$$\frac{\partial q'}{\partial t} + 2u_0\frac{\partial q'}{\partial x} + (gh_0 - u_0^2)\frac{\partial h'}{\partial x} = \frac{u_0}{h_0C_*^2}(-2q' + 2u_0h') - \frac{u_0^2}{C_*^2} - gh_0\frac{dz_0}{dx} - gh'\frac{dz_0}{dx} - gh_0\frac{dz'}{dx} \tag{2.24}$$

for the momentum equation, where u_0 is the average velocity equal to $\frac{q_0}{h_0}$. Assuming the base or average flow as a uniform flow one can write the Chezy's uniform flow formula as:

$$u_0^2 = C_*^2 gh_0S_0 = -C_*^2 gh_0\frac{dz_0}{dx} \tag{2.25}$$

Applying Eq. 2.25 to Eq. 2.24 we find:

$$\frac{\partial q'}{\partial t} + 2u_0\frac{\partial q'}{\partial x} + (gh_0 - u_0^2)\frac{\partial h'}{\partial x} = \frac{u_0}{h_0C_*^2}(-2q' + 3u_0h') - gh_0\frac{dz'}{dx} \tag{2.26}$$

The linearization process followed in this study is similar to other studies done by Liggett (1975), Cunge and Verway (1980), and Hicks (1990). However, in those studies, they did not perturb the channel bed elevation, and the perturbation of the bed elevation is the most important aspect of this study. By perturbing the bed elevation, we can observe the effect of the bed perturbation on the solution variable perturbations.

2.3.5 Non-dimensional Linearized Form

The non-dimensional form of the Saint-Venant equations is used to obtain the non-dimensional parameters that may affect the solution variables. In this study, the Fourier analysis is performed on this form of equations. The non-dimensional form is found using the linearized form of the Saint-Venant equations, i.e., Eq. 2.23 and 2.26.

The non-dimensional form of the equations 2.23 and 2.26 is found by taking: $\varphi = \frac{q'}{q_0}$, $\eta = \frac{h'}{h_0}$, $\zeta = \frac{z'}{h_0}$, $\xi = \frac{x}{L}$, $\tau = \frac{t}{T} = \frac{tu_0}{L}$, where, φ, η, ζ, ξ, and τ are the non-dimensional discharge perturbation, depth perturbation, bed elevation perturbation, longitudinal coordinate, and time coordinate, respectively. L and T are the characteristic length and time scale, respectively. Inserting these variables, Eq. 2.23 becomes:

$$\frac{\partial \eta}{\partial \tau} + \frac{\partial \varphi}{\partial \xi} = 0 \tag{2.27}$$

and Eq. 2.26 becomes:

$$\frac{\partial \varphi}{\partial \tau} + 2\frac{\partial \varphi}{\partial \xi} + (\frac{gh_0}{u_0^2} - 1)\frac{\partial \eta}{\partial \xi} = \frac{L}{h_0 C_*^2}(-2\varphi + 3\eta) - \frac{gh_0}{u_0^2}\frac{d\zeta}{d\xi} \tag{2.28}$$

If we define $Fr_0 = \frac{u_0}{\sqrt{gh_0}}$, and $\beta = \frac{L}{h_0 C_*^2}$, where Fr_0 is called the average flow Froude number and β can be called the Friction number, respectively, then Eq. 2.28 becomes:

$$\frac{\partial \varphi}{\partial \tau} + 2\frac{\partial \varphi}{\partial \xi} + (\frac{1}{Fr_0^2} - 1)\frac{\partial \eta}{\partial \xi} = \beta(-2\varphi + 3\eta) - \frac{1}{Fr_0^2}\frac{d\zeta}{d\xi} \tag{2.29}$$

In flood routing models, β is called the kinematic flow number because it is associated with the kinematic wave flood propagation (Miller and Cunge 1975, Woolhiser 1975). In this study, however, we will call this the Friction number, as this represents the relative importance of the friction term in the Saint-Venant equations.

2.4 2D Saint-Venant Equations

2D depth averaged shallow water modeling is currently applied to a variety of river problems (Waddle 2009, Katopodis 2003, Leclerc and Bechara 2003). Common applications include flow around hydraulic structures, fish habitat modeling, ice modeling, and morphology modeling. 2D modeling has become popular because of its ability to capture local variations as well as better visualization and description of the flow physics compared to 1D simulation (Katopodis 2003, Leclerc and Bechara 2003).

2D models include in an additional (lateral) coordinate, y, and therefore, an additional equation is also required which can be taken as the conservation of momentum in the y-direction. The 2D Saint-Venant equations of open channel flow are written as (Cunge and Verway 1980, Chaudhry 2008, Steffler and Blackburn 2002):

$$\frac{\partial h}{\partial t} + \frac{\partial q_x}{\partial x} + \frac{\partial q_y}{\partial y} = 0 \tag{2.30}$$

$$\frac{\partial q_x}{\partial t} + \frac{\partial (uq_x)}{\partial x} + \frac{\partial (vq_x)}{\partial y} + \frac{g}{2}\frac{\partial (h^2)}{\partial x} = gh(S_{bx} - S_{fx}) + \frac{1}{\rho}\frac{\partial (h\tau_{xx})}{\partial x} + \frac{1}{\rho}\frac{\partial (h\tau_{xy})}{\partial y} \tag{2.31}$$

$$\frac{\partial q_y}{\partial t} + \frac{\partial (uq_y)}{\partial x} + \frac{\partial (vq_y)}{\partial y} + \frac{g}{2}\frac{\partial (h^2)}{\partial y} = gh(S_{by} - S_{fy}) + \frac{1}{\rho}\frac{\partial (h\tau_{yx})}{\partial x} + \frac{1}{\rho}\frac{\partial (h\tau_{yy})}{\partial y} \tag{2.32}$$

where, q_x and q_y are the discharges, u and v are the velocities, S_{bx} and S_{by} are the bed slopes, and S_{fx} and S_{fy} are the frictional slopes in x and y direction, respectively. τ_{xx}, τ_{xy}, τ_{yx}, and τ_{yy} are the components of the horizontal turbulent stress tensor.

Similar to the 1D Saint-Venant equations, the 2D Saint-Venant equations, i.e., Eq. 2.30 to 2.32, can also be written in terms of non-conservative form of the equations. In many cases, e.g., for evaluating wave propagation directions and speeds for numerical upwinding purposes, the non-conservative form of the 2D equations are useful.

2.5 Conclusion

In this particular research, while our ultimate goal is to understand the friction dominated problem for the 2D Saint-Venant equations, we mainly study the 1D Saint-Venant equations. Both the conservative and partial-conservative form of the 1D Saint-Venant equations are used in different numerical schemes to solve the steady state solution for a non-uniform flow test case. The non-conservative, linearized, and non-dimensionalized form of the 1D Saint-Venant equations are mainly used in Fourier analysis.

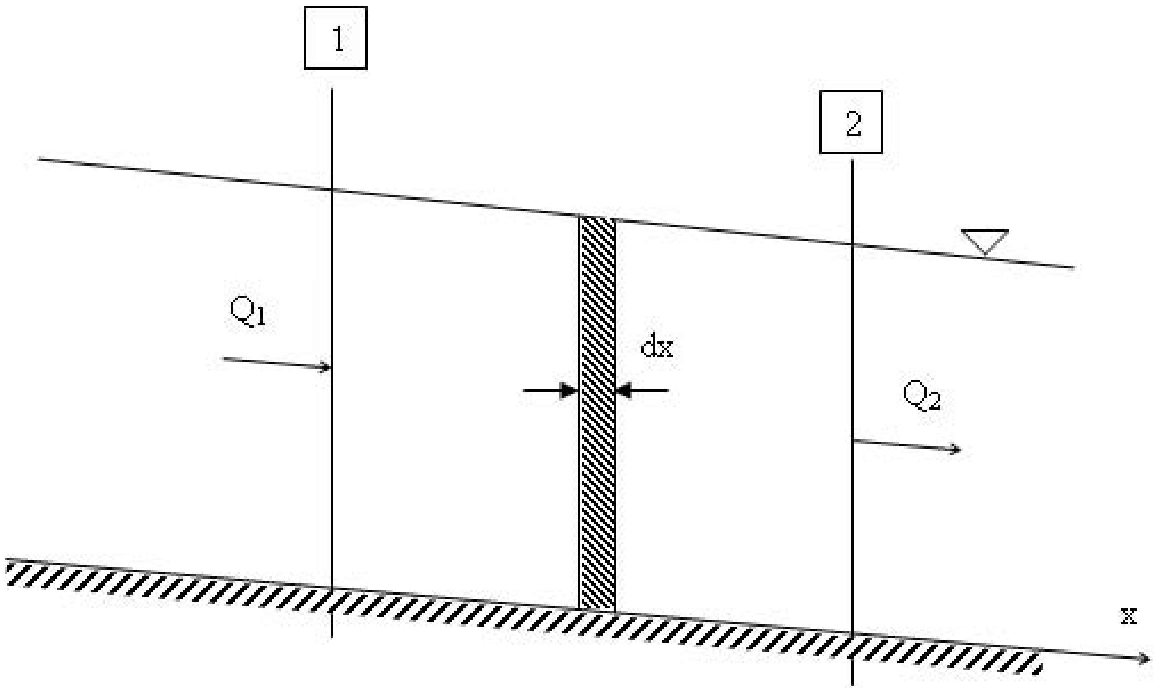

Figure 2.1: Definition sketch for the one-dimensional open channel flow.

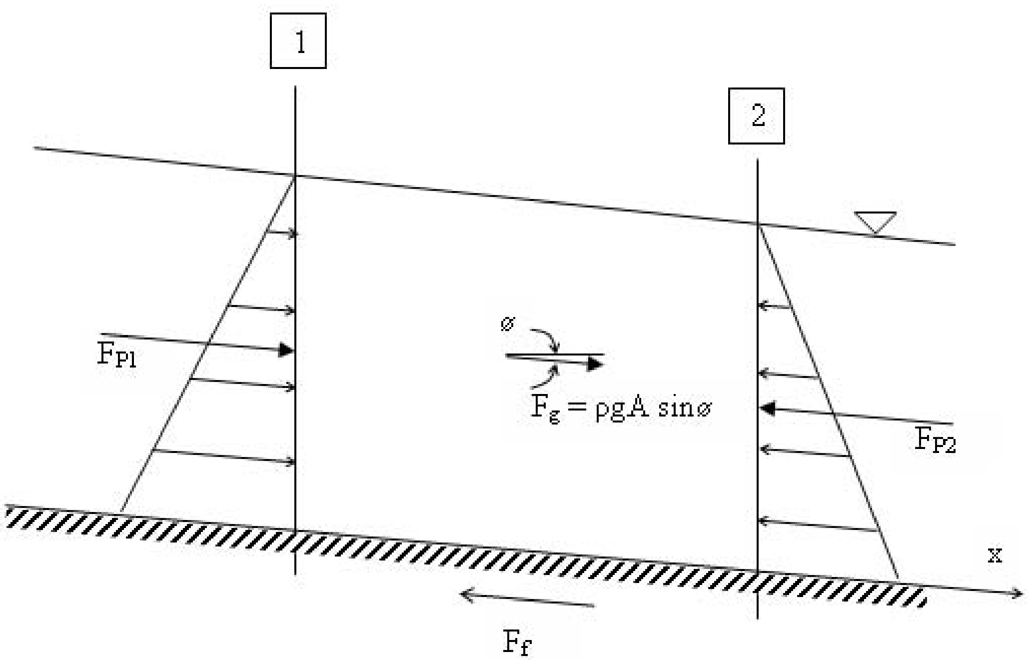

Figure 2.2: Forces acting on the one-dimensional control volume.

Chapter 3

An Analysis Framework to Study Steady State Friction Dominated 1D Saint-Venant Equations

3.1 Introduction

The friction term becomes increasingly important when the depth is small, the discretization is large, the roughness is high, or the slope is steep. A typical problematic situation of friction dominated case is a reach of rapids in a stream or river. To see the effect of these parameters, an analysis framework has been developed using a non-uniform flow test case and Fourier analysis.

In the non-uniform flow test case, abrupt slope changes are introduced, and the steady state solution is solved using full 1D Saint-Venant equations through either the conservative form (Eq. 2.19) or the partially conservative form (Eq. 2.22) of the equations. In the Fourier analysis, a periodic bed perturbation is introduced, and steady state solution is solved using the linearized non-dimensional Saint-Venant equations, i.e., Eq. 2.27 and 2.29.

While the friction dominated problem arises in both transient and steady state case, steady state solution can give us an adequate insight to the problem. Both the non-uniform flow test case and Fourier analysis will provide us the effect of the bed perturbation on the solution variables when the friction term dominates. With this analysis framework, we will be able to identify the controlling parameters and their critical limits for the friction dominated case. The analysis framework presented in this study can be applied to a wide range of numerical schemes.

3.2 Non-uniform Flow Test Case

In this test case, two abrupt slope changes are introduced in a simple open channel to create a non-uniform sub-critical flow. The test reach is relatively long compared to the depth of flow to ensure a friction-dominated regime. Similar non-uniform flow test cases are also used by Bradford and Sanders (2005) and Schippa and Pavan (2008) in their studies.

In our particular case, a 10 km long rectangular channel of very large width is considered where two different slopes are introduced in three parts of the channel. A smaller bed slope (S_{b1}) is used for the first and last third of the channel, and a higher bed slope ($S_{b2} = 3S_{b1}$) is used for the middle third of the channel. A typical bed elevation and water surface elevation profile are shown in Fig. 3.1.

A unit discharge of q_{in} is taken as the inflow boundary condition. A flow depth of h_{out} is taken as the downstream boundary condition, which is the uniform flow depth for S_{b1}, calculated using Chezy's uniform flow equation:

$$h_{out} = (\frac{q_{in}}{C_* \sqrt{gS_{b1}}})^{2/3} \tag{3.1}$$

A unit discharge equal to the inflow rate and a flow depth equal to the downstream depth are used as initial conditions at all nodes.

The non-linear model is run using a transient method until the solution reaches a steady state situation. The simulation is run until the maximum change in any of the solution variables after each time step is reached less than 10^{-10} to ensure the steady state solution. The size of the time step should not affect the final steady state solution. The steady state discharge solution should give a constant value throughout the channel. As the test reach is long enough, the steady state depth solution should give uniform depths in most of the channel except in the areas where the abrupt slope changes produce non-uniform depth profiles.

Two test scenarios are run for each numerical scheme under the non-uniform flow test case. In the first scenario, for the given bed slopes and Chezy coefficient, three different discretizations are used. In the second scenario, for a fixed

This chapter and the next chapter together have been submitted to the Journal of Hydraulic Engineering for publication and parts were also presented in the 33^{rd} IAHR congress in 2009.

discretization, three different values of Chezy coefficient and bed slopes are used. In this scenario, the Chezy coefficient is varied and the bed slopes are calculated using Eq. 3.1 so that the flow rate, the uniform flow depths and the Froude numbers remain the same as in the first scenario. As a result, the effects of slope and Chezy coefficient are not independently distinguished. To do so, would require changes in other parameters and/or variables. In both scenarios q_{in} is taken as 0.164 m^2/sec and h_{out} is taken as 0.28 m. Table 3.1 and 3.2 list the discretizations, Chezy's coefficients and slopes for the two scenarios. The last column of each table shows the average bed slope, $S_0 = (2S_{b1} + S_{b2})/3$, for each case.

Table 3.1: The non-uniform flow test case - effect of discretization.

Δx (m)	C_*	S_{b1}	S_{b2}	S_0
20	15	0.000555	0.001667	0.000926
100	15	0.000555	0.001667	0.000926
200	15	0.000555	0.001667	0.000926

Table 3.2: The non-uniform flow test case - effect of Chezy's coefficient and slope.

Δx (m)	C_*	S_{b1}	S_{b2}	S_0
100	20	0.0003125	0.0009375	0.000521
100	15	0.000555	0.001667	0.000926
100	10	0.00125	0.00375	0.0021

In any individual run, once the final steady solution is found, we calculate nodal percent errors in the discharge and depth solutions by taking the difference between the numerical solution and the reference solution and dividing the error with their reference solution. As we are solving for steady state solution, a constant discharge is the reference solution for the discharge variable. For the depth variable, the reference solution is found by solving the steady state gradually varied flow equation using a fourth-order Runge-Kutta method. In this study, a discretization of 0.1 m is used with an estimated maximum depth error of less than 10^{-5} m.

3.3 Fourier Analysis

The use of Fourier analysis as a tool to study the linear stability of different numerical schemes for the Saint-Venant Equations is common (e.g., Cunge and Verway 1980, Katopodes 1984*b*, Hicks and Steffler 1992). All of these applications, however, are limited to the homogenous form of the equations, neglecting slope and friction terms. Furthermore, all of these studies focus on the propagation of small perturbation amplitudes with time only. Ponce (1977) performed a Fourier analysis of the analytical linearized Saint-Venant equations including the slope and friction terms and was able to show how the dynamic shallow water wave speed and the kinematic wave speed were connected as a function of the wavelength. In this study we will look at the effect of small perturbations of the bed elevation on the numerical steady state depth and discharge solutions. To the best of our knowledge such a study has not been previously attempted.

First the 1D Saint-Venant equations including the source terms are linearized, and then the linearized equations are non-dimensionalized. The linearized form and the non-dimensional form of the Saint-Venant equations are shown in Eq. 2.23 and 2.26 and in Eq. 2.27 and 2.29, respectively. The linearized non-dimensional Saint-Venant equations are then discretized using a numerical scheme. After that, we introduce a periodic bed elevation perturbation to both differential and discrete forms of the non-dimensional linearized Saint-Venant equations. Assuming that the solution variables are also periodic functions, we calculate the analytical and numerical amplitudes of the steady state responses and compare them over a range of non-dimensional parameter values. The differential form of the equations will give us the analytical solution, and the discrete form of the equations will give us the numerical solution. The purpose of the analysis is to identify the controlling non-dimensional parameters and ranges over which objectionable oscillation/errors may be produced.

3.3.1 Analytical Solution

To get the analytical amplitudes of the non-dimensional depth (η) and discharge (φ) perturbations, we introduce a periodic bed elevation perturbation of $\zeta = \mathrm{Z}e^{i\kappa\xi}$ to Eq. 2.27 and Eq. 2.29, where i is the imaginary number equal to $\sqrt{-1}$. Z and κ are the non-dimensional amplitude and wave number of the bed elevation perturbation, respectively. We also assume that $\eta = \mathrm{H}_a e^{i\kappa\xi}$ and $\varphi = \Phi_a e^{i\kappa\xi}$, where H_a and Φ_a are the non-dimensional analytical amplitude of the depth and discharge perturbation, respectively.

For the steady state solution, the non-dimensional analytical amplitude of the discharge perturbation becomes zero, i.e.,

$$\Phi_a = 0 \tag{3.2}$$

and the normalized non-dimensional analytical depth amplitude becomes

$$\frac{\mathrm{H}_a}{\mathrm{Z}} = \frac{1}{-1 + Fr_0^2(1 - \frac{3\beta}{\kappa}i)} \tag{3.3}$$

Three different cases can be identified from Eq. 3.3. The first of these occurs when Fr_0 is equal to zero, which is the quiescent flow case, i.e., $q_0 = 0$. The non-dimensional depth amplitude approaches the state of equaling the non-dimensional bed amplitude with the opposite sign, i.e., $\mathrm{H}_a = -\mathrm{Z}$. Now if we define the non-dimensional water surface elevation as γ, which is equal to $(\eta + \zeta)$, then we can say that for the quiescent flow case the non-dimensional water surface elevation amplitude becomes zero, and therefore, the water surface elevation becomes flat for this case.

The second case arises when the Friction number, β, is equal to zero. In this case, the non-dimensional depth amplitude becomes equal to $(\frac{\mathrm{Z}}{-1+Fr_0^2})$, and for any sub-critical flow, i.e., $Fr_0 < 1$, the water surface elevation will be out of phase with the bed elevation.

The final case occurs when β approaches infinity. In this case, the non-dimensional depth amplitude approaches zero, i.e., $\mathrm{H}_a = 0$, and therefore, the non-dimensional water surface elevation amplitude becomes equal to the non-dimensional bed amplitude and in phase with the bed elevation.

Fig. 3.2 shows the non-dimensional bed elevation (ζ) and bed water surface elevation (γ) with the non-dimensional channel distance (ξ) for three different Friction numbers (i.e., β = 0, 0.1, and 1). In all cases Z = 0.5, $Fr_0 = 0.5$, $\kappa = \pi/25$, and ξ is from 0 to 100. The figure shows that for β equal to zero, γ is out of phase with ζ and has an amplitude of 0.1667. As β increases, the amplitude of γ increases and approaches the bed elevation amplitude, 0.5. The water surface elevation also is in phase with the bed elevation.

3.3.2 Numerical Solution

To get the numerical amplitudes of the non-dimensional depth (η) and discharge (φ) perturbations, we use the discrete form of the linearized non-dimensional Saint-Venant equations and introduce the periodic bed perturbation to the discrete equations. The generalized discrete forms of Eq. 2.27 and Eq. 2.29 with any six (or fewer) point numerical scheme are as follows:

$$a_1\eta_{j-1}^{m+1} + a_2\eta_j^{m+1} + a_3\eta_{j+1}^{m+1} + a_4\varphi_{j-1}^{m+1} + a_5\varphi_j^{m+1} + a_6\varphi_{j+1}^{m+1} + a_7\eta_{j-1}^{m} + a_8\eta_j^{m} + a_9\eta_{j+1}^{m} + a_{10}\varphi_{j-1}^{m} + a_{11}\varphi_j^{m} + a_{12}\varphi_{j+1}^{m} = a_{13}\zeta_{j-1} + a_{14}\zeta_j + a_{15}\zeta_{j+1} \quad (3.4)$$

$$b_1\eta_{j-1}^{m+1} + b_2\eta_j^{m+1} + b_3\eta_{j+1}^{m+1} + b_4\varphi_{j-1}^{m+1} + b_5\varphi_j^{m+1} + b_6\varphi_{j+1}^{m+1} + b_7\eta_{j-1}^{m} + b_8\eta_j^{m} + b_9\eta_{j+1}^{m} + b_{10}\varphi_{j-1}^{m} + b_{11}\varphi_j^{m} + b_{12}\varphi_{j+1}^{m} = b_{13}\zeta_{j-1} + b_{14}\zeta_j + b_{15}\zeta_{j+1} \quad (3.5)$$

where a_r and b_r ($r = 1$ to 15) are the coefficients of the discretization. The superscript m indicates that the variable is evaluated at a known time level and the superscript $m+1$ is the variable at the next unknown time level. The subscript j is the spatial index of the nodal points that are spaced apart by $\Delta\xi = \frac{\Delta x}{L}$.

Now we introduce the bed perturbation of $\zeta_j = \mathrm{Z}e^{ij\kappa\Delta\xi}$ and assume that $\eta_j^{m+1} = \eta_j^m = \mathrm{H}_n e^{ij\kappa\Delta\xi}$ and $\varphi_j^{m+1} = \varphi_j^m = \Phi_n e^{ij\kappa\Delta\xi}$ (i.e., assuming the steady state case), where H_n and Φ_n are the non-dimensional numerical amplitudes of the depth and discharge perturbations, respectively. By assuming $\eta_j^{m+1} = \eta_j^m$ and $\varphi_j^{m+1} = \varphi_j^m$, the time discretization terms for some numerical schemes may cancel each other out, and the solutions may not depend on the time discretization. After introducing the periodic functions, Eq. 3.4 and 3.5 together become a system of equations and can be written as a matrix form, such as:

$$\begin{Bmatrix} \frac{\mathrm{H}_n}{\mathrm{Z}} \\ \frac{\Phi_n}{\mathrm{Z}} \end{Bmatrix} = \begin{bmatrix} M1 & M2 \\ M3 & M4 \end{bmatrix}^{-1} \begin{Bmatrix} R1 \\ R2 \end{Bmatrix} \quad (3.6)$$

where, $M1 = (a_1 + a_7)e^{-i\kappa\Delta\xi} + (a_2 + a_8) + (a_3 + a_9)e^{i\kappa\Delta\xi}$, $M2 = (a_4 + a_{10})e^{-i\kappa\Delta\xi} + (a_5 + a_{11}) + (a_6 + a_{12})e^{i\kappa\Delta\xi}$, $M3 = (b_1 + b_7)e^{-i\kappa\Delta\xi} + (b_2 + b_8) + (b_3 + b_9)e^{i\kappa\Delta\xi}$,

$M4 = (b_4+b_{10})e^{-i\kappa\Delta\xi}+(b_5+b_{11})+(b_6+b_{12})e^{i\kappa\Delta\xi}$, $R1 = a_{13}e^{-i\kappa\Delta\xi}+a_{14}+a_{15}e^{i\kappa\Delta\xi}$, and $R2 = b_{13}e^{-i\kappa\Delta\xi} + b_{14} + b_{15}e^{i\kappa\Delta\xi}$.

The coefficients a_r and b_r for all schemes are presented in the appendices, and it is apparent from those coefficients that for all schemes, $\frac{\mathrm{H}_n}{\mathrm{Z}}$ and $\frac{\Phi_n}{\mathrm{Z}}$ mainly depend on the average flow Froude number (Fr_0) and two non-dimensional parameters, i.e., $\kappa\Delta\xi$ and $\beta\Delta\xi$. Some numerical schemes, e.g., the CDG scheme and MacCormack scheme, may have more non-dimensional parameters in addition to these three parameters.

$\kappa\Delta\xi$ can be written as $\frac{2\pi}{\lambda/\Delta x}$, where λ is the dimensional wavelength of the bed elevation perturbation. $\frac{\lambda}{\Delta x}$ can be interpreted as the number of discretization intervals per wavelength N_λ. Also, $\beta\Delta\xi$ can be written as $\frac{\Delta x}{h_0 C_*^2}$. By comparison with the Friction number, $\beta = \frac{L}{h_0 C_*^2}$, we will call this non-dimensional parameter the numerical Friction number and denote it as $\beta_{\Delta x}$. Note that for all cases, the length scale, L, is canceled out, or, in effect, L is replaced by Δx. In general, we can write:

$$\begin{Bmatrix} \frac{\mathrm{H}_n}{\mathrm{Z}} \\ \frac{\Phi_n}{\mathrm{Z}} \end{Bmatrix} = f(Fr_0, N_\lambda, \beta_{\Delta x}, ...) \tag{3.7}$$

The analytical depth solution, i.e., Eq. 3.3 can also be written in terms of these new parameters as:

$$\frac{\mathrm{H}_a}{\mathrm{Z}} = \frac{1}{-1 + Fr_0^2(1 - \frac{3\beta_{\Delta x} N_\lambda}{2\pi} i)} \tag{3.8}$$

Eq. 3.7 shows that for a given bed elevation perturbation of Z, we have three or more (depending on the schemes) non-dimensional parameters that affect the numerical amplitude of the solution variables. We vary all these non-dimensional parameters, and for each case, we calculate the normalized numerical amplitudes H_n/Z and Φ_n/Z using Eq. 3.6. The corresponding normalized analytical depth amplitude, H_a/Z, is found using Eq. 3.8. The depth amplitude error is, then, calculated by $(\mathrm{H}_n - \mathrm{H}_a)/\mathrm{Z}$. The discharge numerical amplitude, Φ_n/Z, itself represents the error for the discharge variable, as the analytical amplitude of φ is zero. For all cases, Fr_0 is varied from 0.1 to 0.8, $\beta_{\Delta x}$ is varied from 0.01 to 5, and N_λ is varied from 2 to 100.

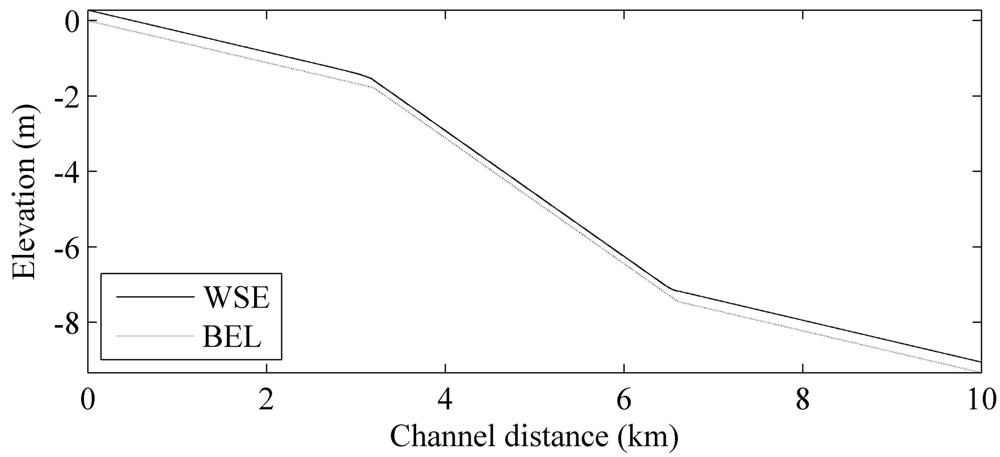

Figure 3.1: A typical bed elevation (BEL) and water surface elevation (WSE) profile for the non-uniform flow test cases.

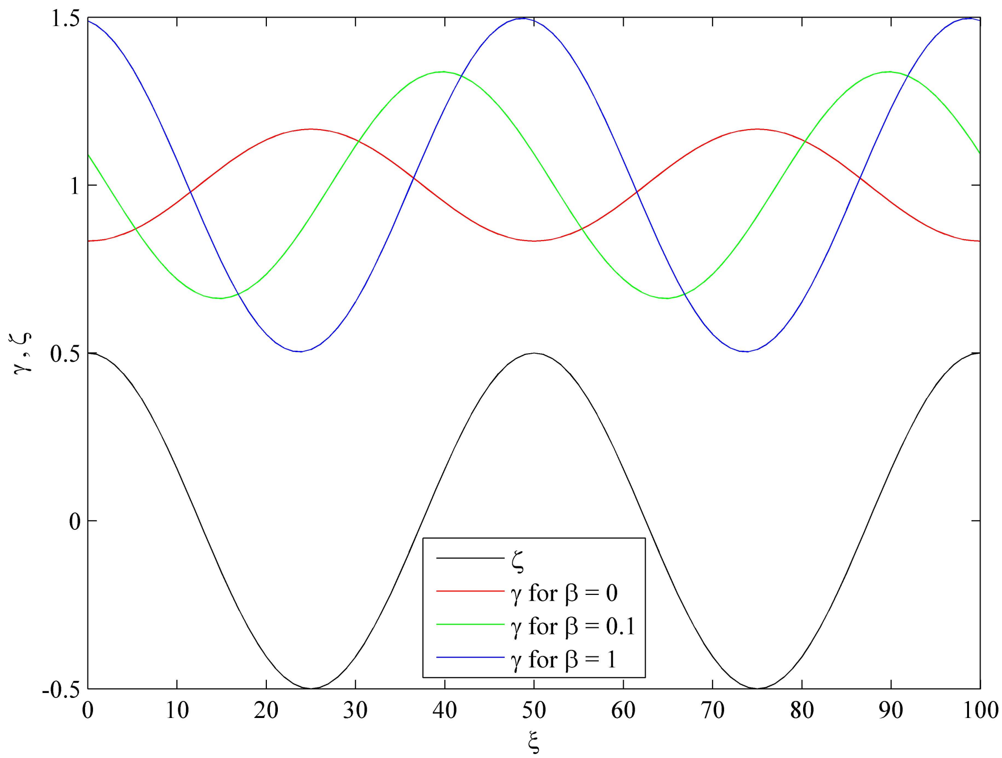

Figure 3.2: The non-dimensional bed elevation (ζ) and non-dimensional analytical water surface elevation (γ) with ξ for three different Friction numbers and $Fr_0 = 0.5$.

Chapter 4

Characteristic Dissipative Galerkin Finite Element Scheme

4.1 Introduction

The finite element method (FEM) is popular due to its geometric flexibility and its underlying mathematical robustness. In FEM, the solution domain is divided into small subdivisions (as shown in Fig. 4.1) that are known as finite elements. Then with the use of approximate trial functions and the variational or weighted residual methods, the governing partial differential equations are transformed into a set of finite element equations. These local equations are collected to form a global system of algebraic equations, which can be solved implicitly or explicitly. In the implicit scheme, an iterative method is needed to solve the non-linear system of equations.

In FEM, the conserved variable vector $\mathbf{U}$ of Eq. 2.19 is approximated with the trial function $\tilde{\mathbf{U}}$ using the interpolation function f_j, i.e.,

$$\mathbf{U} \approx \tilde{\mathbf{U}} = \sum_{1}^{N} f_j \mathbf{U}_j \tag{4.1}$$

where N is the number of nodes in a domain. Using the trial function $\tilde{\mathbf{U}}$, Eq. 2.19 can be written as a weak statement:

$$\int_0^L v_i \{ \frac{\partial \tilde{\mathbf{U}}}{\partial t} + \frac{\partial \mathbf{F}(\tilde{\mathbf{U}})}{\partial x} - \mathbf{S}(\tilde{\mathbf{U}}) \} dx = 0 \tag{4.2}$$

where v_i is the weighting function. The choice between weighting functions leads

This chapter and the previous chapter together are submitted to the Journal of Hydraulic Engineering for publication and also were presented in the 33^{rd} IAHR congress in 2009.

to different finite element schemes, e.g., Bubnov-Galerkin finite element scheme or Petrov-Galerkin finite element scheme.

One simple choice of weighting function is as the interpolation function, which leads to the Bubnov-Galerkin finite element scheme (Brooks and Hughes 1982, Baker 1983):

$$v_i = f_i \tag{4.3}$$

The Bubnov-Galerkin scheme is similar to any central differences scheme and produces non-physical oscillations when convection dominates or gradient becomes steep, and therefore, the scheme requires some form of upwinding to dissipate those non-physical oscillations (Chung 2002, Brooks and Hughes 1982).

In the Petrov-Galerkin type finite element scheme, the upwinding weighted test functions are introduced to provide dissipation as follows (Brooks and Hughes 1982, Hicks 1990):

$$v_i = f_i + w\mathbf{W}\frac{\Delta x}{2}\frac{df_i}{dx} \tag{4.4}$$

where w is a diffusion parameter (or upwinding coefficient), and $\mathbf{W}$ is the upwinding matrix that controls the distribution of the diffusion.

Different choices of $\mathbf{W}$ lead to different upwinding finite element schemes, such as the Dissipative Galerkin (DG) scheme (Katopodes 1984*a*) or the Characteristic Dissipative Galerkin (CDG) scheme (Hicks and Steffler 1992). In this study, we have used the CDG scheme, which is an upwind shock-capturing scheme used in various practical finite element models, e.g., River1D (Hicks 2005), River2D (Steffler and Blackburn 2002), HIVEL2D (Berger and Stockstill 1995), and TELEMAC2D (Bates and Hawkes 1997).

The CDG method is based upon the work of Hughes and Mallet (1986), who examined the application of the Petrov-Galerkin method to symmetric systems of hyperbolic equations. In general, the implementation requires that (Hughes and Mallet 1986, Hicks 1990):

$$\mathbf{W} = \frac{\mathbf{A}}{|\mathbf{A}|} \tag{4.5}$$

Now, $\mathbf{A}$ can be decomposed as:

$$\mathbf{A} = \mathbf{R}\mathbf{\Lambda}\mathbf{R}^{-1} \tag{4.6}$$

where $\mathbf{R}$ is the matrix of right eigenvectors, and $\mathbf{\Lambda} = \begin{bmatrix} \Lambda_1 & 0 \\ 0 & \Lambda_2 \end{bmatrix}$ is the eigenmatrix of $\mathbf{A}$; Λ_i signifies the eigenvalues for $i = 1, 2$. So, the upwinding matrix $\mathbf{W}$ in the CDG scheme for the Saint-Venant equations can be evaluated as (Hicks 1990, Hicks and Steffler 1992):

$$\mathbf{W} = \mathbf{R} \begin{bmatrix} \frac{\Lambda_1}{|\Lambda_1|} & 0 \\ 0 & \frac{\Lambda_2}{|\Lambda_2|} \end{bmatrix} \mathbf{R}^{-1} \tag{4.7}$$

$\mathbf{W}$ for the 1D Saint-Venant equations, i.e., Eq. 2.19, can be found in Hicks (1990) and Hicks and Steffler (1992), and $\mathbf{W}$ for the non-dimensional linearized form of the 1D Saint-Venant equations, i.e., Eq. 2.27 and 2.29, is given in appendix A.

Using a fully implicit time-stepping approach, the discrete finite element equations provide a system of non-linear algebraic equations. These equations are solved using the Newton-Raphson iterative method. The residuals and the Jacobian matrix for the iterative method are calculated using numerical integration and differentiation, respectively. Linear interpolation functions are used throughout.

4.2 Quiescent Flow Test Case

Before moving to the friction term dominated case, we will show that the CDG scheme used in this paper satisfies the quiescent flow test case with a non-level bed. This is done to show that the friction dominated issue is separate from the bed slope source term issue for the CDG scheme. In the quiescent flow test case the non-linear model is run with a non-level bed as shown in Fig. 4.2a with a downstream water surface elevation of 20 m, and an upstream discharge equal to zero. This non-level test case was first proposed by the working group on dam-break modeling (Goutal and Maurel 1997) and also used by other researchers (e.g., Hubbard and Garcia-Navarro 2000, Zhou and Ingram 2001) to test their numerical schemes. The numerical scheme should give a constant water level and a zero discharge without any oscillations due to the non-level bed elevation. Fig. 4.2a and 4.2b show the final steady state water surface elevation and discharge solutions obtained with the CDG scheme, and we find that the CDG scheme produces the exact solution to within machine level accuracy.

4.3 Non-uniform Flow Test Case Results

Fig. 4.3 and 4.4 show the discharge and depth solutions and Table 4.1 and 4.2 show the maximum nodal percent errors in the discharge and depth solutions for both scenarios.

It can be seen from Fig. 4.3a and 4.4a that non-physical oscillations in the discharge are observed, and these oscillations increase as discretization increases, and as roughness (decrease of C_*) and slope increase (as also shown in Table 4.1 and 4.2). The errors in the depth solutions also increase with the increase of these parameter values (as shown in Table 4.1 and 4.2 and Fig. 4.3b and 4.4b) and are of similar magnitude to the discharge errors.

In all cases, the oscillations are confined to a few elements in the vicinity of the slope changes, and they appear as $2\Delta x$ wavelength oscillations (as shown in Fig. 4.3 and 4.4). The discharge oscillations appear both upstream and downstream of the transition, while the depth oscillations occur mainly upstream of the transition. For both depth and discharge solutions, the transition from a steeper slope to a milder slope creates somewhat larger oscillations than the transition from a milder slope to a steeper slope.

Table 4.1: The non-uniform flow test case - effect of discretization with the CDG scheme.

Δx (m)	C_*	S_0	q error (%)	h error(%)
20	15	0.000926	0. 34	0.25
100	15	0.000926	3.41	2.07
200	15	0.000926	11.22	7.29

Table 4.2: The non-uniform flow test case - effect of Chezy coefficient and slope with the CDG scheme.

Δx (m)	C_*	S_0	q error (%)	h error(%)
100	20	0.000521	1.49	0.64
100	15	0.000926	3.41	2.07
100	10	0.0021	13.09	8.38

4.4 Fourier Analysis Results

The coefficients a_r and b_r of Eq. 3.6 for the CDG scheme are shown in Appendix A. From these coefficients, it is found that within the CDG scheme $\frac{\mathrm{H}_n}{\mathrm{Z}}$ and $\frac{\Phi_n}{\mathrm{Z}}$ do not depend on the time step discretization. In addition to the parameters shown in Eq. 3.7, the CDG scheme has one extra parameter, which is the upwinding coefficient, w. So, for the CDG scheme we can rewrite Eq. 3.7 as:

$$\left\{ \begin{matrix} \frac{\mathrm{H}_n}{\mathrm{Z}} \\ \frac{\Phi_n}{\mathrm{Z}} \end{matrix} \right\} = f(Fr_0, N_\lambda, \beta_{\Delta x}, w) \tag{4.8}$$

Fig. 4.5 shows analytical and numerical amplitudes of the depth and discharge variables and the corresponding errors as a function of N_λ with $w = 0.5$, $Fr_0 = 0.5$ and $\beta_{\Delta x} = 1$. The figure shows that the errors in both solution variables are observed for the perturbations in bed elevation. The errors are maximum at the shortest wavelength and tend to diminish as N_λ increases. For this case, the errors appear to be negligible for $N_\lambda > 10$.

Fig. 4.6 shows the variation of the discharge and depth amplitude errors as a function of N_λ for the range of Fr_0 with $w = 0.5$ and $\beta_{\Delta x} = 1$. The figure shows that both the discharge and depth errors are low at a low Fr_0 and increase with increasing Fr_0. The changes in the depth errors as Fr_0 increases are relatively small compared to the changes in the discharge errors. The numerical depth amplitudes are less than the analytical depth amplitudes for $Fr_0 \leq 0.5$ and become greater for $Fr_0 > 0.5$.

Fig. 4.7 shows the variation of the discharge and depth errors as a function of N_λ for the range of $\beta_{\Delta x}$ with $Fr_0 = 0.5$ and $w = 0.5$. The figure shows that, similar to the Fr_0 results, both the discharge and depth errors are also low at low $\beta_{\Delta x}$ and increase with increasing $\beta_{\Delta x}$. The depth amplitude errors (Fig. 4.7b) are within 0.05 to 0.1 for $\beta_{\Delta x} \leq 2$, and a big increase occurs for $\beta_{\Delta x} > 2$. The discharge amplitude errors (Fig. 4.7a) increase continuously as $\beta_{\Delta x}$ increases. The numerical depth amplitudes are less than the analytical depth amplitudes for $\beta_{\Delta x} \leq 1$ and become greater for $\beta_{\Delta x} > 1$.

Fig. 4.8 shows the variation of the discharge and depth errors as a function of $\beta_{\Delta x}$ for the range of Fr_0 with $w = 0.5$ and $N_\lambda = 2$. The figure shows that both errors are low at low Fr_0 and low $\beta_{\Delta x}$ and increase with increasing Fr_0 and

$\beta_{\Delta x}$. From Fig. 4.8a, we can say that for any value of Fr_0, if $\beta_{\Delta x} \leq 0.01$, the discharge errors will be less than 0.03. The same figure shows that the discharge errors can reach up to 1 when both Fr_0 and $\beta_{\Delta x}$ are large. The depth amplitude errors (Fig. 4.8b) can also reach up to 0.5 or more when Fr_0 and $\beta_{\Delta x}$ are large. The numerical depth amplitudes are less than the analytical amplitudes when $\beta_{\Delta x} \leq 1$ and become greater when $\beta_{\Delta x} > 1$.

Fig. 4.9 shows the variation of the discharge and depth amplitude errors as a function of N_λ for the range of upwinding coefficients $w = 0$ to 1, with $Fr_0 = 0.5$ and $\beta_{\Delta x} = 1$. Fig. 4.9a shows that without any upwinding, i.e., $w = 0$, there are no discharge perturbation errors for any N_λ. However, the depth error (Fig. 4.9b), in this case at $N_\lambda = 2$, is the maximum. With a slight upwinding ($w = 0.1$ or less), the depth error at $N_\lambda = 2$ drops significantly, but this introduces a large discharge error. Increasing the upwinding coefficient appears to reduce the short wavelength discharge error but increases the error at longer wavelengths. The changes in depth error in these cases are negligible compared to the discharge error changes. This may explain why we need at least some upwinding for any convection dominated case, and why w is usually used as 0.5 for the CDG scheme (Hicks and Steffler 1992).

4.5 Discussion

From the non-uniform flow test case results, it is found that non-physical discharge and depth oscillations are apparent when the discretization becomes large, or the roughness (decrease of C_*) and slope become large. From the Fourier analysis, we also find that errors in the discharge and depth solutions increase with increasing Fr_0 and $\beta_{\Delta x}$. Since increasing the discretization, roughness, or slope increases $\beta_{\Delta x}$ and/or Fr_0, this is consistent with the non-uniform flow test. The Fourier analysis results show that the maximum error occurs at $N_\lambda = 2$. This is also consistent with the non-uniform flow test as the oscillations appear with a $2\Delta x$ wavelength. The Fourier analysis results also show that the depth and discharge errors can be an order of 1 or more when both Fr_0 and $\beta_{\Delta x}$ are large, and the errors will be negligible when $\beta_{\Delta x} \leq 0.01$.

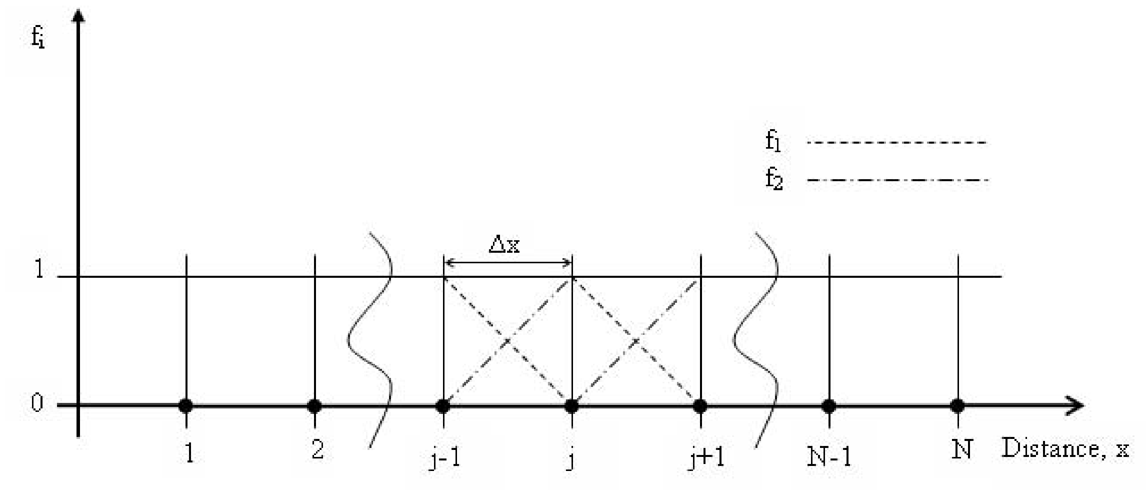

Figure 4.1: Definition sketch of the finite element method for one-dimensional flow.

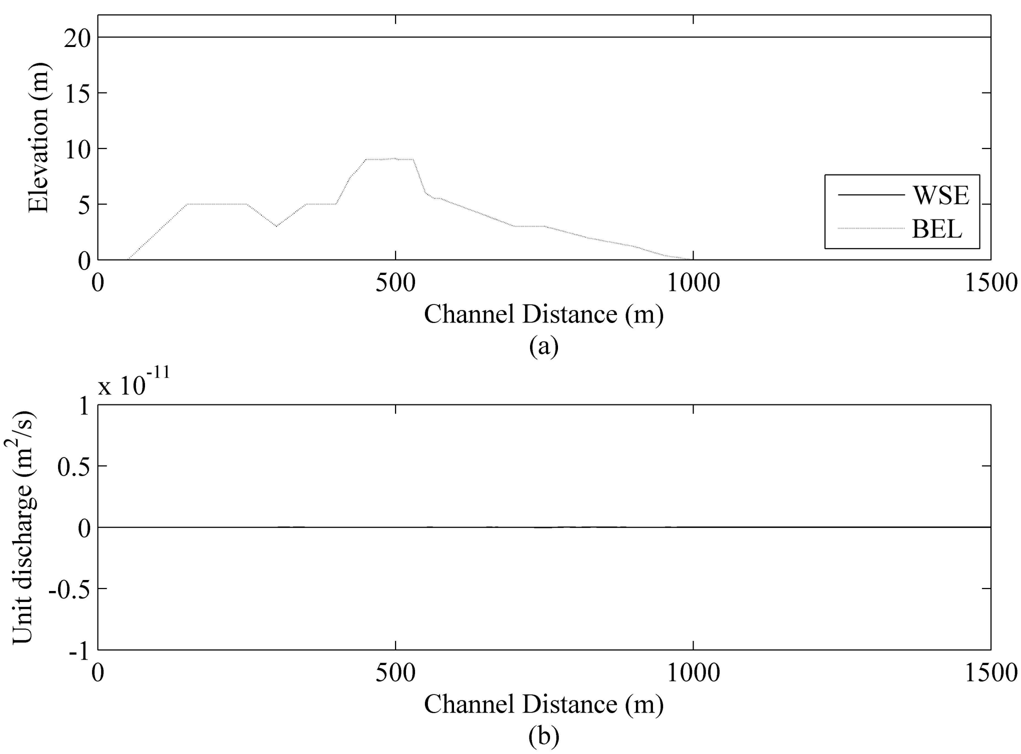

Figure 4.2: (a) Bed elevation (BEL) and water surface elevation (WSE) profile and (b) Discharge solution for the quiescent flow test case with the CDG scheme.

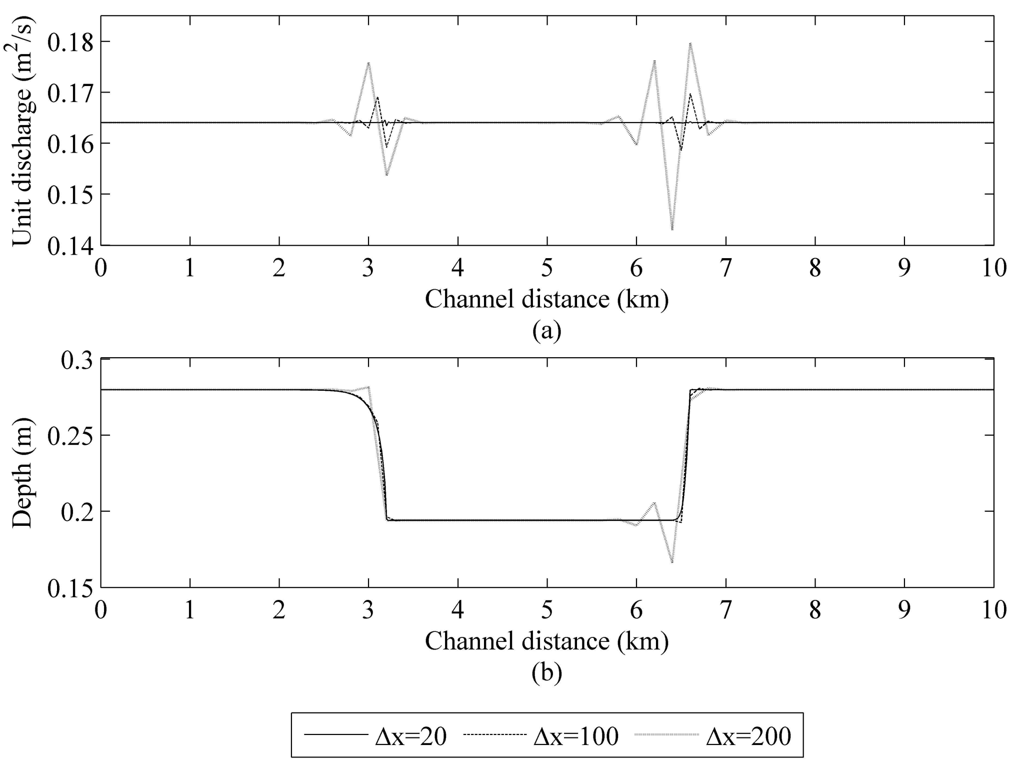

Figure 4.3: (a) Unit discharge and (b) Depth solutions for the non-uniform flow test case with the CDG scheme - effect of discretization.

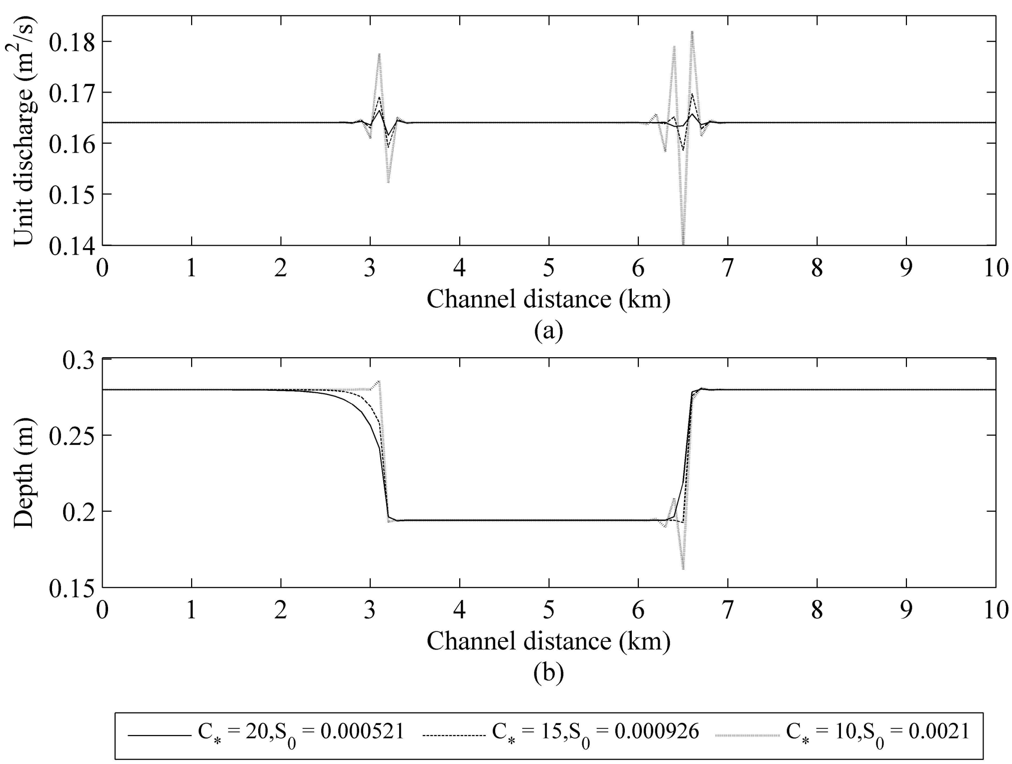

Figure 4.4: (a) Unit discharge and (b) Depth solutions for the non-uniform flow test case with the CDG scheme - effect of Chezy coefficient and slope.

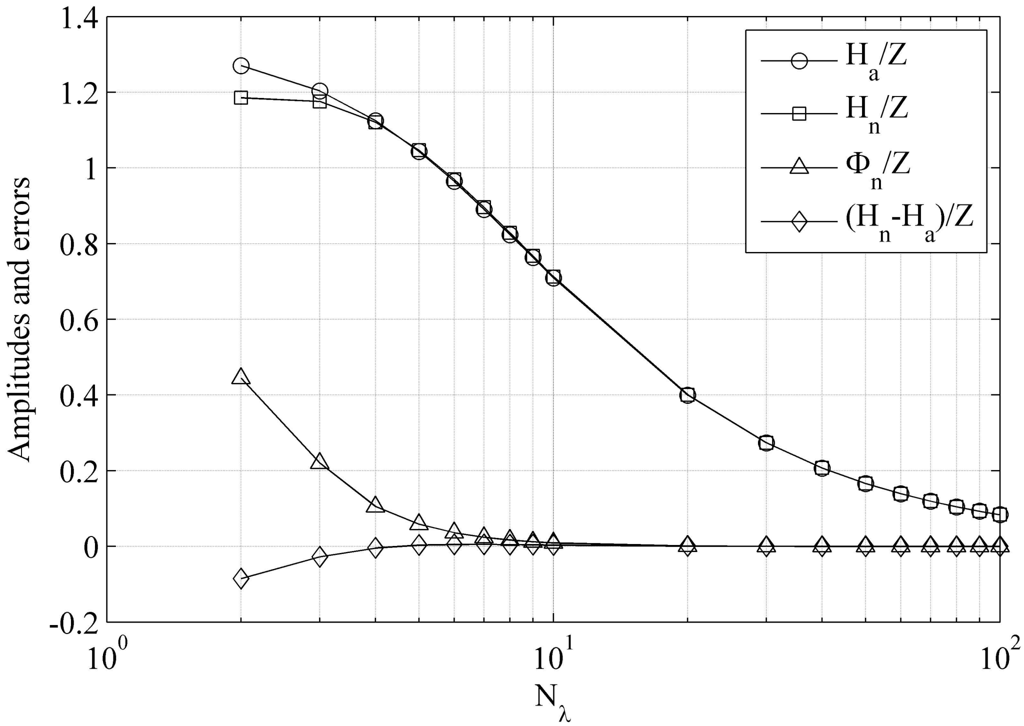

Figure 4.5: Normalized amplitudes and errors as a function of N_λ for $w = 0.5$, $Fr_0 = 0.5$ and $\beta_{\Delta x} = 1$ using the CDG scheme.

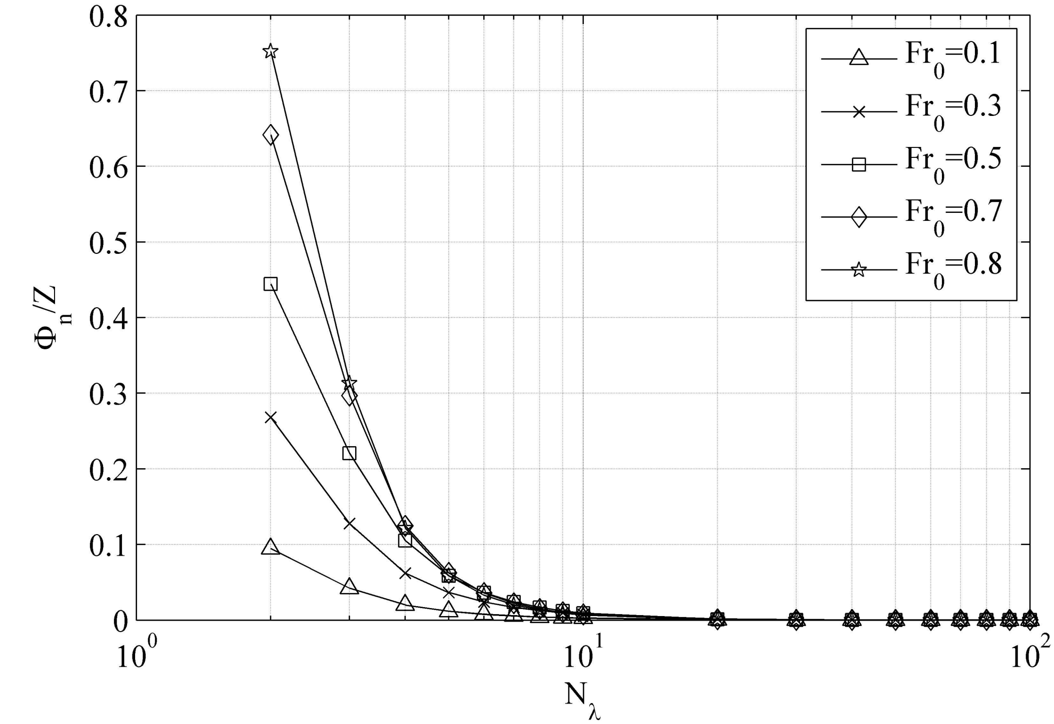

(a)

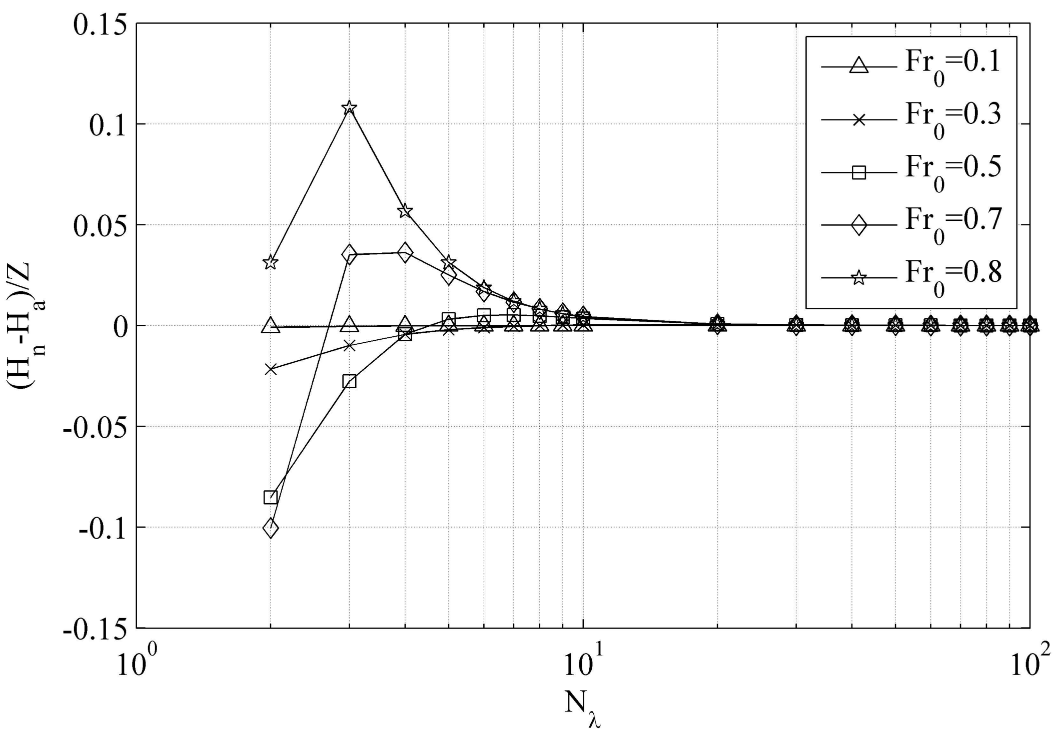

(b)

Figure 4.6: (a) Discharge and (b) Depth amplitude errors as a function of N_λ for a range of Fr_0, $w = 0.5$, and $\beta_{\Delta x} = 1$ using the CDG scheme.

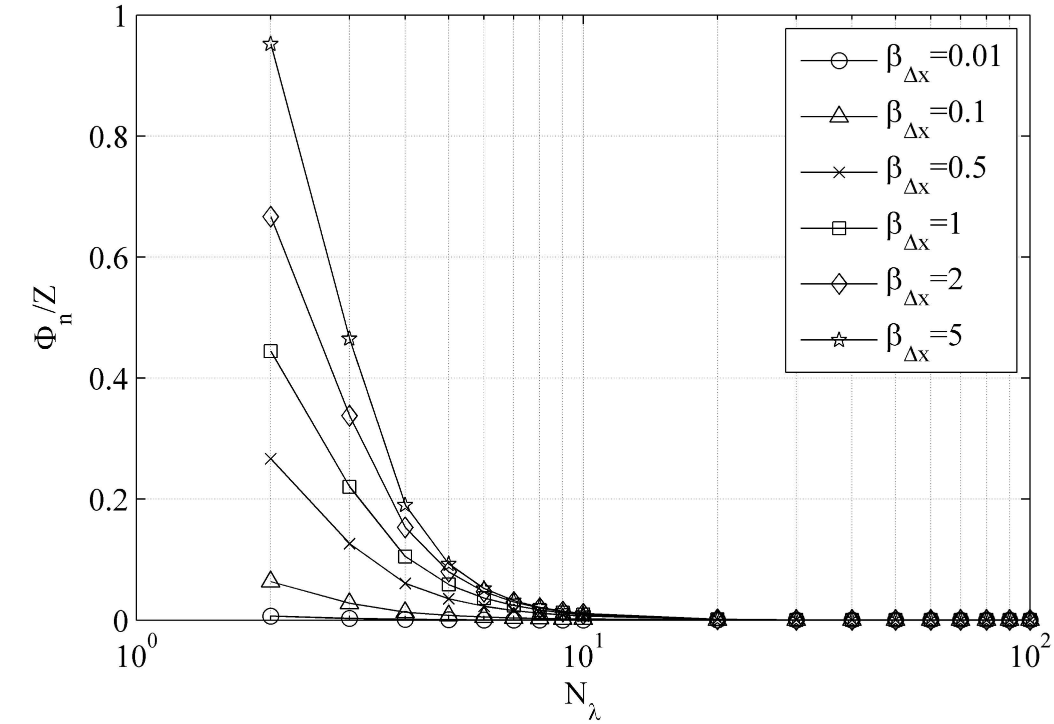

(a)

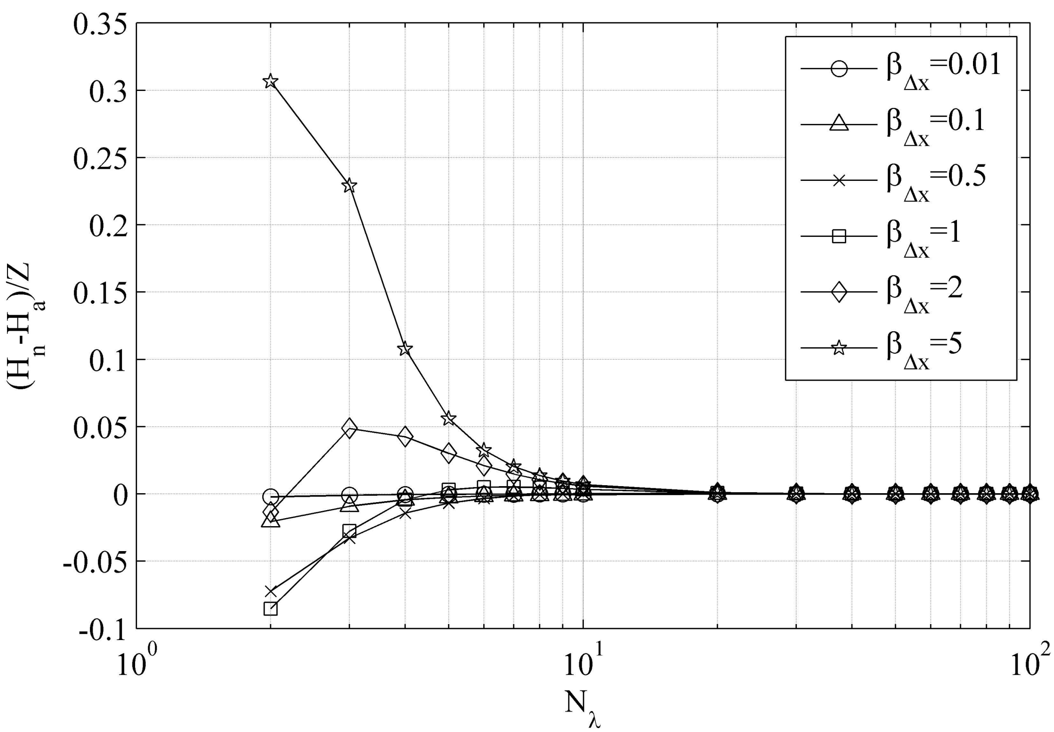

(b)

Figure 4.7: (a) Discharge and (b) Depth amplitude errors as a function of N_λ for a range of $\beta_{\Delta x}$, $w = 0.5$, and $Fr_0 = 0.5$ using the CDG scheme.

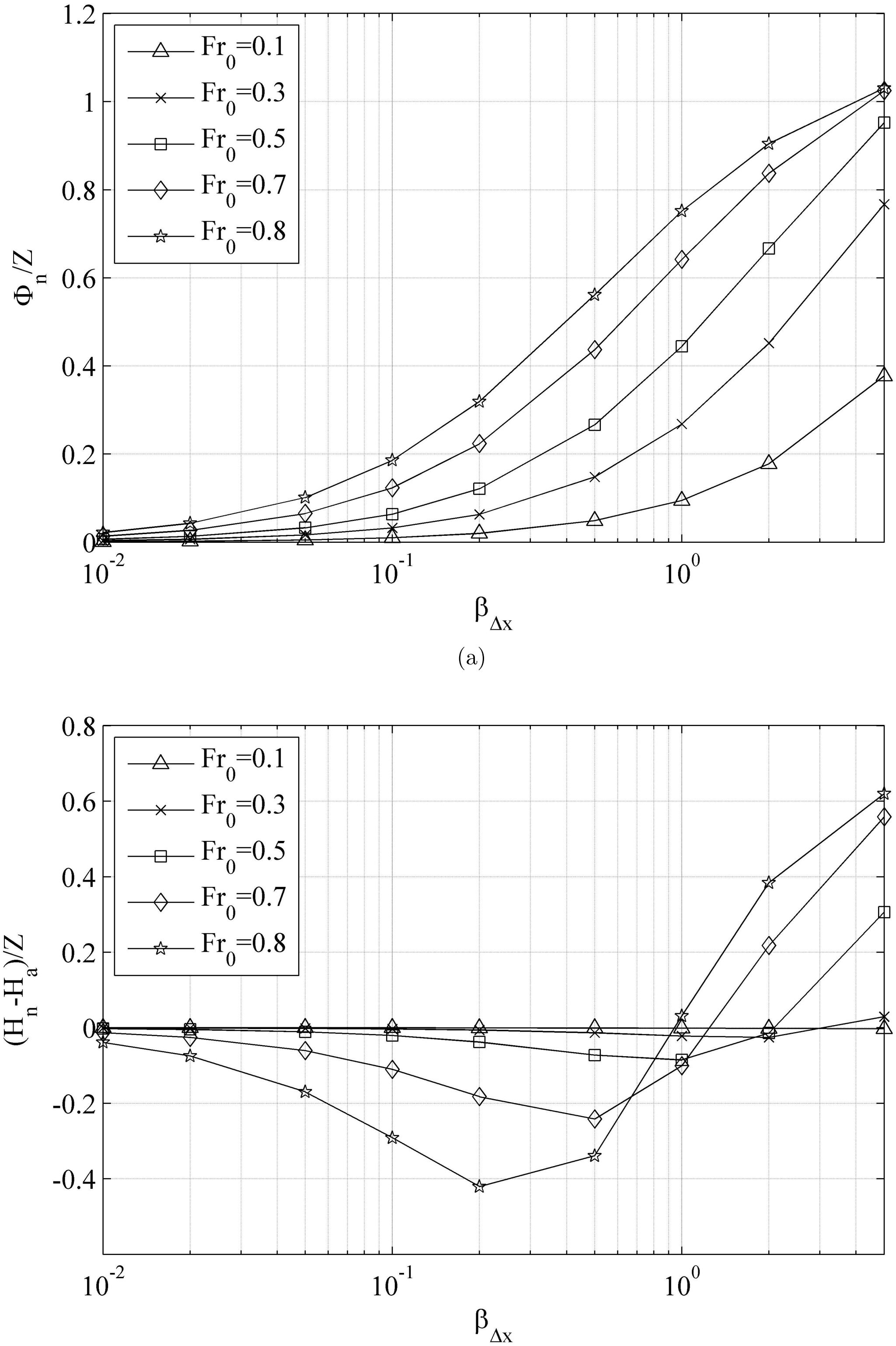

(a)

(b)

Figure 4.8: (a) Discharge and (b) Depth amplitude errors as a function of $\beta_{\Delta x}$ for a range of Fr_0, $w = 0.5$, and $N_\lambda = 2$ using the CDG scheme.

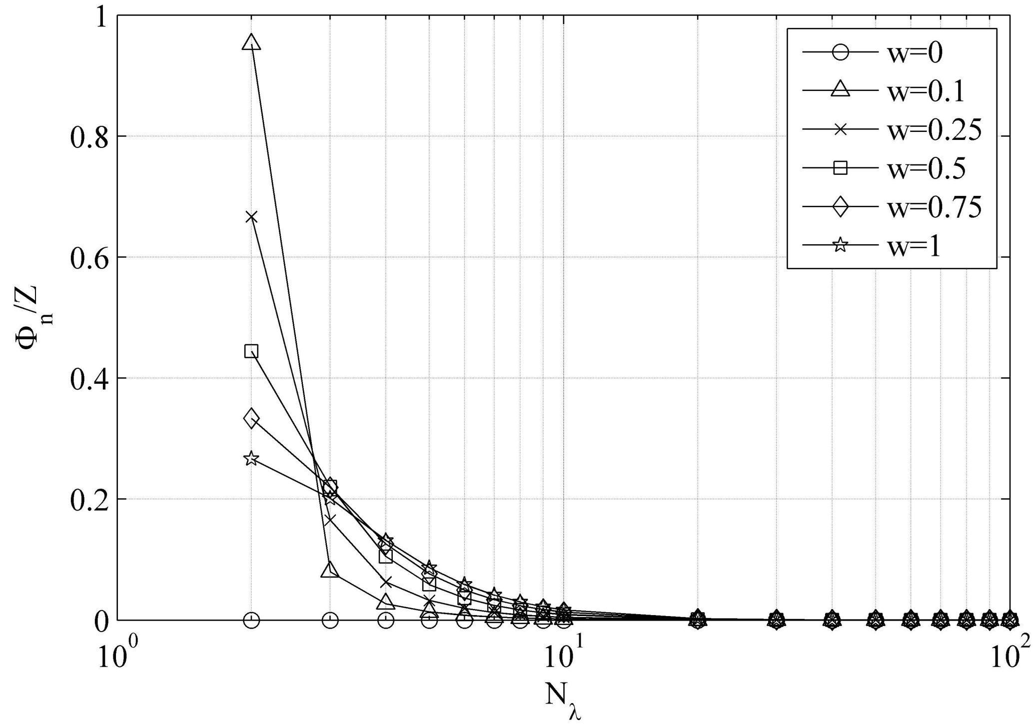

(a)

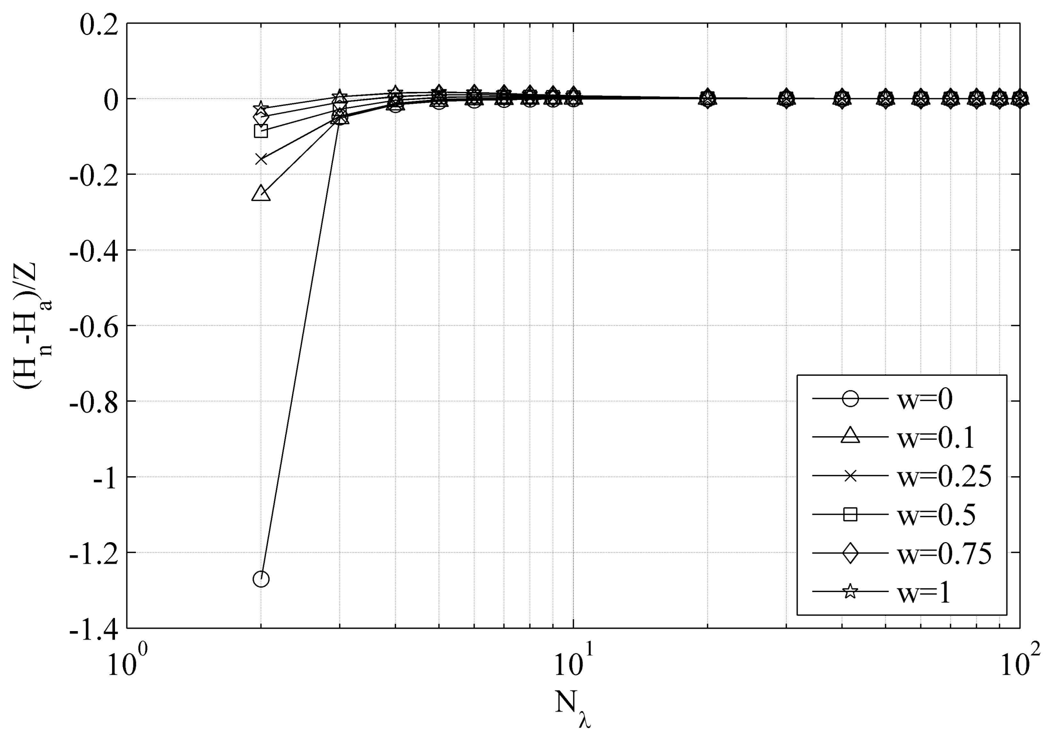

(b)

Figure 4.9: (a) Discharge and (b) Depth amplitude errors as a function of N_λ for a range of w, $\beta_{\Delta x} = 1$, and $Fr_0 = 0.5$ using the CDG scheme.

Chapter 5

Box Finite Difference Scheme

5.1 Introduction

The finite difference method (FDM) is useful because of its simplicity in formulation compared to the other methods. In FDM, the partial derivatives of the differential equations are approximated with finite differences, which results in a set of algebraic equations with all unknowns. These algebraic equations can be solved explicitly or implicitly. FDM uses a structured grid and thus requires grid transformation in multidimensional flow case. A typical finite difference grid is shown in Fig. 5.1. In this study, we have looked at two finite difference schemes: the box finite difference and MacCormack scheme. The analysis with the box finite difference scheme is presented in this chapter.

The box finite difference scheme is also known as the Four-point implicit scheme or Preissmann scheme (Preissmann 1961). Four points are used to construct the scheme. According to this scheme, the partial derivatives and variables are approximated as follows (Cunge and Verway 1980, Chaudhry 2008):

$$\begin{aligned}\frac{\partial \mathbf{U}}{\partial t} &= \frac{(\mathbf{U}_j^{m+1} + \mathbf{U}_{j+1}^{m+1}) - (\mathbf{U}_j^{m} + \mathbf{U}_{j+1}^{m})}{2\Delta t}\\ \frac{\partial \mathbf{U}}{\partial x} &= \frac{\theta(\mathbf{U}_{j+1}^{m+1} - \mathbf{U}_j^{m+1})}{\Delta x} + \frac{(1-\theta)(\mathbf{U}_{j+1}^{m} - \mathbf{U}_j^{m})}{\Delta x}\\ \mathbf{U} &= \frac{1}{2}\theta(\mathbf{U}_{j+1}^{m+1} + \mathbf{U}_j^{m+1}) + \frac{1}{2}(1-\theta)(\mathbf{U}_{j+1}^{m} + \mathbf{U}_j^{m})\end{aligned} \tag{5.1}$$

where θ is a weighting coefficient, which is typically used as $0.6 - 0.7$ (Cunge and Verway 1980, Chaudhry 2008). The superscript m indicates that the variable is taken at a known time level and $m + 1$ indicates the next time level. The subscript j indicates the nodal point spaced apart by the discretization Δx. By substituting Eq. 5.1 into Eq. 2.19, we find:

$$\mathbf{U}_j^{m+1} + \mathbf{U}_{j+1}^{m+1} + 2\frac{\Delta t}{\Delta x}[\theta(\mathbf{F}_{j+1}^{m+1} - \mathbf{F}_j^{m+1}) + (1-\theta)(\mathbf{F}_{j+1}^{m} - \mathbf{F}_j^{m})] \\ + \Delta t[\theta(\mathbf{S}_j^{m+1} + \mathbf{F}_{j+1}^{m+1}) + (1-\theta)(\mathbf{S}_j^{m} + \mathbf{F}_{j+1}^{m})] = \mathbf{U}_j^{m} + \mathbf{U}_{j+1}^{m} \quad (5.2)$$

Eq. 5.2 is a set of non-linear implicit equations and requires an iterative method to solve for the unknowns. In this study, the Newton-Raphson iterative method is used to solve the system of equations. The Jacobian matrix and residual vectors for the iterative method are calculated numerically.

5.2 Non-uniform Flow Test Case Results

Fig. 5.2 and 5.3, and Table 5.1 and 5.2 show the non-uniform flow test case results for both scenarios with the Box scheme. The tables show that there are no errors in the discharge variable, i.e., steady solutions produce exact discharge solutions at all nodes. However, both the figure and table show that the errors in the depth solutions are apparent and the errors increase as discretization increases, and as roughness (decrease of C_*) and slope increase. For $\Delta x = 100$, the depth solution shows a tip of oscillation, and for $\Delta x = 200$, the depth solution shows significant $2\Delta x$ oscillations that spread over five elements. Similar $2\Delta x$ oscillations are also seen for $C_* = 10, S_0 = 0.0025$. In both scenarios, the oscillations are in the upstream region of transition from steep slope to mild slope.

Table 5.1: The non-uniform flow test case - effect of discretization with the Box scheme.

Δx (m)	C_*	S_0	q error (%)	h error(%)
20	15	0.000926	0	0.17
100	15	0.000926	0	6.46
200	15	0.000926	0	22.14

5.3 Fourier Analysis Results

The coefficients a_r and b_r of Eq. 3.6 for the Box scheme are shown in Appendix B. From those coefficients it is found that for the Box scheme $\frac{\mathrm{H}_n}{\mathrm{Z}}$ and $\frac{\Phi_n}{\mathrm{Z}}$ do not

Table 5.2: The non-uniform flow test case - effect of Chezy coefficient and slope with the Box scheme.

Δx (m)	C_*	S_0	q error (%)	h error(%)
100	20	0.000521	0	1.65
100	15	0.000926	0	6.46
100	10	0.0021	0	24.65

depend on the time step discretization. So for the Box scheme, we can write:

$$\left\{ \begin{matrix} \frac{\mathrm{H}_n}{\mathrm{Z}} \\ \frac{\Phi_n}{\mathrm{Z}} \end{matrix} \right\} = f(Fr_0, N_\lambda, \beta_{\Delta x}) \tag{5.3}$$

Fig. 5.4 shows analytical and numerical amplitudes of the depth and discharge variables and the corresponding errors as a function of N_λ with $Fr_0 = 0.5$ and $\beta_{\Delta x} = 1$ for the Box scheme. The figure shows that there are no discharge errors for any N_λ with the Box scheme, which is consistent with the non-uniform flow test case. However, there are depth amplitude errors, and the errors diminish as N_λ increases. For this case, the depth errors appear to be negligible for $N_\lambda > 10$.

Fig. 5.5 shows the variation of the depth amplitude errors as a function of N_λ for the range of Fr_0 with $\beta_{\Delta x} = 1$. The figure shows that the depth errors are low at low Fr_0 and increase with increasing Fr_0. There is a sudden increase in the errors when $Fr_0 > 0.5$, and the errors become greater than 0.4.

Fig. 5.6 shows the variation of the depth amplitude errors as a function of N_λ for the range of $\beta_{\Delta x}$ with $Fr_0 = 0.5$. The figure shows that the depth errors are low at low $\beta_{\Delta x}$ and increase with increasing $\beta_{\Delta x}$. The errors are less than 0.1 for $\beta_{\Delta x} \leq 1$, and a sudden increase in the errors occur for $\beta_{\Delta x} > 1$.

Fig. 5.7 shows the variation of the depth amplitude errors as a function of $\beta_{\Delta x}$ for the range of Fr_0 with $N_\lambda = 2$. The figure shows that the errors are low at low Fr_0 and low $\beta_{\Delta x}$ and increase with the increasing of Fr_0 and $\beta_{\Delta x}$. The figure also shows that for any value of Fr_0, the errors can be negligible when $\beta_{\Delta x} \leq 0.1$. The errors can reach up to 1 or more when both Fr_0 and $\beta_{\Delta x}$ are large.

5.4 Discussion

Both the non-uniform flow test case and Fourier analysis results show that for the Box scheme, there are no oscillations or errors in the discharge solutions.

However, both results also show that there are errors in the depth solutions. The non-uniform flow test results show that the depth errors increase as discretization increases, and as roughness (decrease of C_*) and slope increase. The depth oscillations also appear as $2\Delta x$ wavelength. The Fourier analysis results show that the errors increase as Fr_0 and $\beta_{\Delta x}$ increase. The Fourier analysis results also show that the depth errors can be 1 or more when both Fr_0 and $\beta_{\Delta x}$ are large and the errors are negligible when $\beta_{\Delta x} \leq 0.1$ for this scheme.

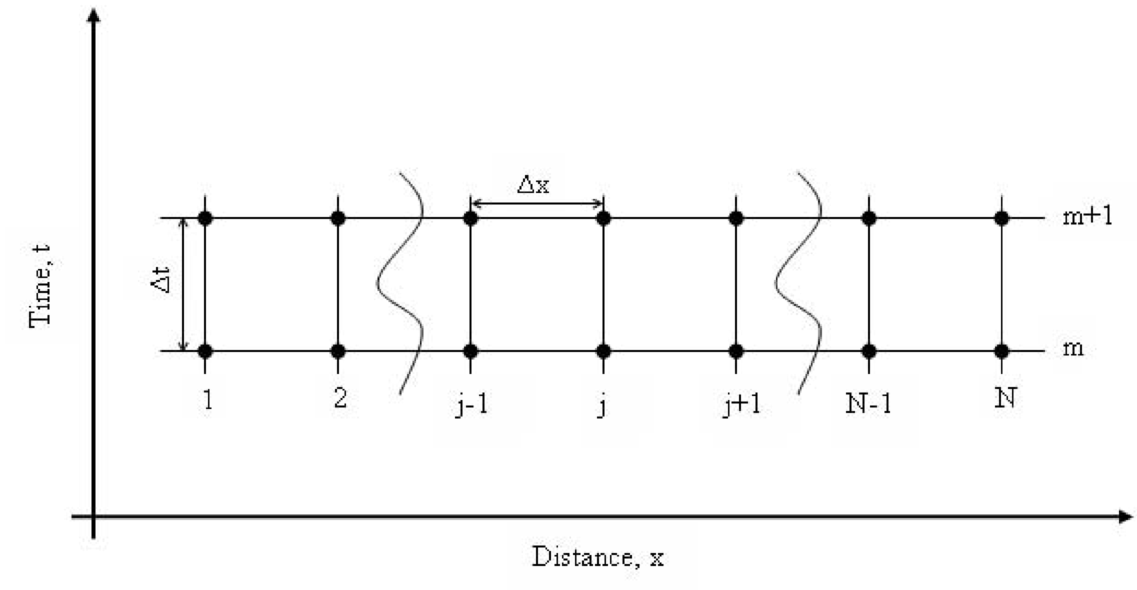

Figure 5.1: Definition sketch of the finite difference grid for one-dimensional flow.

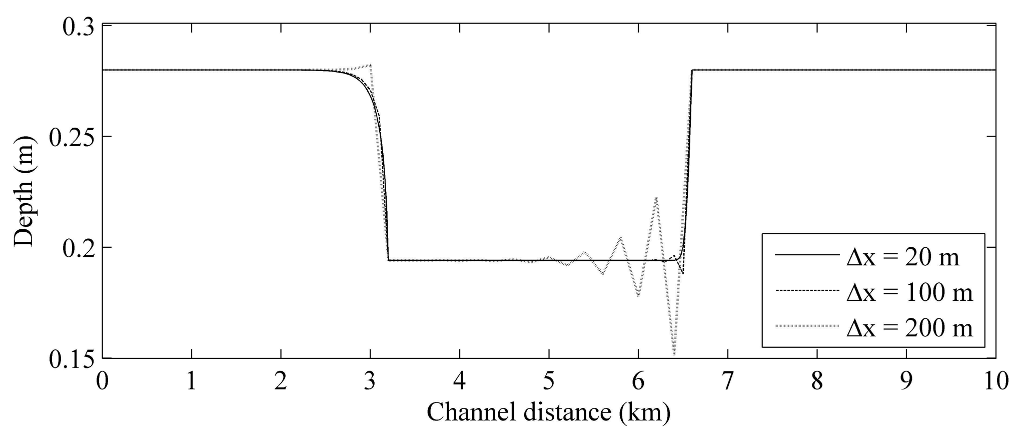

Figure 5.2: Depth solutions for the non-uniform flow test case with the Box scheme - effect of discretization.

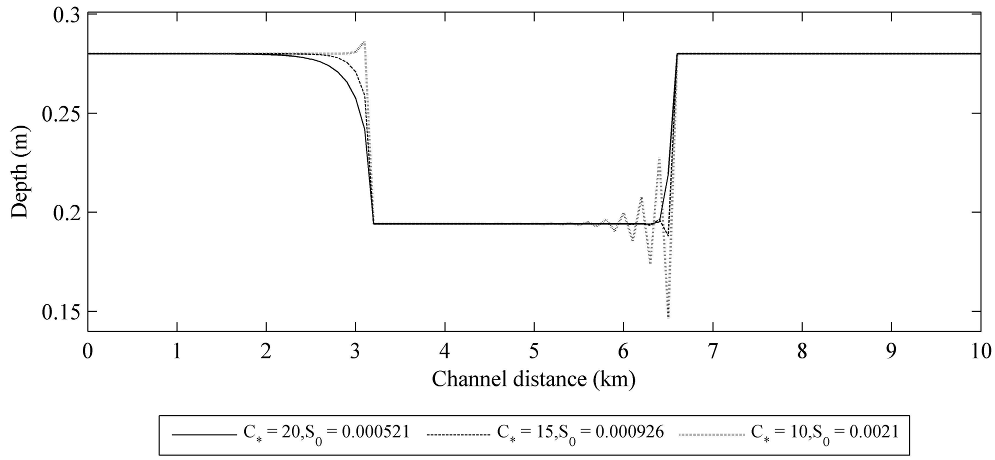

Figure 5.3: Depth solutions for the non-uniform flow test case with the Box scheme - effect of Chezy coefficient and slope.

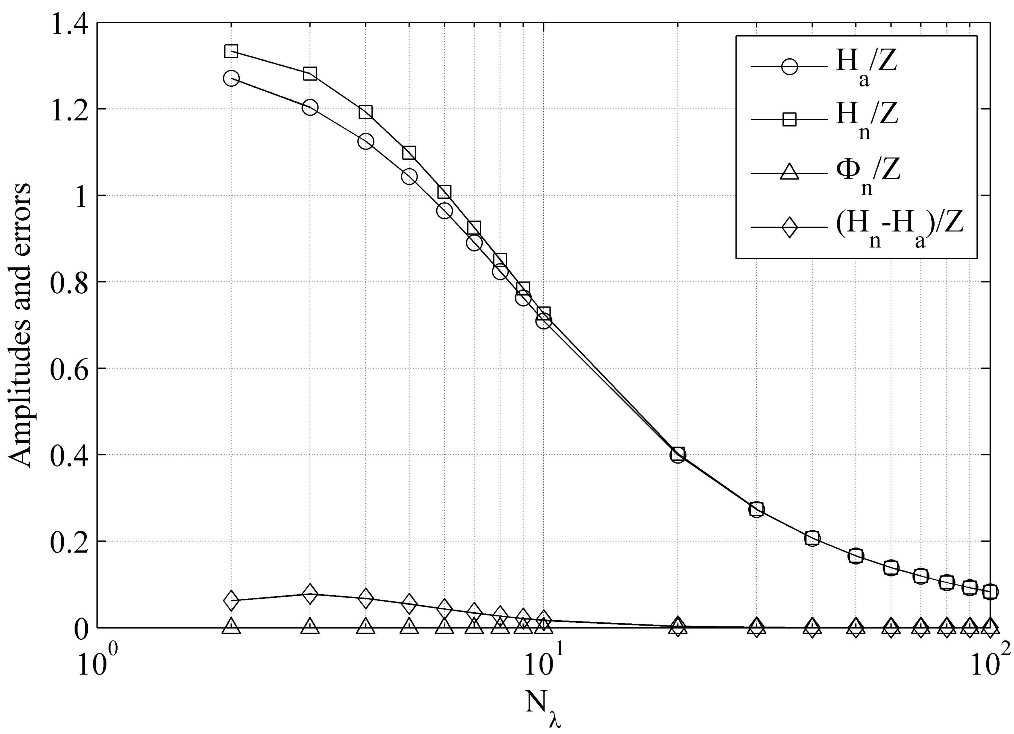

Figure 5.4: Normalized amplitudes and errors as a function of N_λ for $Fr_0 = 0.5$ and $\beta_{\Delta x} = 1$ using the Box scheme.

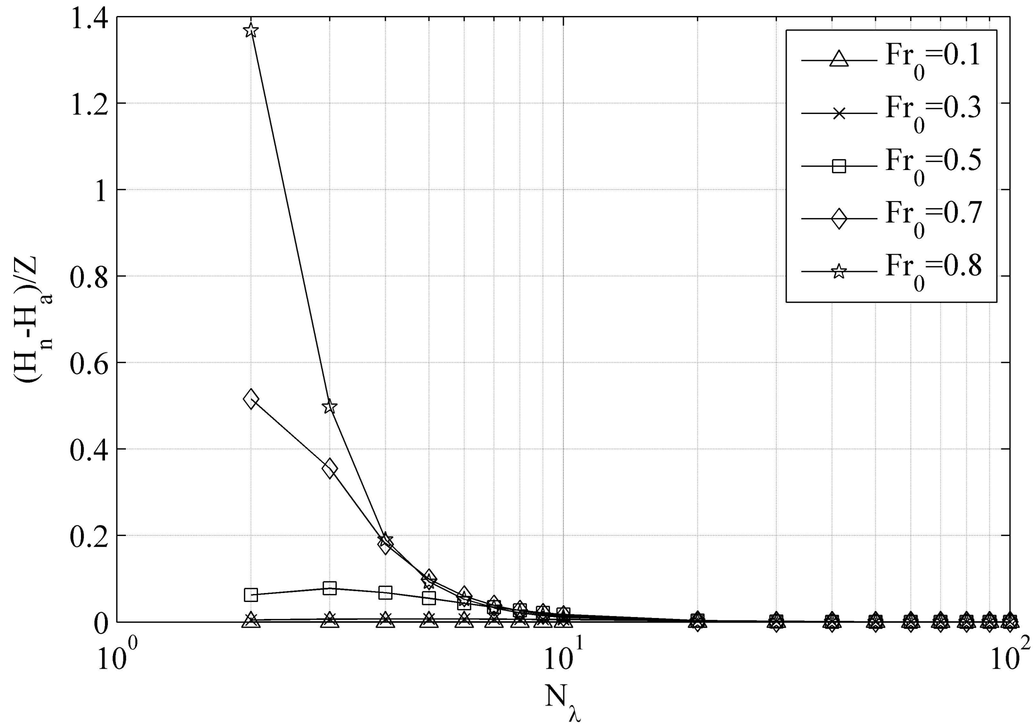

Figure 5.5: Depth amplitude errors as a function of N_λ for a range of Fr_0 and $\beta_{\Delta x} = 1$ using the Box scheme.

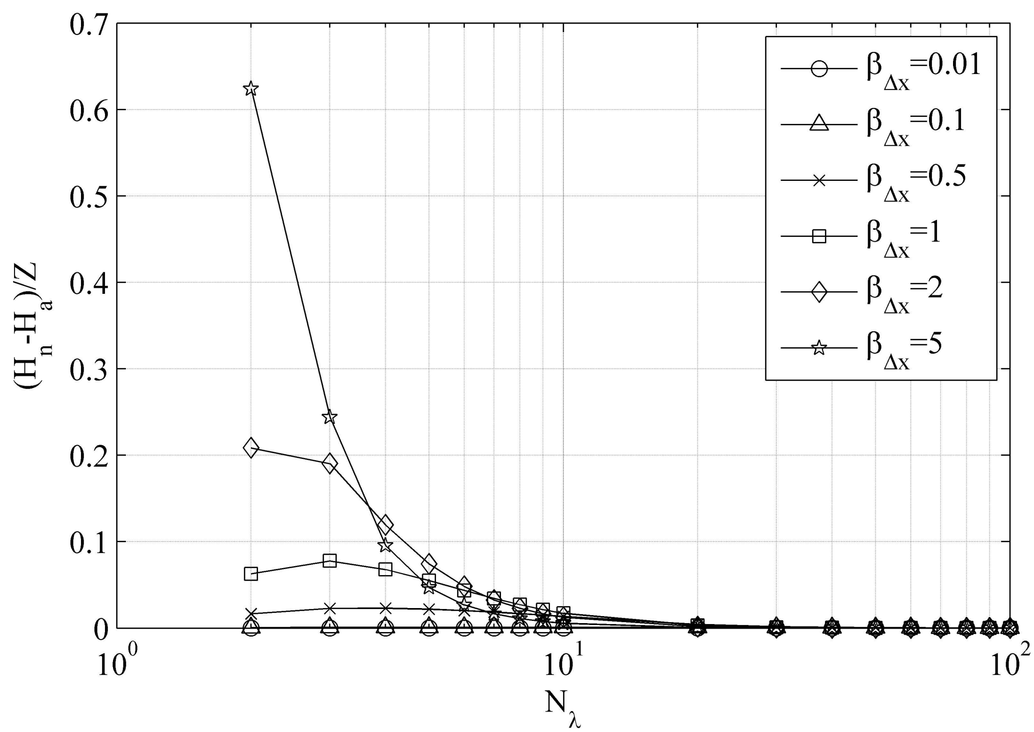

Figure 5.6: Depth amplitude errors as a function N_λ for a range of $\beta_{\Delta x}$ and $Fr_0 = 0.5$ using the Box scheme.

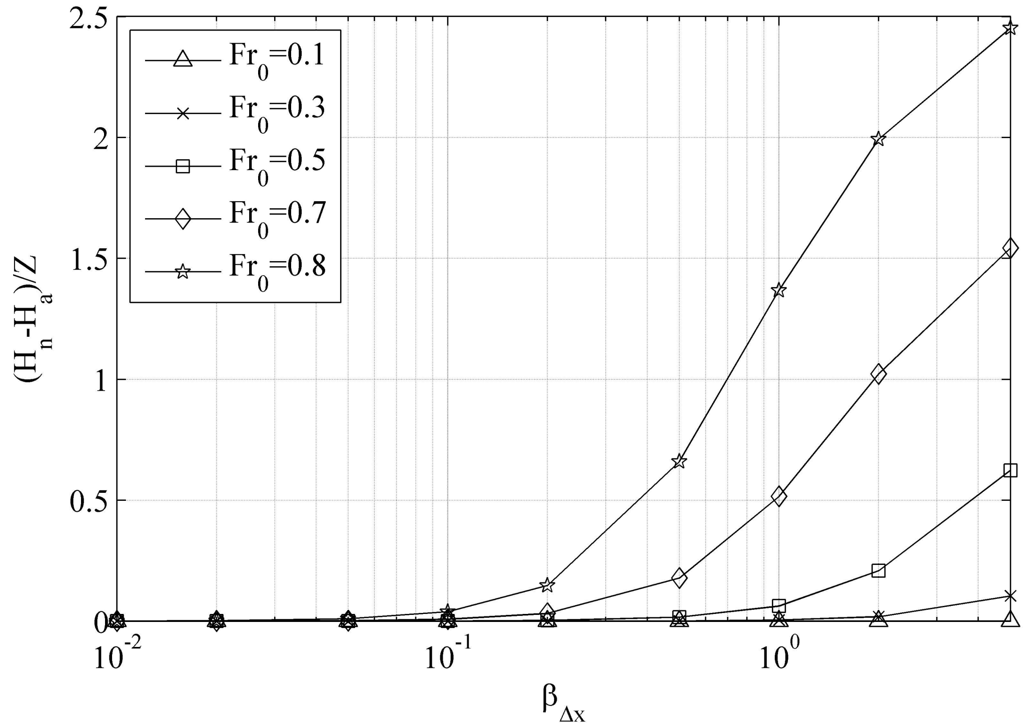

Figure 5.7: Depth amplitude errors as a function of $\beta_{\Delta x}$ for a range of Fr_0 and $N_\lambda = 2$ using the Box scheme.

Chapter 6

MacCormack Finite Difference Scheme

6.1 Introduction

The MacCormack scheme (MacCormack 1969) is an explicit shock-capturing scheme that is second-order accurate both in space and time (Chaudhry 2008). The scheme requires two steps, predictor-corrector, to obtain the solutions. Two alternatives of this scheme are possible for one-dimensional flow. In one alternative, backward finite differences are used in the predictor part and forward differences are used in the corrector part to approximate the spatial partial derivatives (Chaudhry 2008). In the other alternative, forward differences are used in the predictor part and backward differences are used in the corrector part (Chaudhry 2008). For the first alternative, the predictor part is:

$$\begin{aligned} \frac{\partial \mathbf{U}}{\partial t} &= \frac{\mathbf{U}_j^* - \mathbf{U}_j^m}{\Delta t} \\ \frac{\partial \mathbf{F}}{\partial x} &= \frac{\mathbf{F}_j^m - \mathbf{U}_{j-1}^m}{\Delta x} \end{aligned} \tag{6.1}$$

in which superscript (*) refers to the variables computed during the predictor part. Substitution of Eq. 6.1 into Eq. 2.19 yields:

$$\mathbf{U}_j^* = \mathbf{U}_j^m - \frac{\Delta t}{\Delta x}(\mathbf{F}_j^m - \mathbf{F}_{j-1}^m) + \Delta t \mathbf{S}_j^m \tag{6.2}$$

The equation for the corrector part is as follows:

$$\begin{aligned} \frac{\partial \mathbf{U}}{\partial t} &= \frac{\mathbf{U}_j^{**} - \mathbf{U}_j^m}{\Delta t} \\ \frac{\partial \mathbf{F}}{\partial x} &= \frac{\mathbf{F}_{j+1}^* - \mathbf{U}_j^*}{\Delta x} \end{aligned} \tag{6.3}$$

in which superscript (**) refers to the variables computed during the corrector part. Substitution of Eq. 6.3 into Eq. 2.19 yields:

$$\mathbf{U}_j^{**} = \mathbf{U}_j^m - \frac{\Delta t}{\Delta x}(\mathbf{F}_{j+1}^* - \mathbf{F}_j^*) + \Delta t \mathbf{S}_j^* \tag{6.4}$$

The value of $\mathbf{U}_j$ at the next time level $m+1$ can be found as:

$$\mathbf{U}_j^{m+1} = \frac{1}{2}(\mathbf{U}_j^* + \mathbf{U}_j^{**}) \tag{6.5}$$

Eq. 6.5 is an explicit set of equations, where unknowns can be solved directly from the known values.

6.2 Non-uniform Flow Test Case Results

The MacCormack scheme is the only scheme in our study in which the time step discretization affects the final steady state solution. Therefore, the test case scenarios as shown in Table 3.1 and 3.2 are first run for a fixed time step. In addition to these, another test scenario is run where for a fixed spatial discretization, Chezy coefficient, and slope, three different time step discretizations are used (as shown in Table 6.3).

Fig. 6.1 and 6.2 and Table 6.1 and 6.2 show the non-uniform flow test case results for both scenarios with the MacCormack scheme. The figures and tables show that the oscillations and errors in the depth and discharge solutions are apparent. These errors increase as discretization increases, and as roughness (decrease of C_*) and slope increase. Similar to the CDG scheme results, the discharge oscillations in the transition from steep to mild slope are relatively larger than the oscillations in the transition from mild to steep slope.

Fig. 6.3 shows the discharge and depth solutions for the test scenario as shown in Table 6.3. Both the figure and table show that as the time discretizations increase the discharge errors increase. For the depth errors, the errors decrease first as Δt increases from 4.5 sec to 22 sec and then increase as Δt increases from 22 sec to 36 sec.

6.3 Fourier Analysis Results

The coefficients a_r and b_r of Eq. 3.6 for the MacCormack scheme are shown in Appendix C. From those coefficients, it is found that in addition to the parameters

Table 6.1: The non-uniform flow test case - effect of spatial discretization with the MacCormack scheme.

Δx (m)	C_*	S_0	Δt (sec)	q error (%)	h error(%)
20	15	0.000926	4.5	0.50	2.16
100	15	0.000926	4.5	4.70	6.82
200	15	0.000926	4.5	9.34	11.5

Table 6.2: The non-uniform flow test case - effect of Chezy coefficient and slope with the MacCormack scheme.

Δx (m)	C_*	S_0	Δt (sec)	q error (%)	h error(%)
100	20	0.000521	4.5	1.48	5.27
100	15	0.000926	4.5	4.70	6.82
100	10	0.0021	4.5	10.4	11.87

shown in Eq. 3.7, $\frac{\mathrm{H}_n}{\mathrm{Z}}$ and $\frac{\Phi_n}{\mathrm{Z}}$ also depend on $\frac{\Delta\tau}{\Delta\xi}$. $\frac{\Delta\tau}{\Delta\xi}$ can be written as $u_0\frac{\Delta t}{\Delta x}$ and called the average flow Courant number, Cr_0. Therefore, for the MacCormack scheme, we can write:

$$\left\{\begin{matrix} \frac{\mathrm{H}_n}{\mathrm{Z}} \\ \frac{\Phi_n}{\mathrm{Z}} \end{matrix}\right\} = f(Fr_0, N_\lambda, \beta_{\Delta x}, Cr_0) \tag{6.6}$$

Fig. 6.4 shows analytical and numerical amplitudes of the depth and discharge variables and the corresponding errors as a function of N_λ with $Fr_0 = 0.5$, $Cr_0 = 0.5$ and $\beta_{\Delta x} = 1$. The figure shows that errors in both solution variables are observed with the MacCormack scheme. The errors are at their maximum at the shortest wavelength and diminish as N_λ increases. For this case, the depth errors appear to be negligible for $N_\lambda \geq 20$, and the discharge errors become negligible for $N_\lambda \geq 50$.

Fig. 6.5 shows the variation of the discharge and depth amplitude errors as a function of N_λ for the range of Fr_0 with $Cr_0 = 0.5$ and $\beta_{\Delta x} = 1$. The figure shows that both errors are low at low Fr_0. As Fr_0 increases, the discharge errors (Fig. 6.5a) at the shortest wavelength increase. At the higher wavelengths, the errors increase until $Fr_0 \leq 0.5$ and the errors decrease when $Fr_0 > 0.5$. The depth errors (Fig. 6.5b) are small compared to the discharge errors. The numerical depth amplitudes at the shortest wavelength are greater than the analytical depth amplitudes until $Fr_0 \leq 0.5$ and become less when $Fr_0 > 0.5$.

Table 6.3: The non-uniform flow test case - effect of time discretization with the MacCormack scheme.

Δx (m)	C_*	S_0	Δt (sec)	q error (%)	h error(%)
100	15	0.000926	4.5	4.70	6.82
100	15	0.000926	22	12.20	2.97
100	15	0.000926	36	22.37	4.7

Fig. 6.6 shows the variation of the discharge and depth amplitude errors as a function of N_λ for the range of $\beta_{\Delta x}$ with $Fr_0 = 0.5$ and $Cr_0 = 0.5$. The figure shows that both errors are low at low $\beta_{\Delta x}$ and increase with increasing $\beta_{\Delta x}$. The discharge errors are negligible when $\beta_{\Delta x} \leq 0.1$ and reach to 1 or more when $\beta_{\Delta x} > 1$. The depth errors are negligible when $\beta_{\Delta x} \leq 1$. A sudden increase in depth errors occurs when $\beta_{\Delta x} > 1$ and reaches more than 1.

Fig. 6.7 shows the variation of the discharge and depth amplitude errors as a function of $\beta_{\Delta x}$ for the range of Fr_0 with $Cr_0 = 0.5$ and $N_\lambda = 2$. The figure shows that both errors are low at low Fr_0 and low $\beta_{\Delta x}$. For any Fr_0, the discharge errors in 6.7a can be negligible when $\beta_{\Delta x} \leq 0.01$. The figure also shows that the errors can reach up to 1 or more when $\beta_{\Delta x}$ is large, i.e., $\beta_{\Delta x} \geq 1$. The numerical depth amplitudes (Fig. 6.7b) are less than the analytical depth amplitudes when $\beta_{\Delta x} \leq 1$ and become greater for $\beta_{\Delta x} > 1$.

Fig. 6.8 shows the variation of the discharge and depth amplitude errors as a function of N_λ for $Cr_0 = 0.1$ to 1 with $Fr_0 = 0.5$ and $\beta_{\Delta x} = 1$. Fig. 6.8a shows that for the shortest wavelength, the discharge errors are high at low Cr_0 and decrease with increasing Cr_0. However, for the higher wavelengths, the discharge errors are low at small Cr_0 and increase with increasing Cr_0. Fig. 6.8b shows that the numerical depth amplitudes are less than the analytical amplitudes when $Cr_0 \leq 0.3$ and become greater when $Cr_0 > 0.3$ and increase as Cr_0 increases.

6.4 Discussion

The non-uniform flow test results with the MacCormack scheme show that non-physical oscillations in both the depth and discharge solutions are apparent when discretization, roughness and slope are large. The results further shows that the oscillations appear as $2\Delta x$ wavelength oscillations. The Fourier analysis results show that the errors in both variables are apparent and increase with increasing Fr_0 and $\beta_{\Delta x}$. The Fourier analysis results also show that the MacCormack scheme is susceptible to high error at higher $\beta_{\Delta x}$, e.g., $\beta_{\Delta x} \geq 2$.

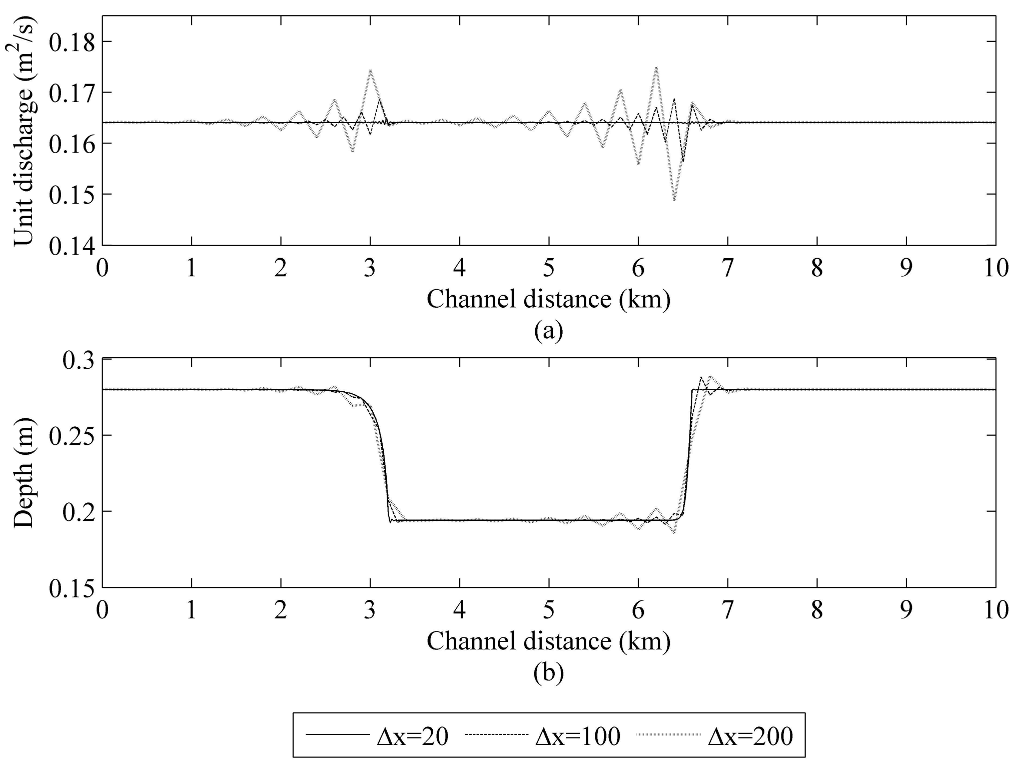

Figure 6.1: (a) Discharge and (b) Depth solutions for the non-uniform flow test case with the MacCormack scheme - effect of discretization.

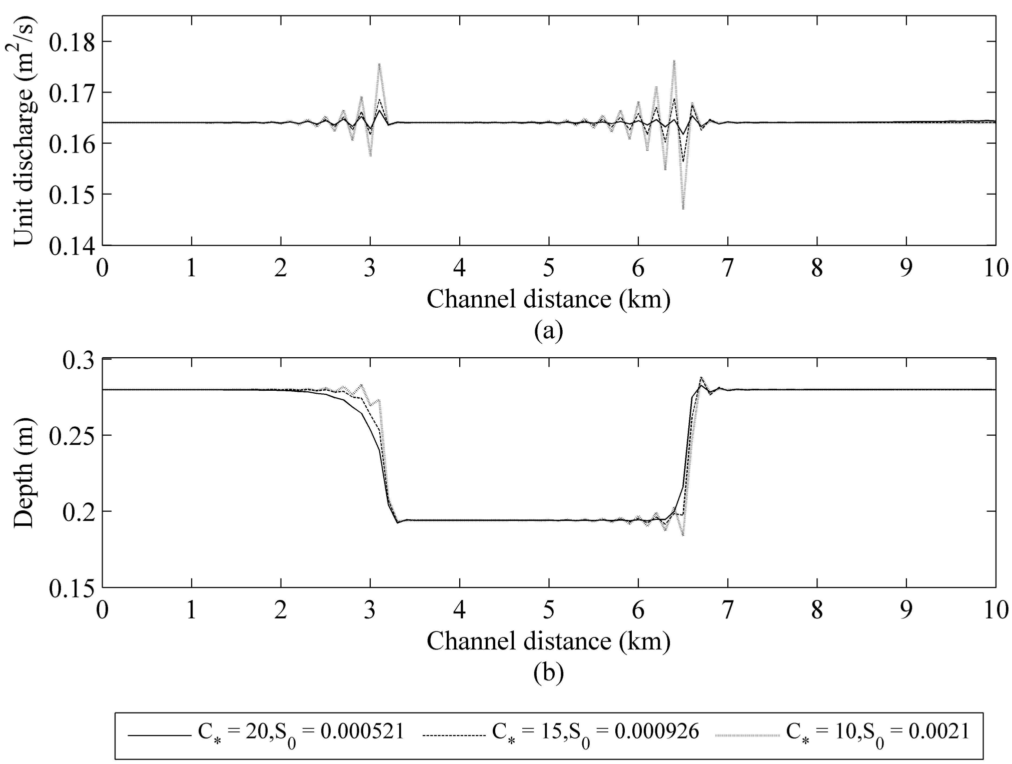

Figure 6.2: (a) Discharge and (b) Depth solution for the non-uniform flow test case with the MacCormack scheme - effect of Chezy coefficient and slope.

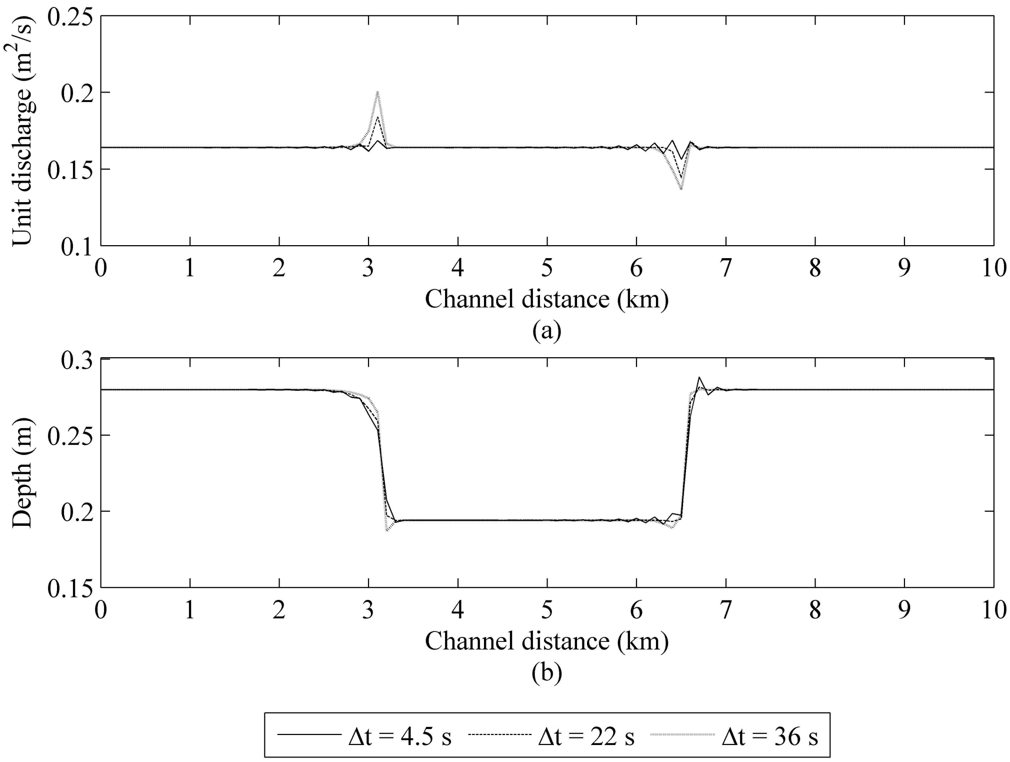

Figure 6.3: (a) Discharge and (b) Depth solution for the non-uniform flow test case with the MacCormack scheme - effect of time discretization.

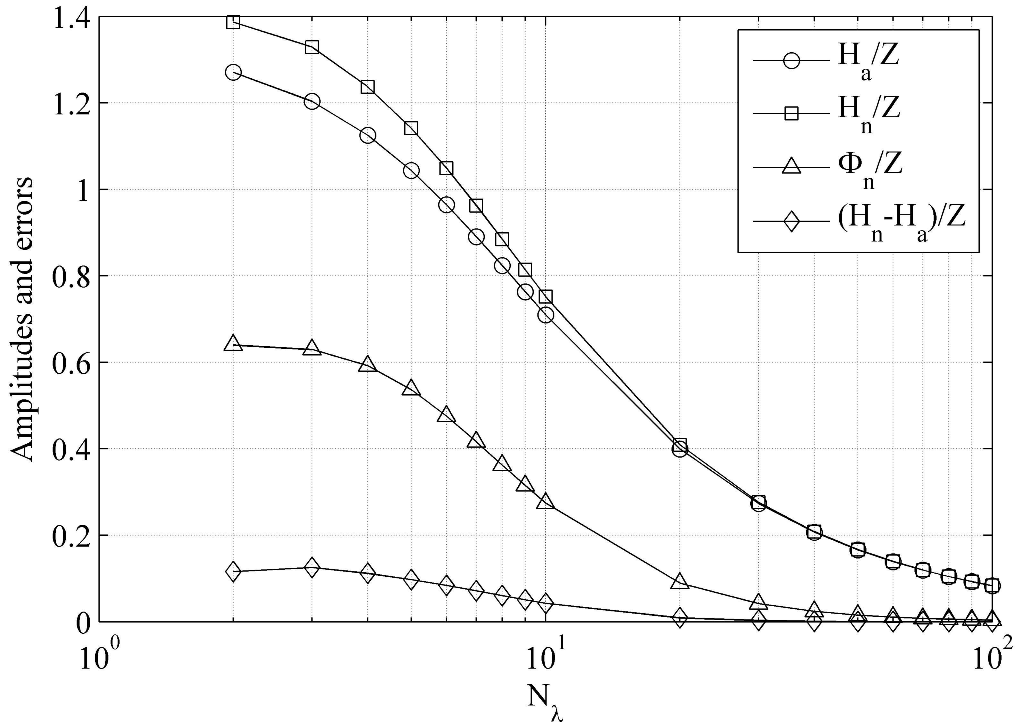

Figure 6.4: Normalized amplitudes and errors as a function of N_λ for $Fr_0 = 0.5$, $Cr_0 = 0.5$, and $\beta_{\Delta x} = 1$ using the MacCormack scheme.

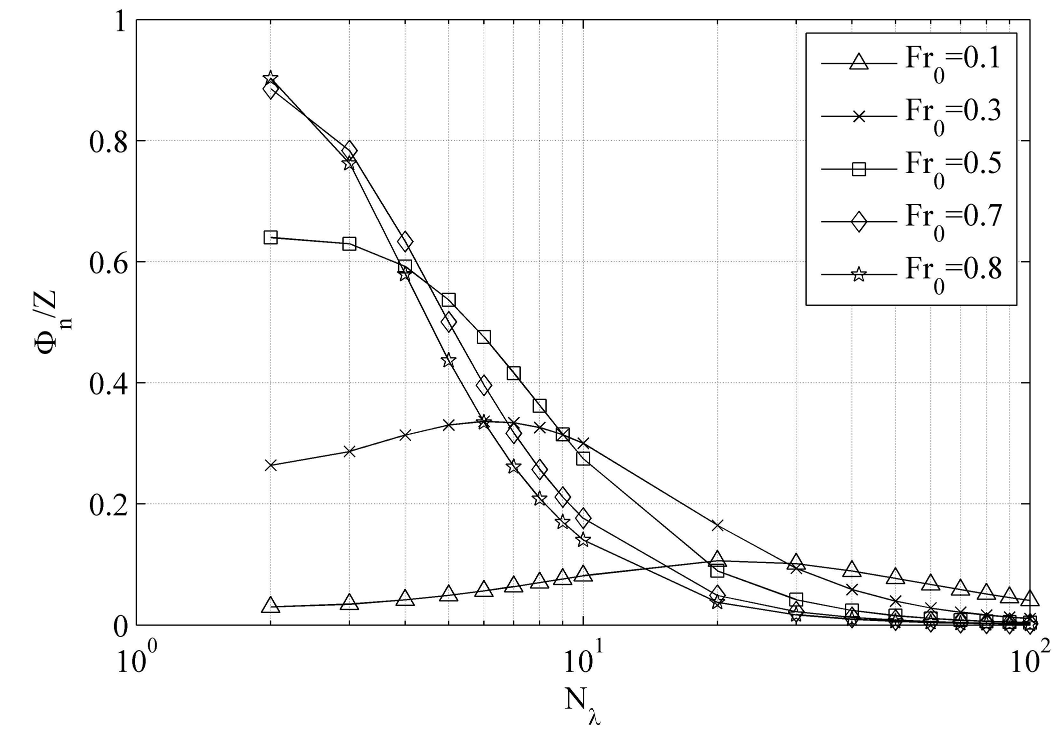

(a)

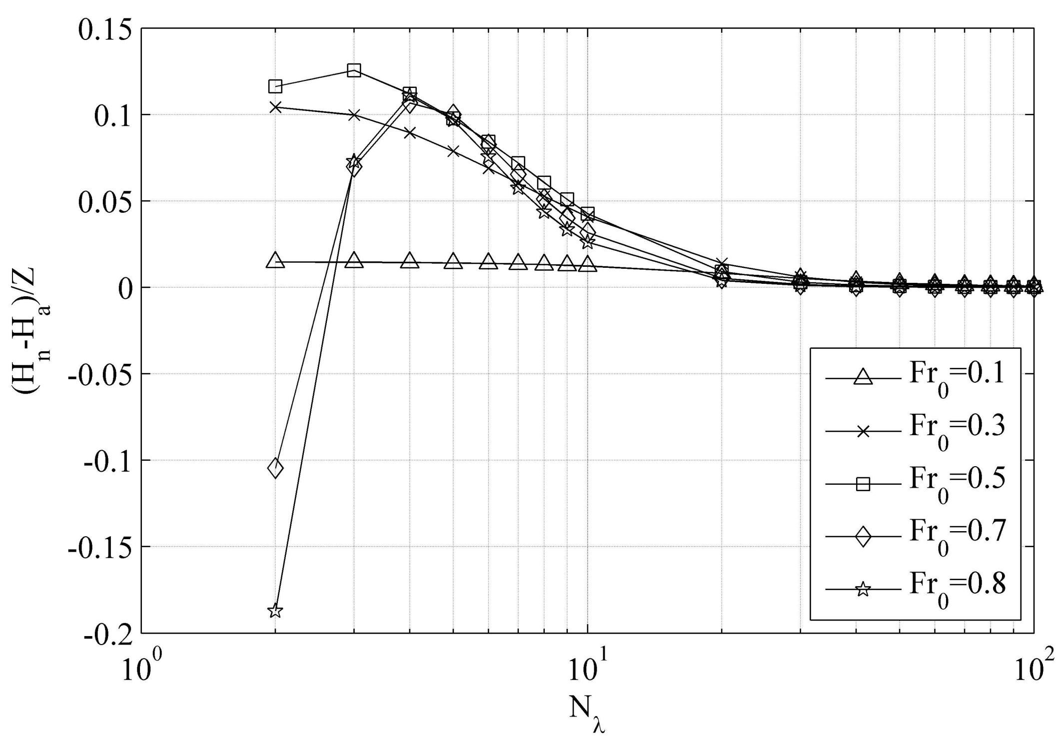

(b)

Figure 6.5: (a) Discharge and (b) Depth amplitude errors as a function of N_λ for a range of Fr_0, $Cr_0 = 0.5$, and $\beta_{\Delta x} = 1$ using the MacCormack scheme.

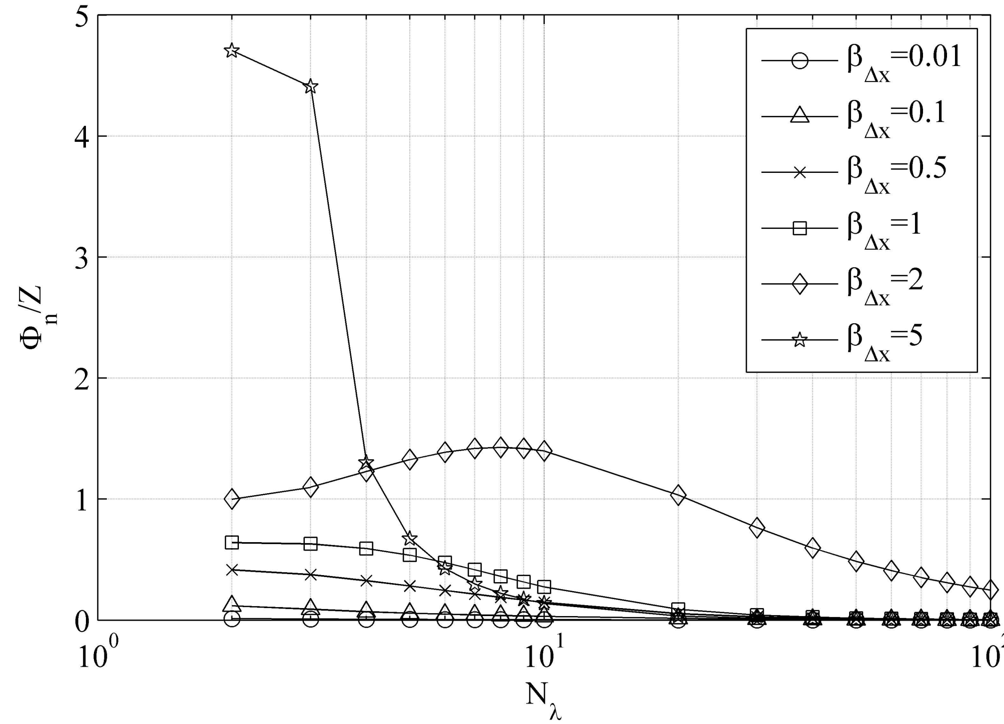

(a)

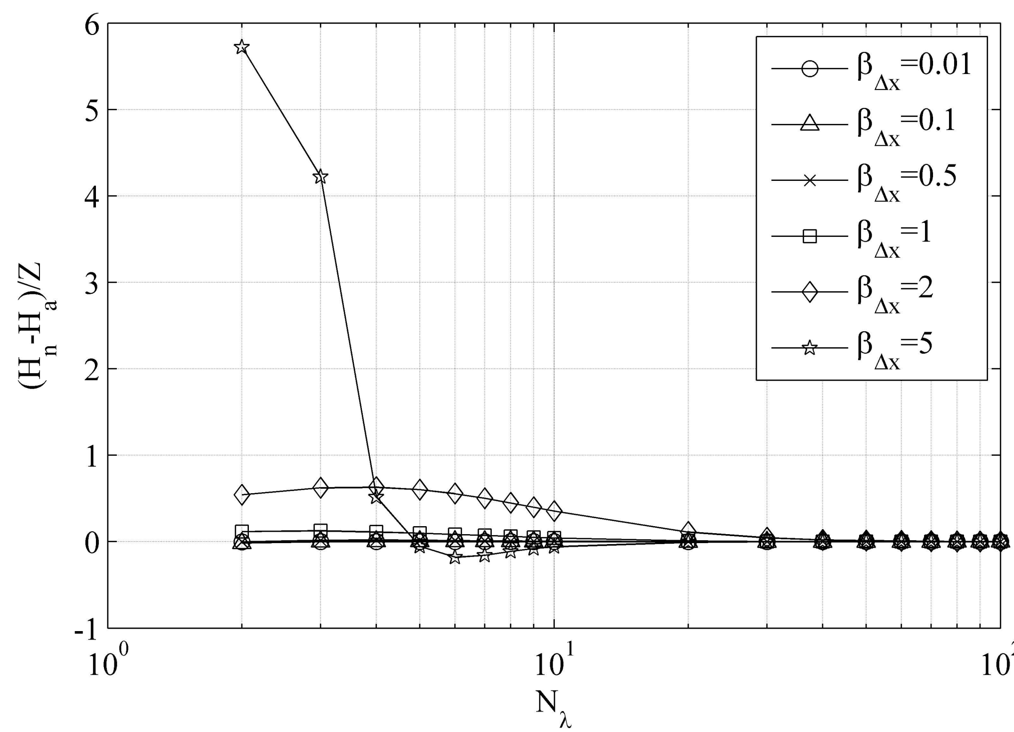

(b)

Figure 6.6: (a) Discharge and (b) Depth amplitude errors as a function of N_λ for a range of $\beta_{\Delta x}$, $Cr_0 = 0.5$, and $Fr_0 = 0.5$ using the MacCormack scheme.

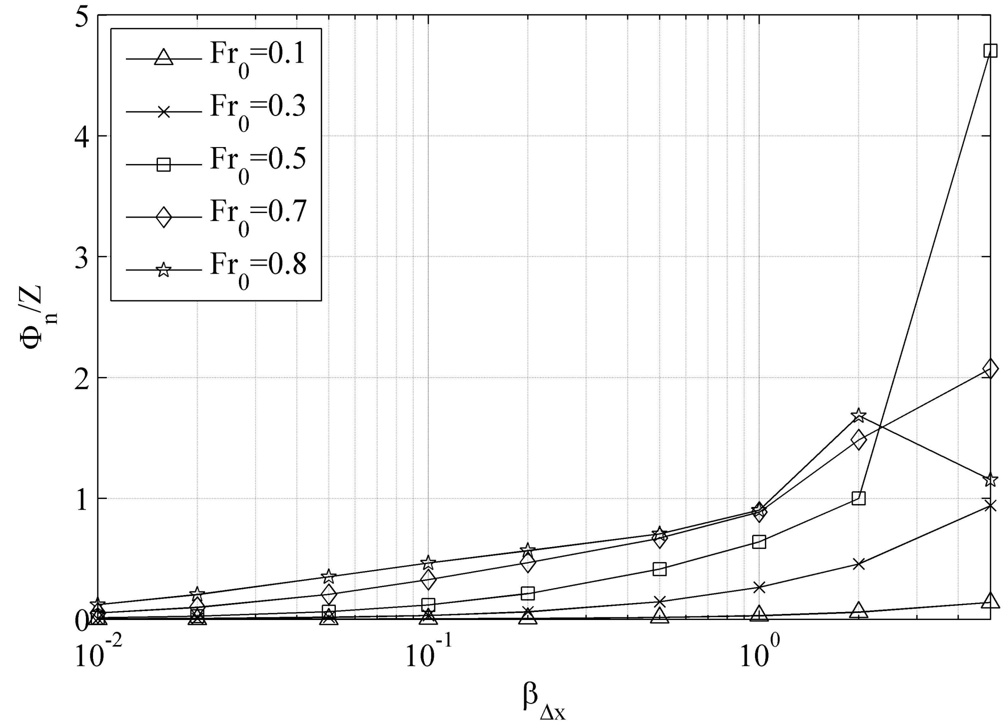

(a)

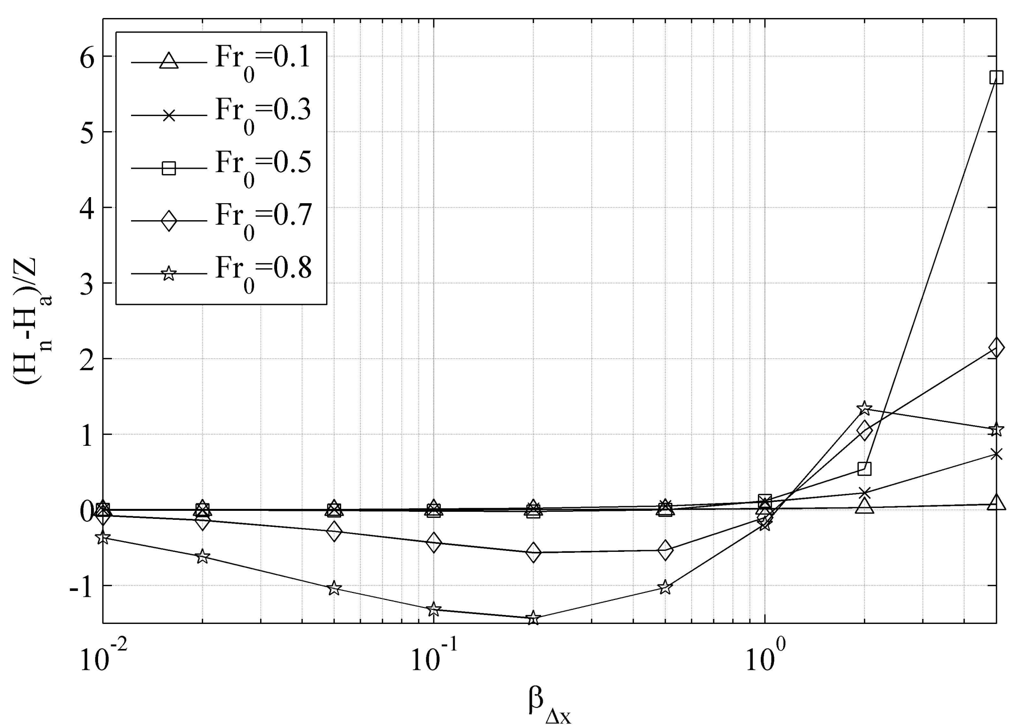

(b)

Figure 6.7: (a) Discharge and (b) Depth amplitude errors as a function of $\beta_{\Delta x}$ for a range of Fr_0, $Cr_0 = 0.5$, and $N_\lambda = 2$ using the MacCormack scheme.

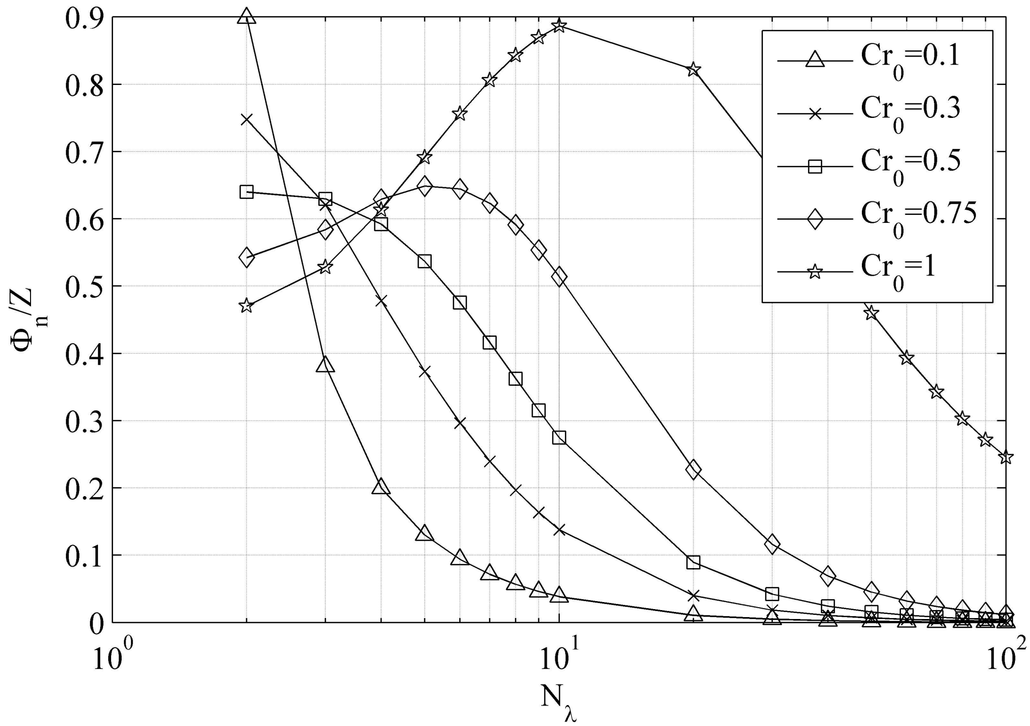

(a)

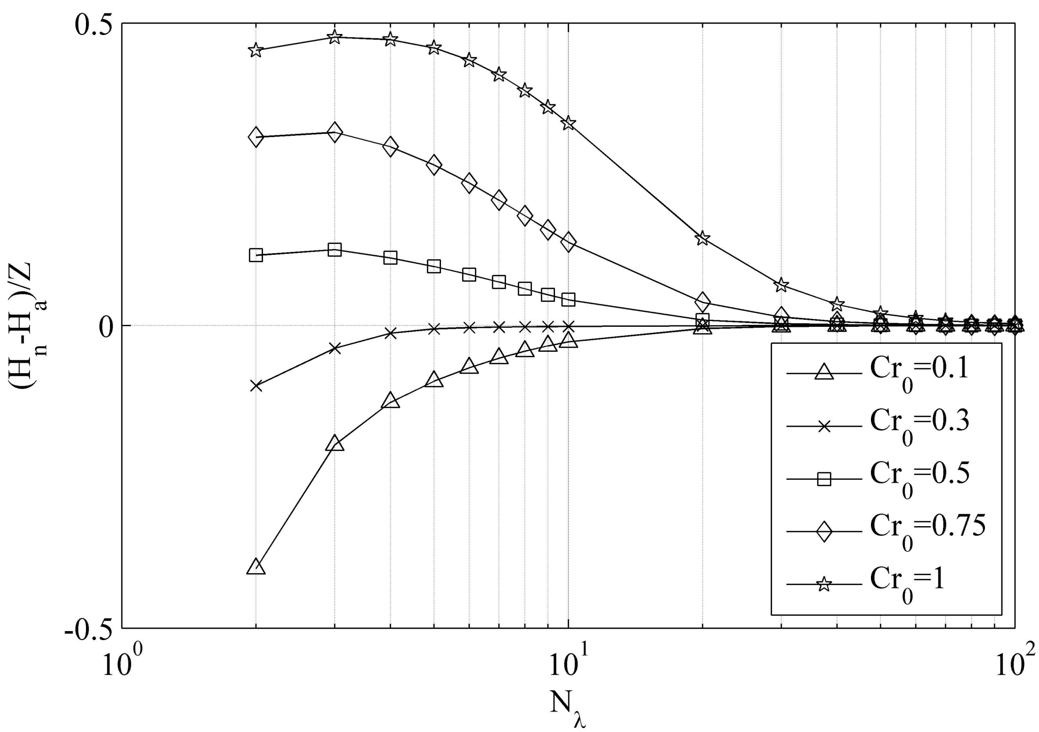

(b)

Figure 6.8: (a) Discharge and (b) Depth amplitude errors as a function of N_λ for a range of Cr_0, $Fr_0 = 0.5$, and $\beta_{\Delta x} = 1$ using the MacCormack scheme.

Chapter 7

Balanced Godunov Finite Volume Scheme

7.1 Introduction

The FVM method is popular today, especially among researchers, because of its advantages over the other two methods, the FDM and FEM. The FVM method has the simplicity of FDM method, but also has the support of unstructured grids like FEM. Moreover, the underlying mathematical formulation that uses the integral form of the Saint-Venant equations instead of the differential form of the equations, guarantees the conservative properties.

In our study, we have studied two first order finite volume methods: a balanced Godunov scheme and a one-sided upwind-downwind scheme. Because a higher-order scheme reduces to a first order scheme to suppress any wiggles when there is a sharp gradient or discontinuity, studying first order schemes can also give us adequate insight into the friction dominated problem. In this chapter, the balanced Godunov scheme and its results are presented, and in the next chapter the other scheme and its results are presented.

The FVM that is considered for our study uses a cell centered grid, as shown in Fig. 7.1. In this case, the cell average values of conservative variables are updated using fluxes computed at the cell boundaries. Integrating Eq. 2.19 over the j^{th} cell with length and applying explicit Euler time stepping, we find:

$$\mathbf{U}_j^{m+1} = \mathbf{U}_j^m - \frac{\Delta t}{\Delta x_j}(\mathbf{F}_{j+1/2}^m - \mathbf{F}_{j-1/2}^m) + \Delta t \mathbf{S}_j^m \tag{7.1}$$

A variation of this chapter and the next chapter together are presented and published in the 34^{th} IAHR congress in 2011.

Different approaches are available to evaluate the inter-cell flux, i.e., $\mathbf{F}^m_{j\pm1/2}$, which construct various conservative numerical schemes. A common practice is to solve the Riemann problem at the interface of two computing finite volumes or cells and construct an upwind scheme utilizing the direction of wave propagation embodied in the Saint-Venant equations. This is the fundamental philosophy of Godunov type finite volume schemes (Chung 2002, Toro 2001, Toro 2009).

Different exact solvers (e.g., Godunov 1976, Gottlieb and Groth 1988, Toro 1989) and approximate solvers (e.g., Roe 1981, Osher and Solomon 1982, Harten and Van Leer 1983) are used to solve the Riemann problem. But the exact solvers are computationally expensive compared to the approximate solvers (Toro 2009). Moreover, the approximate solvers provide sufficient accurate results for a wide range of practical problems and thus are used in most cases.

Roe's approximate solver (Roe 1981) is a simple solver that is used in our study. In Roe's method, the flux difference across the cell boundary are decomposed into two traveling discontinuities, which are then used to estimate the flux at the cell boundary as (Bradford and Sanders 2005):

$$\begin{aligned}\mathbf{F}_{j\pm1/2} &= \mathbf{F}^L_{j\pm1/2} + (\hat{\mathbf{R}}\hat{\mathbf{\Lambda}}^-\hat{\mathbf{R}}^{-1}\mathbf{\Delta U})_{j\pm1/2} \\ &= \mathbf{F}^R_{j\pm1/2} - (\hat{\mathbf{R}}\hat{\mathbf{\Lambda}}^+\hat{\mathbf{R}}^{-1}\mathbf{\Delta U})_{j\pm1/2} \\ &= \frac{1}{2}[\mathbf{F}^L_{j\pm1/2} + \mathbf{F}^R_{j\pm1/2} - (\hat{\mathbf{R}}|\hat{\mathbf{\Lambda}}|\hat{\mathbf{R}}^{-1}\mathbf{\Delta U})_{j\pm1/2}]\end{aligned} \tag{7.2}$$

where $\mathbf{F}^L$ and $\mathbf{F}^R$ denote the fluxes evaluated to the left and right of the boundary, respectively, and $\mathbf{\Delta}$ denotes the finite difference across the cell boundary. $\hat{\mathbf{\Lambda}}^\pm$ are the positive/negative eigenvalues, and $\hat{\mathbf{R}}$ is the right eigenvectors of the matrix $\hat{\mathbf{A}}$. '$\hat{\ }$' denotes that the variables are evaluated at Roe's average state (Roe 1981). Applying Eq. 7.2 to Eq. 7.1, we get:

$$\mathbf{U}^{m+1}_j = \mathbf{U}^m_j - \frac{\Delta t}{\Delta x_j}\left((\hat{\mathbf{R}}\hat{\mathbf{\Lambda}}^+\hat{\mathbf{R}}^{-1}\mathbf{\Delta U})_{j-1/2} + (\hat{\mathbf{R}}\hat{\mathbf{\Lambda}}^-\hat{\mathbf{R}}^{-1}\mathbf{\Delta U})_{j+1/2}\right) + \Delta t\mathbf{S}^m_j \tag{7.3}$$

In the above equation, for the source terms $\mathbf{S}_j$, the nodal variables can be considered at the j^{th} cell and the bed elevation gradient can be taken as cell centered difference, i.e.,

$$\mathbf{S}_j = \begin{bmatrix} 0 \\ -gh_j\frac{z_{j+1/2}-z_{j-1/2}}{\Delta x} - \frac{q_j|q_j|}{C^2_{*j}h^2_j}\end{bmatrix} \tag{7.4}$$

This form of the Godunov scheme is known as the first-order point source Godunov scheme (Hubbard and Garcia-Navarro 2000, Toro 2001). This form of the scheme does not balance the flux and source terms and therefore does not produce exact steady state discharge solutions with a non-level bed, i.e., it produces non-physical oscillations for the cell centered discharge solutions (Bradford and Sanders 2005, Petaccia and Zech 2009, Hubbard and Garcia-Navarro 2000, Zhou and Ingram 2001). Popularity is growing for balanced Godunov schemes in which the source terms are balanced with the flux terms in such a way that they produce exact steady state cell center discharge solutions (e.g. Hubbard and Garcia-Navarro 2000).

In a first-order balanced Godunov scheme, the source terms are discretized in a way similar to the discretization of flux terms (Hubbard and Garcia-Navarro 2000). Thus, Eq. 7.3 becomes:

$$\mathbf{U}_j^{m+1} = \mathbf{U}_j^m - \frac{\Delta t}{\Delta x_j}\left((\hat{\mathbf{R}}\hat{\mathbf{\Lambda}}^+\hat{\mathbf{R}}^{-1}\mathbf{\Delta U})_{j-1/2} + (\hat{\mathbf{R}}\hat{\mathbf{\Lambda}}^-\hat{\mathbf{R}}^{-1}\mathbf{\Delta U})_{j+1/2}\right) + \Delta t\left(\hat{\mathbf{S}}^+_{j-1/2} + \hat{\mathbf{S}}^-_{j+1/2}\right) \tag{7.5}$$

where $\hat{\mathbf{S}}^{\pm}_{j\pm1/2} = (\hat{\mathbf{R}}\mathbf{I}^{\pm}\hat{\mathbf{R}}^{-1})_{j\pm1/2}$ and $\mathbf{I}^{\pm} = \hat{\mathbf{\Lambda}}^{-1}\hat{\mathbf{\Lambda}}^{\pm}$.

Eq. 7.5 is an explicit non-linear system of equations, and the unknowns can be solved directly from the known values. Like any cell centered finite volume schemes, two ghost cells are introduced at the boundaries to complete the systems. The time step discretization may not affect the final steady state solution. However, like any explicit scheme, the time step is chosen to satisfy the Courant condition.

7.2 Non-uniform Flow Test Case Results

Fig. 7.2 and 7.3 and Table 7.1 and 7.2 show the non-uniform flow test case results for both scenarios with the balanced Godunov scheme. The tables show that there are no oscillations or errors in the discharge solutions. However, both the figures and tables show that errors in the depth solutions are apparent. These errors increase as discretization increases, and as roughness (decrease of C_*) and slope increase. The figures also show that for $\Delta x = 200$ m and for $C_* = 10$, $S_0 = 0.0025$, the depth solutions show $2\Delta x$ oscillations. In both scenarios, these oscillations are apparent in the upstream region of the transition from steep slope to mild slope.

Table 7.1: The non-uniform flow test case - effect of discretization with the balanced Godunov scheme.

Δx (m)	C_*	S_0	q error (%)	h error(%)
20	15	0.000926	0	0.28
100	15	0.000926	0	5.05
200	15	0.000926	0	17.5

Table 7.2: The non-uniform flow test case - effect of Chezy coefficient and slope with the balanced Godunov scheme.

Δx (m)	C_*	S_0	q error (%)	h error(%)
100	20	0.000521	0	1.48
100	15	0.000926	0	5.05
100	10	0.0021	0	19.41

7.3 Fourier Analysis Results

The coefficients a_r and b_r of Eq. 3.6 for the balanced Godunov scheme are shown in Appendix D. From those coefficients, it is found that $\frac{\mathrm{H}_n}{\mathrm{Z}}$ and $\frac{\Phi_n}{\mathrm{Z}}$ do not depend on time step discretization. Therefore, for the balanced Godunov scheme, we can write:

$$\begin{Bmatrix} \frac{\mathrm{H}_n}{\mathrm{Z}} \\ \frac{\Phi_n}{\mathrm{Z}} \end{Bmatrix} = f(Fr_0, N_\lambda, \beta_{\Delta x}) \tag{7.6}$$

Fig. 7.4 shows analytical and numerical amplitudes of the depth and discharge variables and the corresponding errors as a function of N_λ with $Fr_0 = 0.5$ and $\beta_{\Delta x} = 1$. The discharge amplitude errors are zero for any N_λ, and the depth amplitude errors are high at small wavelengths and diminish as N_λ increases. For this case, the depth errors appear to be negligible for $N_\lambda > 10$.

Fig. 7.5 shows the variation of the depth amplitude errors as a function of N_λ for the range of Fr_0 with $\beta_{\Delta x} = 1$. The figure shows that the depth errors are low for low Fr_0 and increase as Fr_0 increases. There is a sharp increase in the errors when $Fr_0 > 0.5$.

Fig. 7.6 shows the variation of the depth amplitude errors as a function of N_λ for the range of $\beta_{\Delta x}$ with $Fr_0 = 0.5$. The figure shows that the depth errors are low at low $\beta_{\Delta x}$ and increase as $\beta_{\Delta x}$ increases. The errors are less than 0.1 when $\beta_{\Delta x} \leq 1$ and shift to 0.2 or more when $\beta_{\Delta x} > 1$.

Fig. 7.7 shows the variation of the depth amplitude errors $\beta_{\Delta x}$ for the range of Fr_0 with $N_\lambda = 2$. The figure shows that the errors are low at low Fr_0 and low $\beta_{\Delta x}$ and increase when the same two parameters increase. For any Fr_0, the errors are negligible when $\beta_{\Delta x} \leq 0.1$ and can reach up to 1 or more when both Fr_0 and $\beta_{\Delta x}$ are large.

7.4 Discussion

Both the non-uniform flow test case and Fourier analysis results show that there are no oscillations or errors in the discharge solutions for the balanced Godunov scheme. However, both the results show that there are errors in the depth solutions. The non-uniform flow test results show that the depth errors increase with increasing discretization, roughness and slope, and the Fourier analysis results show that the errors increase with increasing Fr_0 and $\beta_{\Delta x}$. Moreover, the errors can be 1 or more when Fr_0 and $\beta_{\Delta x}$ are large and the errors are negligible when $\beta_{\Delta x} \leq 0.1$ for this scheme.

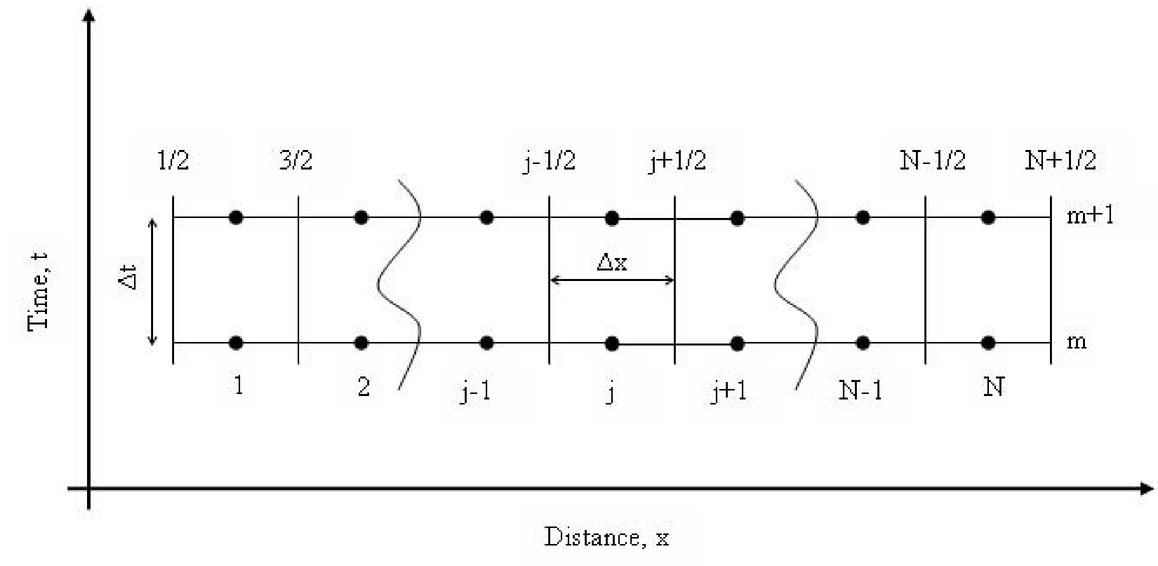

Figure 7.1: Definition sketch of the finite volume cell centered grid for one-dimensional flow.

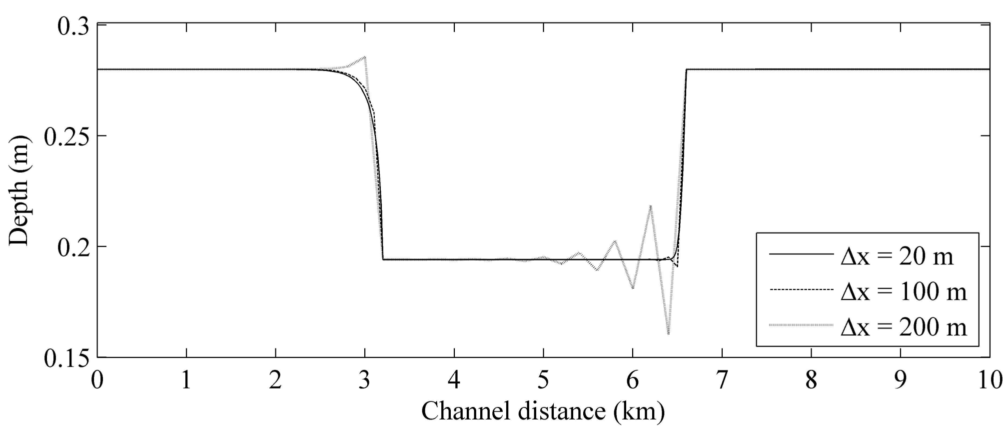

Figure 7.2: Depth solutions for the non-uniform flow test case with the balanced Godunov scheme - effect of discretization.

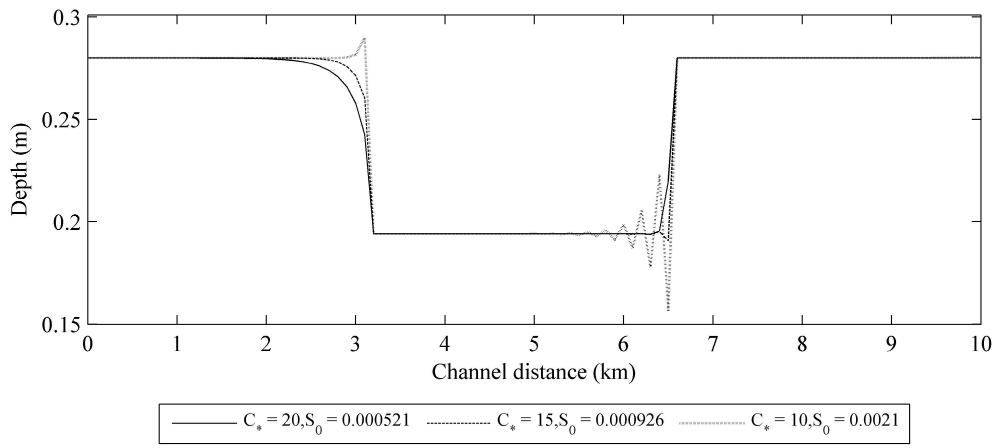

Figure 7.3: Depth solutions for the non-uniform flow test case with the balanced Godunov scheme - effect of Chezy coefficient and slope.

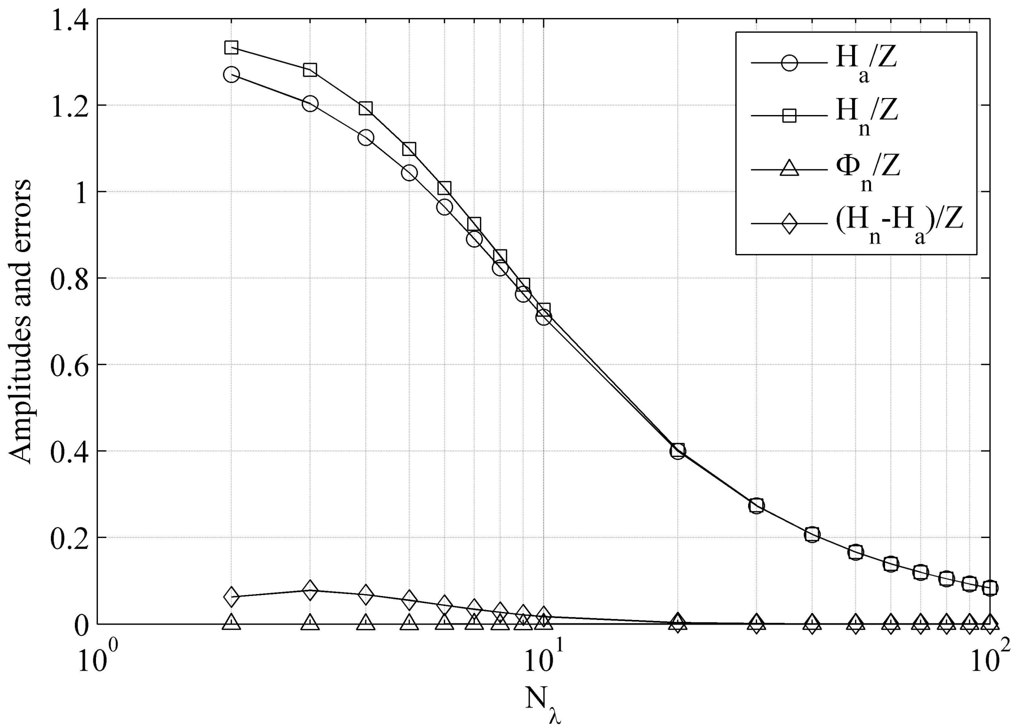

Figure 7.4: Normalized amplitudes and errors as a function of N_λ for $Fr_0 = 0.5$ and $\beta_{\Delta x} = 1$ using the balanced Godunov scheme.

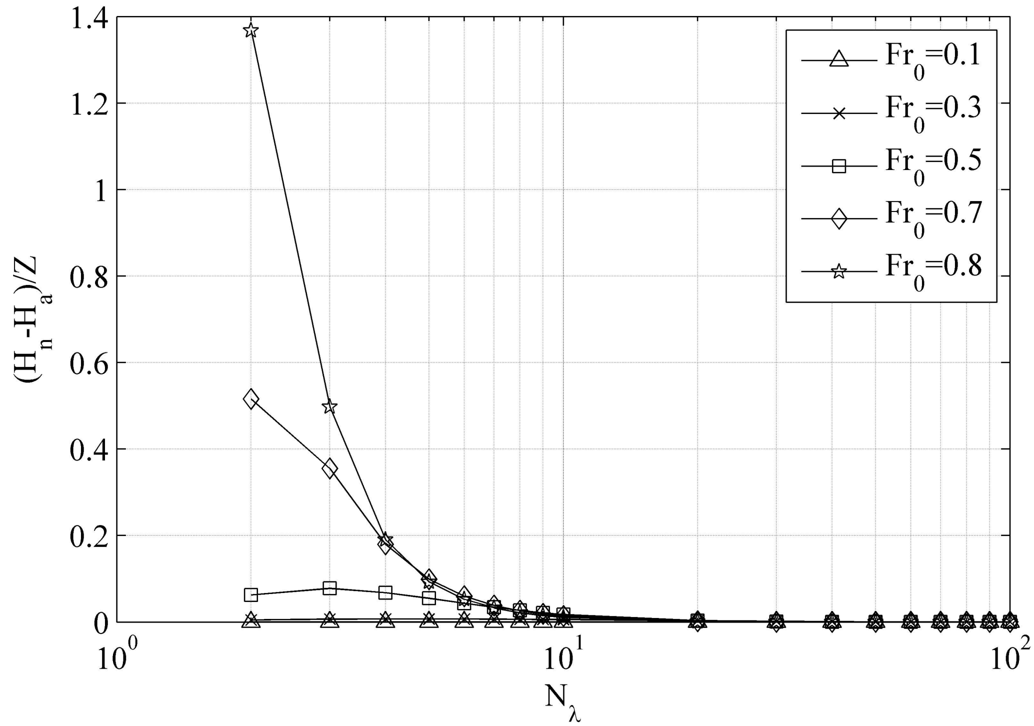

Figure 7.5: Depth amplitude errors as a function of N_λ for a range of Fr_0 and $\beta_{\Delta x} = 1$ using the balanced Godunov scheme.

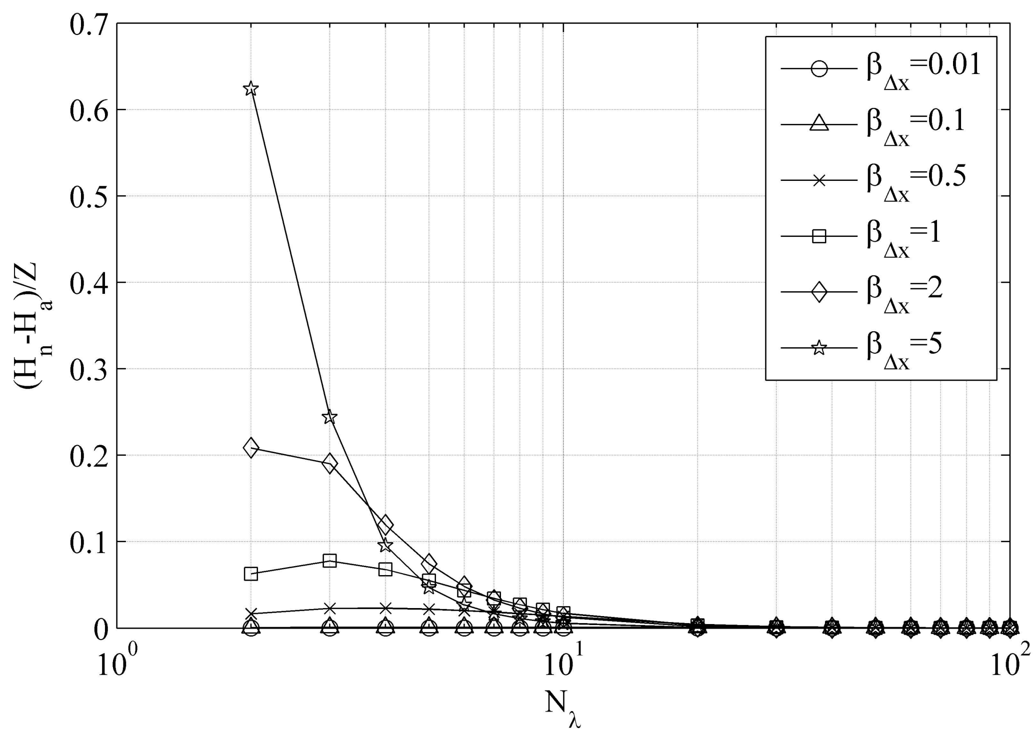

Figure 7.6: Depth amplitude errors as a function of N_λ for a range of $\beta_{\Delta x}$ and $Fr_0 = 0.5$ using the balanced Godunov scheme.

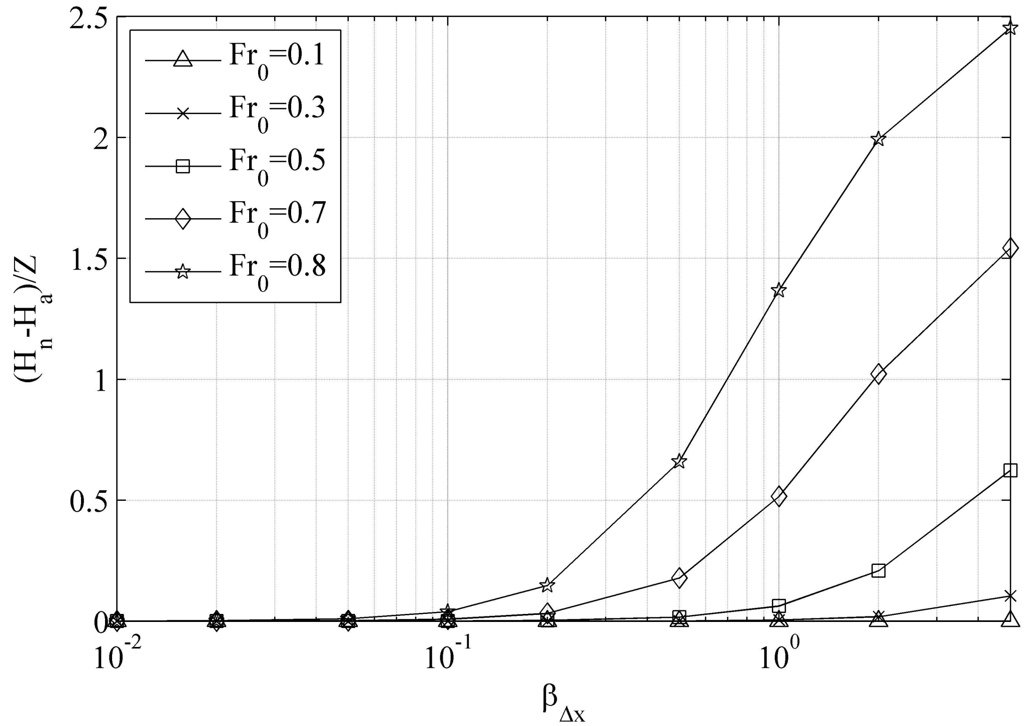

Figure 7.7: Depth amplitude errors as a function of $\beta_{\Delta x}$ for a range of Fr_0 and $N_\lambda = 2$ using the balanced Godunov scheme.

Chapter 8

One-sided Upwind-Downwind Finite Volume Scheme

8.1 Introduction

The Saint-Venant equations can be considered as a system of advection type equations with source terms. In contrast to the 1D advection equation, which produces a stable scheme, one-sided upwind approximation for both the discharge and depth derivatives of the Saint-Venant equations produces an unconditionally unstable scheme (Ying and Wang 2004). Therefore, the upwinding for a system of advection type equations is done based on the characteristics information that is embodied in the equations; this is also a key philosophy for Godunov type schemes (Toro 2001). Godunov type schemes are often used in CFD and Computational Hydraulics (Toro 2001, Toro 2009).

An alternate technique is to apply a one-sided upwind-downwind approximation to the partial-conservative form of the Saint-Venant equations, as in Eq. 2.22 (e.g., Ying and Wang 2004). In this particular technique, the discharge fluxes are taken as the one-sided upwind approximation, and the water surface elevation gradient is taken as the one-sided downwind approximation based on the flow directions.

Similar to the balanced Godunov finite volume scheme, the one-sided upwind-downwind finite volume scheme also uses the cell-centered grids, as shown in Fig. 7.1. The average values of conservative variables at any cell are updated using

A variation of this chapter and the previous chapter together are presented and published in the 34^{th} IAHR congress in 2011.

fluxes computed at the cell boundaries. The same Eq. 7.1 is also applicable to the one-sided upwind-downwind scheme, which is:

$$\mathbf{U}_j^{m+1} = \mathbf{U}_j^m - \frac{\Delta t}{\Delta x_j}(\mathbf{F}_{j+1/2}^m - \mathbf{F}_{j-1/2}^m) + \Delta t \mathbf{S}_j^m \tag{8.1}$$

The definitions of **U**, **F**, and **S** can be found in Eq. 2.22.

For the one-sided upwind-downwind scheme, the inter-cell fluxes of Eq. 8.1 are taken as the upstream node values based on the flow direction (Ying and Wang 2004), i.e.,

$$\mathbf{F}_{j+1/2} = \begin{bmatrix} q_{j+l} \\ (\frac{q^2}{h})_{j+l} \end{bmatrix} \tag{8.2}$$

In the above equation, $l = 0$ if $q_j > 0$ and $q_{j+1} > 0$; $l = 1$ if $q_j < 0$ and $q_{j+1} < 0$; and $l = \frac{1}{2}$ for other cases, where the subscript $j + \frac{1}{2}$ represents the average of values at j and $j + 1$ grid points. The variables in the source term are taken at the j^{th} cell and the water surface gradient is taken as the downstream nodes based on the flow direction. The source term in Eq. 7.1 is written as (Ying and Wang 2004):

$$\mathbf{S}_j = \begin{bmatrix} 0 \\ -gh_j \frac{H_{j+1-l} - H_{j-l}}{\Delta x} - \frac{q_j|q_j|}{C_{*j}^2 h_j^2} \end{bmatrix} \tag{8.3}$$

Similar to the balanced Godunov scheme, Eq. 8.1 is an explicit non-linear system of equations, and the unknowns can be solved directly from the known values. Like any cell-centered finite volume scheme, two ghost cells are introduced at the boundaries to complete the systems. Moreover, like any explicit scheme, the time step is chosen to satisfy the Courant condition.

The downwind approximation of the water surface elevation gradient produces a stable scheme, but the scheme is of first-order accuracy (Ying and Wang 2004). The scheme can capture shocks, model dam-break flows with initial dry/wet beds, and handle a non-level bed without producing any non-physical oscillations in the discharge solutions (Ying and Wang 2004). However, behavior of the scheme for the friction dominated case has not yet been studied, which we will try to achieve in this study.

8.2 Non-uniform Flow Test Case Results

Fig. 8.1 and 8.2 and Table 8.1 and 8.2 show the non-uniform flow test case results for both scenarios with the one-sided upwind-downwind scheme. The tables show that, similar to the balanced Godunov scheme, there are no errors or oscillations in the discharge variable. However, the figure and table both show that errors in the depth solutions exist. One can see in the figures (i.e., Fig.8.1 and 8.2) that these depth errors are diffusive, and the diffusion increases as the discretization increases, and as roughness (decrease of C_*) and slope increase. However, the tables also show that the maximum value of the errors does not change much with a changing parameter.

Table 8.1: The non-uniform flow test case - effect of discretization with the one-sided upwind-downwind scheme.

Δx (m)	C_*	S_0	q error (%)	h error(%)
20	15	0.000926	0	2.52
100	15	0.000926	0	8.84
200	15	0.000926	0	7.40

Table 8.2: The non-uniform flow test case - effect of Chezy coefficient and slope with the one-sided upwind-downwind scheme.

Δx (m)	C_*	S_0	q error (%)	h error(%)
100	20	0.000521	0	5.44
100	15	0.000926	0	8.84
100	10	0.0021	0	7.44

8.3 Fourier Analysis Results

The coefficients a_r and b_r of Eq. 3.6 for the one-sided upwind-downwind scheme are shown in Appendix E. From these coefficients it is found that $\frac{\mathrm{H}_n}{\mathrm{Z}}$ and $\frac{\Phi_n}{\mathrm{Z}}$ do not depend on the time step discretization for the one-sided upwind-downwind scheme. Therefore, for the one-sided upwind-downwind scheme we can write:

$$\begin{Bmatrix} \frac{\mathrm{H}_n}{\mathrm{Z}} \\ \frac{\Phi_n}{\mathrm{Z}} \end{Bmatrix} = f(Fr_0, N_\lambda, \beta_{\Delta x}) \tag{8.4}$$

Fig. 8.3 shows analytical and numerical amplitudes of the depth and discharge variables and the corresponding errors as a function of N_λ with $Fr_0 = 0.5$ and $\beta_{\Delta x} = 1$. The discharge amplitude errors are zero for any N_λ, and the depth amplitude errors are at their maximum at the shortest wavelength and diminish as N_λ increases. For this case, the errors become negligible when $N_\lambda \geq 20$.

Fig. 8.4 shows the variation of the depth amplitude errors as a function of N_λ for the range of Fr_0 with $\beta_{\Delta x} = 1$. The figure shows that the depth errors are low at low Fr_0 and increase as Fr_0 increases for the shortest wavelength. For the higher wavelengths, the errors increase until $Fr_0 \leq 0.5$ and decrease when $Fr_0 > 0.5$ with increasing Fr_0. For all Fr_0, the numerical depth amplitudes are less than the analytical depth amplitudes.

Fig. 8.5 shows the variation of the depth amplitude errors as a function of N_λ for the range of $\beta_{\Delta x}$ with $Fr_0 = 0.5$. The figure shows that the errors are low at low $\beta_{\Delta x}$. For the shortest wavelength, the errors increase with increasing $\beta_{\Delta x}$ until $\beta_{\Delta x} \leq 2$, and after that the errors decrease as $\beta_{\Delta x}$. For the higher wavelengths, the errors increase until $\beta_{\Delta x} \leq 0.5$ and decrease when $\beta_{\Delta x} > 0.5$ with increasing $\beta_{\Delta x}$. Similar to the Fr_0 results, the numerical amplitudes are less than the analytical amplitudes for all $\beta_{\Delta x}$.

Fig. 8.6 shows the variation of the depth amplitude errors as a function of $\beta_{\Delta x}$ for the range of Fr_0 with $N_\lambda = 2$. The figure shows that the errors are low at low Fr_0 and low $\beta_{\Delta x}$, and increase when the same two parameters increase. The figure also shows that for any Fr_0, the errors will be less than 0.1 for $\beta_{\Delta x} \leq 0.01$. Moreover, for the highest value of Fr_0, the depth errors are maximum at $\beta_{\Delta x} = 0.5$ and then decrease as $\beta_{\Delta x}$ increases. The numerical amplitudes are less than the analytical amplitudes for any value of Fr_0 and $\beta_{\Delta x}$.

8.4 Discussion

Both the non-uniform flow test case and Fourier analysis results show that there are no oscillations or errors in the steady state discharge solutions for the one-sided upwind-downwind scheme. However, both results also show that the depth errors are apparent, and the depth errors are diffusive. The Fourier analysis results also show that the numerical depth amplitudes are less than the analytical depth amplitudes for any value of Fr_0 and $\beta_{\Delta x}$, and therefore, the depth errors are diffusive in nature. Moreover, from the non-uniform flow test and Fourier analysis results, we can see that the one-sided upwind-downwind scheme appears to be unconditionally stable for any value of discretization, roughness, and slope. Therefore, the one-sided upwind-downwind scheme can be used in the friction dominated case.

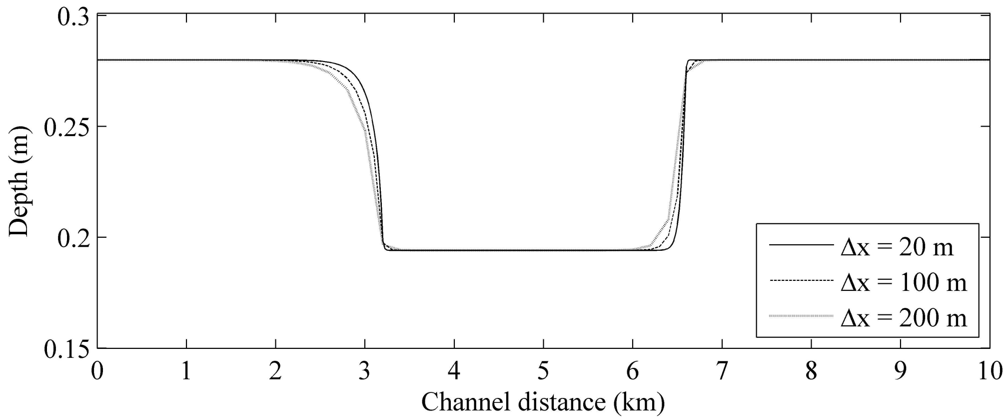

Figure 8.1: Depth solutions for the non-uniform flow test case with the one-sided upwind-downwind scheme - effect of discretization.

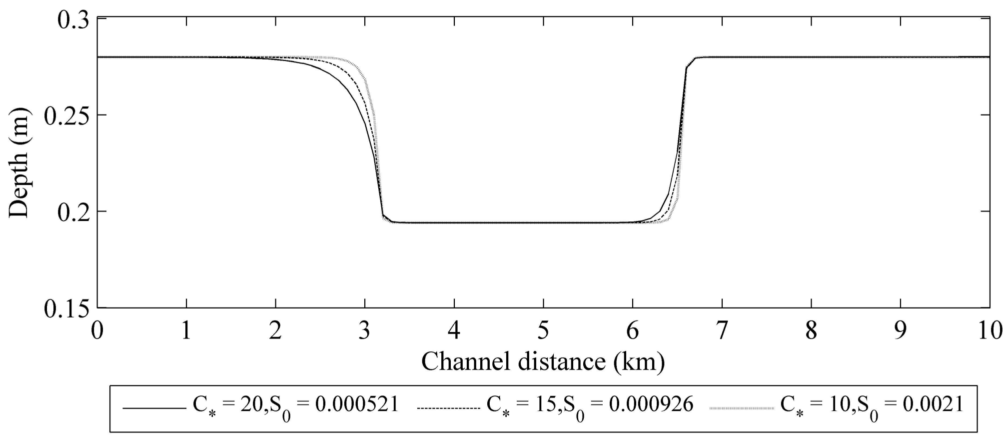

Figure 8.2: Depth solutions for the non-uniform flow test case with the one-sided upwind-downwind scheme - effect of Chezy coefficient and slope.

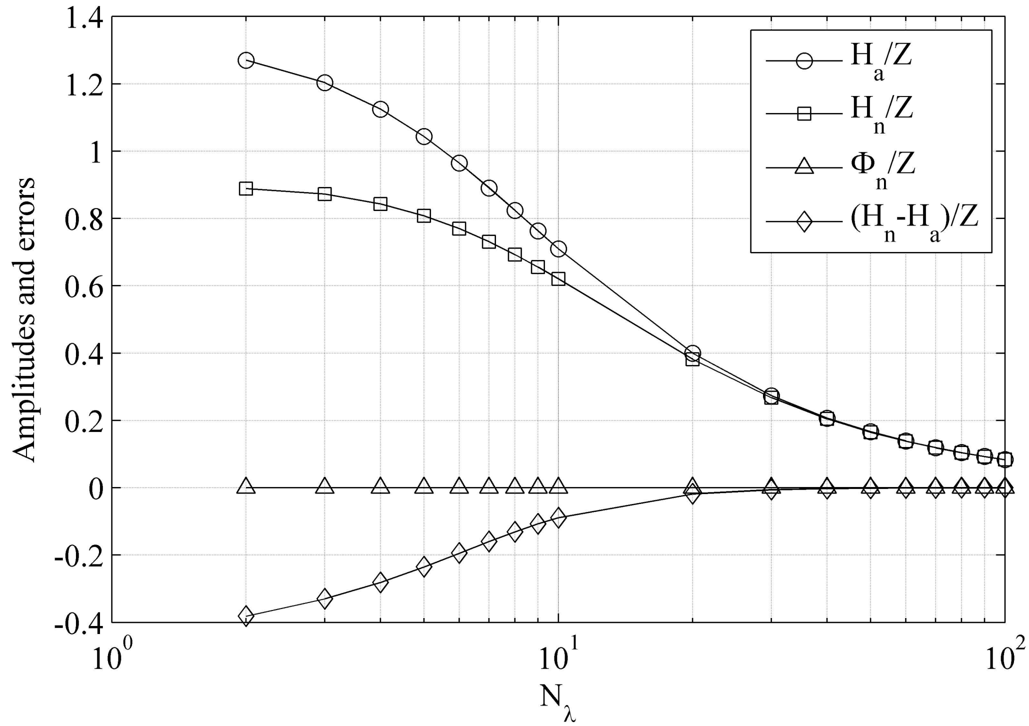

Figure 8.3: Normalized amplitudes and errors as a function of N_λ for $Fr_0 = 0.5$ and $\beta_{\Delta x} = 1$ using the one-sided upwind-downwind scheme.

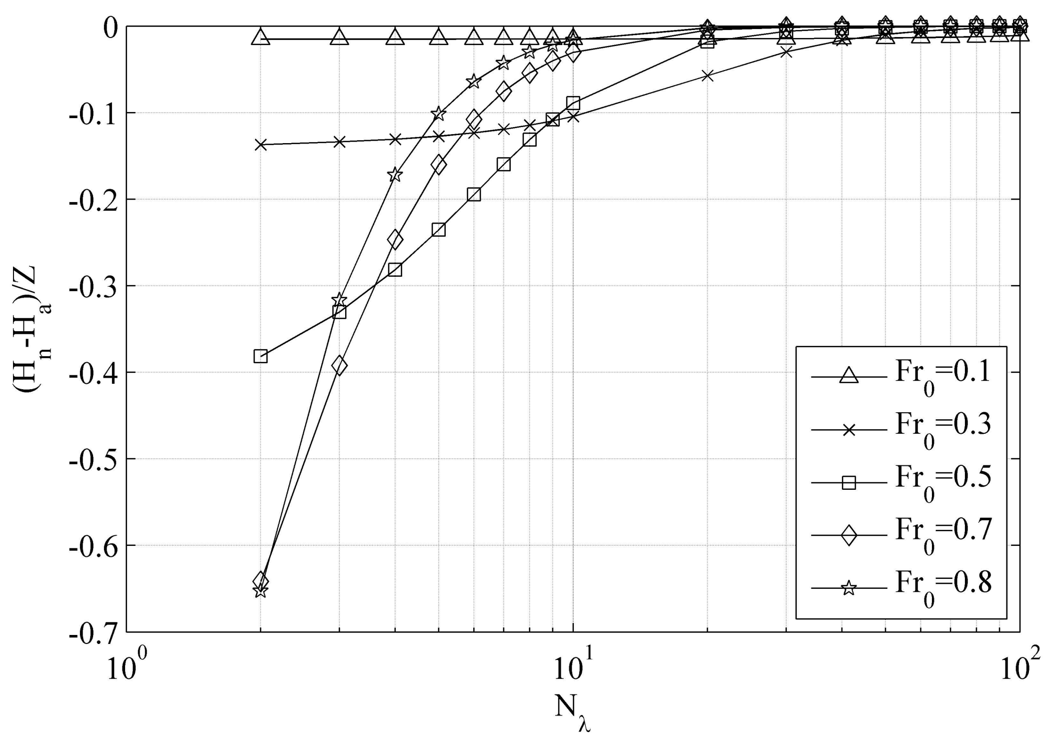

Figure 8.4: Depth amplitude errors as a function of N_λ for a range of Fr_0 and $\beta_{\Delta x} = 1$ using the one-sided upwind-downwind scheme.

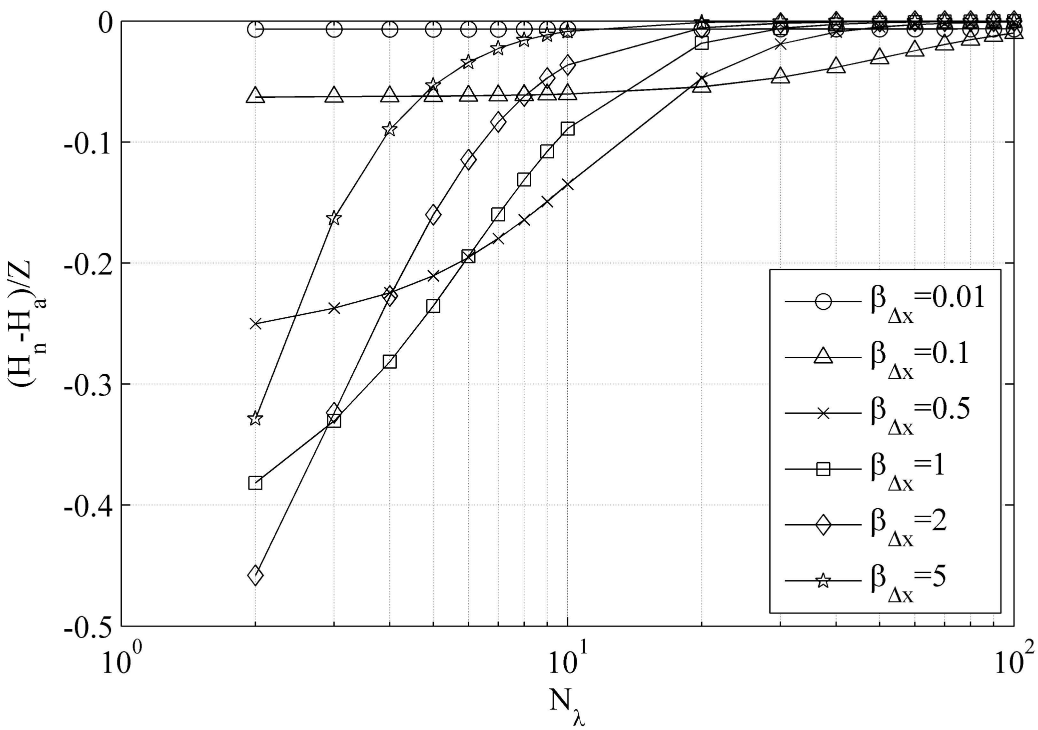

Figure 8.5: Depth amplitude errors as a function of N_λ for a range of $\beta_{\Delta x}$ and $Fr_0 = 0.5$ using the one-sided upwind-downwind scheme.

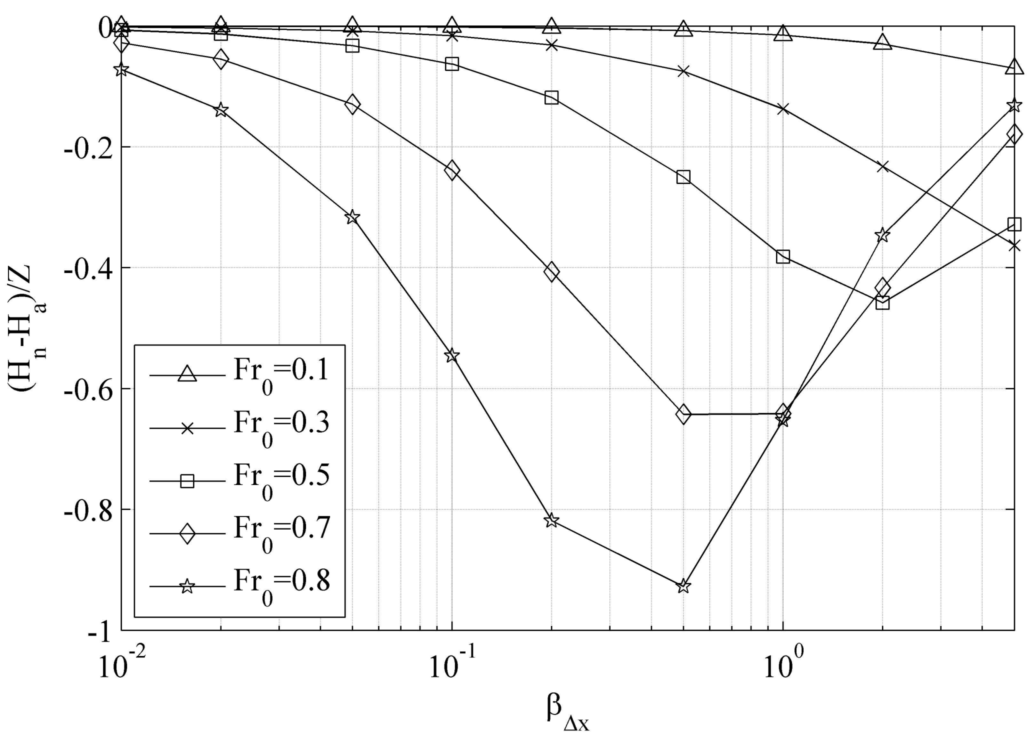

Figure 8.6: Depth amplitude errors as a function of $\beta_{\Delta x}$ for a range of Fr_0 and $N_\lambda = 2$ using the one-sided upwind-downwind scheme.

Chapter 9

Bubnov-Galerkin Finite Element Scheme

9.1 Introduction

From the elementary CFD, it is known that center difference schemes are not suitable for advection dominated flows, as this type of scheme produces non-physical oscillations when steep gradients form (Brooks and Hughes 1982, Baker 1983, Chung 2002, Toro 2009). However, it would be interesting to learn how this type of scheme behaves when the friction term dominates in the Saint-Venant equations. Do they generate non-physical oscillations like upwinding schemes, or do they generate diffusive errors like the one-sided upwind-downwind scheme, when the friction term dominates? With these questions in mind, we study the Bubnov-Galerkin scheme as a representative scheme for center difference type schemes. The Bubnov-Galerkin scheme is chosen because it is a special case of the CDG scheme, i.e., $w = 0$.

In Chapter 4, we mentioned that the Bubnov-Galerkin finite element scheme could be found by assuming the weighting function, v_i, as the interpolation function, f_i, for Eq. 4.2, i.e.,

$$\int_0^L f_i\{\frac{\partial \tilde{\mathbf{U}}}{\partial t} + \frac{\partial \mathbf{F}(\tilde{\mathbf{U}})}{\partial x} - \mathbf{S}(\tilde{\mathbf{U}})\}dx = 0 \tag{9.1}$$

The definitions of the variables in Eq. 9.1 can be found in Eq. 4.1.

9.2 Non-uniform Flow Test Case Results

Fig. 9.1 and 9.2 and Table 9.1 and 9.2 show the non-uniform flow test case results for both scenarios with the Bubnov-Galerkin scheme. The tables show that there are no errors or oscillations in the discharge variable for the Bubnov-Galerkin scheme. However, the figures and tables also show that errors in the depth solutions exist. These errors increase as discretization increases, and as roughness (decrease of C_*) and slope increase. The depth oscillations for the Bubnov-Galerkin scheme mainly appear on the steep to mild slope transition region, as with the previous upwind schemes. But, in contrast to the previous upwind schemes, in which the depth oscillations appear on the upstream elements of the transition, the depth oscillations for the Bubnov-Galerkin scheme appear on the downstream elements of the transition.

Table 9.1: The non-uniform flow test case - effect of discretization with the Bubnov-Galerkin scheme.

Δx (m)	C_*	S_0	q error (%)	h error(%)
20	15	0.000926	0	0.87
100	15	0.000926	0	5.20
200	15	0.000926	0	11.9

Table 9.2: The non-uniform flow test case - effect of Chezy coefficient and slope with the Bubnov-Galerkin scheme.

Δx (m)	C_*	S_0	q error (%)	h error(%)
100	20	0.000521	0	3.00
100	15	0.000926	0	5.20
100	10	0.0021	0	12.88

9.3 Fourier Analysis Results

Fig. 9.3 shows analytical and numerical amplitudes of the depth and discharge variables and the corresponding errors as a function of N_λ with $Fr_0 = 0.5$ and $\beta_{\Delta x} = 1$ for the Bubnov-Galerkin scheme. The discharge amplitude errors are zero for any N_λ, and the depth amplitude errors are at their maximum at the shortest wavelength and diminish as N_λ increases. Because of the central difference approximation, the numerical depth amplitude at $N_\lambda = 2$ is equal to zero. For this case, the depth errors become negligible when $N_\lambda \geq 4$.

Fig. 9.4 shows the variation of the depth amplitude errors as a function of N_λ for the range of Fr_0 with $\beta_{\Delta x} = 1$. The figure shows that at $N_\lambda = 2$, the depth errors start at -1 and increase as Fr_0 increases. For the other wavelengths, the errors are low at low Fr_0 and increase with increasing Fr_0. However, the errors at $N_\lambda > 2$ are much smaller compared to the errors at $N_\lambda = 2$.

Fig. 9.5 shows the variation of the depth amplitude errors as a function of N_λ for the range of $\beta_{\Delta x}$ with $Fr_0 = 0.5$. The figure shows that at $N_\lambda = 2$, the depth errors are maximum at low $\beta_{\Delta x}$ and decrease with increasing $\beta_{\Delta x}$. For the other wavelengths, the errors are low at low $\beta_{\Delta x}$ and increase as $\beta_{\Delta x}$ increases. Similar to the Fr_0 results, the errors at $N_\lambda > 2$ are much smaller compared to the errors at $N_\lambda = 2$.

Fig. 9.6 shows the variation of the depth amplitude errors as a function of $\beta_{\Delta x}$ for the range of Fr_0 with $N_\lambda = 2$. Because of the central difference approximation, the figure shows that for low Fr_0, e.g., $Fr_0 = 0.1$, the errors stay at -1 for any $\beta_{\Delta x}$. For higher Fr_0, as $\beta_{\Delta x}$ increases the errors decrease and the errors become less than -1 when $\beta_{\Delta x} > 1$. The errors approach zero, when both Fr_0 and $\beta_{\Delta x}$ are large.

9.4 Discussion

For the Bubnov-Galerkin scheme, both the non-uniform flow test case and Fourier analysis results show that there are no discharge oscillations. However, the depth oscillations are apparent for the Bubnov-Galerkin scheme when the discretization, roughness and slope are large. The depth oscillations also appear as $2\Delta x$ wavelength for this scheme. This is also consistent with the Fourier analysis results, as the depth errors are at their maximum at $N_\lambda = 2$.

However, in contrast to the non-uniform flow test results, the Fourier analysis results show that the depth errors at $N_\lambda = 2$ decrease as $\beta_{\Delta x}$ increases for a fixed Fr_0 (shown in Fig. 9.5 and 9.6). It is not clear why this anomaly occurred. However, one possible reason could be the effect of the non-linear term present in the Saint-Venant equations. The Fourier analysis uses the linearized form of the Saint-Venant equations, which is incapable of catching the effect of a non-linear term.

Still, the analysis with the Bubnov-Galerkin scheme is valuable, as it at least shows that a center difference scheme produces oscillatory solution when the friction term dominates.

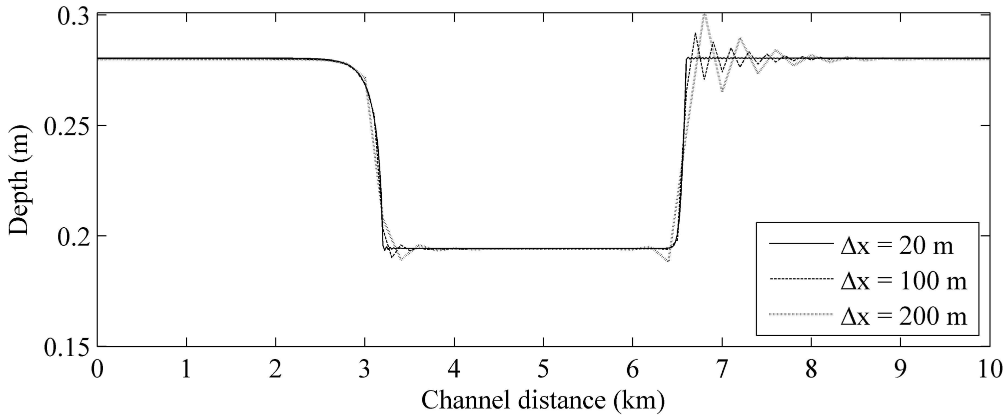

Figure 9.1: Depth solutions for the non-uniform flow test case with the Bubnov-Galerkin scheme - effect of discretization.

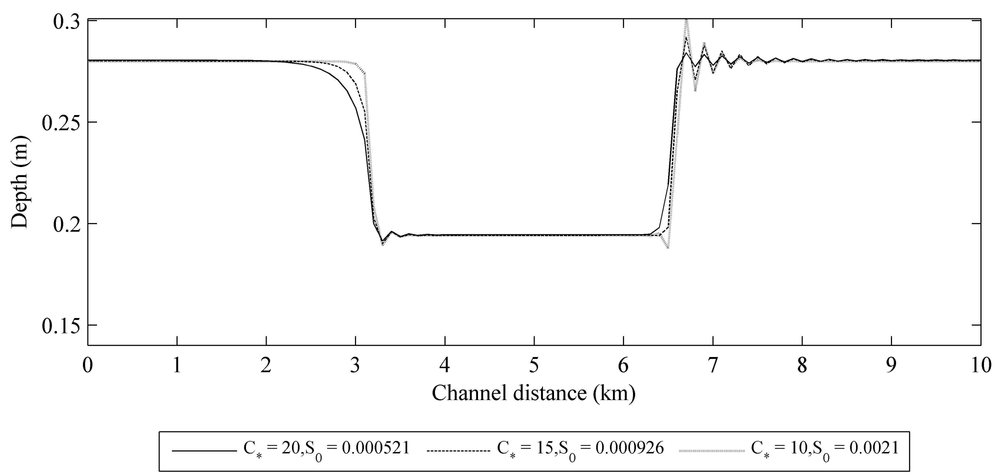

Figure 9.2: Depth solutions for the non-uniform flow test case with the Bubnov-Galerkin scheme - effect of Chezy coefficient and slope.

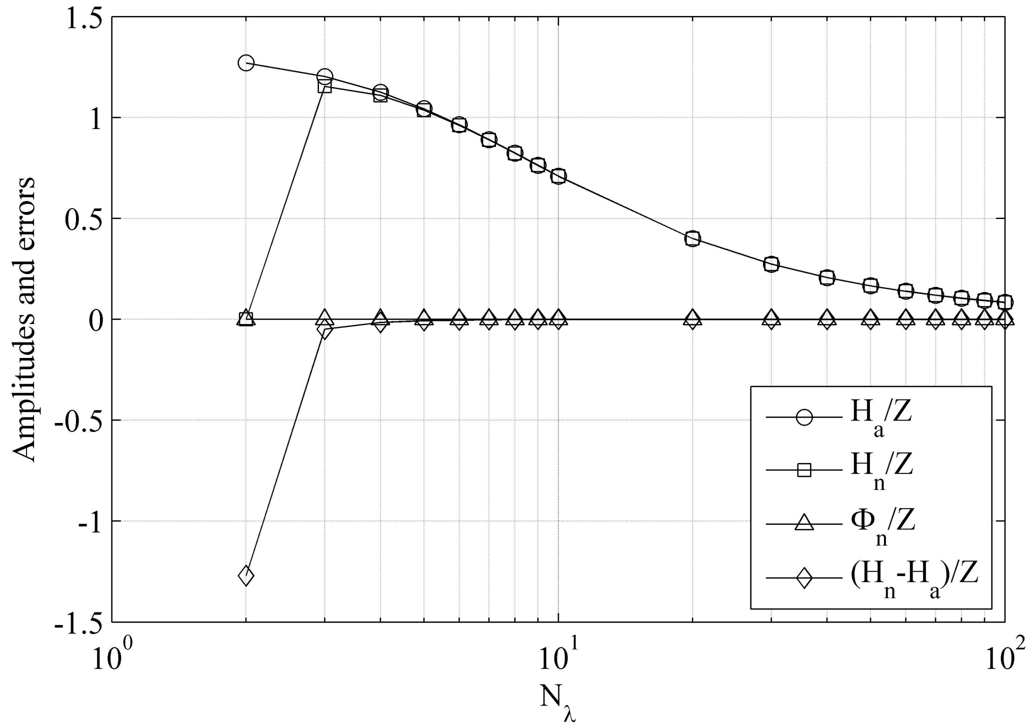

Figure 9.3: Normalized amplitudes and errors as a function of N_λ for $Fr_0 = 0.5$ and $\beta_{\Delta x} = 1$ using the Bubnov-Galerkin scheme.

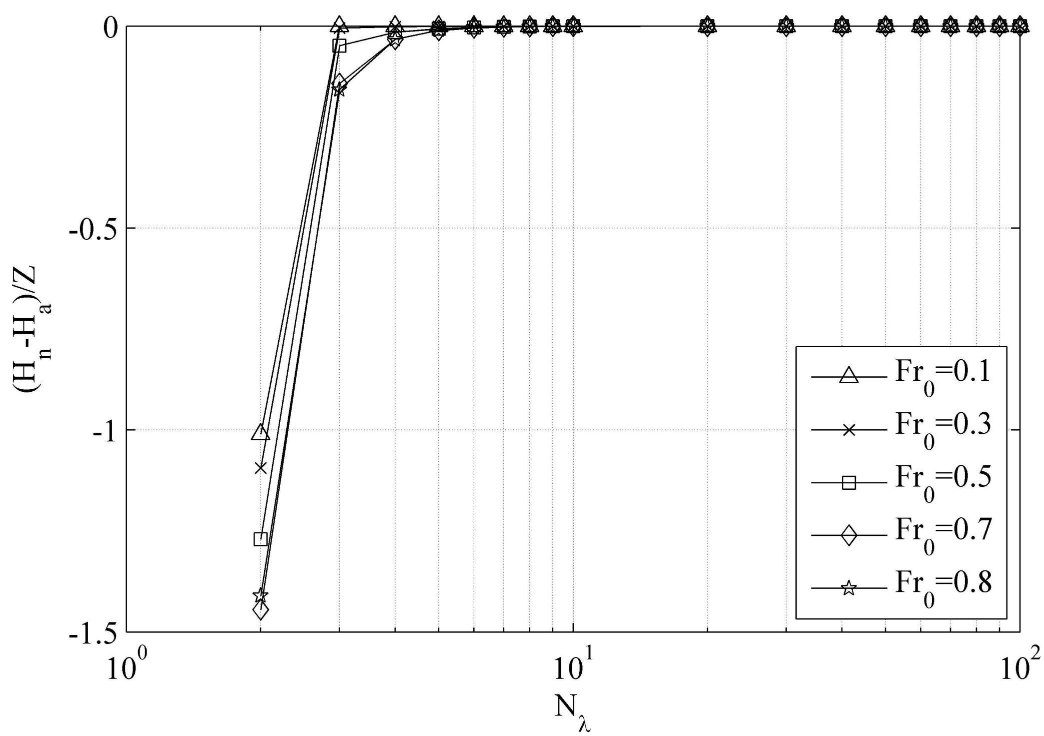

Figure 9.4: Depth amplitude errors as a function of N_λ for a range of Fr_0 and $\beta_{\Delta x} = 1$ using the Bubnov-Galerkin scheme.

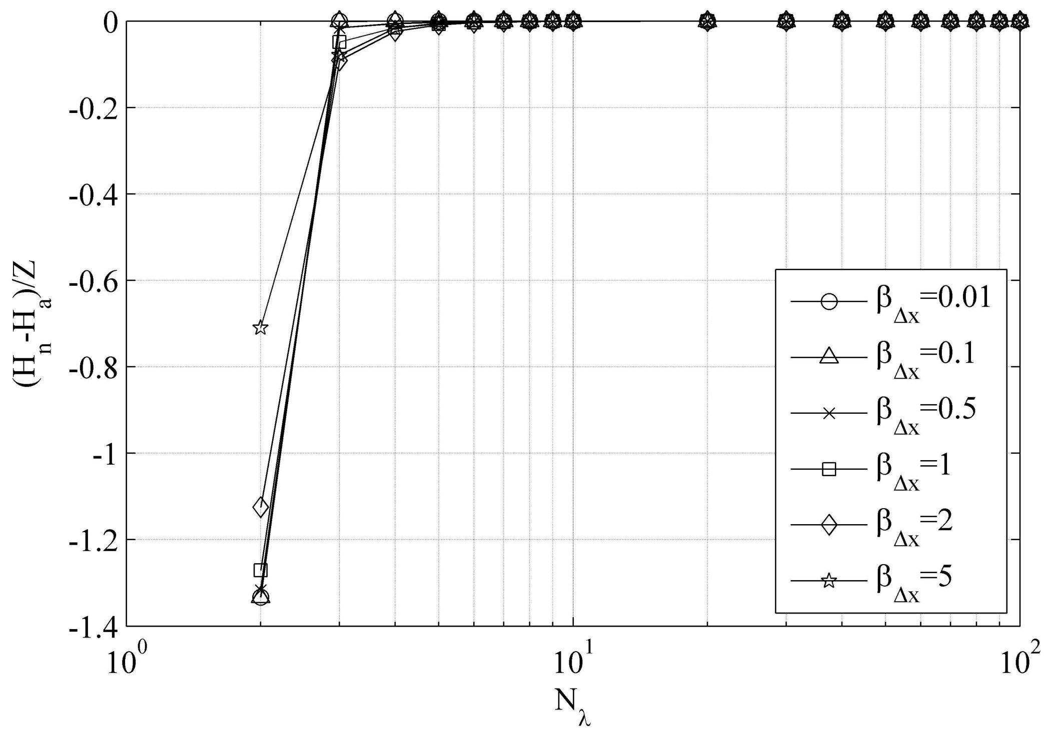

Figure 9.5: Depth amplitude errors as a function of N_λ for a range of $\beta_{\Delta x}$ and $Fr_0 = 0.5$ using the Bubnov-Galerkin scheme.

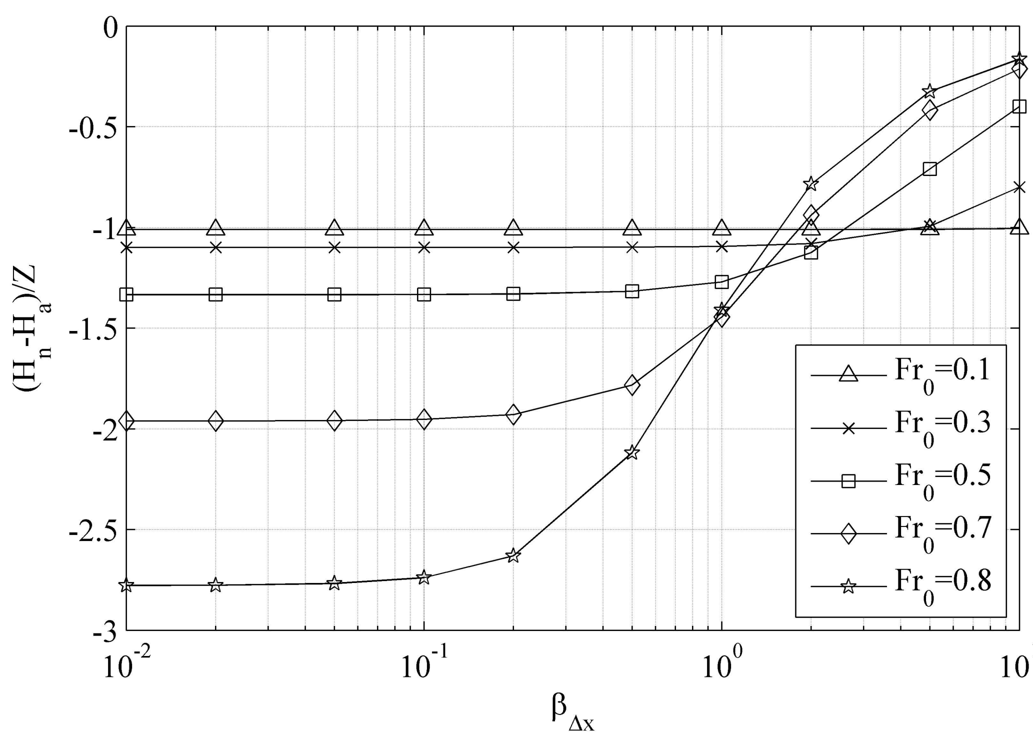

Figure 9.6: Depth amplitude errors as a function of $\beta_{\Delta x}$ for a range of Fr_0 and $N_\lambda = 2$ using the Bubnov-Galerkin scheme.

Chapter 10

Discussions on the Non-uniform Flow Test Case and Fourier Analysis Results

10.1 Non-uniform Flow Test Case Results

Table 10.1 lists a summary of the non-uniform flow test case results for all different schemes. From the table, we see that errors and oscillations in the discharge variable exist for the non-balanced shock-capturing schemes, such as the CDG and MacCormack schemes, even though the steady state solution is solved. The table also shows that there are no discharge errors or oscillations with a balanced shock-capturing scheme, e.g., the balanced Godunov scheme, or with a non-shock capturing scheme, e.g., the Box or Bubnov-Galerkin schemes.

Table 10.1: A summary of the non-uniform flow test case results with all schemes.

Scheme	Shock-capturing	Maximum q-error (%)	Maximum h-error (%)	Nature of error
CDG	Yes	13.09	8.38	Oscillatory
Box	No	0	24.65	Oscillatory
MacCormack	Yes	10.4	11.87	Oscillatory
Balanced Godunov	Yes	0	19.41	Oscillatory
One-sided upwind-downwind	Yes	0	8.84	Diffusive
Bubnov-Galerkin	No	0	12.88	Oscillatory

Oscillations in the steady state discharge solution are unwanted. However, these oscillations are unavoidable with a non-balanced shock-capturing scheme.

Shock-capturing schemes are designed to capture the discontinuity in the depth or velocity variables, which in effect introduce a fixed error in the discharge variable (Bradford and Sanders 2005). In a way, the total errors are divided into both depth and discharge variables.

Similar discharge oscillations with a point-source Godunov scheme, which is also a non-balanced shock-capturing scheme, were reported by several researchers (e.g., Petaccia and Zech 2009, Hubbard and Garcia-Navarro 2000, Zhou and Ingram 2001, Bradford and Sanders 2005). But the use of a point-source term does not balance the source terms and the flux terms with a non-level bed, and therefore generates oscillations at cell center discharges (Hubbard and Garcia-Navarro 2000), even though fluxes at the cell boundaries are non-oscillatory (Hubbard and Garcia-Navarro 2000, Bradford and Sanders 2005, Petaccia and Zech 2009).

In a balanced Godunov type scheme (e.g., Hubbard and Garcia-Navarro 2000), the scheme is written in such a way that the discharge solution at the center of an element becomes continuous. However, balancing the source and flux terms is not sufficient to avoid the oscillations in the depth solution when the friction term dominates, as is inevitable with the balanced Godunov scheme.

From Table 10.1 we also find that errors in the depth variable exist for all schemes. As the errors are divided in the non-balanced shock capturing schemes, the depth errors for these schemes are smaller than the depth errors with the Box or balanced Godunov scheme. Except for in the one-sided upwind-downwind scheme, where the depth errors are diffusive, the depth errors are oscillatory and appear as $2\Delta x$ wavelength for all schemes. For these schemes, the depth oscillations appear on the transitions from a steep slope to a mild slope. The depth oscillations for the Bubnov-Galerkin scheme appear on the downstream elements of the transition, while the depth oscillations for all other schemes appear on the upstream elements of the transition.

For all schemes, the non-uniform flow test case results show that the errors in the discharge and/or in the depth variables increase as discretization increases, and as roughness (decrease of C_*) and slope increase.

10.2 Fourier Analysis Results

Fourier analysis results are consistent with the non-uniform flow test results. Table 10.2 lists the maximum errors in the discharge and depth amplitudes found within the Fourier analysis results for all different schemes. The Fourier analysis results, similar to the non-uniform flow test results, show that there are errors in the discharge amplitudes for the CDG and MacCormack schemes, and that there are no discharge errors for the rest of the four schemes. However, depth errors are still apparent for all schemes. Four schemes (i.e., the CDG, MacCormack, Box, and balanced Godunov) have positive depth errors: the numerical depth amplitude (H_n) is greater than the analytical depth amplitude (H_a), and we expect to see depth oscillations for these schemes, which is consistent with the non-uniform flow test results. The one-sided upwind-downwind scheme has negative errors with maximum depth errors of less than (below) -1, and therefore, the depth error acts as a diffusive error. For the Bubnov-Galerkin scheme, the depth errors are negative, but are greater than (above) -1, and therefore, the depth errors are oscillatory. The results with the one-sided upwind-downwind and Bubnov-Galerkin schemes are also consistent with the non-uniform flow test results.

In all schemes except the one-sided upwind-downwind and Bubnov-Galerkin scheme, errors in the discharge and/or in the depth variables increase as the numerical friction number, $\beta_{\Delta x}$, increases, and as the average Froude number, Fr_0, increases. This is also consistent with the non-uniform flow test results. An increase in Δx, increase in roughness (decrease in C_*), or decrease in depth, increases $\beta_{\Delta x}$, and an increase in slope increases Fr_0.

The non-uniform flow test results can be connected with the Fourier analysis results. For both the scenarios (as shown in table 3.1 and 3.2), the average flow depth, h_0, was taken as 0.222 m and the base unit discharge was taken as 0.164 m^2/sec. Thus, the average flow Froude number, Fr_0, was 0.5. Changing the discretization and Chezy coefficient changes the value of $\beta_{\Delta x}$, which is equal to $\frac{\Delta x}{C_*^2 h_0}$. Table 10.3 shows all the discretization and C_* that are used in the non-uniform flow test case, the corresponding average $\beta_{\Delta x}$, and the errors for both scenarios with the CDG scheme.

Table 10.2: A summary of the Fourier analysis results with all schemes.

Scheme	Maximum $\frac{\Phi_n}{Z}$	Maximum $\frac{(H_n - H_a)}{Z}$
CDG	1.03	0.62
Box	0	2.45
MacCormack	4.70	5.72
Balanced Godunov	0	2.45
One-sided upwind-downwind	0	-0.93
Bubnov-Galerkin	0	-2.78

Table 10.3: The non-uniform flow test case - effect of average $\beta_{\Delta x}$ for the CDG scheme.

Δx (m)	C_*	$\beta_{\Delta x}$	q-error (%)	h-error(%)
20	15	0.4	0. 34	0.25
100	20	1.125	1.49	0.64
100	15	2	3.41	2.07
200	15	4	11.22	7.29
100	10	4.5	13.09	8.38

Fig. 10.1 shows the discharge and depth errors as a function of $\beta_{\Delta x}$ from the non-uniform flow test case with the CDG scheme. The figure reveals that the errors increase linearly in log scale as $\beta_{\Delta x}$ increases. From this figure we can say that any further increase in $\beta_{\Delta x}$ will cause the errors to reach 100 percent or more and may result in negative depths or imaginary solutions. Though the exact error values from the non-uniform flow test case are not directly comparable with the Fourier analysis results, this increasing error with increasing $\beta_{\Delta x}$ appears consistent with the Fourier analysis results, at least qualitatively.

The numerical friction number, $\beta_{\Delta x}$ (which is equal to $\frac{\Delta x}{C_*^2 h_0}$), identified in the Fourier analysis in our study, is exactly the same as the parameter found by Burguete and Gracia-Palacin (2007) as shown in Eq. 1.2, i.e., $\frac{\Delta x g n^2}{R^{4/3}} \leq 2$ (note that C_* and n are connected by the relationship $C_* = \frac{R^{1/6}}{n\sqrt{g}}$, which is given in Eq. 2.13). However, their limit doesn't capture the variation of error for different values of Fr_0. In this research, we capture the variation of the error for a range of Froude numbers, i.e., 0.1 to 0.8 (sub-critical flow), using the full Saint-Venant equations.

10.3 A Combined Friction Parameter

As the errors increase with both increasing Fr_0 and $\beta_{\Delta x}$, it is interesting to see the combined effect of these two, say, $\beta_{\Delta x} Fr_0^2$. For the base uniform flow $Fr_0^2 = C_*^2 S_0$, and therefore, this combined friction parameter could also be written as $\frac{\Delta x}{h_0/S_0}$. The denominator h_0/S_0 can easily be interpreted as a length scale associated with the length of a backwater curve. This combined friction parameter can then be interpreted as the number of elements over a backwater curve. It is well known from elementary hydraulics that backwater curve solutions can be unreliable and may oscillate if an insufficient number of computation points are used. In complex natural channels and especially in 2D models, effective backwater curves are caused by changes in depth, bed slope, or channel geometry, and may have a locally short length.

This combined friction parameter can also be thought of as analogous to the grid Peclet number, $\frac{\Delta x u}{D}$, for advection-diffusion problems. D/u is the length scale associated with a boundary layer caused by a fixed value downstream boundary condition. When the grid Peclet number is high, e.g., $\frac{\Delta x u}{D} \geq 2$, the algebraic equations become advection dominated and oscillations may occur in the vicinity of steep gradients. Similarly, we can say that when the combined friction parameter is high, we will have a friction dominated case, and non-physical oscillations in the solution may occur in the vicinity of abrupt changes in bed topography.

The results of the Fourier analysis for different Fr_0 and $\beta_{\Delta x}$ with the CDG scheme, (i.e. Fig. 4.8), are re-plotted using the combined friction parameter and are shown in Figure 10.2. Similarly to Fig. 4.8, this figure shows that the errors increase as $\beta_{\Delta x} Fr_0^2$ increases and that the errors can reach up to 1 or more when $\beta_{\Delta x} Fr_0^2 \geq 1$. We can also see that if $\beta_{\Delta x} Fr_0^2 \leq 0.01$ the errors will be negligible for any value of Fr_0. From the point of view of backwater curve length scales, the former value corresponds to a single element over the backwater curve length scale and the latter corresponds to 100 elements.

The combined friction parameter is intended as an approximate simplification for practical application. Comparing Fig. 4.8 and Fig. 10.2 we can find that the error variation with the separate parameters is not completely captured with the combined friction parameter. However, from Fig. 4.8a and practical experience, we know that problems are generally not encountered at low Froude numbers. Fig. 4.8a shows that the combined friction parameter does capture the error variation for moderate to high (0.3 to 0.8, sub-critical) Froude numbers. In particular, one can use Fig. 10.2a to set a limiting value of the combined friction parameter, based on an acceptable error tolerance.

We can use this combined friction parameter as a potential error indicator. We can expect that when this combined friction parameter is high the errors will be high and when this parameter is low the errors will be low. In complex natural channels, shallow areas with relatively low velocities or deep areas with low or high velocities will have low $\beta_{\Delta x} Fr_0^2$ values, and we don't usually see any spurious velocities in those areas. On the other hand, shallow areas with high velocities will have a high value of $\beta_{\Delta x} Fr_0^2$, and those are the areas where we usually see spurious velocities.

Fig. 10.3 shows velocity vectors and the combined friction parameter contours for a natural channel with the River2D model that uses the CDG shock capturing scheme. The combined friction parameter for each node in this case is calculated using nodal depth, nodal roughness and nodal velocity. The discretization length is taken as the square root of the average of the areas of the elements connected to a node. The figure shows the contours from 0.01 to 85. The combined friction parameter values in most parts of the channel are well below 0.01 and we can see smooth parallel velocity vectors in those areas. At a few nodes the combined friction parameter values are greater than 0.1 and among them two nodes have very high values, 41 and 81. The velocity vectors for those nodes are larger than expected and appear to have spurious directions as well.

When this combined friction parameter is high there are several possible courses of action. Mesh refinement is one obvious option to choose. As the discretization is reduced, the parameter value is also reduced and thus the error should be reduced. However, one can imagine that in complex natural channels, as the discretization is reduced, the depth at newly introduced nodes can also be reduced and the parameter value may remain the same or even be increased. Moreover, as one can see in Fig. 10.3, the combined friction parameter values can be of the order of 100 or even more. To reduce the parameter down to at most

0.1, one would need a mesh refinement at least 1000 times finer, which would be computationally impractical.

Smoothing the bed is another option when the parameter value is high. Perturbations in the solution variables are due to the perturbations in the bed. Thus bed smoothing reduces the bed perturbation amplitude, and may reduce the errors in the solution variables.

A third approach is to switch to an alternate set of equations when the parameter value is high. A minimum depth is normally used to make this switch, which is usually a very small depth, e.g. 0.01 m in River2D (Steffler and Blackburn 2002). But, as we can see from this analysis, a friction dominated case can occur at a higher depth than that minimum depth. So, taking 0.1 as a practical maximum limit for the combined friction parameter, one can calculate a minimum depth for a given discretization length, velocity, and roughness. This will give graded minimum depths rather than a fixed minimum depth for all nodes.

The last, and perhaps most desirable approach is to switch to alternate numerical schemes when the parameter value is high. Analogous to the advection dominated problem, a numerical scheme that will not produce any oscillations for the friction dominated case can be used, if such a scheme is available. Existing shock capturing schemes should be tested for the friction dominated case, and if none are suitable, new schemes should be researched. The analysis presented in this paper can be used as a framework to test such numerical schemes.

For the case of perturbation in a uniform flow, this new combined friction parameter becomes same as the parameter proposed by Hannah and Wright (1995), which was developed from the analytical study of wind-driven flow in the coastal ocean. However, in Hannah and Wright's (1995) parameter, they have used the local bed slope, whereas, we have used the average bed slope. Furthermore, for the case of a non-uniform flow, instead of the average bed slope, one can use any of the three slopes, i.e., friction slope, water surface slope, or bed slope.

10.4 A Conservative Shock-capturing Scheme Suitable for the Friction Dominated Case

The one-sided upwind-downwind scheme is a prominent candidate for the friction term dominated case. Both the non-uniform flow test case and Fourier analysis results show that there are no discharge errors or oscillations for this scheme. Moreover, in contrast to the upwind or center difference schemes, the depth errors are not oscillatory, but diffusive. The scheme appears to be unconditionally non-oscillatory for any value of discretization, roughness, and slope, or, Fr_0 and $\beta_{\Delta x}$.

The diffusive behaviors with the one-sided upwind-downwind scheme for the friction dominated case can be explained by the elementary hydraulics. In this scheme, the water surface elevation gradient term is taken as downwinding approximation, while in all other schemes the depth gradient or the pressure gradient term is taken as upwind or center difference approximation. When the governing Saint-Venant equations are advection dominated, the characteristics of the equations necessitate upwinding. But when the governing equations become friction dominant, the nature of the equations are changed. From the elementary hydraulics, we know that to calculate a backwater curve for a steady state subcritical flow case, the solution should march from the downwind stream end, i.e., downwinding is required. This is what we see when the friction term dominates in the Saint-Venant equations. Use of any upwinding type schemes or any center difference type schemes will produce oscillations in the depth solutions in the friction dominated case. Only the downwinding of the depth gradients provides sufficient diffusion to suppress the wiggles that produce non-oscillatory solutions in the friction dominated case, as is found with the one-sided upwind-downwind scheme.

The effect of the downwinding can be shown through further example. To show this, we add a second-order depth derivative term, $D_n \frac{\partial^2 h}{\partial x^2}$, to the momentum equation, where D_n stands for the numerical diffusion coefficient. This second-order derivative term will provide an artificial diffusion to the depth solution. We solve these modified Saint-Venant equations with the Bubnov-Galerkin scheme. Fig. 10.4 shows the non-uniform flow test case results with the Bubnov-Galerkin scheme for three different values of D_n, with $\Delta x = 100$ m, $C_* = 15$, and $S_0 = 0.00111$. We already know from the Bubnov-Galerkin results that without any artificial diffusion, i.e., $D_n = 0$, non-physical depth oscillations appear in the downstream elements of the steep to mild transition. With a positive diffusion, i.e., $D_n = 10,000$, the depth oscillations shift from the downstream elements to the upstream elements of the transition (as shown in Fig. 10.4), and the oscillations increase from 5.20 percent to 15 percent. The negative diffusion, i.e., $D_n = -10,000$, provides sufficient downwinding effect to suppress the depth oscillations and produce a non-oscillatory depth solution (as shown in Fig. 10.4).

It is worth mentioning that in many wetting/drying algorithms, researchers use a zero inertia momentum equation or reduced momentum equation to represent the dry nodes or very shallow depth flows (e.g., Tchamen and Kahawita 1998, Dietrich 2006). However, our study shows that simply dropping the inertia term in the Saint-Venant equations will not prevent it from becoming a friction dominated case and therefore, will not help to suppress the oscillations. The only way to avoid the non-physical oscillations for the friction dominated case is to use the correct numerical schemes, i.e., the one-sided upwind-downwind scheme, or to apply the right amount of negative numerical diffusion.

The one-sided upwind-downwind scheme that is used in this research following the Ying and Wang (2004) scheme does not use the full conservative form of the Saint-Venant equations. It considers the non-conservative form of the pressure gradient term, i.e., $gh\frac{\partial h}{\partial x}$, and applies the downwind approximation to that term. However, the downwinding approximation can also be applied to the conservative form of the pressure gradient term, i.e., $\frac{\partial (gh^2/2)}{\partial x}$. Thus, in this new scheme, based on the flow direction, the inter-cell discharge flux can be taken as the upstream node value while the conservative pressure flux can be taken as the downstream node value. Therefore, a flux at a cell boundary in Eq. 7.1 can be expressed as:

$$\mathbf{F}_{j+1/2} = \begin{bmatrix} q_{j+l} \\ (\frac{q^2}{h})_{j+l} + (\frac{gh^2}{2})_{j+1-l} \end{bmatrix} \tag{10.1}$$

The variables in the source term are taken at the j^{th} cell, and the bed elevation gradient is taken as downwind discretization:

$$\mathbf{S}_j = \begin{bmatrix} 0 \\ -gh_j \frac{z_{j+1-l} - z_{j-l}}{\Delta x} - \frac{q_j |q_j|}{C_{*j}^2 h_j^2} \end{bmatrix} \tag{10.2}$$

Fig. 10.5 and Table 10.4 show the non-uniform flow test results for different discretization with the fully conservative form of the Saint-Venant equations for the one-sided upwind-downwind scheme. Comparing Fig. 10.5 and Table 10.4 to Fig. 8.1 and Table 8.1 respectively, we can see that the results with the fully conservative form of equations give similar results to the non-conservative form results, with slightly higher depth errors. The linearized version of both forms appears to be exactly the same.

Table 10.4: The non-uniform flow test case - effect of discretization with the one-sided upwind scheme using the conservative form of the Saint-Venant equations.

Δx (m)	C_*	S_0	q-error (%)	h-error(%)
20	15	0.000926	0	3.03
100	15	0.000926	0	10.09
200	15	0.000926	0	8.17

10.5 Conclusion

Thus the one-sided upwind-downwind scheme proves to be a suitable scheme for the friction dominated case. The only limitation is that the scheme is of first-order, and therefore, over-diffusive. However, similar to the TVD concept, higher-order methods can be applied in smooth regions or in advection dominated regions, and this first-order method or the negative artificial diffusion can be applied in the friction term dominated regions. The proposed combined friction parameter can be used as an indicator to identify the friction dominated regions.

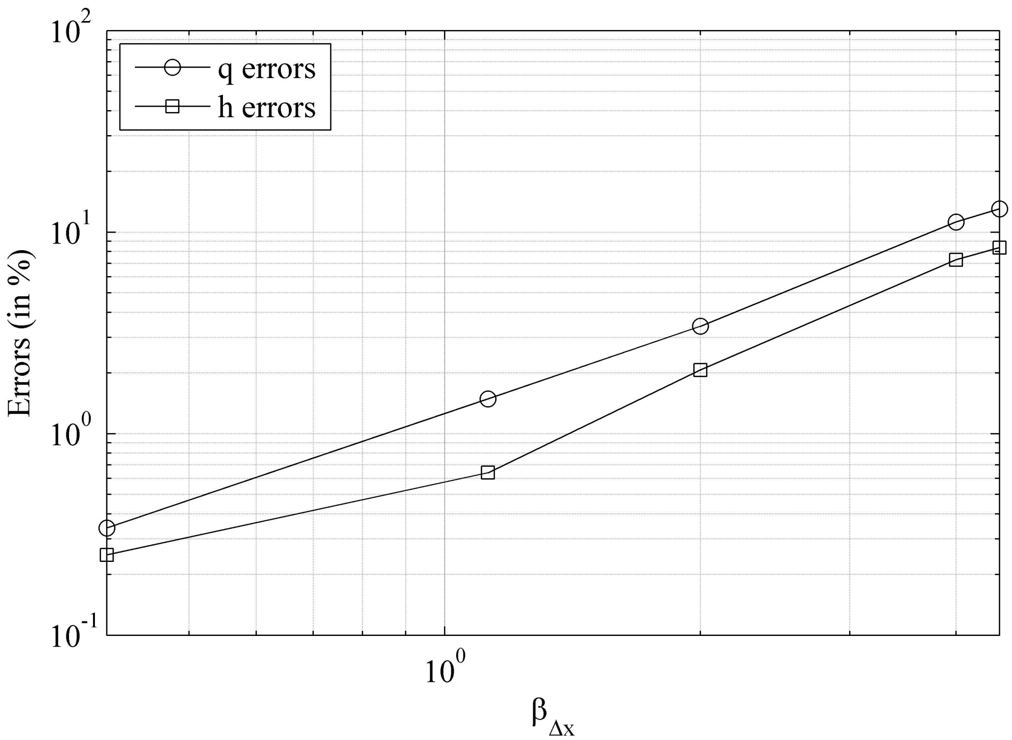

Figure 10.1: Errors as a function of $\beta_{\Delta x}$ with the CDG scheme from the non-uniform flow test case.

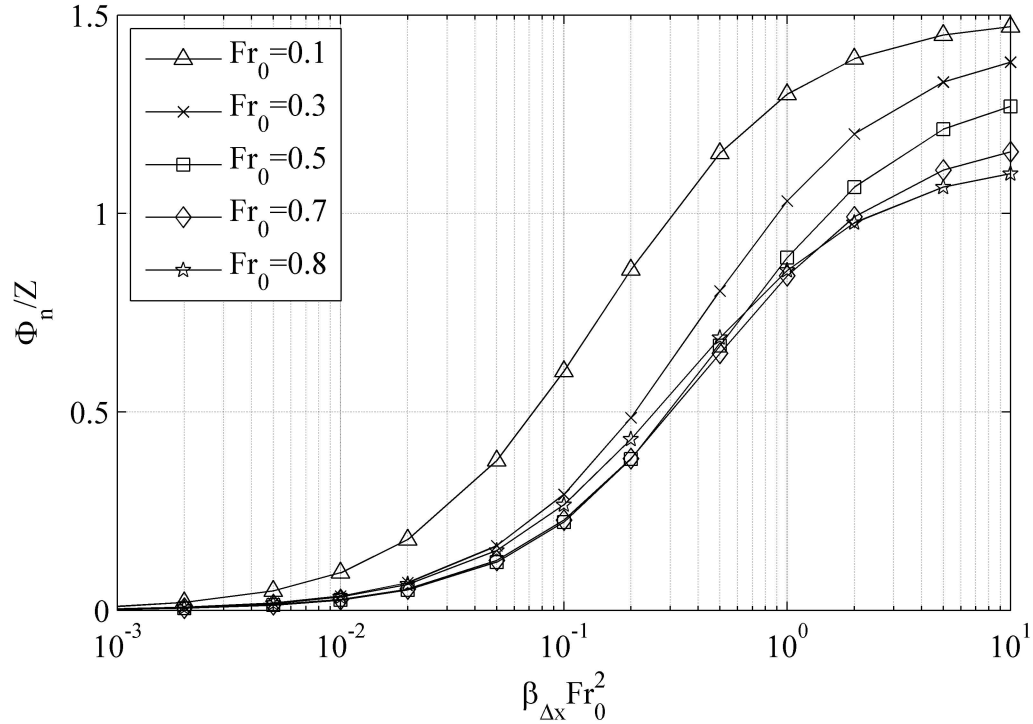

(a)

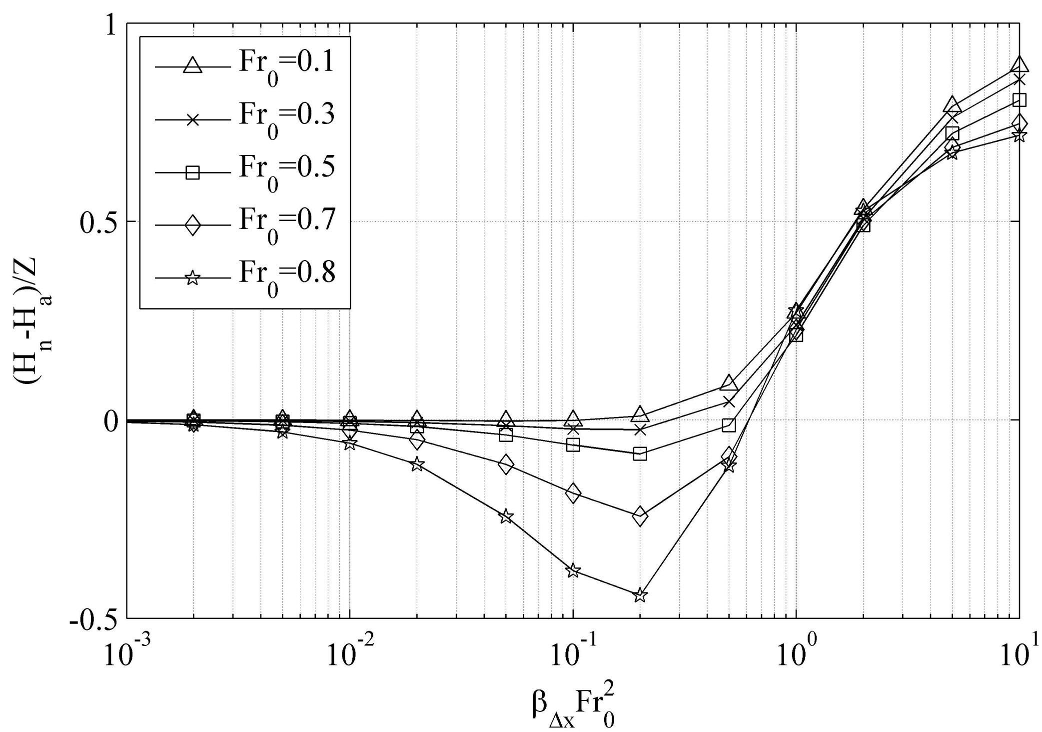

(b)

Figure 10.2: (a) Discharge and (b) Depth amplitude errors as a function of $\beta_{\Delta x}Fr_0^2$ for a range of Fr_0, $w = 0.5$, and $N_\lambda = 2$ using the CDG scheme.

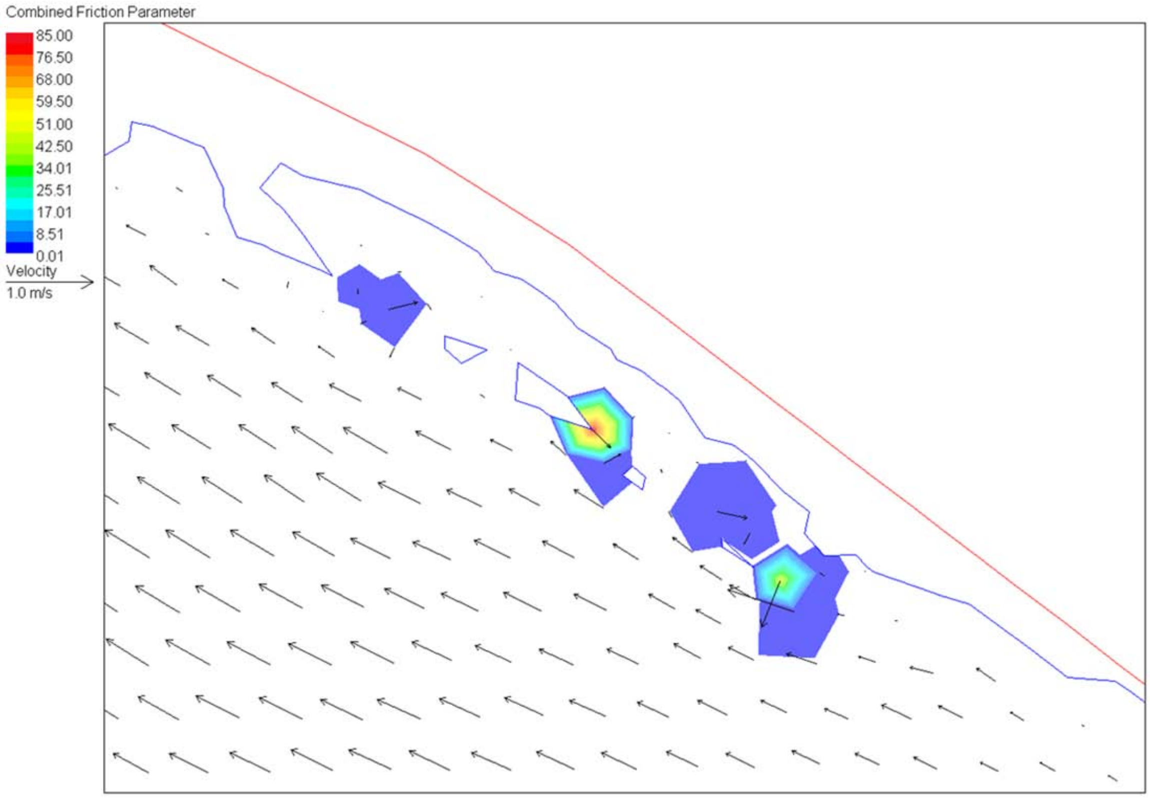

Figure 10.3: A typical contour plot of $\beta_{\Delta x} Fr_0^2$ and velocity vectors plot using the River2D open channel flow model.

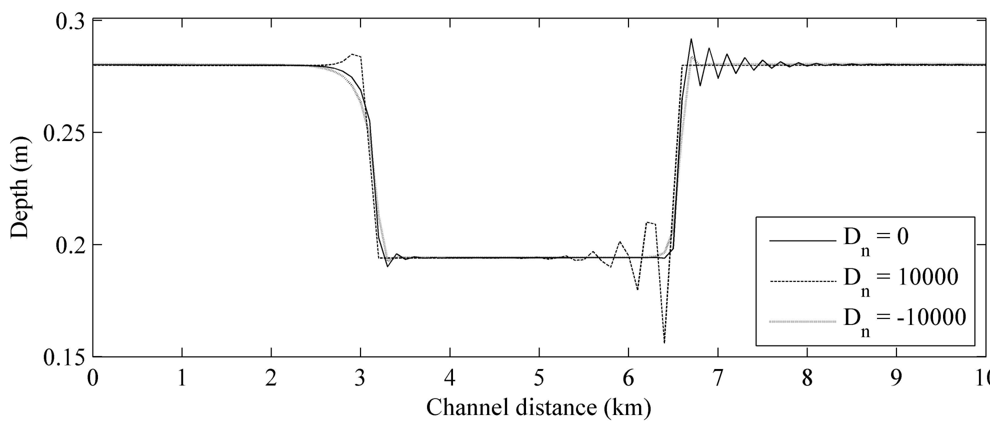

Figure 10.4: Depth solutions for the non-uniform flow test case with the Bubnov-Galerkin scheme - effect of artificial diffusion.

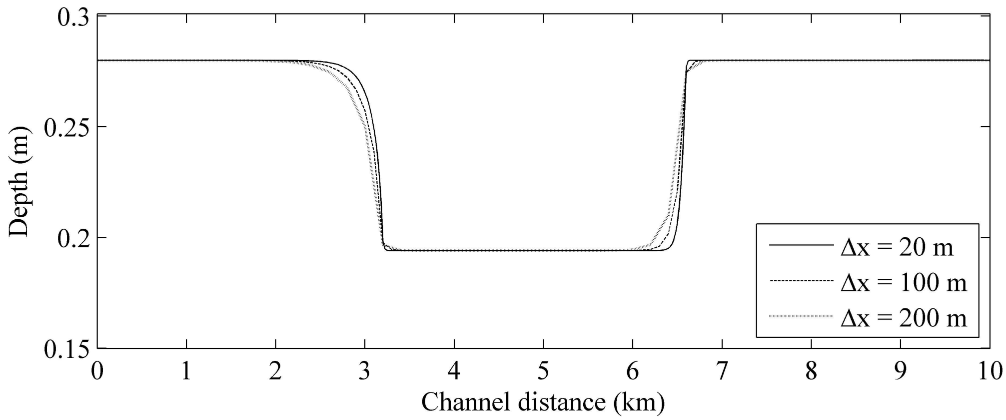

Figure 10.5: Depth solutions for the non-uniform flow test case with the one-sided upwind-downwind scheme using the conservative form of the Saint-Venant equations - effect of discretization.

Chapter 11

Application to 2D Open Channel Flow Model

11.1 Introduction

2D depth averaged shallow water modeling is currently applied to a variety of river problems (Waddle 2009, Katopodis 2003, Leclerc and Bechara 2003). Common applications include flow around hydraulic structures, fish habitat modeling, ice modeling, and morphology modeling. 2D modeling is popular because of its ability to capture local variations and to offer a better visualization and description of the flow physics compared to 1D simulation (Katopodis 2003, Leclerc and Bechara 2003). FDM, FEM, and FVM are the same three numerical methods used to solve the depth averaged 2D Saint-Venant equations, i.e., Eq. 2.30 to 2.32. However, unstructured meshes in FEM and FVM have the advantage of better geometric flexibility than FDM and the ability to do local mesh refinement, and therefore these two are widely used in 2D modeling (Marrocu and Ambrosi 1999).

Although 2D depth averaged modeling has a variety of applications, they are challenging to use for mountainous streams because of the highly variable bed topography, steep gradients, and small depths, not to mention the presence of pool/riffle regions and large boulders/rocks. Local variations in bed topography can lead to sub-critical/supercritical transitions necessitating a conservative upwind shock-capturing numerical scheme. Moreover, when the depth becomes

A variation of this chapter was presented and published in the annual conference of Canadian Society for Civil Engineers (CSCE) in 2010.

small compared to the discretization scale, which is common with mountainous streams, the source and friction terms generally dominate in the Saint-Venant equations, making them even more difficult to model.

In earlier chapters, we studied friction dominated problem with the 1D Saint-Venant equations. We found that the upwinding or center-difference numerical schemes give non-physical oscillations in the discharge and/or depth solutions when the friction term dominates. From the 1D non-uniform flow test case results we have shown that a friction dominated case occurs when discretization, roughness and slope become large, or when depth becomes very small.

From the Fourier analysis, we have also found that the errors increase with Fr_0 and $\beta_{\Delta x}$. Moreover, a combined friction parameter was intended for the practical purpose of capturing the effect of the two separate parameters. The proposed combined friction parameter $\beta_{\Delta x} Fr_0^2$ captures the variation of the errors for moderate to high Froude numbers, i.e., 0.3 to 0.8 (sub-critical flow). Moreover, we showed in Fig. 10.3 that we can use this combined friction parameter as a possible error indicator.

We also discussed that we can use this error indicator to do local mesh refinement or to calculate minimum depth in order to switch to an alternate equation, e.g., the ground water equation, in 1D or 2D open channel flow models. In this chapter, we will explore the two applications of the combined friction parameter in 1D and 2D models. First, a brief literature review on the existing mesh refinement indicators for the 2D model will be presented. Then, different options to calculate the combined friction parameter will be discussed. These different options will be applied and compared with a 1D flow test case, flow over a hump, and with two 2D flow test cases, flow past a submerged groin and flow in a natural river. Finally, the combined friction parameter will be used as a criterion to calculate variable minimum depths with which to switch to the ground water model.

11.2 A New Mesh Refinement Indicator for Open Channel Flow Models

Modelers are often faced with spurious velocity vectors or stability problem when modeling natural channels (e.g., Bates and Hawkes 1997, Tchamen and Kahawita 1998, Heniche and Leclerc 2002, Dietrich 2006). Natural channels have many variations in topography that makes modeling of flow challenging, especially when wetting/drying areas, very shallow areas, or very steep gradient areas are present.

Gresho and Lee (1981) argued not to suppress the wiggles because those spurious velocities give us a chance to reconsider the mesh. These errors indicate that either the discretization is too coarse to resolve the physics of that area, or the generated flow is beyond the capacities of the existing model scope. Generally mesh refinement helps to remove those wiggles.

An appropriate mesh is necessary for the accuracy and stability of numerical models. Moreover, variable graded mesh is often required for 2D depth averaged shallow water modeling with large domains, e.g., flood plain modeling and ocean modeling, in order to minimize the computational effort. Having a criterion for mesh refinement would be helpful for the 2D depth average modeling, but there are few existing criteria or guidelines for specifying the discretization, especially for the shallow water model (Hagen and Kolar 2000, Hagen and Horstmann 2001).

A number of good literature reviews on mesh refinement indicators are available in Hagen and Kolar (2000), Tate and Stockstill (2006), and Dietrich and Dresback (2008). Westerink and Muccino (1994) proposed a mesh refinement indicator using the wavelength of a tide to the grid size ratio, but the limitation of this indicator is that the local areas with a high rate of bathymetric change, such as shelf break and steep continental slope, are not properly resolved (Hagen and Kolar 2000).

Another criterion was given by Hannah and Wright (1995), which was based on the ratio of the topographic length scale to the discretization scale. According to Hannah and Wright (1995):

$$\frac{\Delta x S_b}{h} \leq \epsilon \tag{11.1}$$

where S_b is the local bed slope and ϵ is the mesh generation criterion. Eq. 11.1

incorporates bathymetry and the gradient of the bathymetry into the mesh generation process. However, the refinement is not necessarily required only on the steep bathymetric changes, but also required where the solution variables change rapidly (Hagen and Horstmann 2001, Dietrich and Dresback 2008). Furthermore, their parameter was developed from the analytical study of wind-driven flow in the coastal ocean.

Based on a posteriori analysis, Hagen and Kolar (2000) and Hagen and Horstmann (2001) introduced the localized truncation error analysis (LTEA) method for mesh refinement. The limitation of this method is that the technique requires a priori calculation of the truncation errors which require knowledge of the 'true' solution, typically obtained from a uniformly and highly refined mesh (Dietrich and Dresback 2008).

In recent years, mass balance error has been used as a mesh refinement indicator by several researchers (e.g., Dietrich and Dresback 2008, Tate and Stockstill 2006, Berger and Howington 2002, Marrocu and Ambrosi 1999). This is also a posteriori method. In the mass balance error method, differences between the consistent mass fluxes and nodal discharges are calculated, and those differences are minimized using mesh refinement.

Except for the parameter introduced by Hannah and Wright (1995), no method considers the depth explicitly and therefore may not be able to capture the friction dominated case. The proposed combined friction parameter, $\beta_{\Delta x} Fr_0^2$, has shown its efficacy to indicate the friction dominated area. Therefore, this combined friction parameter can be used as a mesh refinement indicator and its use as such will be investigated in this study.

11.2.1 Different Options for the Combined Friction Parameter

The proposed combined friction parameter, i.e., $\frac{\Delta x Fr_0^2}{C_*^2 h_0}$, incorporates various other parameters and variables. The combined friction parameter has its origins in the linearized non-dimensional form of the Saint-Venant equations. For the non-linearized Saint-Venant equations, there are several ways to calculate this combined parameter. In the linearized equations, Fr_0 and h_0 are considered to be the average quantities. In the non-linear equations, one obvious option is to use the nodal quantities instead of the average quantities. Therefore, our first option for the combined friction parameter is $\frac{\Delta x Fr^2}{C_*^2 h}$, where Fr, C_* and h are considered the nodal values, and we will call this parameter a basic combined friction parameter.

Following Chezy's uniform flow equation, for a uniform flow we can write that $Fr^2 = C_*^2 S_f = C_*^2 S_w = C_*^2 S_b$, where S_f is the local friction slope, S_w is the local water surface slope, and S_b is the local bed slope, respectively. Applying these relationships in the basic combined friction parameter, we can write the parameter as $\frac{\Delta x}{h/S_f}$, $\frac{\Delta x}{h/S_w}$, and $\frac{\Delta x}{h/S_b}$, respectively. The denominators h/S_f, h/S_w, or h/S_b can be viewed as a characteristic length scale, L. The use of S_b gives the same parameter as Hannah and Wright's (1995) parameter, i.e., Eq. 11.1. We will call these three parameters as the parameter with friction slope, water surface slope, and bed slope, respectively. Table 11.1 lists all the different options to calculate the combined friction parameter.

For a uniform flow, we know that the local friction slope, local water surface slope, and local bed slope all become equal. Therefore, for a uniform flow, all the four parameters are equal. However, these parameters are not equal when flows are not uniform. In this chapter, we will explore the applications of these four parameters with 1D and 2D flow test cases, where the flows are non-uniform. Our objective is to find which parameter gives the best representation of the characteristic length scale, or which parameter locates the problematic areas most effectively in case of non-uniform flow.

Table 11.1: Different options for the combined friction parameter.

Options	Parameters
Basic combined friction parameter	$\frac{\Delta x Fr^2}{C_*^2 h}$
Parameter with friction slope	$\frac{\Delta x S_f}{h}$
Parameter with water surface slope	$\frac{\Delta x S_w}{h}$
Parameter with bed slope	$\frac{\Delta x S_b}{h}$

11.2.2 1D Flow Test Case: Flow Over a Hump

In this test case, a small hump of 0.5 m height is introduced in a 2500 m long rectangular channel. The length of the hump crest is 100 and the average channel slope is 0.00111. An inflow of 100 m^3/s and a normal depth of 0.74 m are used as inflow and outflow boundary conditions. Initial flows equal to the inflow and initial depths equal to the downstream boundary depth are used as the initial conditions for all nodes. The non-dimensional Chezy coefficient (C_*) is taken as 15 for all nodes. The test case is run until the solution reaches a steady state solution.

For this particular test case, we have used the CDG finite element scheme to solve the final steady state solution. We have already studied different numerical schemes with the 1D non-uniform flow test case, and we have found that except the one-sided upwind-downwind scheme, all schemes give oscillations in the discharge and/or depth solutions for the friction dominated case. Therefore, except the one-sided upwind-downwind scheme, we can use any scheme for this test case, and the CDG scheme is used for this test case because the same scheme has also been used in the River2D model which will be used for the 2D flow test cases.

Fig. 11.1 shows the final steady state solutions for $\Delta x = 100$ m. Fig. 11.1a shows the bed elevation and water surface elevation, Fig. 11.1b shows the discharge solution, and Fig. 11.1c shows the four friction parameters as a function of longitudinal channel distance. From the figure, it is clear that the discharge oscillations appear where the combined friction parameters are high. Fig. 11.1c shows that the basic combined friction parameter values are almost double in magnitude compared to the other three parameters' values.

Fig. 11.2 shows the final steady solutions for $\Delta x = 10$ m. As it is expected, the discharge oscillations are reduced significantly, i.e., from 14% to 0.71%, due to the reduction of Δx. The combined friction parameter values are also reduced from a maximum value of 1.72 to 0.15.

This 1D flow test case shows that the combined friction parameter with the four different options as listed in Table 11.1 can be used as an indicator of the error. The test case also shows that refinement does help to reduce the parameter as well as the error.

11.2.3 2D Flow Test Case: Flow Past a Submerged Groin

In this test case, the four different combined friction parameters (as listed in Table 11.1) are implemented in the River2D model (Steffler and Blackburn 2002) and compared with an idealized 2D flow test case, flow past a submerged groin. This 2D flow test case is chosen for its similarity to the 1D flow test case, but has a more complex flow field. The flow is sub-critical; it has large local changes in topography as well as in the solution variables, and the depth is quite small at the crest and steep gradient sections.

To calculate the combined friction parameters at a node in a 2D model, we need an estimation of the discretization length, Δx, and an estimation of different nodal slopes (friction, water and bed). The estimation of the discretization length is found by taking the square root of the average of the areas of the elements connected to a node. Similarly, the different nodal slopes are calculated by taking the average of the slopes of the elements connected to a node. The depth, the Froude number, and the Chezy coefficient are taken at the nodal values.

In this 2D flow test case, a rectangular channel of 130 m long, 100 m wide, and 0.0025 bed slope is taken. An idealized submerged groin with sloping sides is placed on one side of the rectangle channel at a distance of 60 m. The groin has a height of 0.15 m, a crest width of 10 m, and a length of 40 m. A typical bed elevation contour of the test case is presented in Fig. 11.3, while Fig. 11.4 shows the longitudinal and cross-section bed profile of the test case.

An inflow of 7 m^3/s and a downstream depth of 0.14 m are used as inflow and outflow boundary conditions, respectively. An initial flow equal to zero and depth equal to the downstream boundary depth are used as the initial conditions for all nodes. The test case is run until the solution reaches a steady state solution. Two locations, one at $y = 40$ m and the other at $x = 70$ m (as shown in Fig.11.4), are the main foci for this test case, where major bathymetric changes take place. Oscillations or errors are expected to be maximum at these two locations.

The test case is run, first, with a coarse grid which has a uniform discretization length of 4 m with 2178 elements. The River2D model has a useful feature, the break-line method, which allows the user to capture any topographic changes with a minimum number of elements. This feature is used in the test case to generate the mesh, and Fig. 11.5 shows the final coarse mesh. One can see in the figure that the whole groin feature (i.e., 30 m length along the longitudinal direction) is covered in the coarse mesh with six to ten elements, while the individual sloping or crest part is covered with two or three elements only. From practical experience, we know that these few elements are not sufficient to capture the flow features correctly in the groin areas.

To compare the coarse mesh solution, a reference solution is obtained by finding a nearly grid-independent solution for the test case problem. Continuous refinements are done for the whole domain until the changes in the solutions are negligible. The reference solution has an estimated maximum of errors in velocity or depth solution of less than 2.4% and has an average of less than 0.0008%. The final fine mesh has nearly 750,000 elements with a maximum discretization size of 0.027 m, which is nearly 150 times smaller than the size of the coarse discretization. The final fine mesh is not shown here, as that figure is almost black due to the large number of elements.

Fig. 11.6 shows the Froude number contour for the fine and coarse grid. Comparing Fig.11.6a and 11.6b, we can see that spurious oscillations in the coarse grid solution are apparent in the groin areas. However, at the outside of the groin areas, both solutions look similar, at least qualitatively. To explore further and to quantify the errors, we extract velocity and depth solutions at two cross-sections, $y = 40$ and $x = 70$ m. Error at each node for each discretization solution is calculated by taking the absolute differences from the reference solution and by dividing the error with the reference solution.

Fig. 11.7 shows the velocity and depth solutions, Fig. 11.8 shows the relative velocity and depth errors, and Fig. 11.9 shows the basic combined friction parameter with the longitudinal distance for different uniform discretization at $y = 40$ m. Fig. 11.8 shows that the relative errors are maximum for $\Delta x = 4$ m (27.7%), the errors decrease as the discretization decreases, and the maximum error for $\Delta x = 0.08$ m is 2.4%. Comparing 11.8 and 11.9, we can see that the combined friction parameters are high where the errors are high. The maximum parameter for $\Delta x = 4$ m is 3.3, and the maximum parameter for $\Delta x = 0.027$ m is 0.18.

Fig. 11.10 shows the velocity and depth solution, Fig. 11.11 shows the relative velocity and depth errors, and 11.12 shows the basic combined friction parameter with the cross-sectional distance for different uniform discretization at $x = 70$ m. Similar to the results at $y = 40$ m, the relative errors are maximum for $\Delta x = 4$ m (17%), and the errors are minimum for $\Delta x = 0.08$ m (1.6%) (as shown in Fig. 11.11). Moreover, the errors are also high where the combined friction parameters are high (as shown in 11.11 and 11.12). The maximum parameter for $\Delta x = 4$ m is 2.17, and the maximum parameter for $\Delta x = 0.027$ m is 0.12. In addition, one can see that the non-physical oscillations in the velocity solutions are present for the coarse discretizations, e.g., $\Delta x = 4$ or 2 m (as shown in 11.10a).

The results for this particular 2D flow test case show that as the discretization decreases, the error decreases, and so does the combined friction parameter. Therefore, the combined friction parameter can be used as a measure of error. Moreover, the errors are high where the combined friction parameters are high, and therefore, the friction parameter can also be used as an indicator of error. Thus, we can use the combined friction parameter as a mesh refinement indicator. In this study, we have used all four different friction parameters to do the mesh refinement, and the results for all refined meshes are compared.

A typical refinement process in the River2D model using the friction parameter is as follows. First, the combined friction parameters are calculated at all nodes, and then a check is made for each element through-out the domain. If any element has a single node that has a friction parameter value greater than a maximum allowable limit (0.1 for this test case), a new node is created in the center of that element as well as in the adjacent three elements (as shown in Fig. 11.13). The whole mesh is then re-triangulated (as shown in Fig. 11.14). Most of the times, the new triangulated mesh generates a poor quality of triangles, and therefore, in the River2D model, a tool called 'smoothing' is used in which triangles are stretched out to obtain a better triangle quality (Steffler and Blackburn 2002). Fig. 11.15 shows the final mesh after four to six smoothing processes. A new steady state solution is solved for the new mesh, and the combined friction parameters are calculated using the new solution. The check for the refinement is made for each element again, and this refinement process continues until all nodes have parameter values less than the maximum allowable limit.

The final meshes after being refined with the four different combined friction parameters are shown in Fig. 11.16, 11.17, 11.18, and 11.19, respectively. The first three meshes have almost the same number of elements, i.e., 11650, 11317, and 11138, respectively, and the last mesh has a higher number of elements, i.e., 14296. Again, the velocity and depth solutions are extracted at $y = 40$ and $x = 70$ m for all these meshes, and the results are compared.

Fig. 11.20 shows the relative velocity and depth error at $y = 40$ m for the refined meshes. We can see that refinement with all four different friction parameters does help to reduce the errors. The maximum error is reduced from 27.7% to 6% with the first three parameters and to 2.7% with the fourth parameter.

Fig. 11.21 shows the relative velocity and depth error at $x = 70$ m for the refined meshes. Similar to the results at $y = 40$ m, we can see that refinement with all the four different friction parameters does help to reduce the errors. The maximum error is reduced from 17% to 3% with the first three parameters and to 2.2% with the fourth parameter.

For this particular test case, the mesh with the friction parameter with bed slope generates more elements, but gives less errors compared to the other three meshes. This is because the parameter with bed slope refines the upstream areas of the crest (as shown in Fig. 11.19), whereas the other meshes don't refine the upstream areas with a maximum parameter limit of 0.1.

Comparing Fig. 11.16 to 11.19, we can see that, similar to the 1D flow test case results, the results of this test case shows that all four options more or less capture the high error areas, and refinement takes place in those areas. All four options suggest the need for refinement in the downstream of the crest areas, where the velocities are high, the depths are small and the slopes are high. Moreover, Fig. 11.20 and 11.21 show that we can achieve solutions with refined mesh which have errors of less than 6% with around 11,000 elements only.

11.2.4 2D Flow Test Case: Flow in a Natural River

In this particular test case a natural river is modeled; the test case area is located in the South Platte River (Colorado) (as shown in Fig. 11.22). A portion of that river channel was modified in order to increase diversity of channel morphology and improve trout habitat which includes placement of boulders in the channel (Waddle 2009). To evaluate the effect of modification, detailed velocity and depth measurements were taken at two large boulder locations (as shown in Fig. 11.23) for three different discharges, i.e., 1.133, 1.529 and 4.531 m^3/s. A numerical model has also been created by Waddle (2009) for the study area. In this study, we will simulate only one flow rate case, that is 1.529 m^3/s, and the results will be compared with the observed data and Waddle (2009) solution.

Waddle's (2009) model consists of nearly 130,000 elements which capture all small/large boulders present in the study area. Fig. 11.24 shows the mesh that was used by him. In this particular study, our objective is to model the same channel with a minimum number of elements, while still getting a solution as close as possible to Waddle's (2009) model solution, especially in the main boulder region.

Several meshes are developed in this study. Table 11.2 lists all the different meshes that are used in this test case. First a coarse uniform discretization, i.e., $\Delta x = 3$ m, is used to create an initial mesh, which is named *Mesh1* (as shown in Fig. 11.25). A problem with the very coarse mesh is that it doesn't capture all the variability in the topography, for example large or small boulders. Therefore, the next mesh, i.e., *Mesh2* (as shown in Fig. 11.26), is created by capturing all the small/large boulders that are present at the main velocity measurement region using fixed nodes. A few local refinements are done to provide a smooth transition in the mesh. This mesh is considered to capture the most geometric features with a minimum number of elements. Thus, *Mesh2* will be our base mesh on which regional or local refinement, or the minimum depth criterion, will be implemented. The third mesh, *Mesh3* (as shown in Fig. 11.27), is created by doing the first level of regional refinement. Refinement is done only at the main boulder region. The fourth mesh, *Mesh4* (as shown in Fig. 11.28), is found by doing another level of regional refinement.

Near the two main large boulders (as shown in Fig. 11.23), velocity and depth solutions for different meshes are compared at four cross-sections with

Table 11.2: Different meshes that are used in the natural river test case.

Meshes	Description	Number of elements
Mesh1	Uniform discretization mesh	21,182
Mesh2	Mesh with boulders	26,956
Mesh3	First level of regional refinement	35,406
Mesh4	Second level of regional refinement	59,834

the observed data and Waddle's (2009) solution. Fig. 11.29 to 11.32 present the depth solutions and Fig. 11.33 to 11.36 present the velocity solutions at those four cross-sections. Moreover, Table 11.3 shows the average and maximum differences in depth and velocity solutions for all the different meshes compared to the Waddle (2009) solution.

From the figures and table, we find that except for the uniform mesh, i.e., *Mesh1*, all meshes give solutions close to the Waddle (2009) solution. For these three meshes the average of the absolute differences in depth solutions are less than 0.03 m and in velocity solutions are less than 0.09 m/s. Moreover, the differences between the last three meshes' solutions are negligible. This is because the combined friction parameters are small in these measured locations. The maximum basic combined friction parameter is found in these locations to be 0.05 and the average combined friction parameter is found to be 0.003. Thus, it is expected that the refinement does not help very much to improve the solutions at these locations.

Table 11.3: A summary of the solutions from different meshes in the natural river test case.

	Depth (m)		Velocity (m/s)	
Difference between	Average	Maximum	Average	Maximum
Waddle's mesh-Mesh1	0.083	0.620	0.186	0.84
Waddle's mesh-Mesh2	0.026	0.146	0.086	0.396
Waddle's mesh-Mesh3	0.021	0.087	0.067	0.402
Waddle's mesh-Mesh4	0.021	0.086	0.063	0.398
Waddle's mesh-Observed	0.030	0.287	0.105	0.395

However, even though the solution at the boulder areas are close to the observed values with the last three meshes, there are few places where spurious high velocity vectors are present. Fig. 11.37 plots the velocity vectors which are greater than twice the average velocity for the *Mesh2* solution, and one can see the spurious high velocity vectors. Similar spurious high velocity vectors are observed with Waddle's (2009) model solution (as shown in Fig. 11.38). These spurious high velocity vectors normally slow down the solution convergence rate, and in some cases, produce instability.

The combined friction parameter is effective at locating these spurious high velocity vectors. Fig. 11.39 and Fig. 11.40 show the same velocity vectors plots where the basic combined friction parameters are greater than 0.5. Comparing Fig. 11.37 and Fig. 11.39, or Fig. 11.38 and Fig. 11.40, we can see that the combined friction parameter not only locates the spurious high velocity vectors, but also locates the vectors which are not high but spurious.

Once the high velocity vectors are located, we can do local refinement or use minimum depth criterion to eliminate or reduce these spurious high velocity vectors. In this section, the use of the local refinement using the friction parameters is presented. Refinement is done where the parameter values are greater than a maximum allowable limit, and for the natural river test case, we use 0.5 as a maximum allowable limit. A typical refinement process in the River2D model using the combined friction parameter was described in the previous section.

A typical issue with the local refinement using the combined friction parameter in a natural river is that the combined friction parameter reaches up to an order of 100 or even 1,000 in a few locations. Therefore, to reduce the parameter up to a reasonable limit (0.5 in this case) requires an excessive level of local refinements. Moreover, in a few cases, local refinement finds a new bathymetry which has a steeper gradient or shallower depth, either of which increases the value of the combined friction parameter, or at least keeps the parameter the same. Therefore, local refinement may not be able to eliminate the high spurious velocity vectors for these cases. However, the refinement is still a useful step as it confines the high velocity vectors to a small region when it can not eliminate them.

In this particular test case, we do local refinement on the *Mesh2* using the basic friction parameter and the parameter with local bed slope. As the basic friction parameter, parameter with friction slope, and parameter with water surface slope all refine more or less the same areas (as found with the flow past a submerged groin test case), we use just one parameter from these three parameters. Up to four levels of local refinements are done using the basic friction parameter and the parameter with bed slope, and the results are compared.

Table 11.4 shows the number of elements after each level of local refinement using both parameters, and Fig. 11.41 and Fig. 11.42 show the final mesh after four levels of local refinement. Fig. 11.43 and Fig. 11.44 show the velocity vectors which are greater than twice the average velocity for those two meshes, respectively.

Table 11.4: Number of elements after local refinement using the friction parameters in the natural river test case.

Refinement level	Number of elements using the basic friction parameter	Number of elements using the parameter with bed slope
First	27,561	46,696
Second	28,287	80,407
Third	29,091	137,447
Fourth	31,111	231,351

Comparing Fig. 11.37, Fig. 11.43, and Fig. 11.44 we find that the local refinements using both parameters more or less eliminate some of the spurious high velocity vectors. However, both parameters also produce a few new spurious high velocity vectors. After four levels of local refinement, there are still a few locations where the parameters are higher than 0.5, and therefore, not all the spurious high velocity vectors are eliminated with the local refinements.

Comparing the number of elements after refining using each parameter (as is shown in Table 11.4), we see that the meshes using the parameter with local bed slope always have more elements compared to the meshes using the basic friction parameter. This is also consistent with the flow past a submerged groin test case result. However, in the flow past a submerged groin test case, the mesh using the parameter with local bed slope has only 1.22 times more elements than the meshes with the basic friction parameter. In the natural river test case, meshes using the parameter with local bed slope have 2 to 8 times more elements than the meshes with the basic friction parameter. A natural river has too many variations in local topography, which necessitates too many refinements with the parameter with local bed slope. Therefore, for a natural river, the basic friction parameter, or the friction parameter with friction slope or water surface slope, is more effective at locating the high velocity vectors than the friction parameter with bed slope.

11.3 A New Minimum Depth Criterion for Open Channel Flow Models

While solving the Saint-Venant equations numerically, if depth becomes negative or zero, the solution becomes indeterminate or imaginary. To avoid this particular issue, in every numerical model the common practice is to use a minimum depth beyond which the code will terminate or switch to an alternate set of equations, e.g., a reduced momentum equation (Tchamen and Kahawita 1998, Dietrich 2006), modified Saint-Venant equations (Bates and Hervouet 1999, Defina 2000, Heniche and Leclerc 2002), or a ground water equation (Khan 2000, Steffler and Blackburn 2002).

However, there is no fixed criterion for choosing a minimum depth, and therefore, a wide range of minimum depths, e.g., 0.01 m to 0.1 m, are observed in practical modeling. Furthermore, a fixed minimum depth is normally used for a domain, which may be too conservative or may be ineffective depending on the situation. For example, in the River2D model (Steffler and Blackburn 2002), 0.01 m is used as a minimum water depth. When depth becomes less than 0.01 m, the ground water equation (Khan 2000, Steffler and Blackburn 2002) is used to calculate the water surface elevation, and the surface water flow is set to zero. However, from the practical modeling experience and from Fig. 11.37, we find that in a few cases spurious velocities are observed where the depths are greater than 0.01 m. The high value of the combined friction parameter in this case indicates that these nodes are of the friction dominated case. This indicates that the depths are small compared to the discretization scale, and either refinement should be done or the node should be considered a dry node.

In the previous section, local refinement was done using the combined friction parameter. In this section, we use the ground water model to eliminate the high vectors using the combined friction parameter. In this approach, a nodal combined friction parameter will be calculated at all nodes. If any nodal parameter value is greater than a maximum allowable limit, the ground water model will be activated for that node. In this test case, we use 0.5 as the maximum allowable limit so that the ground water model is applied only to a few nodes.

Use of the combined friction parameter as a criterion to switch to the ground water equation is similar to the use of variable minimum depths rather than a fixed minimum depth. In other words, by using 0.5 as the maximum allowable limit of the combined friction parameter, variable minimum depths can be calculated for all nodes. If any depth is smaller than the calculated minimum depth, then the wetting/drying treatment will be applied to that node.

Fig. 11.45 shows the final velocity vectors which are greater than twice the average velocity after implementing this approach, and comparing Fig. 11.37, 11.39, and Fig. 11.45, we see that the spurious high velocity vectors are eliminated with this approach, even though the solution at the main boulder region does not change.

As the parameters at a few nodes are higher than the allowable limit, applying the ground water model should not affect the overall solution significantly, provided that the dry areas are not too big. To avoid too many areas being dry, this approach can be applied in conjunction with the local refinement. Local refinement can be done first, where the combined friction parameters are higher than the maximum allowable limit. Local refinement will confine the high velocity vectors to a small region, and then, if the local refinement alone is not able to eliminate/reduce the high velocity vectors, the ground water model can be applied.

One important thing to note here is that while implementing the ground water model with the combined friction parameter, from practical experience, we have found that the combined friction parameter with the friction slope or water surface slope is more suitable in implementation than the basic combined friction parameter. This is because when the ground water model is applied to any node, surface water flow rate is forced to zero on that node, which makes the basic combined friction parameter equal to zero. This makes that node wet again, and the alternate wet/dry condition hampers the convergence rate, while the parameter with the friction slope or the water slope does not change that much after applying the ground water model.

11.4 Conclusion

The results of the 1D flow test case, flow over a hump, and of the 2D flow test case, flow past a submerged groin, show that the proposed friction parameter can be used as a measure of error and an indicator of error. The 2D flow test case results with a submerged groin show that the proposed friction parameters can be used as a mesh refinement indicator and that all four options used to calculate the combined friction parameter more or less capture the problematic areas. However, mesh using the parameter with local bed slope generates more elements (e.g., 3,000) than the meshes with the other three parameters.

The results of the 2D flow test case with a natural river show that the proposed friction parameter is effective at locating high velocity vectors in natural rivers, and therefore can be used as an indicator for the mesh refinement or to switch to a ground water equation. Local mesh refinement using the basic friction parameter or the parameter with local bed slope does help to reduce/eliminate some of the spurious velocity vectors. However, meshes using the parameter with local bed slope produces more elements (2 to 8 times) than the meshes with the basic friction parameter. The natural river test case results by applying ground water model using the friction parameter show that the spurious velocity vectors are successfully eliminated with this approach. However, in order to avoid too many areas being dry, this approach should be applied in conjunction with local refinement.

It is to be noted here that (as we have also discussed in section 10.3) the friction parameter with the local bed slope becomes same as Hannah and Wright's (1995) parameter. However, both the 2D test cases, i.e., flow past a submerged groin and flow in a natural river, results show that Hannah and Wright's (1995) parameter generates too many refinements, especially in a natural river case. This suggests that, in a natural river, the use of a local bed slope as a mesh refinement indicator is not very effective. Therefore, for a natural river, the basic combined friction parameter, or the parameter with friction slope or water surface slope, should be used as an indicator for the mesh refinement or to switch to a ground water equation.

The proposed combined friction parameters can detect steep gradient of depth changes, water elevation changes, and velocity changes. Moreover, they can detect the small depth areas with steep gradients. Furthermore, these parameters are easy to calculate and implement in any open channel flow model. The use of the proposed friction parameters can lead to an automated mesh refinement process in open channel model.

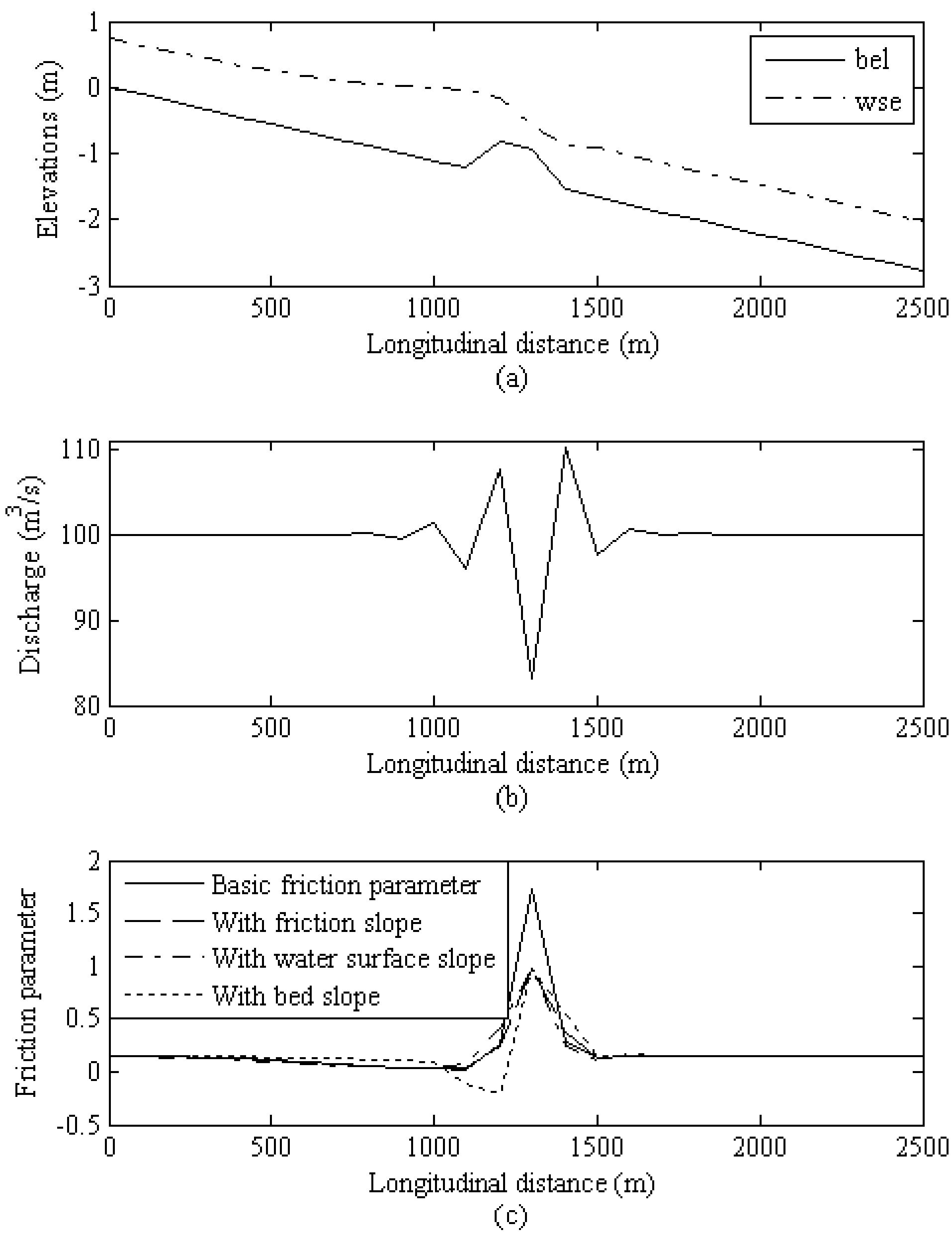

Figure 11.1: 1D flow over a hump test results with $\Delta x = 100$ m (a) Bed elevation (bel) and water surface elevation (wse) profile (b) Discharge solution and (c) Combined friction parameter with four different options.

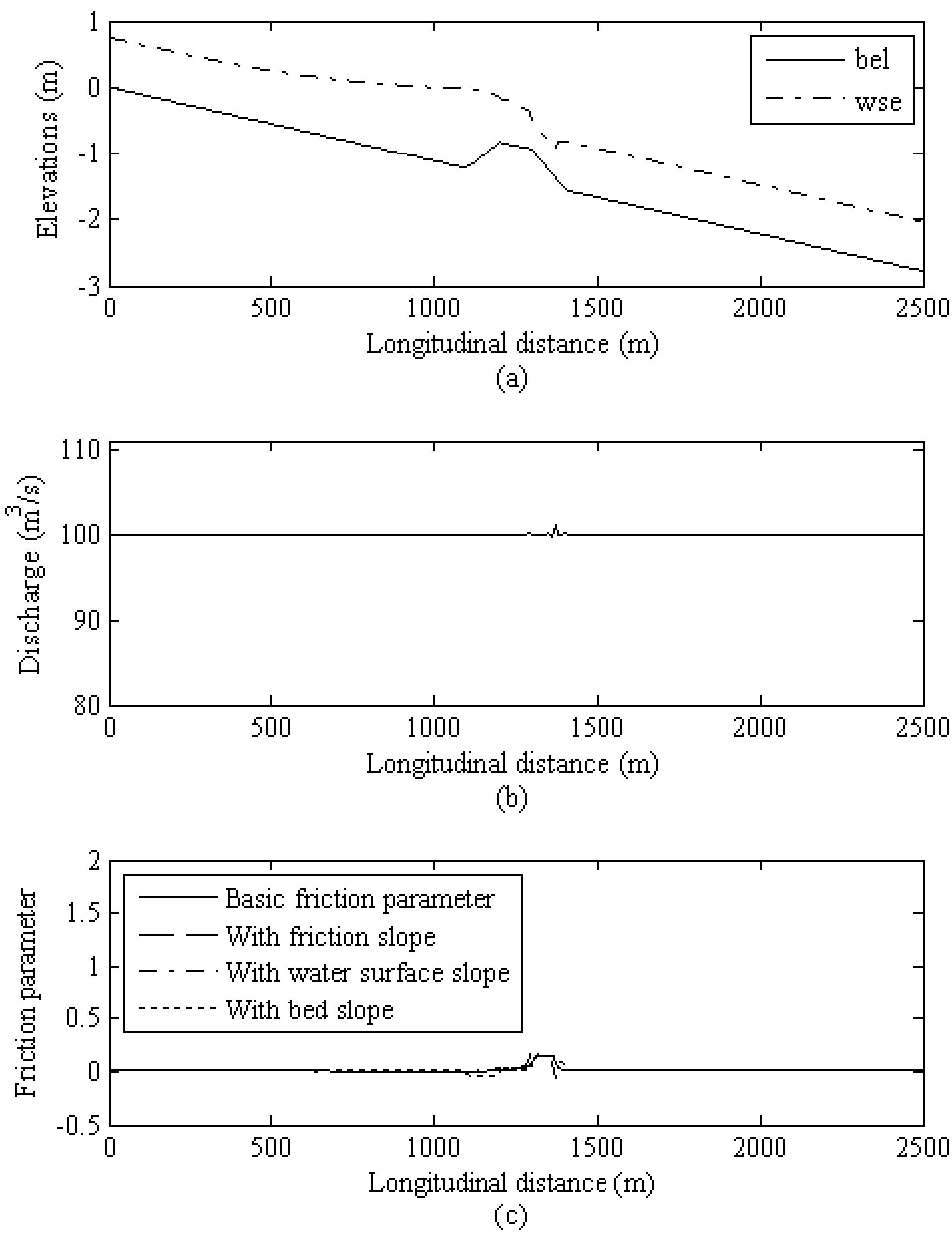

Figure 11.2: 1D flow over a hump test results with $\Delta x = 10$ m (a) Bed elevation (bel) and water surface elevation (wse) profile (b) Discharge solution and (c) Combined friction parameter with four different options.

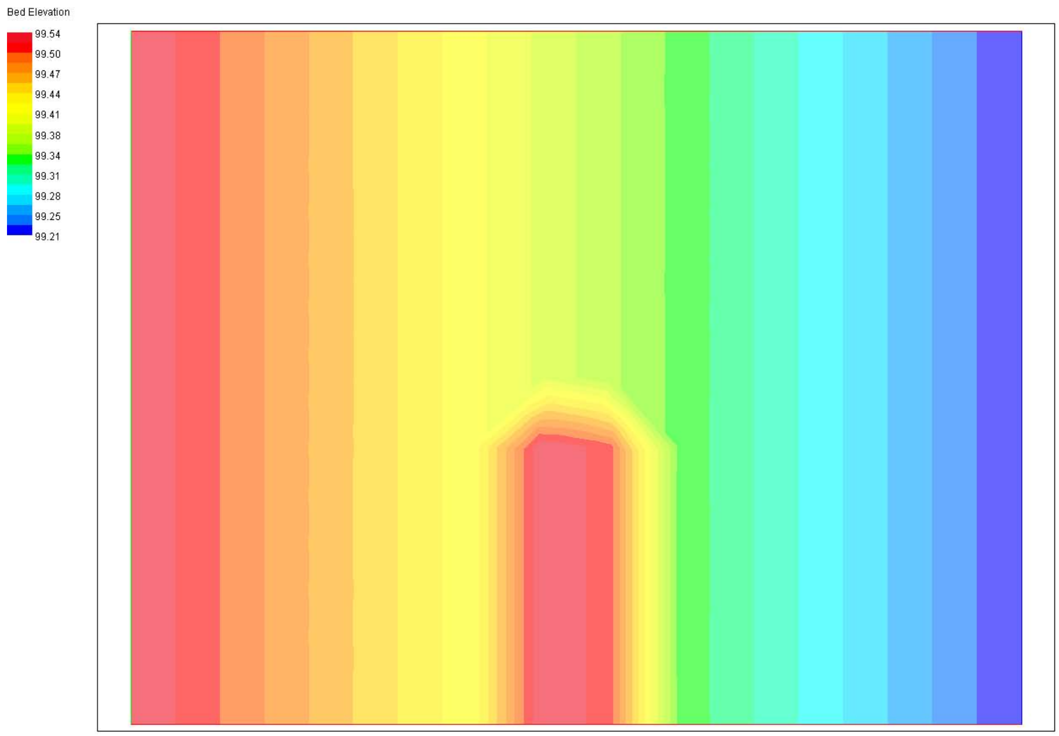

Figure 11.3: Bed elevation contour for the flow past a submerged groin test case.

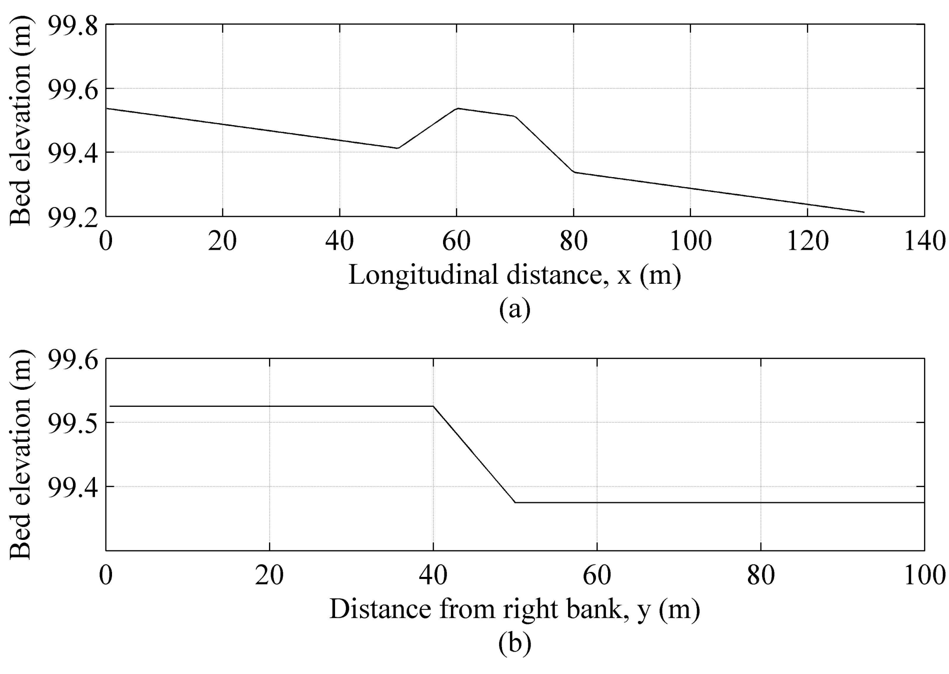

Figure 11.4: (a) Longitudinal bed elevation profile at $y = 40$ m and (b) Cross-sectional bed elevation profile at $x = 70$ m for the flow past a submerged groin test case.

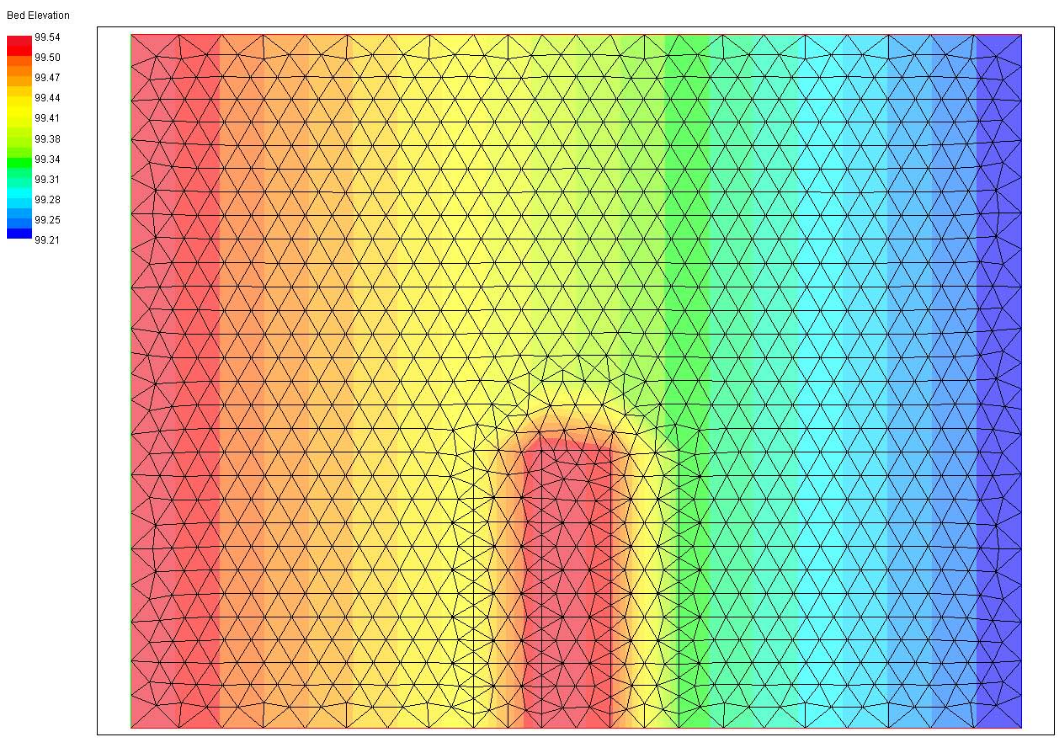

Figure 11.5: Generated mesh with uniform discretization of 4 m for the flow past a submerged groin test case.

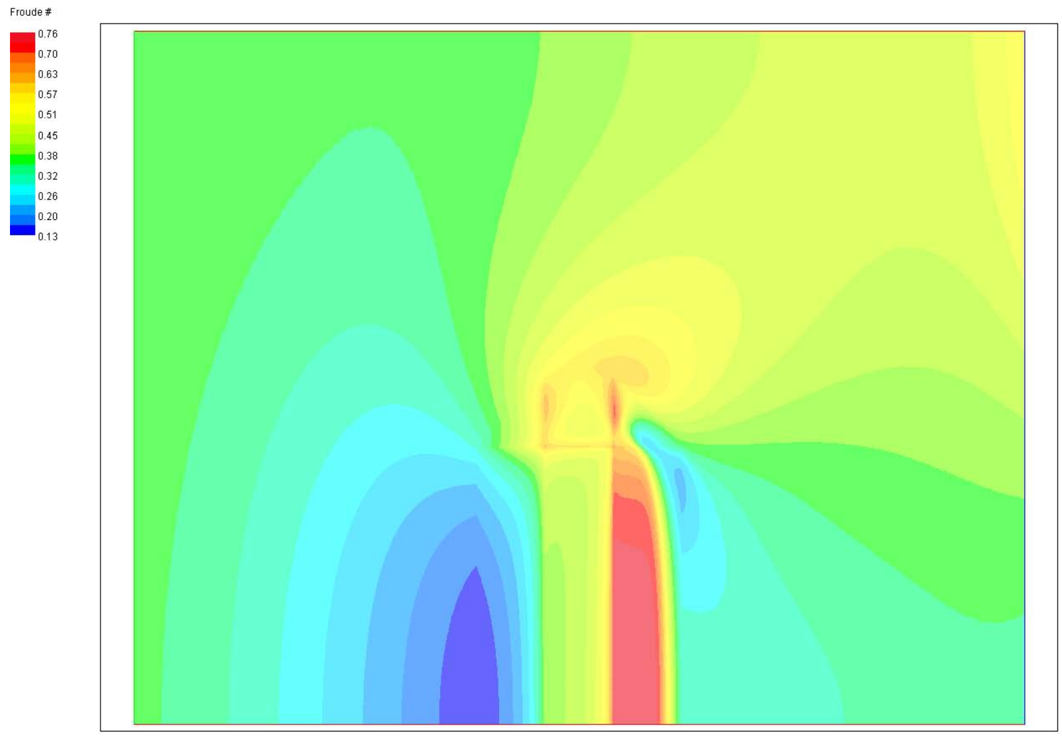

(a)

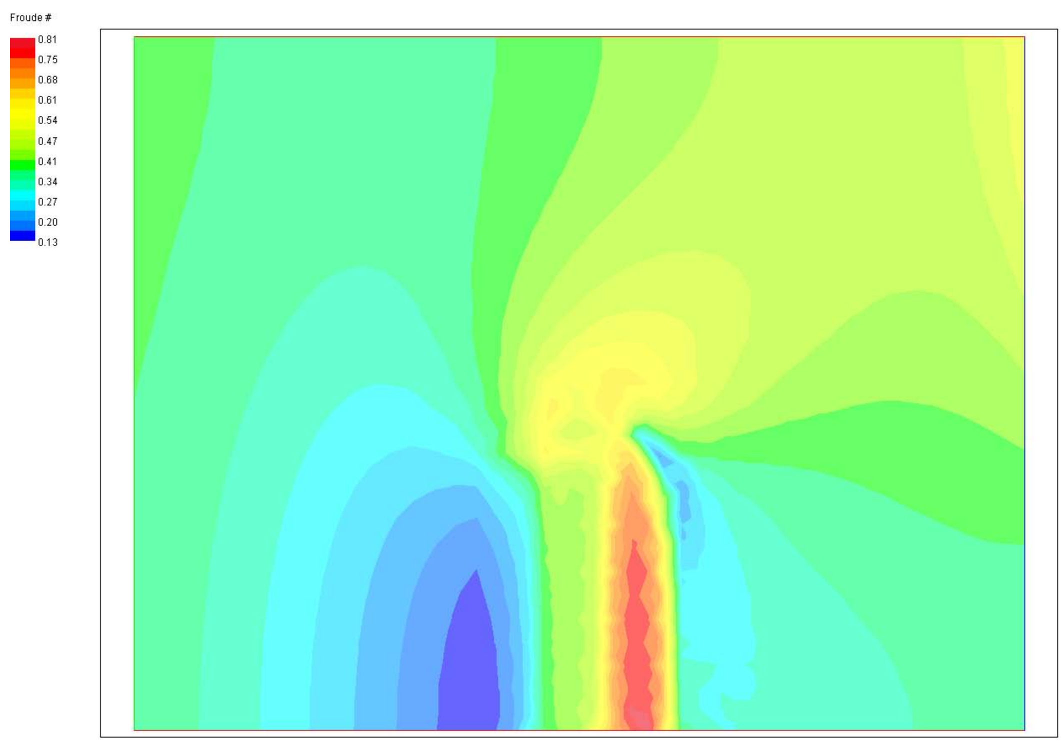

(b)

Figure 11.6: Contour of the Froude number solutions for the 2D flow past a groin test case (a) Fine mesh and (b) Coarse mesh.

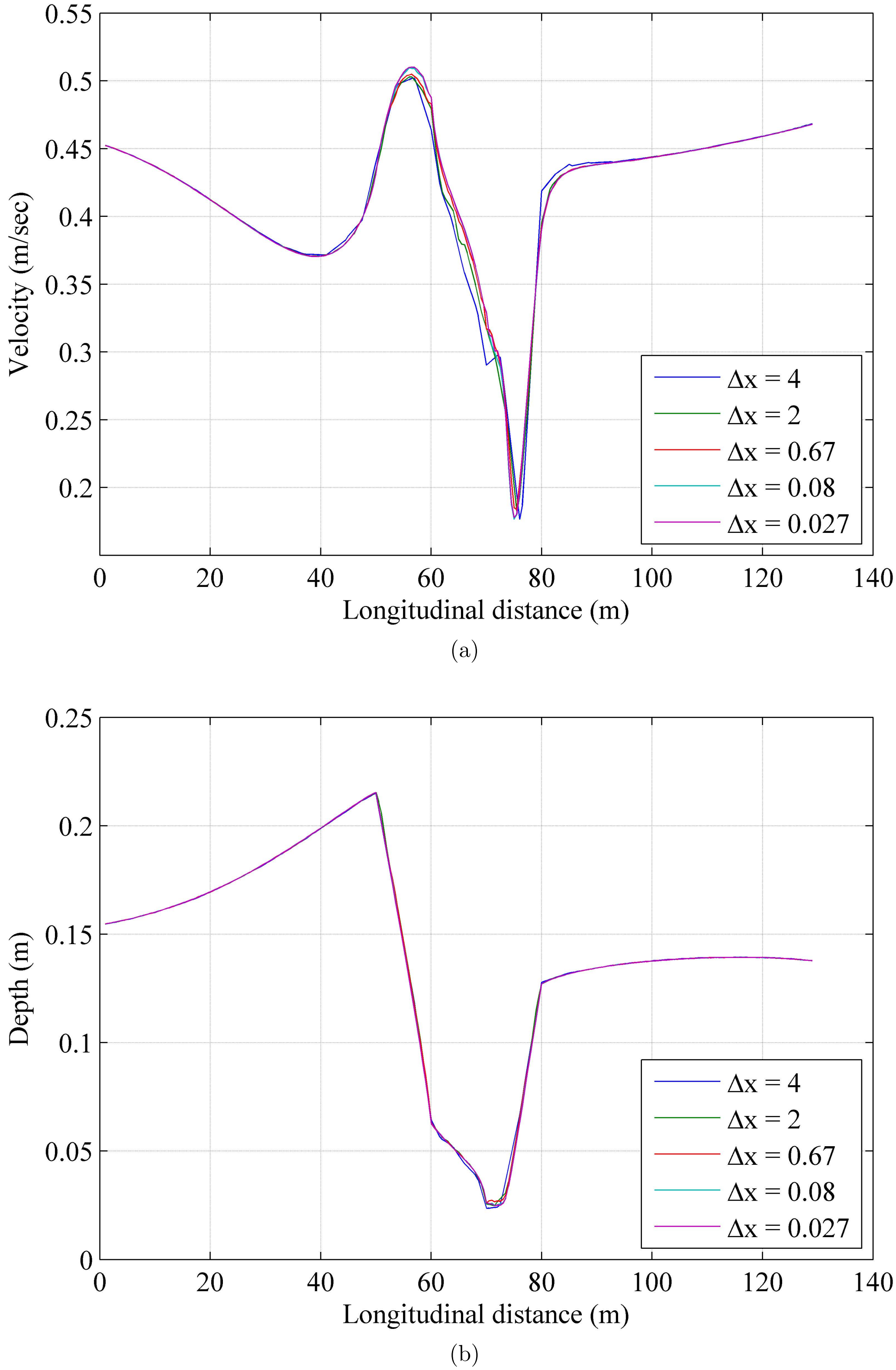

Figure 11.7: (a) Velocity and (b) Depth solutions at $y = 40$ m for different uniform discretization meshes.

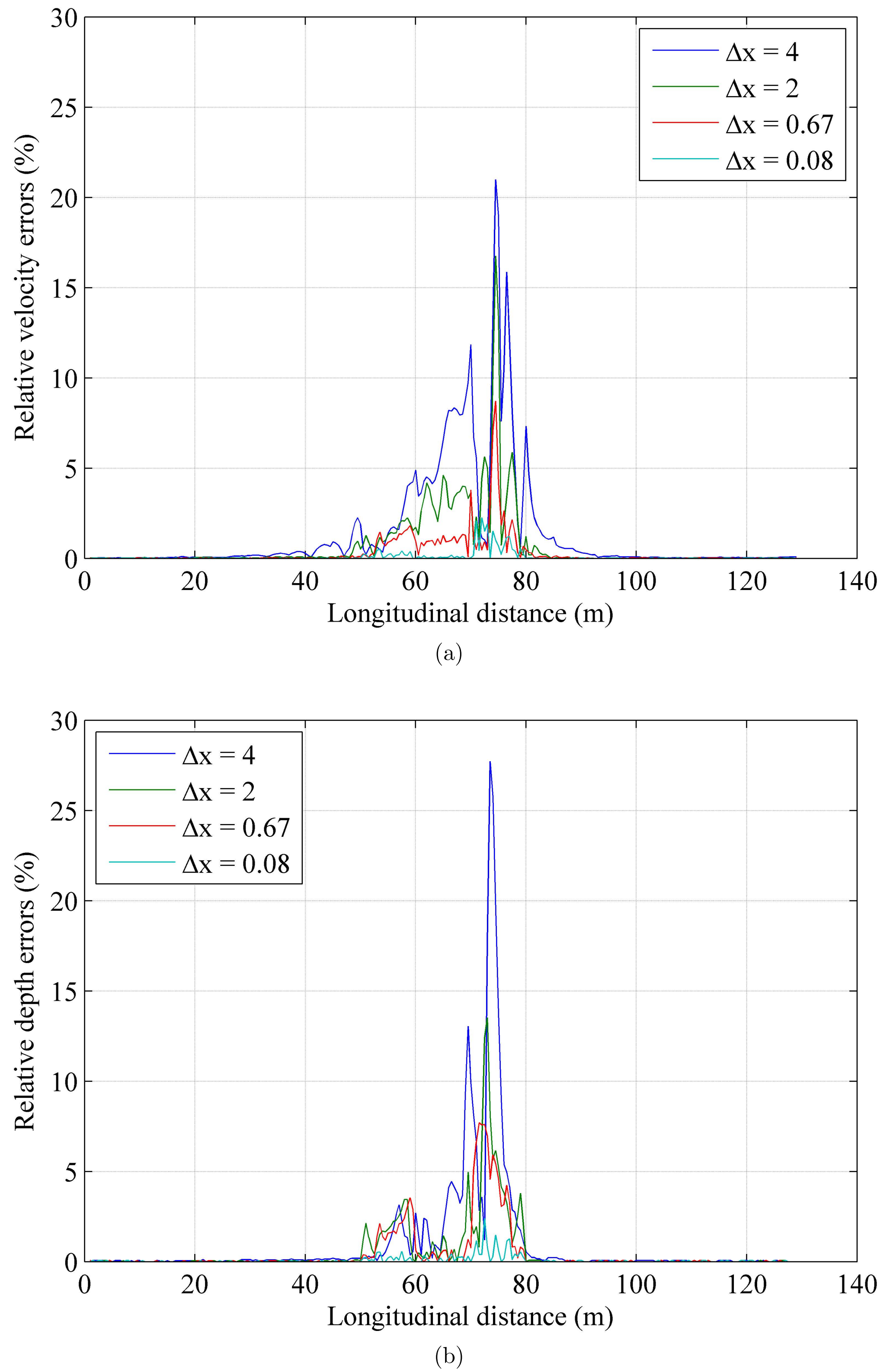

(a)

(b)

Figure 11.8: (a) Velocity and (b) Depth errors at $y = 40$ m for different uniform discretization meshes.

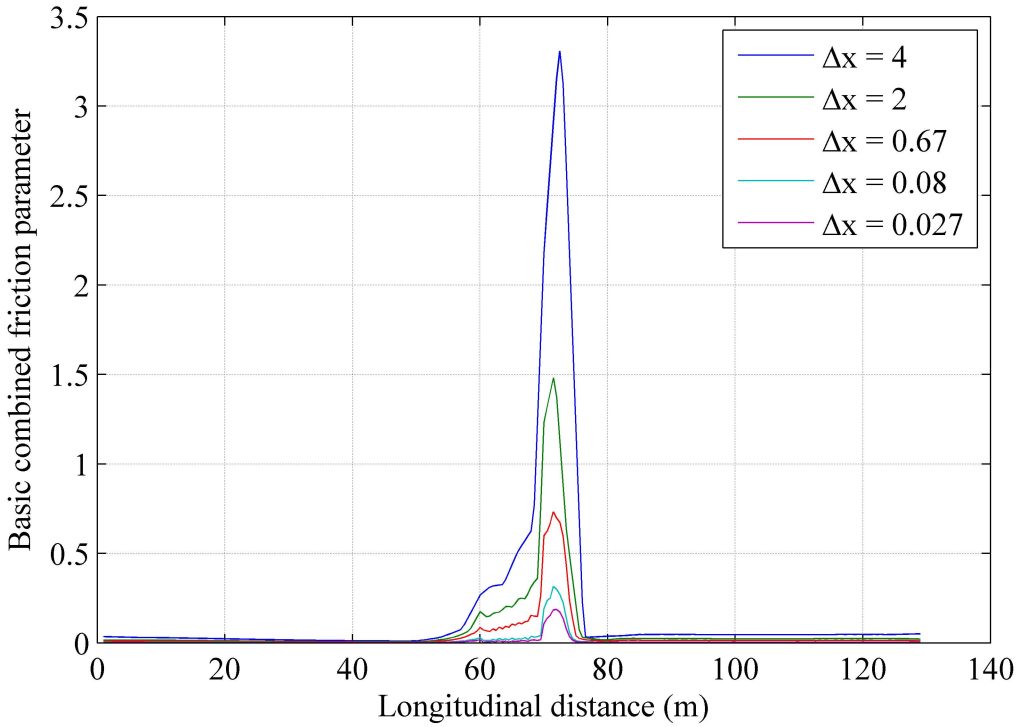

Figure 11.9: Combined friction parameters at $y = 40$ m for different uniform discretization meshes.

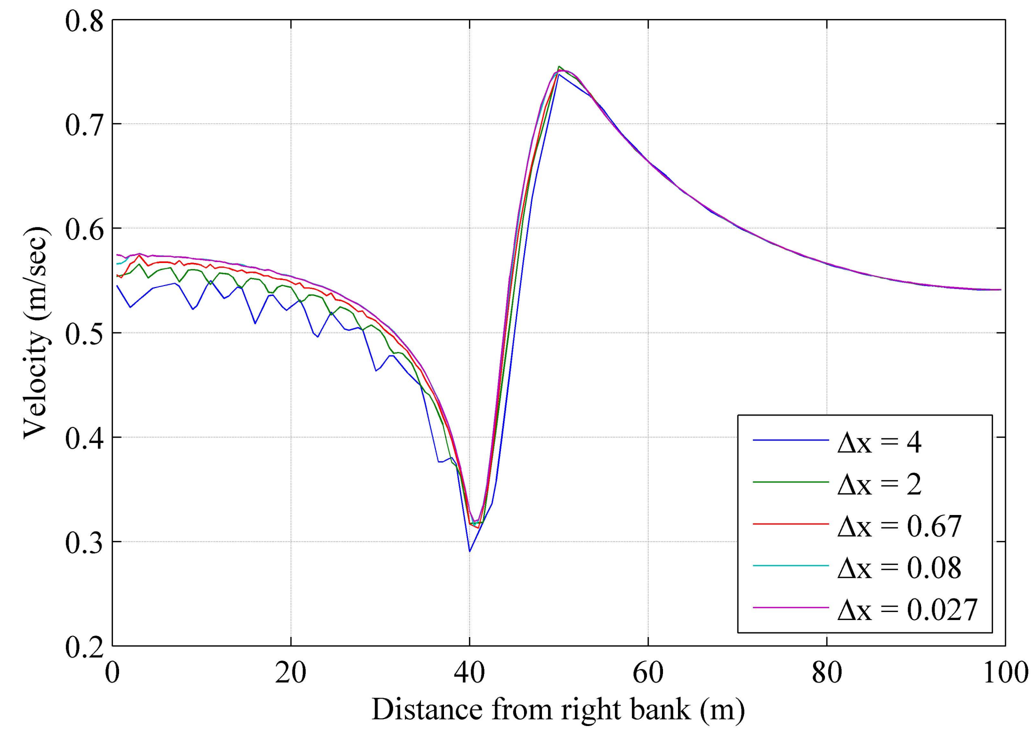

(a)

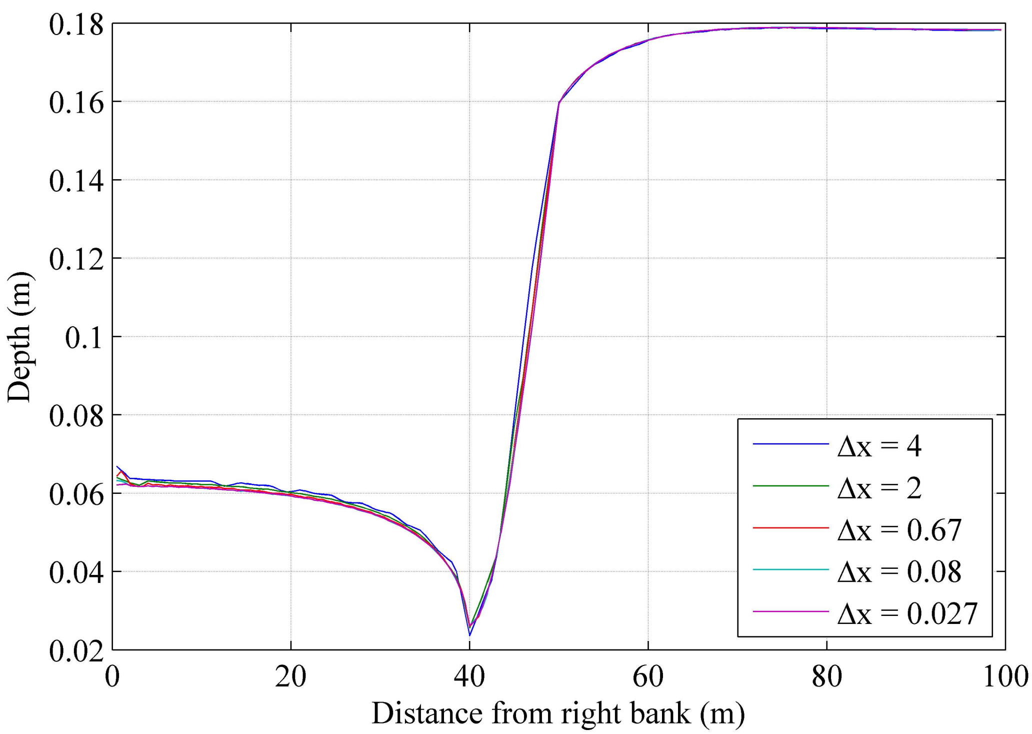

(b)

Figure 11.10: (a) Velocity and (b) Depth solutions at $x = 70$ m for different uniform discretization meshes.

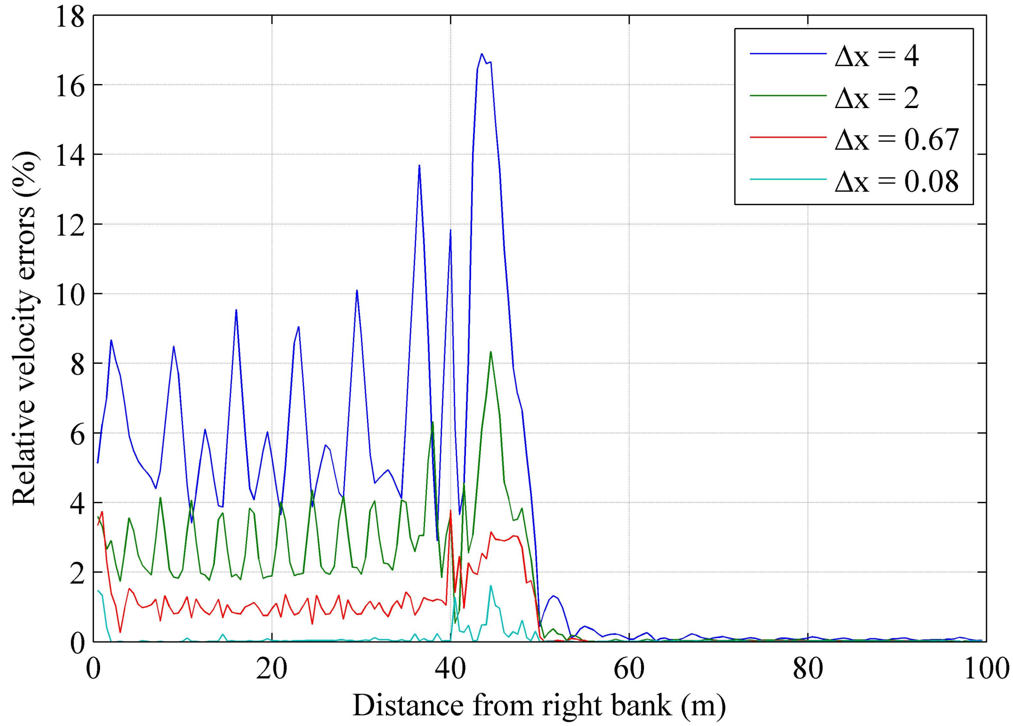

(a)

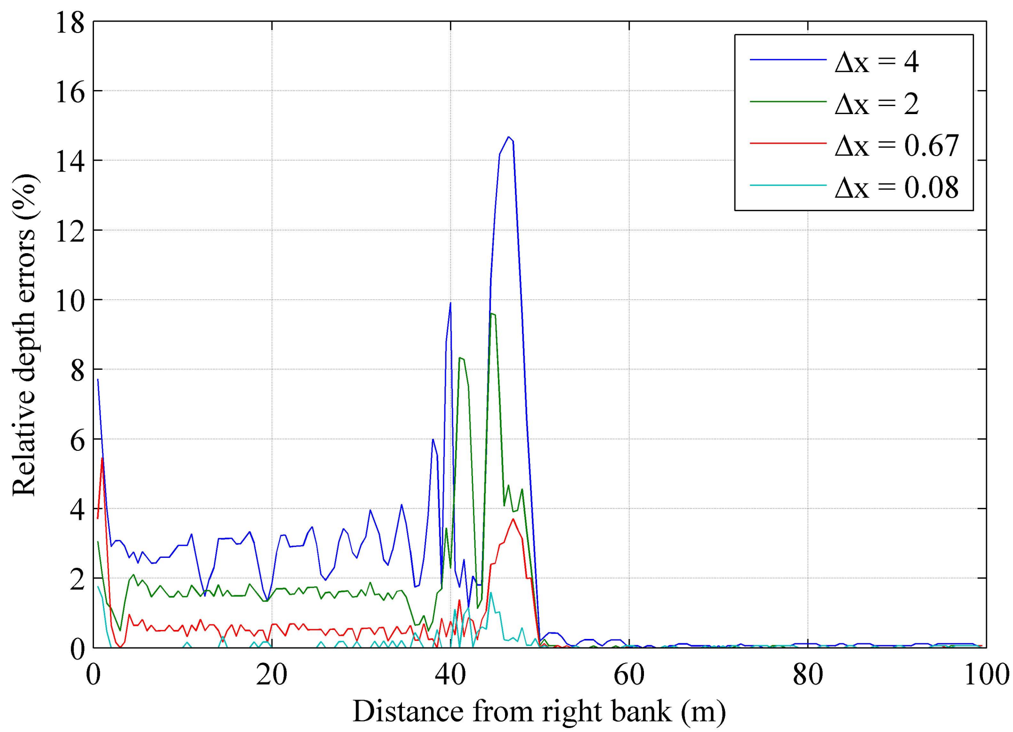

(b)

Figure 11.11: (a) Velocity and (b) Depth errors at $x = 70$ m for different uniform discretization meshes.

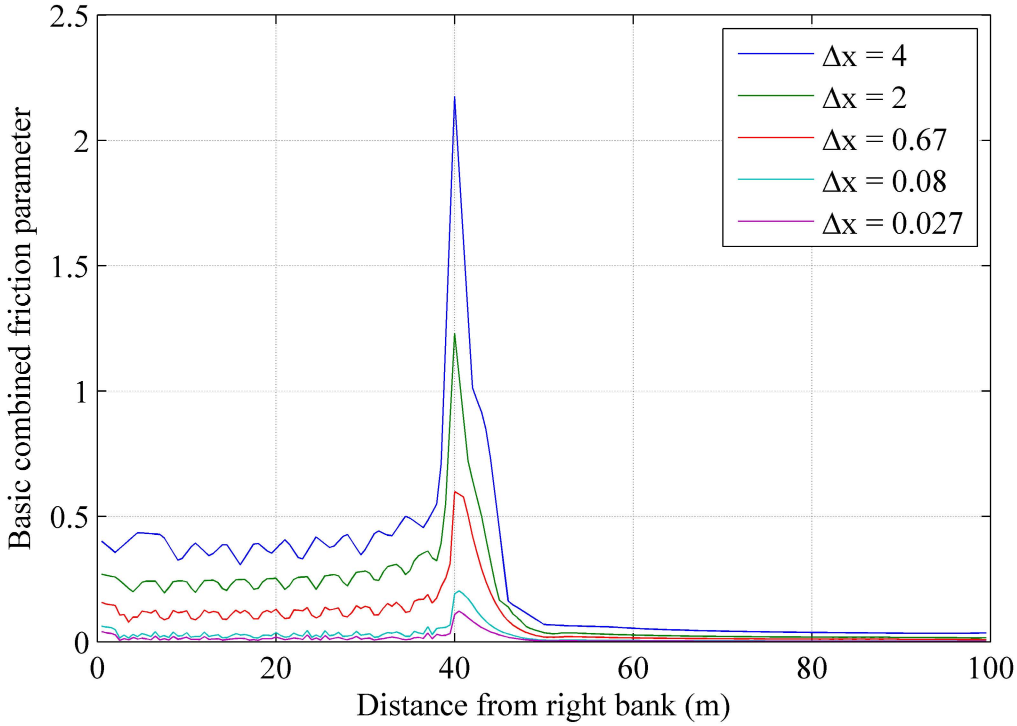

Figure 11.12: Combined friction parameters at $x = 70$ m for different uniform discretization meshes.

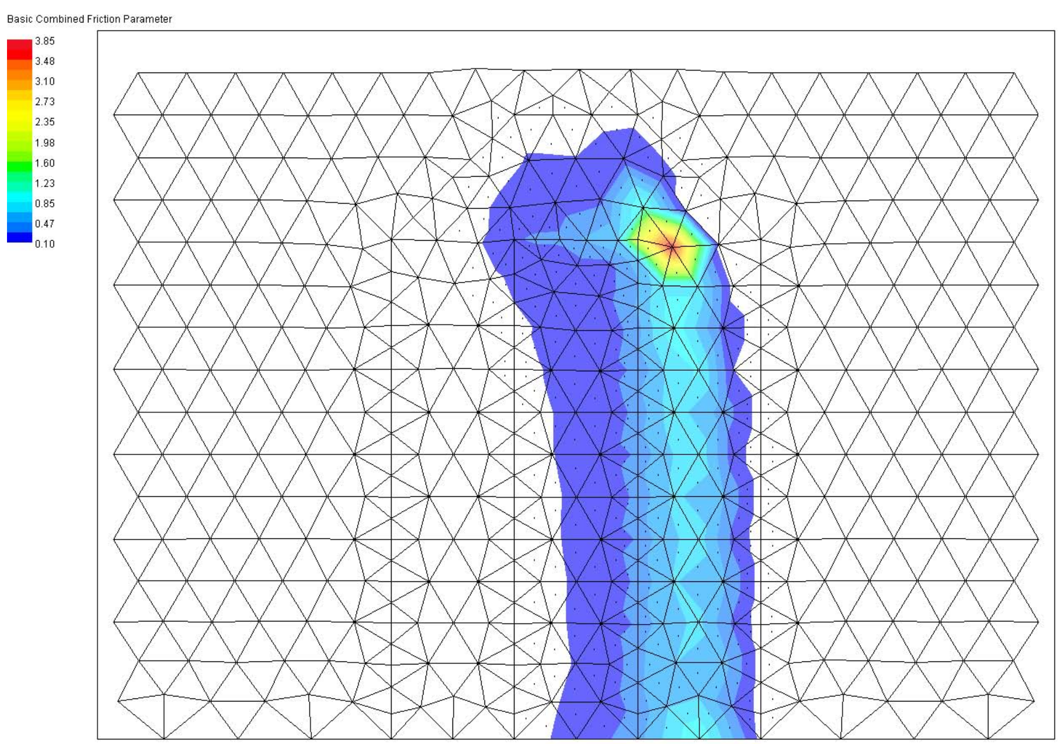

Figure 11.13: Placing of new nodes at the center of elements where friction parameter is greater than the allowable limit.

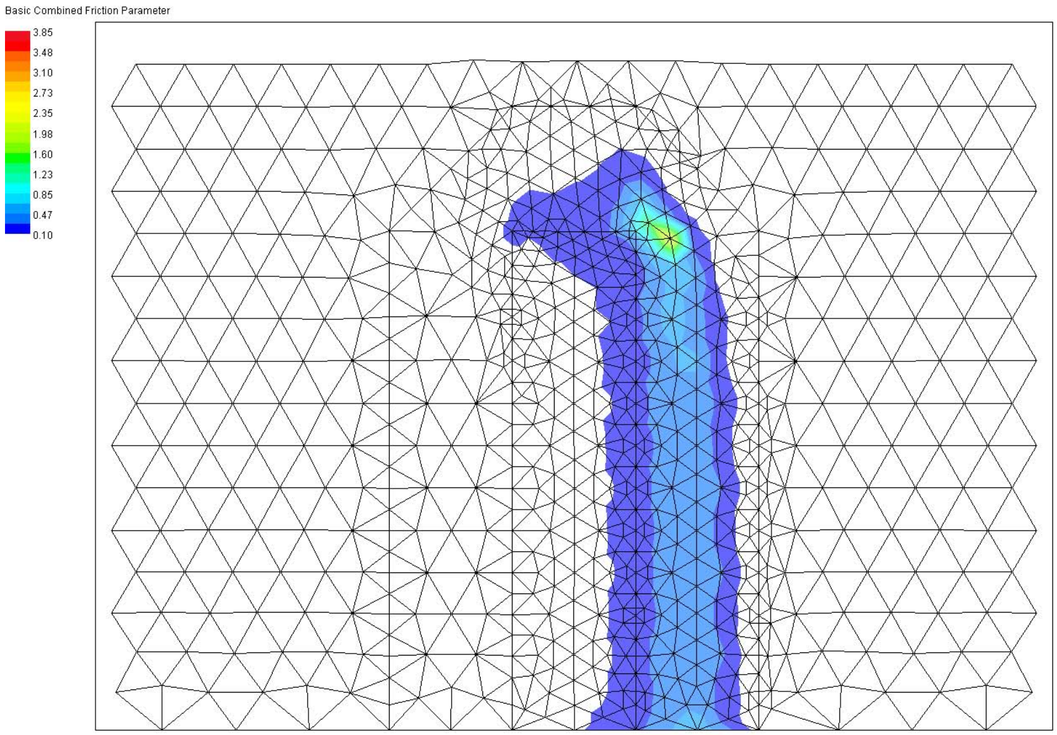

Figure 11.14: Re-triangulation of the mesh after placing new nodes.

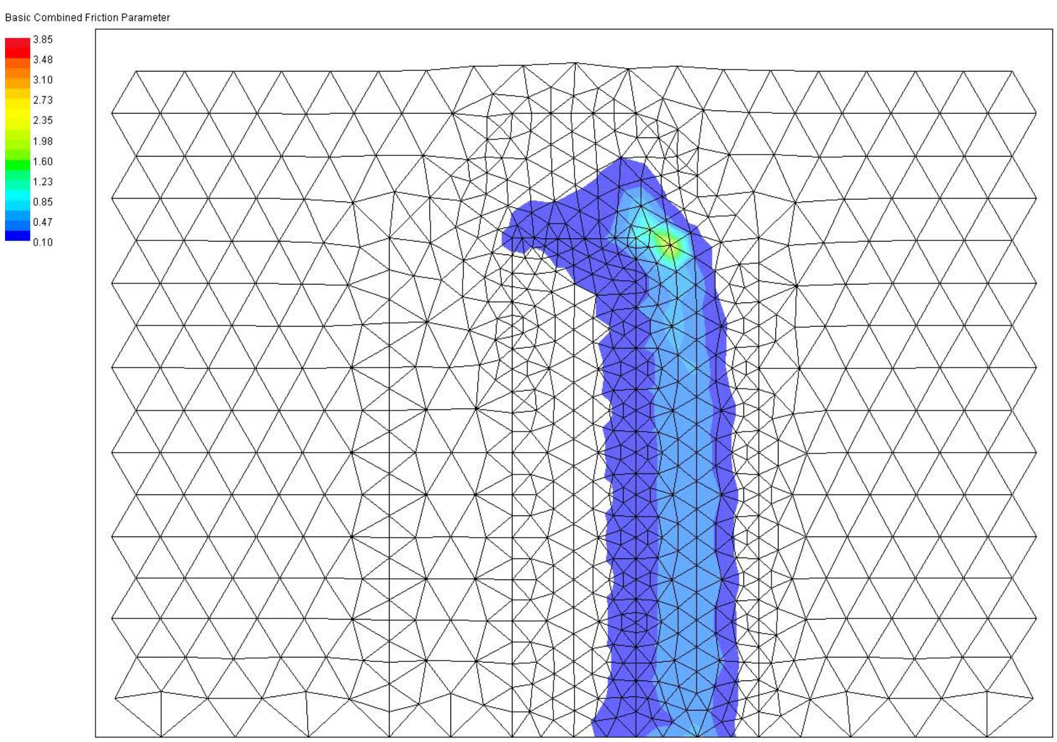

Figure 11.15: Refined mesh after four to six smoothing processes.

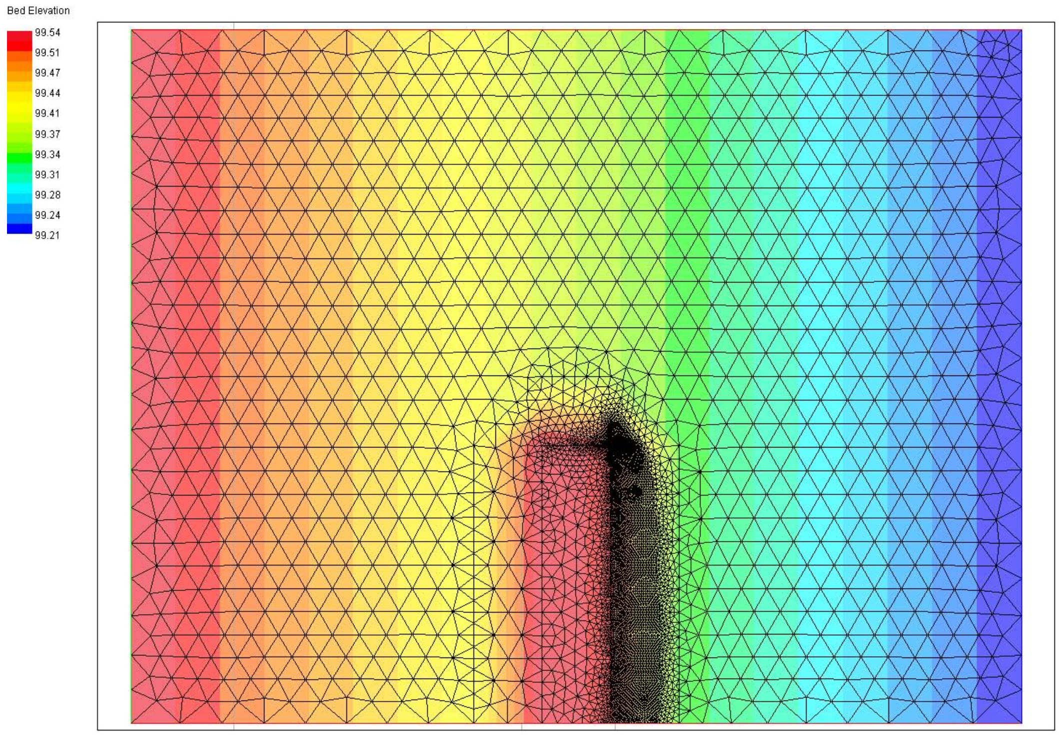

Figure 11.16: Final mesh refined with the basic combined friction parameter.

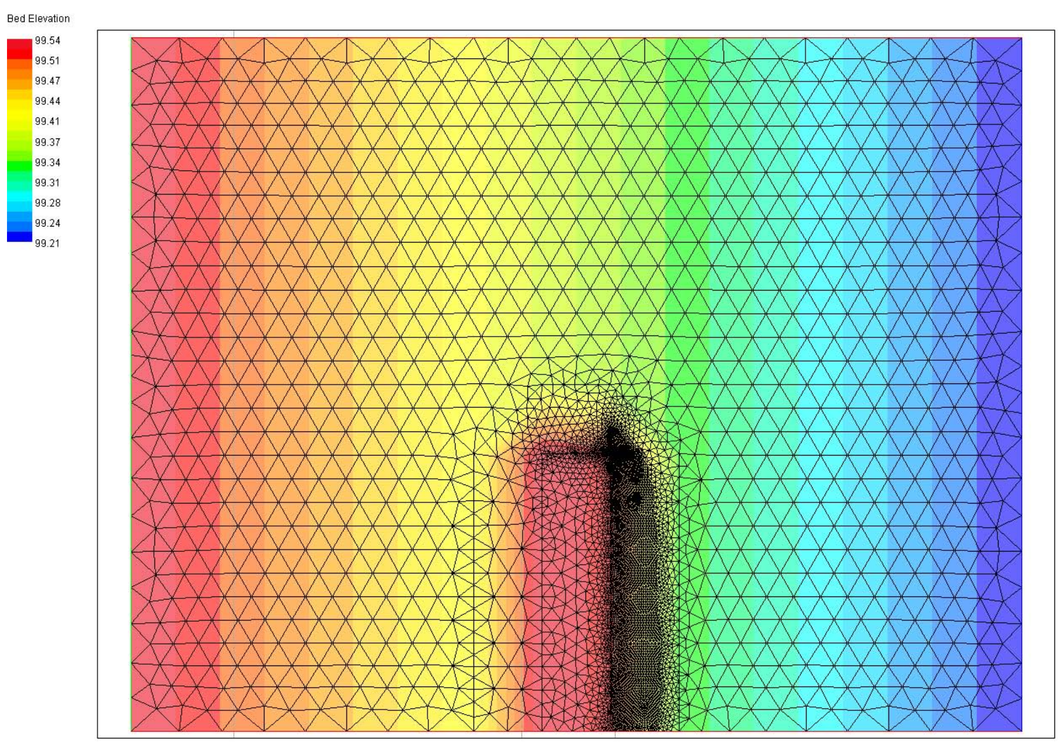

Figure 11.17: Final mesh refined with the friction parameter with friction slope.

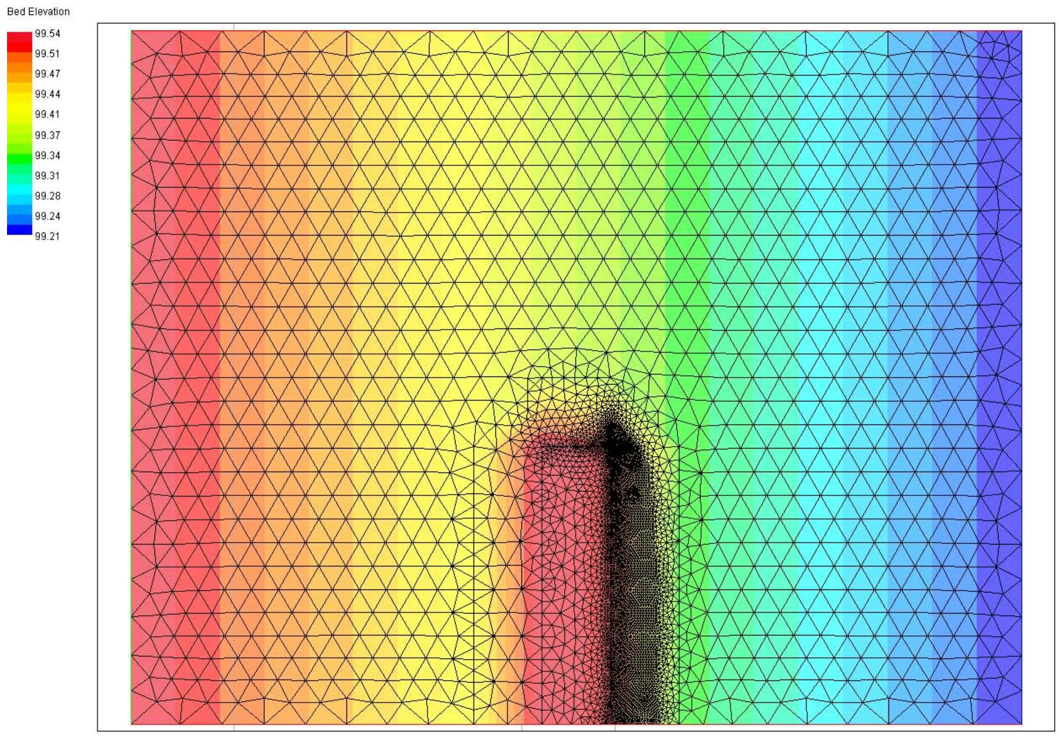

Figure 11.18: Final mesh refined with the friction parameter with water surface slope.

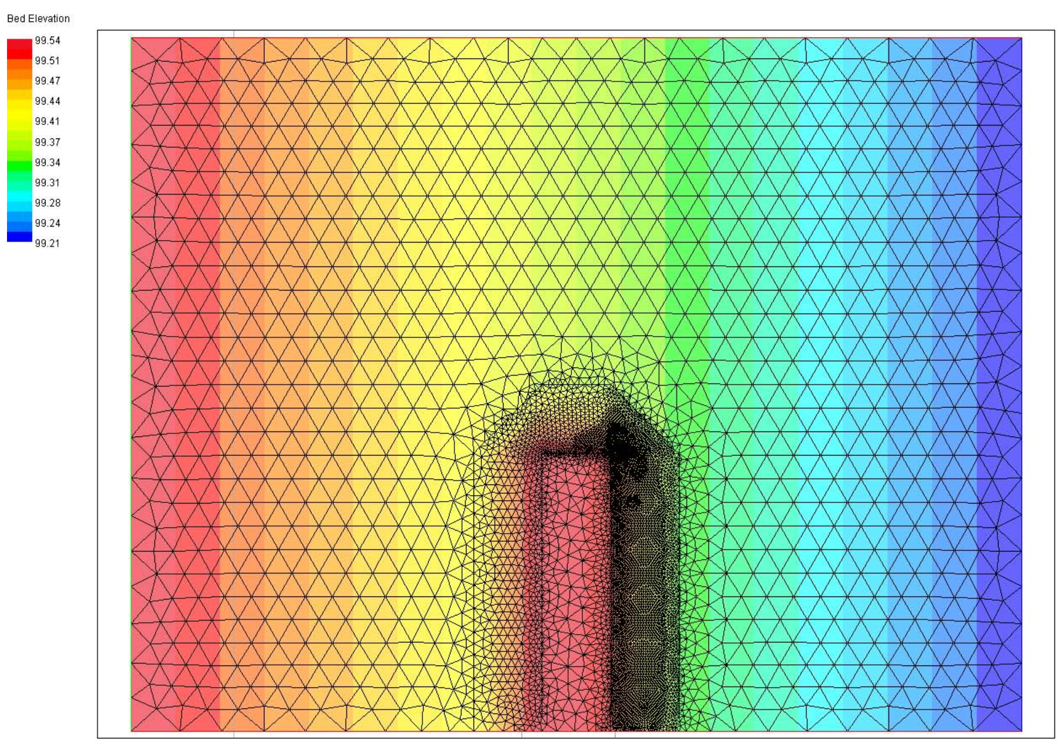

Figure 11.19: Final mesh refined with the friction parameter with bed slope.

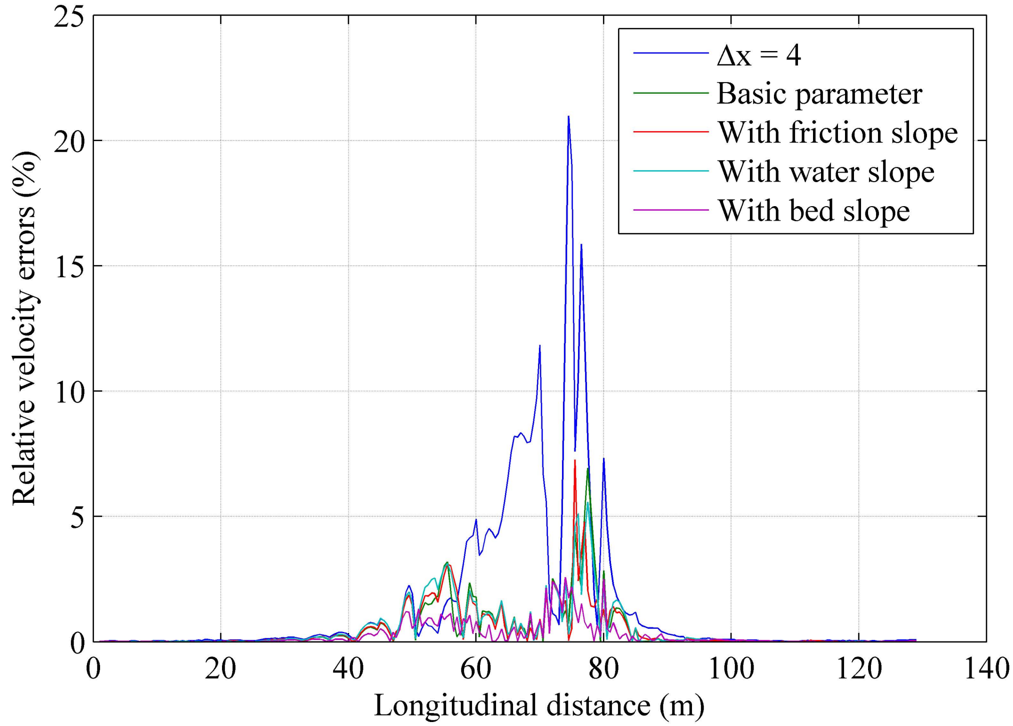

(a)

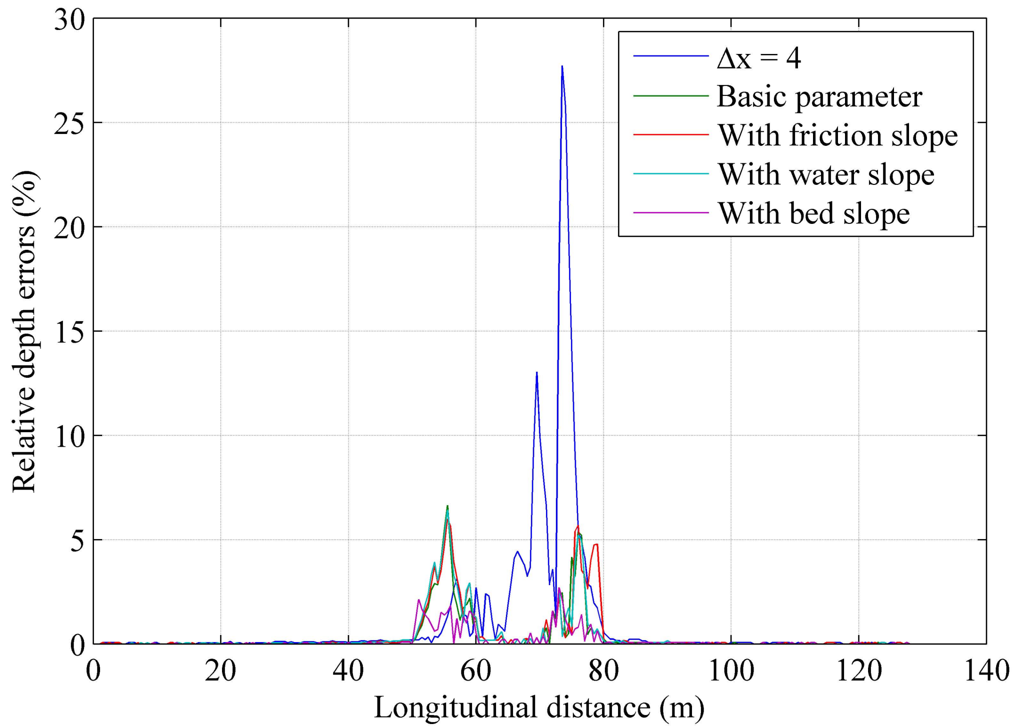

(b)

Figure 11.20: (a) Velocity and (b) Depth errors at $y = 40$ m for refined meshes.

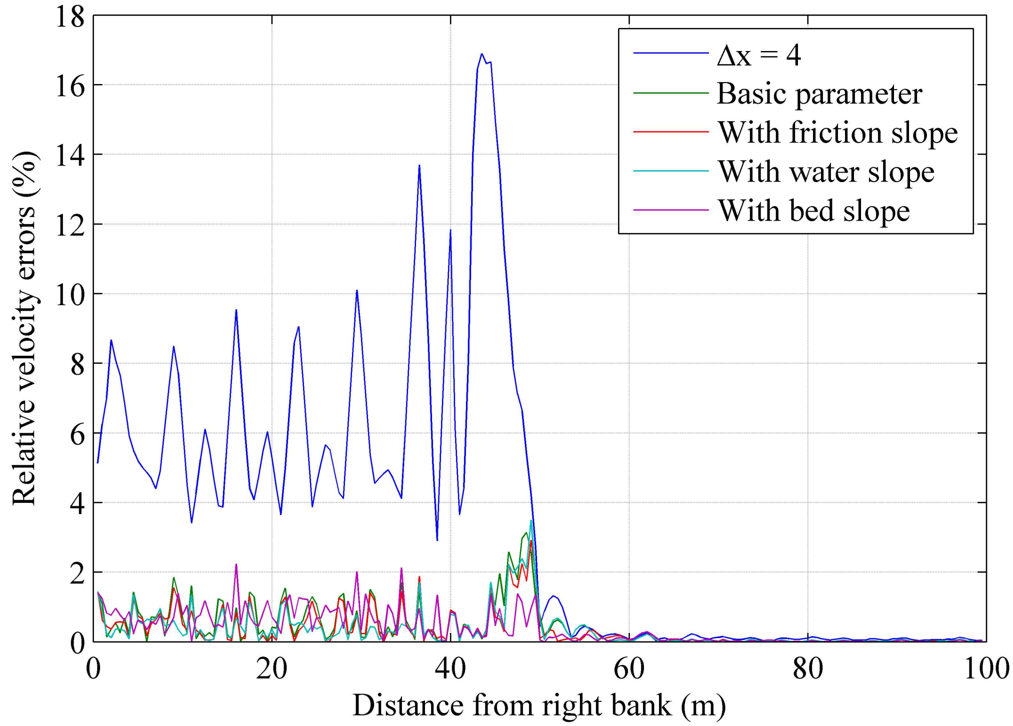

(a)

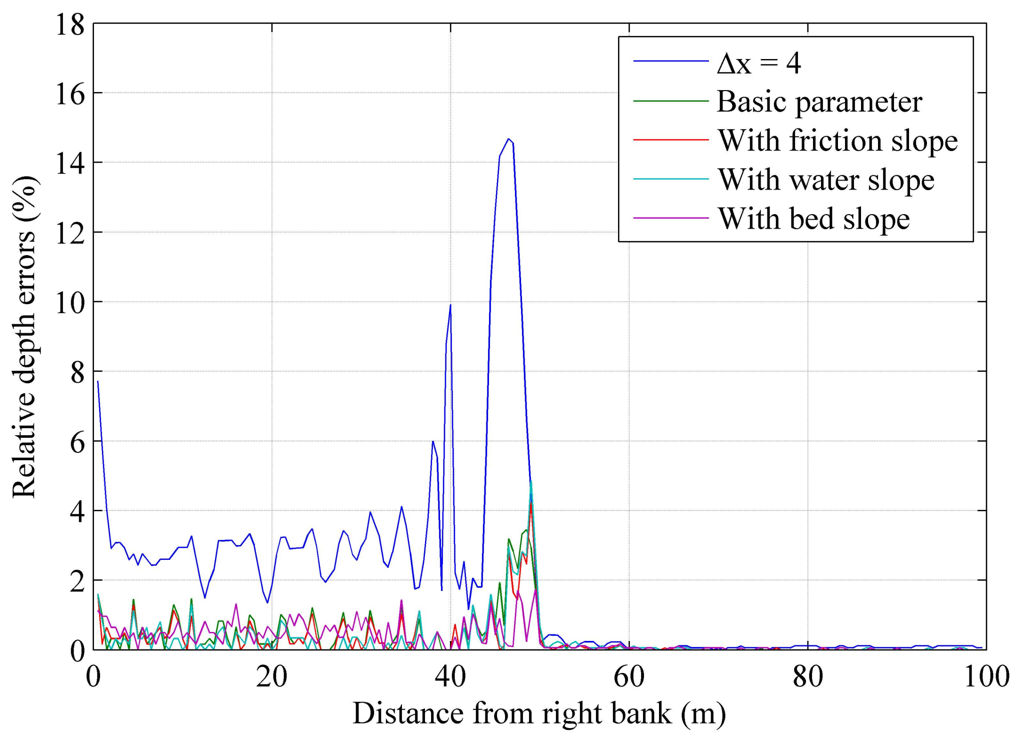

(b)

Figure 11.21: (a) Velocity and (b) Depth errors at $x = 70$ m for refined meshes.

Figure 11.22: South Platte River study area (red line) and velocity measurement area (yellow segment)[1].

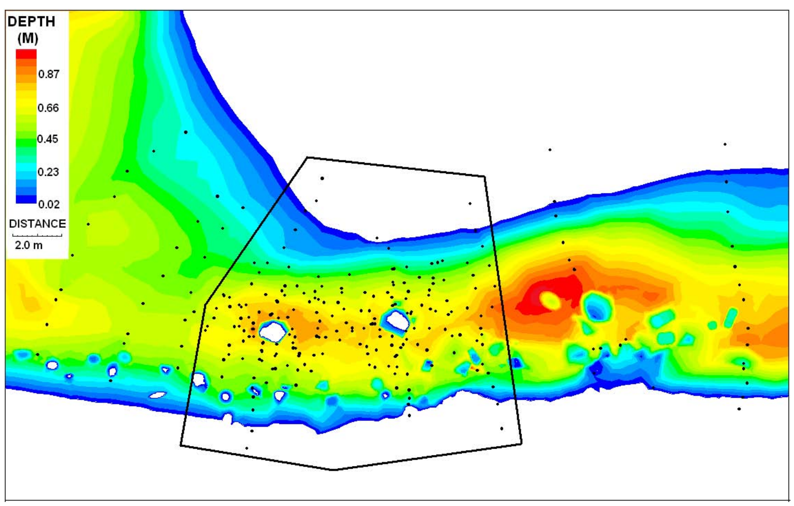

Figure 11.23: Velocity and depth measurement points near two main large boulders[1].

[1]Theses two figures have been collected from personal communication with the author of the Waddle (2009) paper and published in this research for the purpose of review under the s.29 Fair Dealing provision in the Canadian *Copyright Act*.

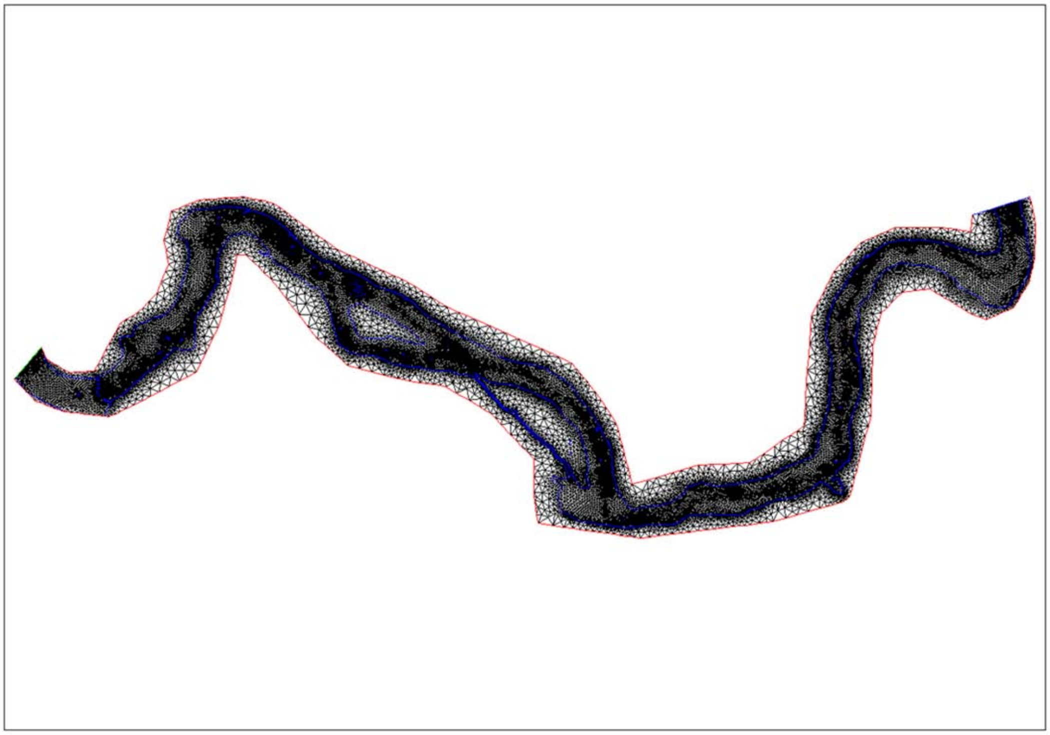

Figure 11.24: Mesh from the Waddle (2009) model.

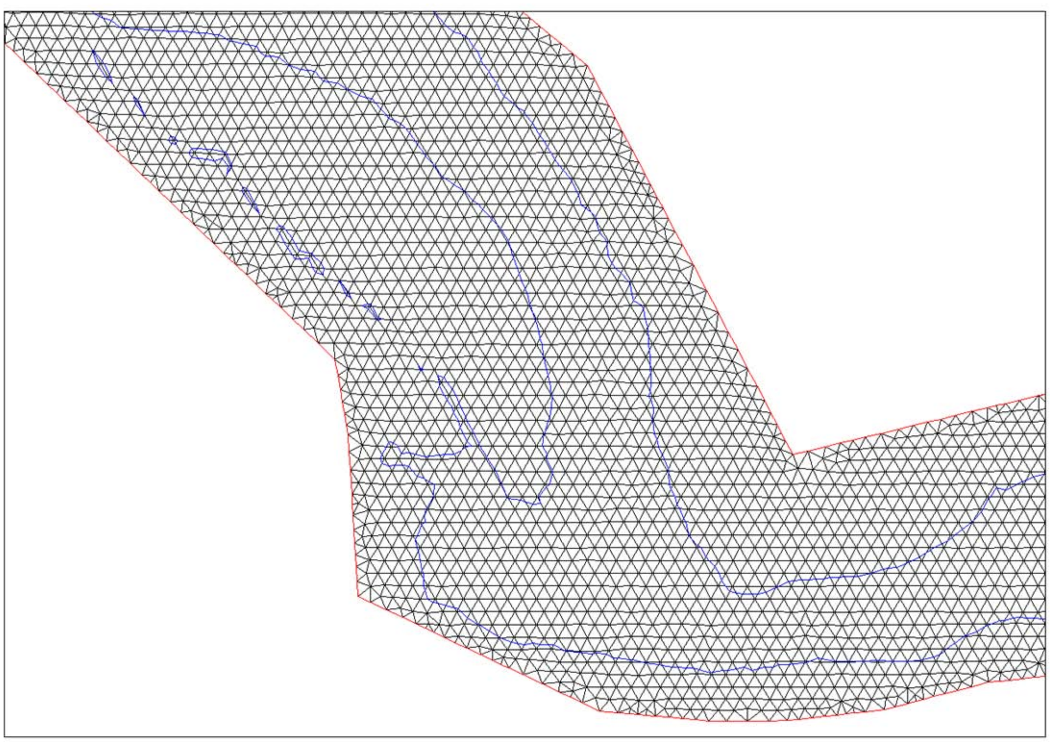

Figure 11.25: *Mesh1* (Uniform discretization mesh).

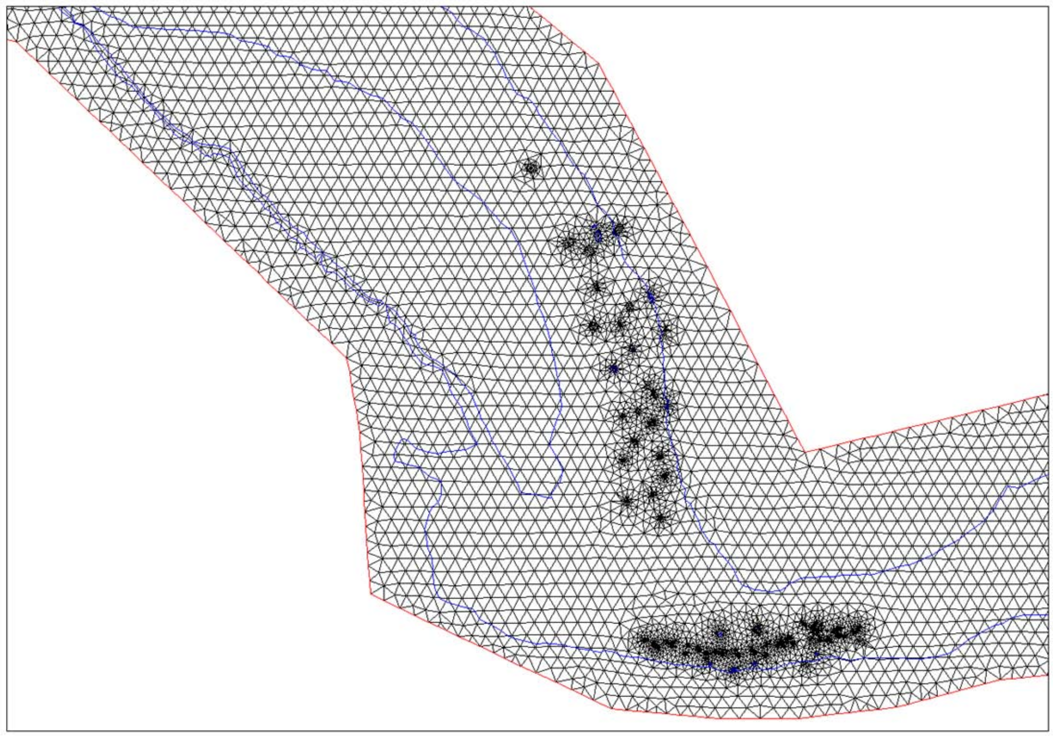

Figure 11.26: *Mesh2* (Mesh with boulders).

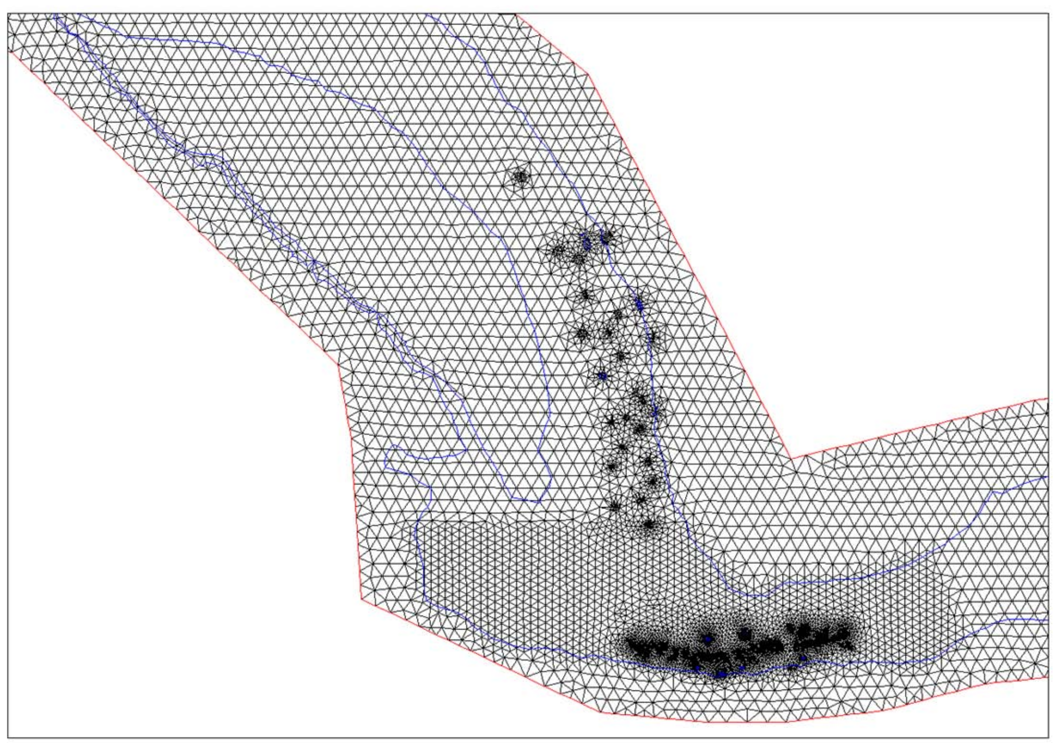

Figure 11.27: *Mesh3* (First level of regional refinement).

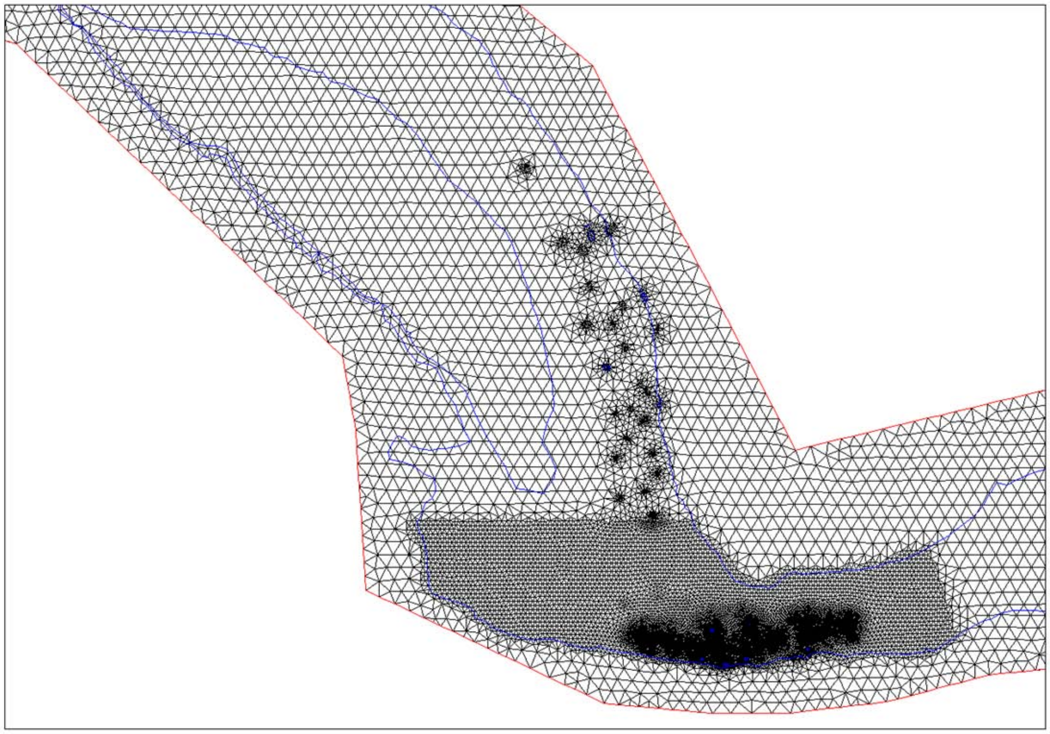

Figure 11.28: *Mesh4* (Second level of regional refinement).

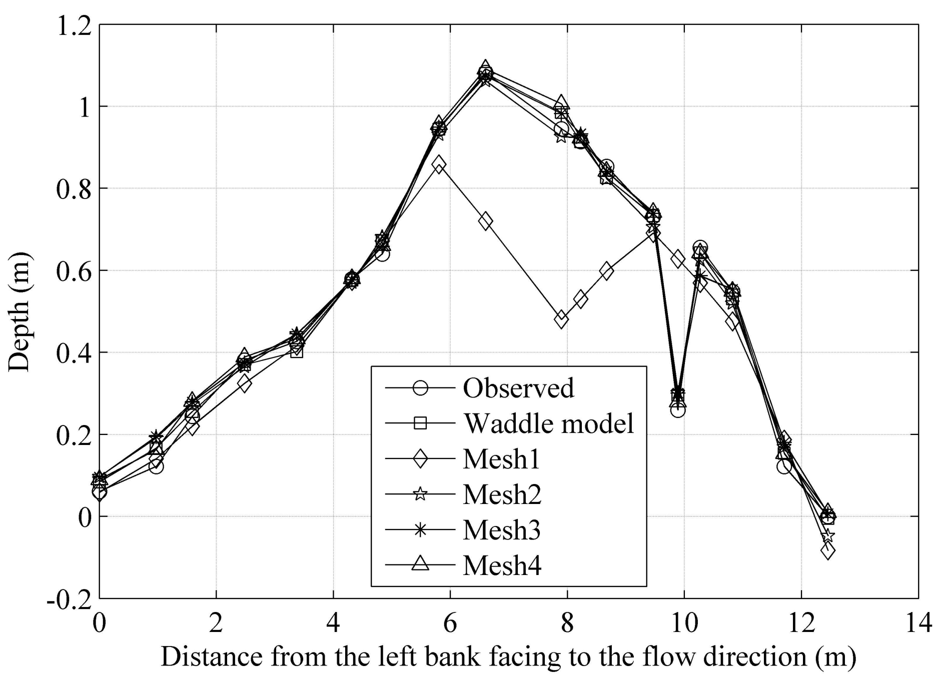

Figure 11.29: Depth solutions at first cross-section for different meshes.

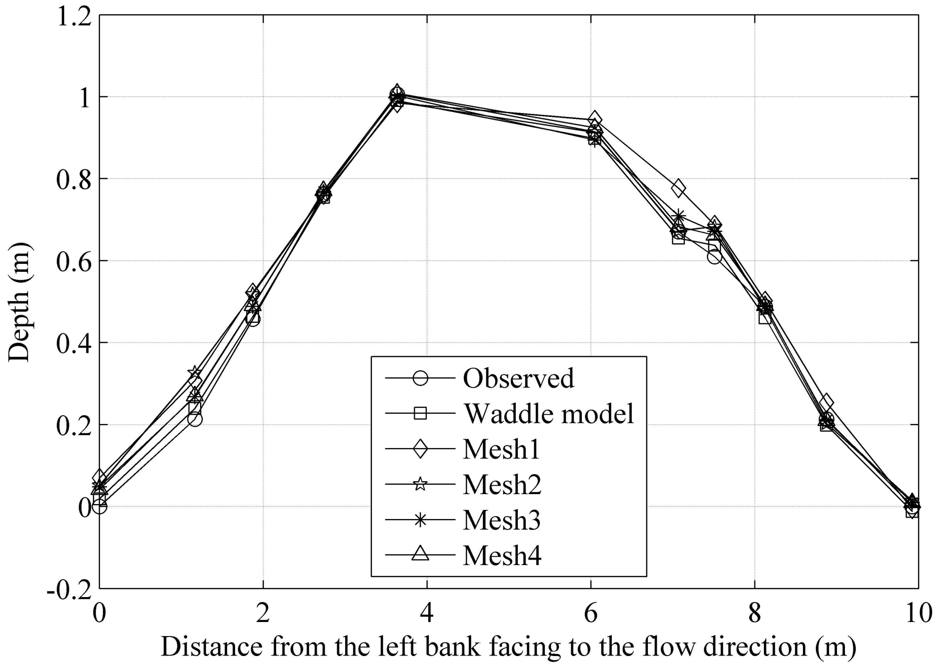

Figure 11.30: Depth solutions at second cross-section for different meshes.

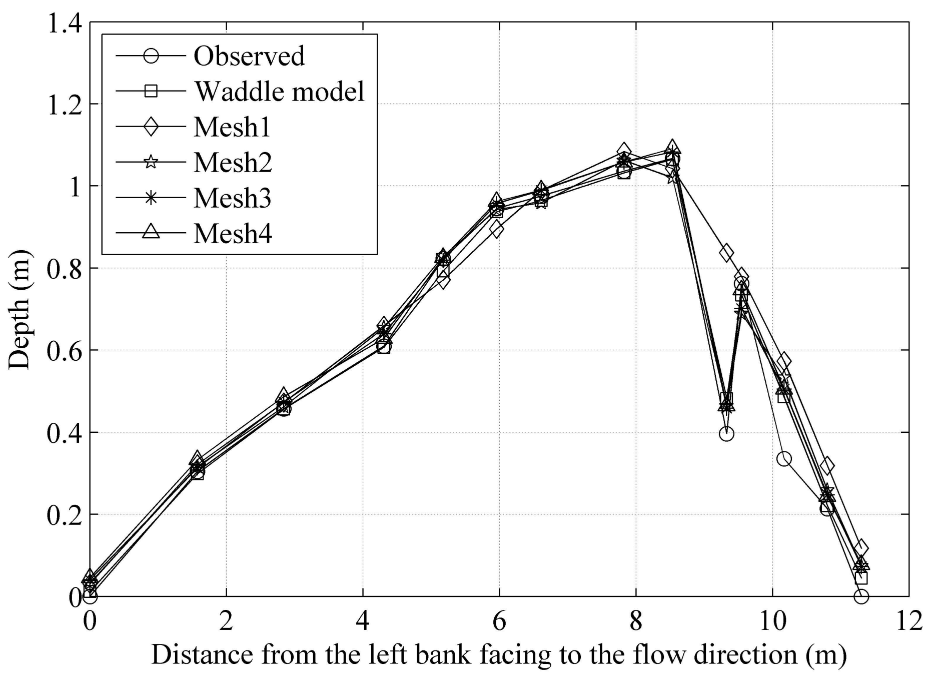

Figure 11.31: Depth solutions at third cross-section for different meshes.

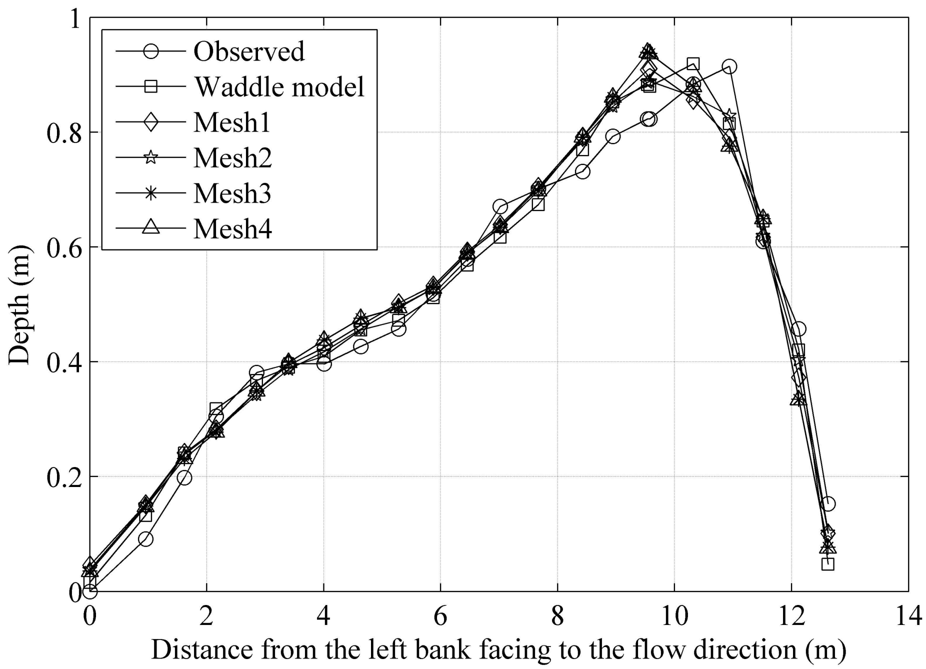

Figure 11.32: Depth solutions at fourth cross-section for different meshes.

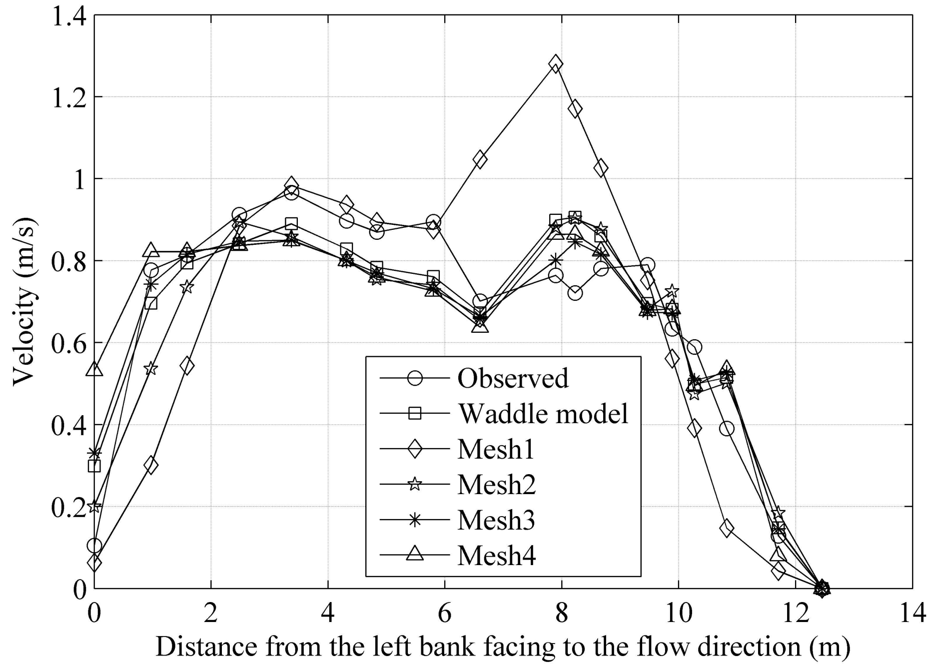

Figure 11.33: Velocity solutions at first cross-section for different meshes.

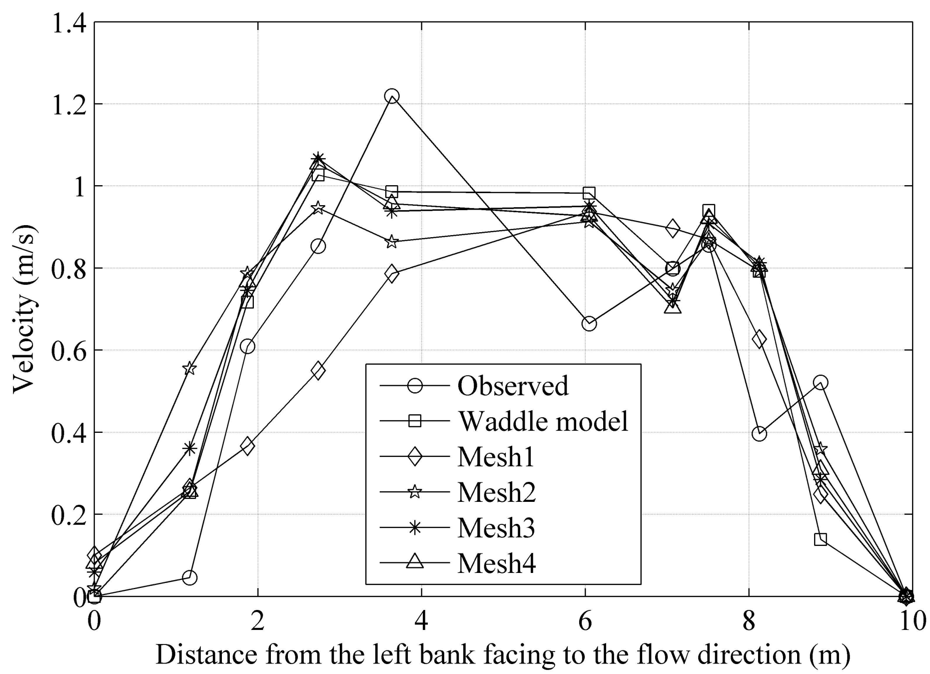

Figure 11.34: Velocity solutions at second cross-section for different meshes.

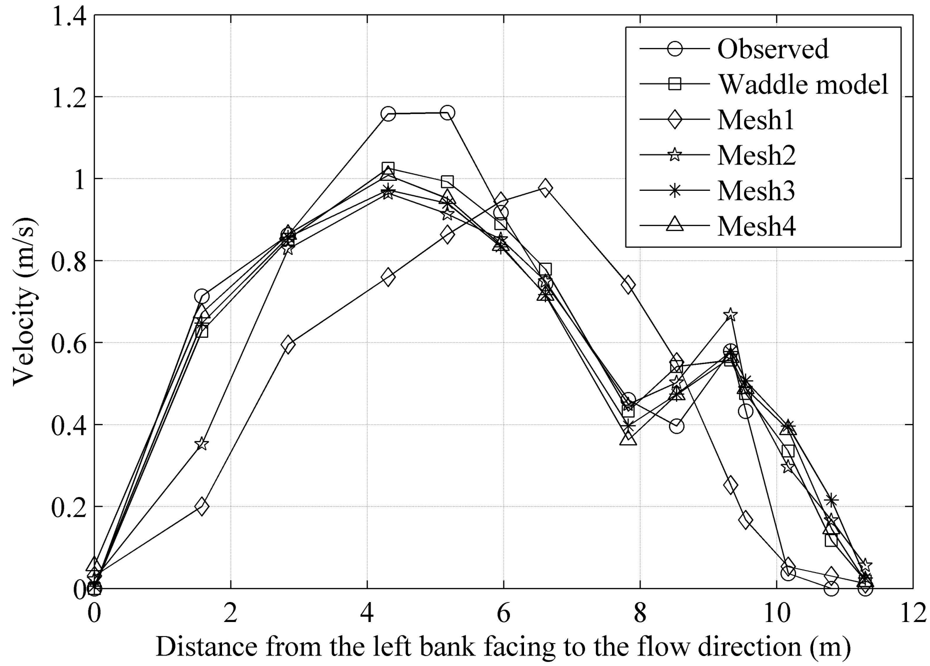

Figure 11.35: Velocity solutions at third cross-section for different meshes.

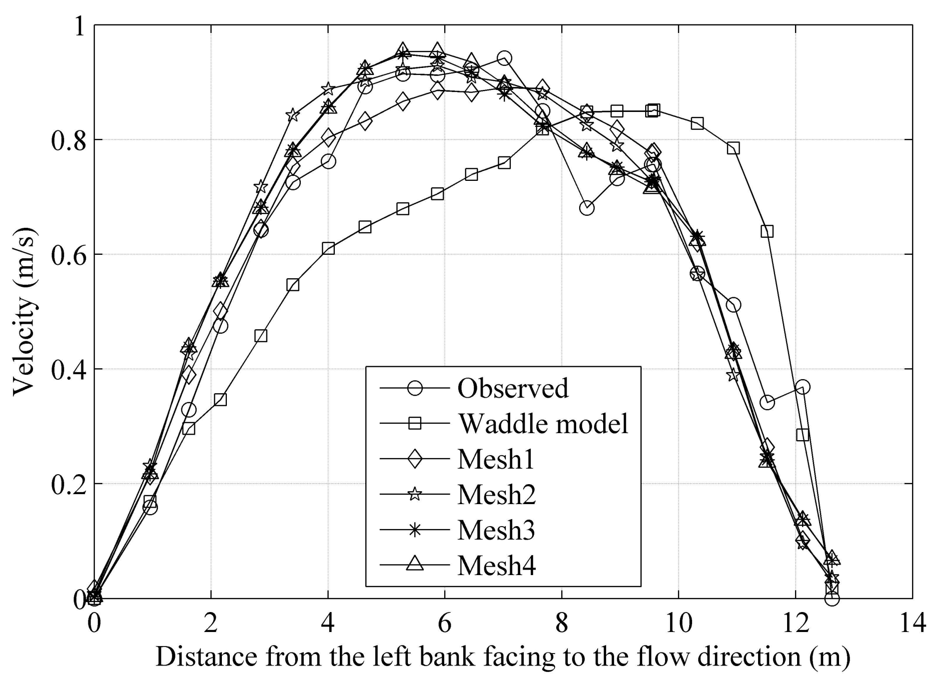

Figure 11.36: Velocity solutions at fourth cross-section for different meshes.

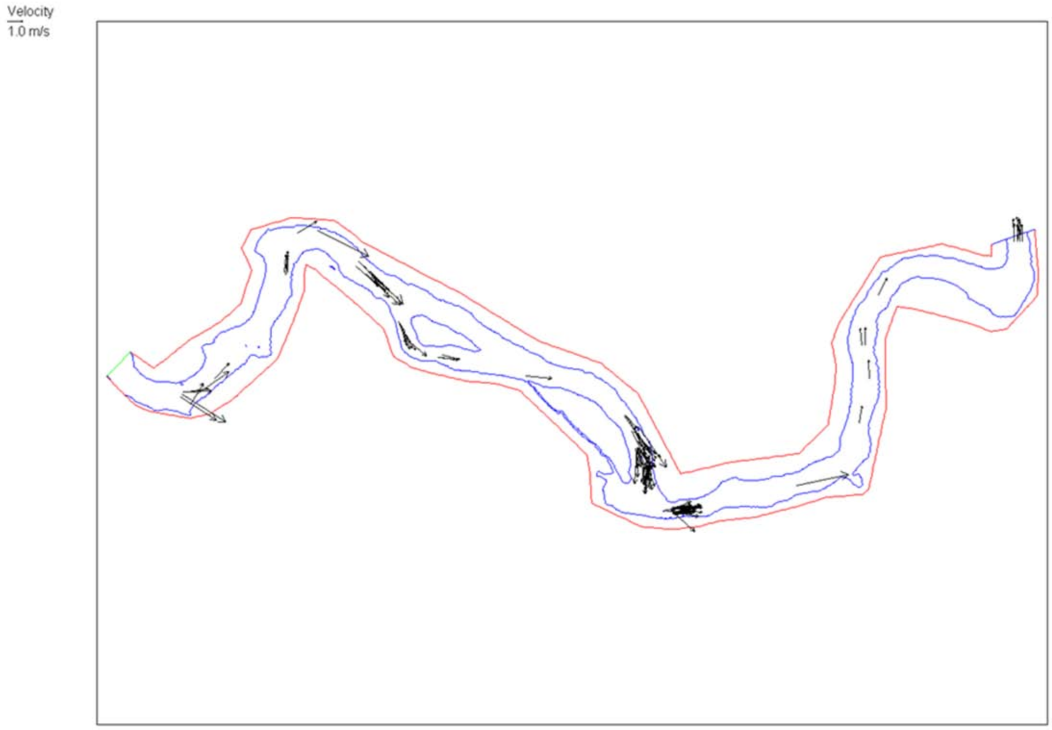

Figure 11.37: Plot of velocity vectors which are greater than twice the average velocity from the *Mesh2* solution.

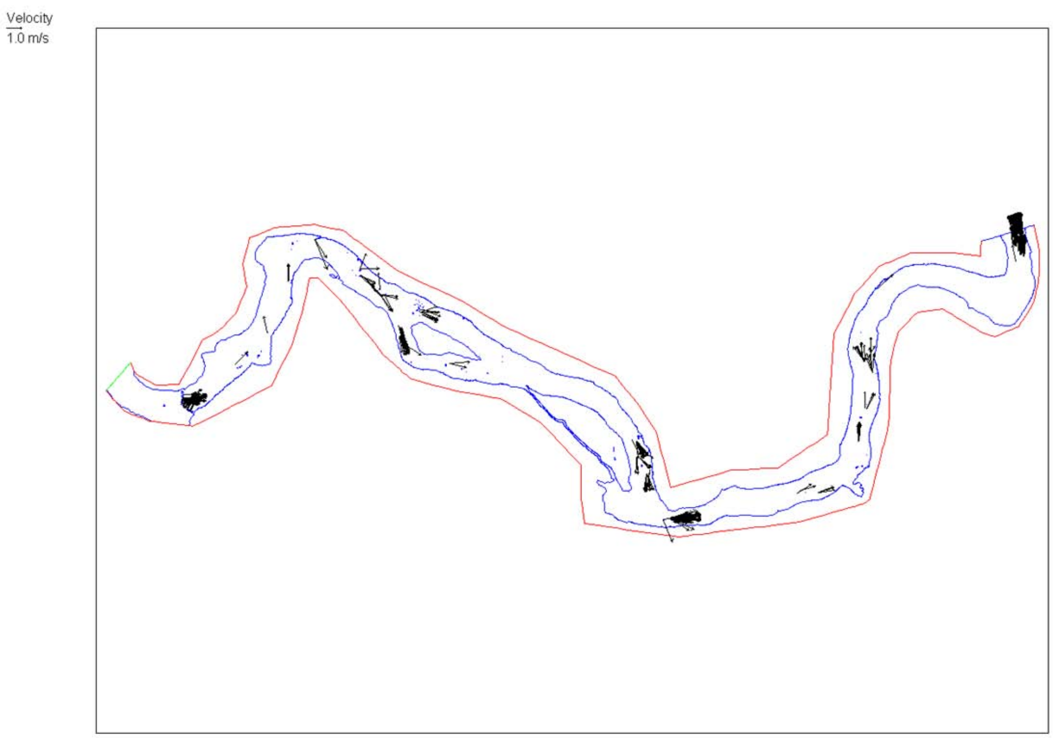

Figure 11.38: Plot of velocity vectors which are greater than twice the average velocity from the Waddle (2009) model.

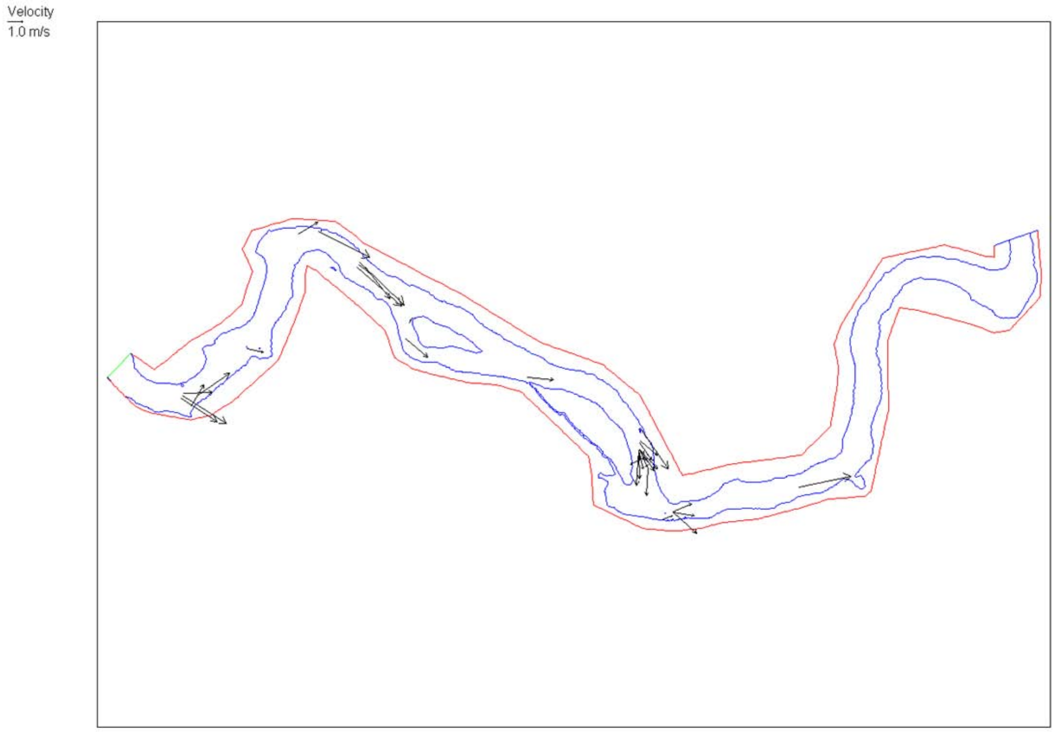

Figure 11.39: Velocity vectors plot from the *Mesh2* solution where the combined friction parameters are greater than 0.5.

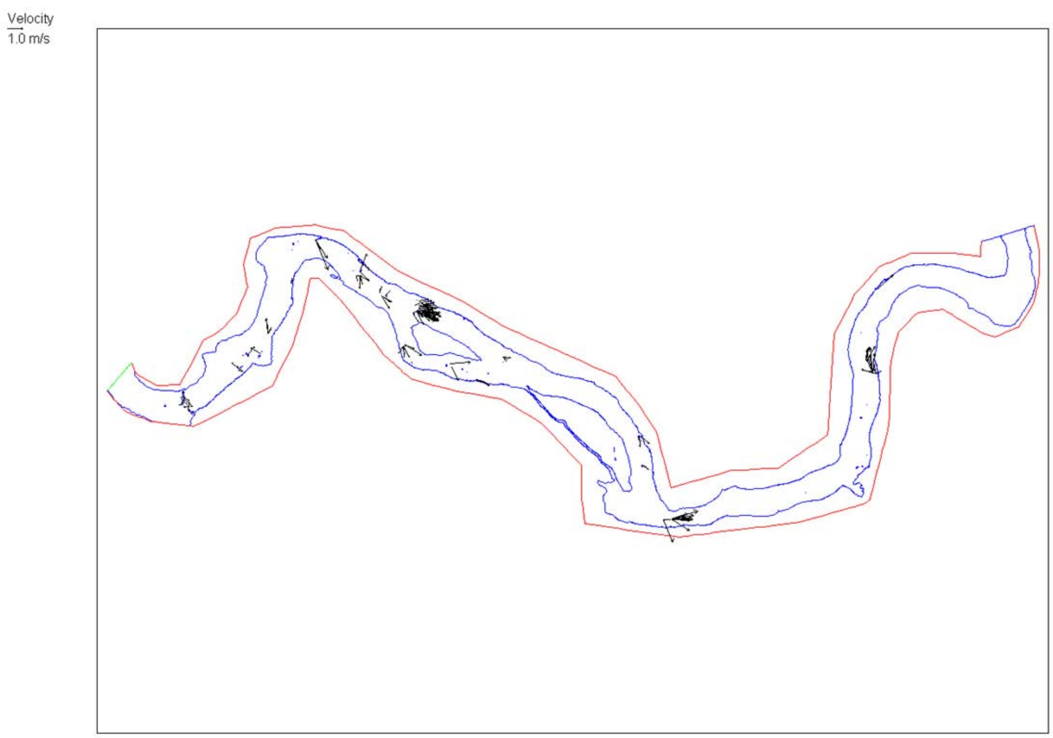

Figure 11.40: Velocity vectors plot from the Waddle (2009) model where the combined friction parameters are greater than 0.5.

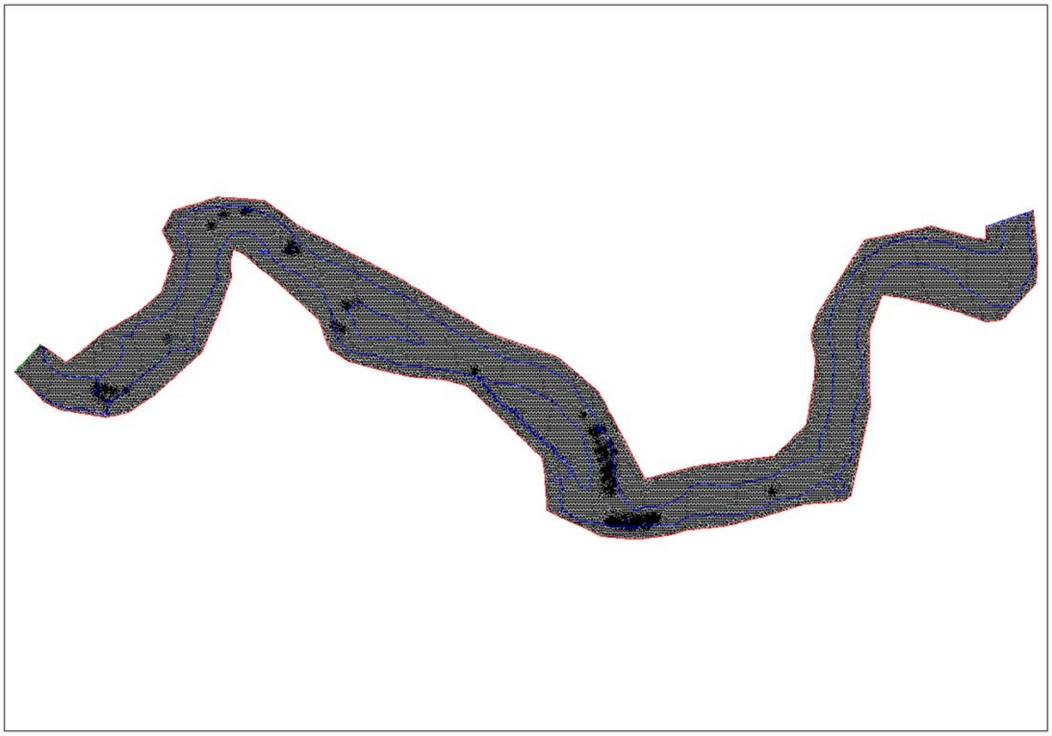

Figure 11.41: Final mesh after four levels of local refinement using the basic combined friction parameter.

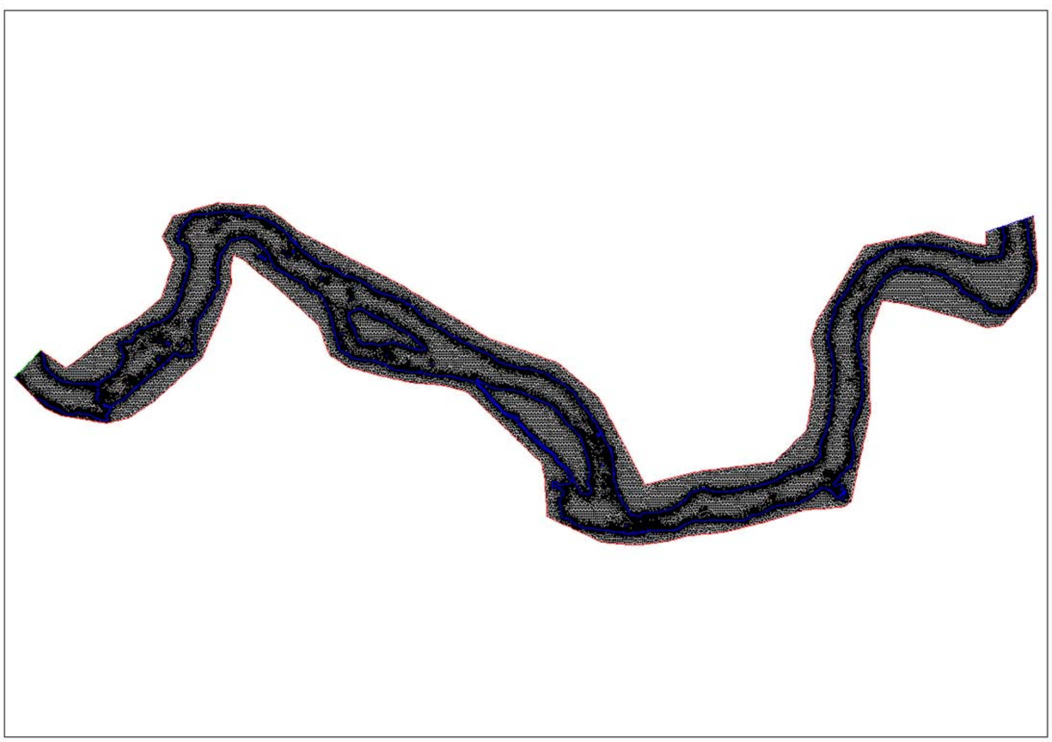

Figure 11.42: Final mesh after four levels of local refinement using the friction parameter with local bed slope.

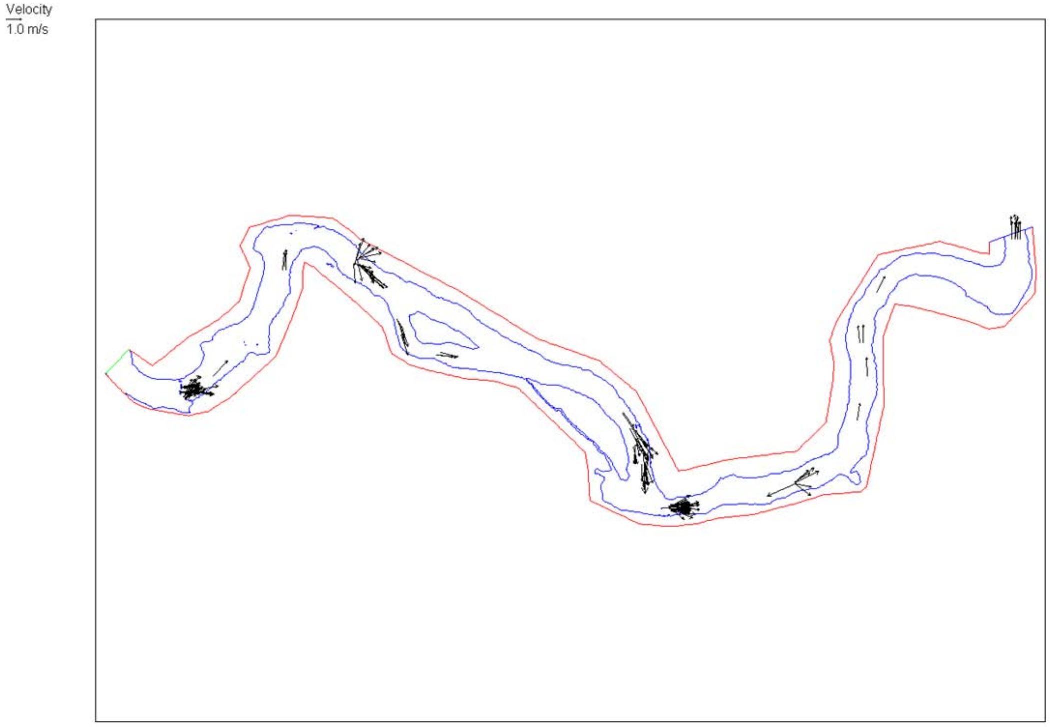

Figure 11.43: Plot of velocity vectors which are greater than twice the average velocity from the refined mesh using the basic combined friction parameter.

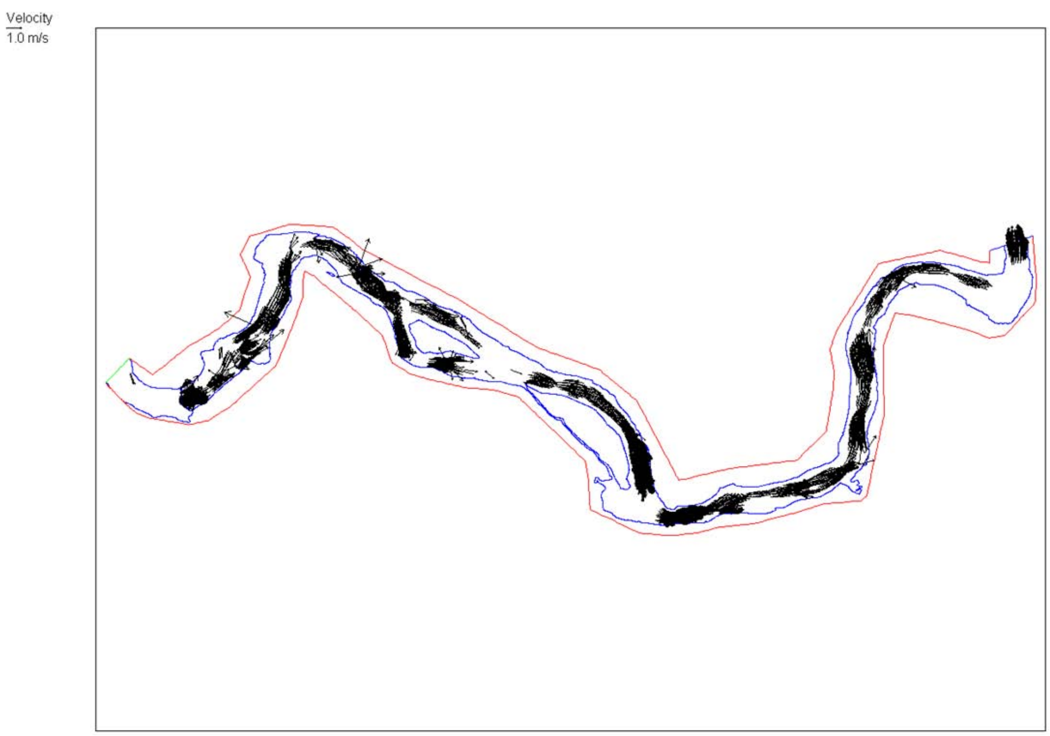

Figure 11.44: Plot of velocity vectors which are greater than twice the average velocity from the refined mesh using the friction parameter with local bed slope.

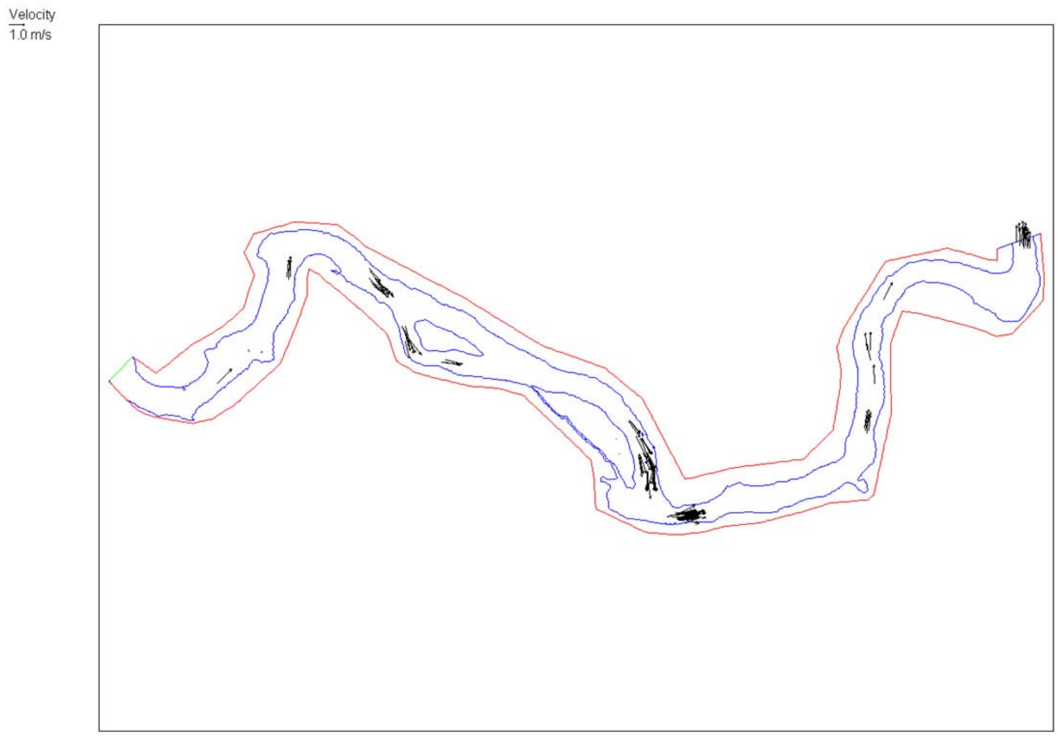

Figure 11.45: Plot of velocity vectors which are greater than twice the average velocity after using the ground water model where the combined friction parameters are greater than 0.5.

Chapter 12

Conclusions and Recommendations

This research undertakes the highly understudied issue of the friction dominated case in open channel flow. Very few studies have been done for this issue and none have been done using the full form of the Saint-Venant equations. There is no analysis framework from which to study friction dominated Saint-Venant equations. This significant gap in Computational Hydraulics led us to formulate an analysis framework using a non-uniform flow test case and a Fourier analysis.

In the non-uniform test case a sudden bed elevation change is introduced and a steady state solution is solved for the test case using the Saint-Venant equations. In the Fourier analysis a periodic bed elevation perturbation is introduced and the effect of the bed elevation perturbation on the solution variables is observed by solving the steady state solution using the linearized form of the Saint-Venant equations. To the best of our knowledge, use of the Fourier analysis to study the steady state solution of the Saint-Venant equations, which includes the bed slope and the friction terms, has never been attempted.

Six different numerical schemes comprised of two schemes for each numerical methods (FDM, FEM, and FVM) are studied for the friction dominated case using the analysis framework. The non-uniform flow test case results show that errors and/or oscillations in the discharge and/or depth solutions are observed when the discretization, roughness, and slope are large, and the errors increase when these parameters increase.

The Fourier analysis results show that for the sub-critical flow, errors in the discharge and/or depth solutions are observed whenever there is any perturbation in the bed elevation. The results also show that these errors are highly dependent on the numerical Friction number, $\beta_{\Delta x}$, and the average Froude number, Fr_0, and increase with increasing $\beta_{\Delta x}$ and Fr_0. The errors can be an order of 1 or greater depending on the value of these two non-dimensional parameters. Moreover, for any value of Froude number, the errors can be negligible if $\beta_{\Delta x}$ is less than 0.01.

The results with all six different numerical schemes show that errors and oscillations in the steady state discharge solution exist only for the non-balanced shock-capturing schemes, such as the CDG and MacCormack schemes. However, errors in the steady state depth solution exist for all schemes, and except in the one-sided upwind-downwind scheme, where the depth errors are diffusive, the depth errors are all oscillatory and appear as $2\Delta x$ wavelength. The downwinding of the pressure term or the depth gradient term in the case of the one-sided upwind-downwind scheme produces sufficient negative diffusion to suppress any wiggles because of the friction term dominance.

As the errors increase with both increasing Fr_0 and $\beta_{\Delta x}$, a combined friction parameter, $\beta_{\Delta x} Fr_0^2$, is intended for practical purposes to capture the effect of the separate parameters. The proposed combined friction parameter captures the variation of the errors for moderate to high Froude numbers, i.e., 0.3 to 0.8 (sub-critical flow) for the CDG scheme. This combined friction parameter can be interpreted as the number of elements over a backwater curve and can also be thought of as analogous to the grid Peclet number. Similar to the advection dominated case, when the combined friction parameters are high, we will have a friction dominated case, and non-physical oscillations in the solution may occur in the vicinity of abrupt changes in bed topography.

The proposed combined friction parameter can be used as a measure of error and an indicator of error. Moreover, the proposed combined friction parameter is easy to calculate and implement in any open channel flow model. In this study, we have investigated the applicability of the proposed combined friction parameter with a 1D flow test case (flow over a hump) and with two 2D flow test cases (flow past a submerged groin and flow in a natural river). All the test cases show that the proposed combined friction parameter is an effective indicator for the error-prone areas. The proposed combined friction parameter has also been used as a mesh refinement indicator and to calculate the minimum depths to switch to a ground water model. The results show that applying mesh refinement or the ground water model using the combined friction parameter is successful at eliminating/reducing spurious high velocity vectors from the solution.

Besides the aforementioned two approaches, a third approach, and perhaps the most desirable approach, is to use a numerical scheme that will not produce numerical oscillations for the friction dominated case. The diffusive behavior of the one-sided upwind-downwind scheme in 1D Saint-Venant equations shows that this scheme can be a suitable numerical scheme for the friction dominated case. However, an appropriate downwinding method for the 2D Saint-Venant equations requires further study, which has not been done in this thesis because of time limitations.

Furthermore, other numerical schemes that have not been studied in this research, but used in Computational Hydraulics, can also be investigated for the friction dominated case. The analysis framework presented in this thesis can be used for that purpose. A non-oscillatory numerical scheme for the friction dominated case helps the open channel model become more robust, accurate, and generally applicable.

Bibliography

Abott, M. B. (1979). *Computational Hyadraulics: Elements of the Theory of Free Surface Flows*. Pitman Publishing Ltd., London.

Abott, M. B. and A. Verwey (1970). Four-point method of characteristics. *J. of Hydraulic Division* **96**(12), 2549–2564.

Alcrudo, F. and P. Garcia-Navarro (1992). Flux difference splitting for 1D open channel flow equations. *Int. J. for Numerical Methods in Fluids* **14**, 1009–1018.

ANSYS (2009a). *ANSYS FLUENT 12.0 Getting Started Guide*. ANSYS, Inc., USA.

ANSYS (2009b). *ANSYS CFX Introduction*. ANSYS, Inc., USA.

Baker, A. J. (1973). Finite element solution algorithm for viscous incompressible fluid dynamics. *Int. J. for Numerical Methods in Engineering* **6**, 89–101.

Baker, A. J. (1983). *Finite Element Computational Fluid Mechanics*. Hemisphere Publishing Corp., New York.

Barbara, P. D. (2006a). *Users Guide to RMA2 WES Version 4.6*. US Waterways Experiment Station, Coastal and Hydraulics Laboratory (CHL), USA.

Barbara, P. D. (2006b). *Users Guide to SED2D WES Version 4.6*. US Waterways Experiment Station, Coastal and Hydraulics Laboratory (CHL), USA.

Barbara, P. D. (2008). *Users Guide to RMA4 WES Version 4.5*. US Waterways Experiment Station, Coastal and Hydraulics Laboratory (CHL), USA.

Bates, P. D., Aderson M. G. Hervouet J. M. and J. C. Hawkes (1997). Investigating the behavior of two-dimensional finite element models of compound channel flow. *Earth Surface Process and Landform* **22**, 3–17.

Bates, P. D. and J. Hervouet (1999). A new method for moving-boundary hydrodynamic problems in shallow water. *Proc. Royal Society London. A* **455**, 3107–3128.

Berger, R. C. (1997). *HIVEL 2D v2.0 User's Manual*. US Waterways Experiment Station, Coastal and Hydraulics Laboratory (CHL), USA.

Berger, R. C. and R. L. Stockstill (1995). Finite-element model for high-velocity channels. *J. of Hydraulic Engineering* **121**(10), 710–716.

Berger, R. C. and S. E. Howington (2002). Discrete fluxes and mass balance in finite elements. *J. of Hydraulic Engineering* **128**(1), 87–92.

Bermudez, A. and M. E. Vazquez (1994). Upwind methods for hyperbolic conservation laws with source terms. *Computers and Fluids* **23**(8), 1049–1071.

Berthon, C. Marche, F. and R. Turpault (2011). An efficient scheme on wet/dry transitions for shallow water equations with friction. *Computer and Fluids* **48**, 192–201.

Bradford, S. F. and B. F. Sanders (2005). Performance of high-resolution, nonlevel bed, shallow-water models. *J. of Engineering Mechanics* **131**(10), 1073–1081.

Brooks, A. N. and T. J. R. Hughes (1982). Streamline upwind/Petrov-Galerkin formulations for convection dominated flows with particular emphasis on the incompressible Navier-Stokes equations. *Computer Methods in Applied Mechanics and Engineering* **32**(1-3), 199–259.

Brunner, G. W. (2008). *HEC-RAS, River Analysis System Hydraulic Reference Manual*. US Army Corps of Engineers, Hydrologic Engineering Center (HEC), USA.

Burguete, J., Garcia-Navarro P. and J. Murillo (2008). Friction term discretization and limitation to preserve stability and conservation in the 1D shallow-water model: Application to unsteady irrigation and river flow. *Int. J. for Numerical Methods in Fluids* **58**, 403–425.

Burguete, J., Garcia-Navarro P. Murillo J. and I. Gracia-Palacin (2007). Analysis of the friction term in the one-dimensional shallow-water model. *J. of Hydraulic Engineering* **133**(9), 1048–1063.

Chanson, H. (1999). *The Hydraulics of Open Channel Flow*. John Wiley and Sons Inc., New York.

Chaudhry, M. H. (2008). *Open-channel Flow*. Springer, New York.

Chow, V. T. (1959). *Open-channel Hydraulics*. McGraw-Hill Inc., New York.

Chung, T. J. (2002). *Computational Fluid Dynamics*. Cambridge University Press, UK.

Courant, R., Friedrichs-K. and H. Lewy (1928). Uber die partieller differenzenglichungen der mathematischen physik. *Mathematische Annalen* **100**, 32–74.

Courant, R., Isaacson-E. and M. Rees (1952). On the solution of non-linear hyperbolic differential equations by finite differences. *Communications on Pure and Applied Mathematics* **5**, 243–255.

Cunge, J. A., Holly F. M. Jr. and A. Verway (1980). *Practical Aspects of Computational River Hydraulics*. Pitman Publishing Limited, London.

Date, A. W. (2005). *Introduction to Computational Fluid Dynamics*. Cambridge University Press, New York.

Defina, A. (2000). Two-dimensional shallow flow equations for partially dry areas.. *Water Resources Research* **36**, 3251–3264.

DHI (2003). *MIKE 11 - A Modeling System for Rivers and Channels*. Danish Hydraulic Institue (DHI), Denmark.

DHI (2005). *MIKE21 and MIKE3 Flow Model FM, Hydrodynamic and Transport Module, Scientific Documentation*. Danish Hydraulic Institue (DHI), Denmark.

Dhonida, J. F. and G. S. Stelling (2004). Sobek 1D-2D integrated hydraulic model for flood simulation - its capabilites and features explained. In: *Sixth Int. Conference on Hydrodynamics* (Liong P. and Babovic, Eds.). World Publishing Company, Singapore.

Dietrich, J. C. (2006). Refinements in continuous Galerkin wetting and drying algorithms. In: *Proc. of the Int. Conference on Estuarine and Coastal Modeling*. pp. 637–656.

Dietrich, J. C. Kolar, R. L. and K. M. Dresback (2008). Mass residuals as a criterion for mesh refinement in continuous Galerkin shallow water models. *J. of Hydraulic Engineering* **134**(5), 520–532.

FHA (2002). *User's Manual for FESWMS Flo2DH - Two-dimensional Depth-averaged Flow and Sediment Transport Model*. US Department of Transportation, Federal Highway Administration (FHA), USA.

Galloute, T., Herard J. and N. Sequin (2003). Some approximate Godunov schemes to compute shallow-water equations with topography. *Computers and Fluids* **32**, 497–513.

Gentry, R. A., Martin R. E. and B. J. Daly (1966). An Eulerian differencing method for unsteady compressible flow problems. *J. of Computational Physics* **1**, 87–118.

Glaister, P. (1987). *Difference Schemes for the Shallow Water Equations*. Technical report 9/87, Department of Mathematics, University of Reading, England.

Glaister, P. (1992). Prediction of supercritical flow in open channels. *Communications on Pure and Applied Mathematics* **24**, 69–75.

Godunov, S. K. (Ed.) (1976). *Numerical Solution of Multi-Dimensional Problems in Gas Dynamics*. Nauka Press, Moscow.

Godunov, S.K. (1959). A difference method for numerical calculation of discontinuous solutions of the equations of hydrodynamics. *Matematicheskii Sbornik* **47**, 271–306.

Gottlieb, J. J. and C. P. T. Groth (1988). Assessment of Riemann solvers for unsteady one-dimensional inviscid flows of perfect gases. *J. of Computational Physics* **78**, 437–458.

Goutal, N. and Maurel, F., Eds.) (1997). *Proceedings of the 2nd Workshop on Dam-Break Wave Simulation*. number HE-43/97/016/B.

Gray, W. G. (1980). Do finite element models simulate surface flow?. In: *Proc. of the Third Int. Conference on Finite Element in Water Resources*. University of Mississippi, USA. pp. 1.122–1.136.

Gresho, P. M. and R. L. Lee (1981). Don't suppress the wiggles - they're telling you something. *Computers and Fluids* **9**, 223–253.

Grotkop, G. (1973). Finite element analysis of long-period water waves. *Computer Methods in Applied Mechanics and Engineering* **2**, 147–157.

Hagen, S. C. Westerink, J. J. and R. L. Kolar (2000). One-dimensional finite element grids based on a localized truncation error analysis. *Int. J. for Numerical Methods in Fluids* **32**(2), 241–261.

Hagen, S. C. Westerink, J. J. Kolar R. L. and O. Horstmann (2001). Two-dimensional unstructured mesh generation for tidal models. *Int. J. for Numerical Methods in Fluids* **35**(6), 669–686.

Hannah, C. G. and D. G. Wright (1995). Depth dependent analytical and numerical solutions for wind-driven flow in the coastal ocean. *Quantitative Skill Assessment for Coastal Ocean Models, American Geophysical Union* **47**, 125–152.

Harten, A. and S. Osher (1987). Uniformity high-order accurate non-oscillatory schemes.. *SIAM J. on Numerical Analysis* **24**, 279–309.

Harten, A., Lax P. D. and B. Van Leer (1983). On upstream differencing and Godunov-type schemes for hyperbolic conservation laws. *SIAM Review* **25(1)**, 3561.

Heniche, M., Secretan Y. Boudreau P. and M. Leclerc (2002). Dynamic tracking of flow boundaries in rivers with respect to discharge. *J. of Hydraulic Research* **40**(5), 589–602.

Hicks, F. E. an Steffler, P. M. (1990). Finite element modeling of open channel flow. Technical Report WRE 90-6. Department of Civil Engineering. University of Alberta, Canada.

Hicks, F. E. and P. M. Steffler (1992). Characteristic Dissipative Galerkin scheme for open channel flow. *J. of Hydraulic Engineering* **118**(2), 337–352.

Hicks, F.E. (2005). *River1D Hydraulic Flood Routing Model, Model Description and User's Manual*. University of Alberta, Canada.

Hirt, C. W. and B. D. Nichols (1988). *Flow-3D User's Manual, Technical Report*. Flow Sciences, Inc., USA.

Hubbard, M. E. and P. Garcia-Navarro (2000). Flux difference splitting and the balancing of source terms and flux gradients. *J. of Computational Physics* **165**, 89–125.

Hughes, T. J. R. and M. Mallet (1986). A new finite element formulation for computational fluid dynamics: III. The generalized streamline operator for multidimensional advective-diffusive systems. *Computer Methods in Applied Mechanics and Engineering* **58**(3), 305–328.

Jia, Y. and S. S. Y. Wang (2001). CCHE2D: Two-dimensional hydrodynamic and sediment transport model for unsteady open channel flows over loose bed. Technical Report NCCHE-TR-2001-1. National Center for Computational Hydroscience and Engineering. University of Mississippi, U. S. A.

Katopodes, N. D. (1984*a*). A dissipative Galerkin scheme for open-channel flow. *J. of Hydraulic Engineering* **110**(4), 450–466.

Katopodes, N. D. (1984*b*). Fourier analysis of dissipative FEM channel flow model. *J. of Hydraulic Engineering* **110**(7), 927–944.

Katopodis, C. (2003). Case studies of instream flow modeling for fish habitat in Canadian prairie rivers. *Canadian Water Resources Journal* **28**(2), 199–216.

Khan, A. A. (2000). Modeling flow over an initially dry bed. *J. of Hydraulic Research.* **38**(5), 383–388.

Koren, V. I. and L. S. Kuchment (1967). Numerical integration of de Saint-Venant's equations with explicit schemes when computing the unsteady flow in rivers. *Trudy G. N. I.*

Lang, P. (2010). *TELEMAC Modeling System, 2D Hydrodynamics TELEMAC-2D Software Version 6.0 Reference Manual.* Électricité de France Reserach and Innovation (EDF R&D), France.

Lax, P. D. (1957). Hyperbolic systems of conservation laws II. *Communications on Pure and Applied Mathematics* **10**, 537–566.

Lax, P. D. and B. Wendroff (1960). Systems of conservation laws. *Communications on Pure and Applied Mathematics* **13**, 217–237.

Leclerc, M. Saint-Hilaire, A. and J. Bechara (2003). State-of-the-art and perspectives of habitat modeling for determining conservation flows. *Canadian Water Resources Journal* **28**(2), 135–151.

LeVeque, R. J. (1998). Balancing source terms and flux gradients in high-resolution Godunov methods: The quasi-steady wave-propagation algorithm. *J. of Computational Physics* **146**, 346–365.

LeVeque, R. J. (2002). *Finite Volume Methods for Hyperbolic Problems.* Cambridge University Press, UK.

Liang, Q. and F. Marche (2009). Numerical resolution of well-balanced shallow water equations with complex sources terms. *Advances in Water Resources* **32**(6), 873–884.

Liggett, J. A. (1975). Basic equations of unsteady flow. In: *Unsteady Flow in Open Channels* (K. Mahmood and V. Yevjevich, Eds.). Vol. 1. Water Resources Publications, Fort Collins, Colorado, USA. pp. 485–508.

Liggett, J. A. and D. A. Woolhisher (1967). Difference solutions of shallow water equations. *J. Engineering Mechanics Division* **93**(EM2), 39–71.

Liggett, J. A. and J. A. Cunge (1975). Numerical methods of solution of the unsteady flow equations. In: *Unsteady Flow in Open Channels* (K. Mahmood and V. Yevjevich, Eds.). Vol. 1. Water Resources Publications, Fort Collins, Colorado, USA. pp. 485–508.

Lynch, D. R. and W. G. Gray (1980). Finite element simulation of flow deforming regions. *J. Computational Physics* **36**, 135–153.

MacCormack, R. W. (1969). The effect of viscosity in hyper-velocity impact cratering. *AIAA paper* **66**, 354.

Marrocu, M. and D. Ambrosi (1999). Mesh adaptation strategies for shallow water flow. *Int. J. for Numerical Methods in Fluids* **31**(2), 497–512.

Massau, J. (1905). L'integration graphique des equations aux derivées parcielles. *Assoc. Ingénieurs Sortis des Ecoles Specials de Gand. Annales* **4**, 65.

Miller, W. A. and J. A. Cunge (1975). Simplified equations of unsteady flow. In: *Unsteady Flow in Open Channels* (K. Mahmood and V. Yevjevich, Eds.). Vol. 1. Water Resources Publications, Fort Collins, Colorado, USA. pp. 485–508.

Morgali, J. R. and R. K. Linsley (1965). Computer analysis of overland flow. *J. Hydraulic Division* **91**(HY3), 81–100.

Norrie, D. H. and G. de Vries (1978). A survey of the finite element applications in fluid mechannics. In: *Finite Elements in Fluids: Vol. 3*. pp. 363–396.

Norton, W. R., King I. P. and G. T. Orlob (1973). *A Finite Element Model for Lower Granite Reservoir.* Walla Walla District, U.S. Army Corps of Engineers, USA.

Nujic, M. (1995). Efficient implementation of non-oscillatory schemes for the computation of free-surface flows. *J. of Hydraulic Research* **33**(1), 100–111.

Oden, J. T. (1972). *Finite Elements of Nonlinear Continua*. MacGraw-Hill, New York.

Olson, M. E. (1972). Formulation of a variational principle-finite element method for viscous flows. In: *Proc. of Int. Conference on Variationl Methods in Engineering*. Southampton University. pp. 5.27–5.38.

OpenCFD (2009). *Open∇FOAM, The Open Source CFD Toolbox, User Guide Version 1.6*. OpenCFD Ltd., USA.

Osher, S. (1984). Riemann solvers, the entropy condition and difference approxiamtions. *SIAM J. on Numerical Analysis* **21**, 217–235.

Osher, S. and F. Solomon (1982). Upwind difference schemes for hyperbolic systems of conservation laws. *Mathematics of Computation* **38(158)**, 339374.

Partridge, P. W. and C. A. Brebbia (1976). Quadratic finite elements in shallow water problems. *J. of Hydraulics Division* **102**(9), 1299–1313.

Patankar, S. V. (1980). *Numerical Heat Transfer and Fluid Flow*. Hemisphere Publishing Corp., New York.

Petaccia, G., Velickovic M. Soares-Frazo S. Asselman N. Savi F. Natale L. and Y. Zech (2009). Flood wave propagation in a steep mountain river: comparison of four simulation tools. In: *Proc. of 33rd IAHR congress: Water Engineering for a Sustainable Environment*. Vancouver, Canada. pp. 5896–5903.

Ponce, V. M. (1977). Shallow wave propagation in open channel flow.. *J. of Hydraulics Division* **103**(12), 1461–1476.

Preissmann, A. (1961). Propagation des intumescencs dans les canaux et rivieres. In: *1st Congr. des. I'Assoc. Francaise de Calcul*. Association Francaise de Calcul, Grenoble, France. pp. 433–442.

Raithby, G. D. and K. E. Torrence (1974). Upstream-weighted difference schemes and their application to elliptical problems involving fluid flow. *Computers and Fluids* **2**, 191–206.

Roe, P. L. (1981). Approximate Riemann solvers, parameter vectors and difference schemes. *J. of Computational Physics* **43**, 357–372.

Rouse, H. and S. Ince (1957). *History of Hydraulics*. Institute of Hydraulic Research, IOWA.

Runchal, A. K. (1972). Convergence and accuracy of three finite difference schemes for a two-dimensional conduction and convection problem. *Int. J. for Numerical Methods in Engg.* **4**, 541–550.

Saint-Venant, De (1871). Théorie du mouvement non-permanent des eaux avec application aux crues des rivières et à l'intrduction des marées dans leur lit. *Acad. Sci. Comptes Rendus* **73**, 148–154,237–240.

Schippa, L. and S. Pavan (2008). Analytical treatment of source terms for complex channel geometry. *J. of Hydraulic Research* **46**(6), 753–763.

Steffler, P. and J. Blackburn (2002). *River2D: Two-Dimensional Depth-averaged Model of River Hydrodynamics and Fish Habitat, Introduction to Depth Averaged Modeling and User's Manual*. University of Alberta, Canada.

Steger, J. L. and R. F. Warming (1981). Flux vector splitting of the inviscid gas-dynamic equations with applications to finite difference methods. *J. of Computational Physics* **40**, 263–293.

Stoker, J. J. (1957). Water waves. *Interscience*.

Szymkiewicz, R. (2010). *Numerical Modeling in Open Channel Hydraulics*. Springer, New York.

Tate, J. N. Berger, R. C. and R. L. Stockstill (2006). Refinement indicator for mesh adaptation in shallow-water modeling. *J. of Hydraulic Engineering* **138**(8), 854–857.

Taylor, C. and J. Davis (1972). *Tidal and Long Wave Propagation - A Finite Element Approach*. Civil Engg. Dept., University of Wales, Swansea, C/R189/72.

Tchamen, G. W. and R. A. Kahawita (1998). Modeling wetting and drying effects over complex topography. *Hydrological Processes* **12**, 1151–1182.

Toro, E. F. (1989). A fast Riemann solver with constant covolume applied to the random choice method. *Int. J. for Numerical Methods in Fluids* **9**, 11451164.

Toro, E. F. (2001). *Shock-capturing Methods for Free-surface Shallow Flows*. Wiley, New York.

Toro, E. F. (2009). *Riemann Solvers and Numerical Methods for Fluid Dynamics: A Prcatical Introduction*. Springer, New York.

Toro, E. F. and P. Garcia-Navarro (2007). Godunov-type methods for free-surface shallow flows: A review. *J. of Hydraulic Research* **45**(6), 736–751.

Van Leer, B. (1974). Towards the ultimate conservative difference scheme. II. monotonicity and conservation combined in a second order scheme. *J. of Computational Physics.* **14**, 361–370.

Van Leer, B. (1979). Towards the ultimate conservative difference scheme. V. a second order sequel to Godunovs method. *J. of Computational Physics.* **32**, 101–136.

Waddle, T. (2009). Field evaluation of a two-dimensional hydrodynamic model near boulders for habitat calculation. *River Research and Applications* p. DOI: 10.1002/rra.1278.

Westerink, J. J. Luettich, R. A. Jr. and J. C. Muccino (1994). Modeling tides in the western north Atlantic using unstructured graded grids. *Tellus* **46A**, 178–199.

WL|Delft, Hydraulics (2006). *Simulation of Multi-Dimensional Hydrodynamic Flows and Transport Phenomena, Including Sediments: User Manual.* WL|Delft Hydraulics, The Netherlands.

Wool, T. A., Ambrose R. B. Martin J. L. and E. A. Comer (2004). *Water Quality Analysis Simulation Program (WASP) Version 6.0 Draft: User's Manual.* US Enviornmental Protection Agency - Region 4, Atlanta.

Woolhiser, D. A. (1975). Simulation of unsteady overland flow. In: *Unsteady Flow in Open Channels* (K. Mahmood and V. Yevjevich, Eds.). Vol. 2. Water Resources Publications, Fort Collins, Colorado, USA.. pp. 485–508.

Wu, W. and D. A. Vieira (2002). One-dimensional channel network model, CCHE1D version 3.0 -technical manual. Technical Report NCCHE-TR-2002-1. National Center for Computational Hydroscience and Engineering. University of Mississippi, USA.

Yee, H. C. (1987). Upwind and symmetric shock-capturing schemes. Technical Report NASA Technical Memorandoum 89464. Ames Research Center. Moffett Field, California.

Ying, X., Khan A. A. and S. S. Y. Wang (2004). Upwind conservative scheme for the Saint-Venant equations. *J. of Hydraulic Engineering* **130**(10), 977–987.

Zeienkiewicz, O. C. and Y. K. Cheung (1965). Finite elements in the solution of field problems. *The Engineer* pp. 507–510.

Zhou, J. G., Causon D. M. Mingham C. G. and D. M. Ingram (2001). The surface gradient method for the treatment of source terms in the shallow-water equations. *J. of Computational Physics* **168**, 1–25.

Appendix A

Coefficients of the CDG Finite Element Scheme

The upwind matrix $\mathbf{W}$ of EQ. 4.7 can be written as:

$$\mathbf{W} = \begin{bmatrix} W_{aa} & W_{aq} \\ W_{qa} & W_{qq} \end{bmatrix}$$

where W_{aa}, W_{aq}, W_{qa} and W_{qq} are the coefficients of the upwinding matrix. $\mathbf{W}$ for the non-dimensional linearized Saint-Venant equations, i.e. Eq. 2.27 and 2.28 are:

$W_{aa} = \frac{(1-Fr_0^2)}{2}\left(\frac{1}{|Fr_0+1|} - \frac{1}{|Fr_0-1|}\right)$; $W_{aq} = \frac{(Fr_0)}{2}\left(\frac{Fr_0+1}{|Fr_0+1|} - \frac{Fr_0-1}{|Fr_0-1|}\right)$;

$W_{qa} = \frac{(1-Fr_0^2)}{2Fr_0}\left(\frac{Fr_0+1}{|Fr_0+1|} - \frac{Fr_0-1}{|Fr_0-1|}\right)$; and $W_{qq} = \frac{1}{2}\left(\frac{(Fr_0+1)^2}{|Fr_0+1|} - \frac{(Fr_0-1)^2}{|Fr_0-1|}\right)$

By defining $\alpha = (\frac{1}{Fr_0^2} - 1)$ in Eq. 2.28 the coefficients a_r and b_r, for r = 1 to 15 of Eq. 3.6 using CDG scheme are:

$a_1 + a_7 = wW_{aq}(-\frac{\alpha}{2} - \frac{3\beta\Delta\xi}{4})$;

$a_2 + a_8 = wW_{aq}\alpha$;

$a_3 + a_9 = wW_{aq}(-\frac{\alpha}{2} + \frac{3\beta\Delta\xi}{4})$;

$a_4 + a_{10} = -\frac{1}{2} - wW_{aa}\frac{1}{2} + wW_{aq}(-1 + \frac{\beta\Delta\xi}{2})$;

$a_5 + a_{11} = wW_{aa} + 2wW_{aq}$;

$a_6 + a_{12} = \frac{1}{2} - wW_{aa}\frac{1}{2} + wW_{aq}(-1 - \frac{\beta\Delta\xi}{2})$;

$a_{13} = wW_{aq}\frac{1}{2Fr_0^2}$;

$a_{14} = -wW_{aq}\frac{1}{Fr_0^2}$;

$a_{15} = wW_{aq}\frac{1}{2Fr_0^2}$.

$b_1 + b_7 = -\frac{\alpha}{2} - \frac{\beta\Delta\xi}{2} + wW_{qq}(-\frac{\alpha}{2} - \frac{3\beta\Delta\xi}{4})$;

$b_2 + b_8 = -2\beta\Delta\xi + wW_{qq}\alpha$;

$b_3 + b_9 = \frac{\alpha}{2} - \frac{\beta\Delta\xi}{2} + wW_{qq}(-\frac{\alpha}{2} + \frac{3\beta\Delta\xi}{4});$

$b_4 + b_{10} = -1 + \frac{\beta\Delta\xi}{3} - wW_{qa}\frac{1}{2} + wW_{qq}(-1 + \frac{\beta\Delta\xi}{2});$

$b_5 + b_{11} = \frac{4\beta\Delta\xi}{3} + wW_{qa} + 2wW_{qq};$

$b_6 + b_{12} = 1 + \frac{\beta\Delta\xi}{3} - wW_{qa}\frac{1}{2} + wW_{qq}(-1 - \frac{\beta\Delta\xi}{2});$

$b_{13} = \frac{1}{2Fr_0^2} + wW_{qq}\frac{1}{2Fr_0^2};$

$b_{14} = -wW_{qq}\frac{1}{Fr_0^2};$

$b_{15} = -\frac{1}{2Fr_0^2} + wW_{qq}\frac{1}{2Fr_0^2}.$

Appendix B

Coefficients of the Box Finite Difference Scheme

The coefficients a_r and b_r, for r = 1 to 15 of Eq. 3.6 using Box scheme are:

$a_1 + a_7 = 0;$

$a_2 + a_8 = 0;$

$a_3 + a_9 = 0;$

$a_4 + a_{10} = 0;$

$a_5 + a_{11} = -1;$

$a_6 + a_{12} = 1;$

$a_{13} = 0;$

$a_{14} = 0;$

$a_{15} = 0.$

$b_1 + b_7 = 0;$

$b_2 + b_8 = -\alpha - \frac{3\beta\Delta\xi}{2};$

$b_3 + b_9 = \alpha - \frac{3\beta\Delta\xi}{2};$

$b_4 + b_{10} = 0;$

$b_5 + b_{11} = -2 + \beta\Delta\xi;$

$b_6 + b_{12} = 2 + \beta\Delta\xi;$

$b_{13} = 0;$

$b_{14} = \frac{1}{Fr_0^2};$

$b_{15} = -\frac{1}{Fr_0^2}.$

Appendix C

Coefficients of the MacCormack Finite Difference Scheme

The coefficients a_r and b_r, for r = 1 to 15 of Eq. 3.6 using MacCormack scheme are:

$a_1 + a_7 = -\frac{\alpha}{2}$;

$a_2 + a_8 = \alpha - \frac{3\beta\Delta\xi}{2}$;

$a_3 + a_9 = -\frac{\alpha}{2} + \frac{3\beta\Delta\xi}{2}$;

$a_4 + a_{10} = -\frac{\Delta\xi}{2\Delta\tau} - 1$;

$a_5 + a_{11} = 2 + \beta\Delta\xi$;

$a_6 + a_{12} = \frac{\Delta\xi}{2\Delta\tau} - 1 - \beta\Delta\xi$;

$a_{13} = \frac{1}{2Fr_0^2}$;

$a_{14} = -\frac{1}{Fr_0^2}$;

$a_{15} = \frac{1}{2Fr_0^2}$.

$b_1 + b_7 = -\frac{\alpha\Delta\xi}{2\Delta\tau} - \alpha + \alpha\beta\Delta\xi$;

$b_2 + b_8 = -3\beta\Delta\xi\frac{\Delta\xi}{\Delta\tau} + 2\alpha - 3\beta\Delta\xi - \alpha\beta\Delta\xi + 3(\beta\Delta\xi)^2$;

$b_3 + b_9 = -\frac{\alpha\Delta\xi}{2\Delta\tau} - \alpha + 3\beta\Delta\xi$;

$b_4 + b_{10} = -\frac{\Delta\xi}{\Delta\tau} - \frac{\alpha}{2} - 2 - \frac{3\beta\Delta\xi}{2} + 2\beta\Delta\xi$;

$b_5 + b_{11} = 2\beta\Delta\xi\frac{\Delta\xi}{\Delta\tau} + \alpha + 4 + \frac{3\beta\Delta\xi}{2} - 2(\beta\Delta\xi)^2$;

$b_6 + b_{12} = \frac{\Delta\xi}{\Delta\tau} - \frac{\alpha}{2} - 2 - 2\beta\Delta\xi$;

$b_{13} = \frac{1}{2Fr_0^2}\frac{\Delta\xi}{\Delta\tau} + \frac{1}{Fr_0^2} - \frac{\beta\Delta\xi}{Fr_0^2}$;

$b_{14} = -\frac{2}{Fr_0^2} + \frac{\beta\Delta\xi}{Fr_0^2}$;

$b_{15} = -\frac{1}{2Fr_0^2}\frac{\Delta\xi}{\Delta\tau} + \frac{1}{Fr_0^2}$.

Appendix D

Coefficients of the Balanced Godunov Scheme

For the non-dimensional linearized Saint-Venant equations, i.e. Eq. 2.27 and 2.28,

$$\mathbf{A} = \begin{bmatrix} 0 & 1 \\ (\frac{1}{Fr_0^2} - 1) & 2 \end{bmatrix}$$

$$\mathbf{\Lambda} = \begin{bmatrix} (1 + \frac{1}{Fr_0}) & 0 \\ 0 & (1 - \frac{1}{Fr_0}) \end{bmatrix}$$

$$\mathbf{R} = \begin{bmatrix} 1 & 1 \\ (1 + \frac{1}{Fr_0}) & (1 - \frac{1}{Fr_0}) \end{bmatrix}$$

$$\mathbf{R\Lambda^+R}^{-1} = \frac{Fr_0}{2} \begin{bmatrix} -(1 - \frac{1}{Fr_0^2}) & (1 + \frac{1}{Fr_0}) \\ -(1 + \frac{1}{Fr_0})(1 - \frac{1}{Fr_0^2}) & (1 + \frac{1}{Fr_0})^2 \end{bmatrix} = \begin{bmatrix} A_{11}^+ & A_{12}^+ \\ A_{21}^+ & A_{22}^+ \end{bmatrix}$$

$$\mathbf{R\Lambda^-R}^{-1} = \frac{Fr_0}{2} \begin{bmatrix} (1 - \frac{1}{Fr_0^2}) & -(1 - \frac{1}{Fr_0}) \\ (1 - \frac{1}{Fr_0})(1 - \frac{1}{Fr_0^2}) & -(1 - \frac{1}{Fr_0})^2 \end{bmatrix} = \begin{bmatrix} A_{11}^- & A_{12}^- \\ A_{21}^- & A_{22}^- \end{bmatrix}$$

$$\mathbf{RI^+R}^{-1} = \frac{Fr_0}{2} \begin{bmatrix} -(1 - \frac{1}{Fr_0}) & 1 \\ -(1 - \frac{1}{Fr_0^2}) & (1 + \frac{1}{Fr_0}) \end{bmatrix} = \begin{bmatrix} S_{11}^+ & S_{12}^+ \\ S_{21}^+ & S_{22}^+ \end{bmatrix}$$

$$\mathbf{RI^-R}^{-1} = \frac{Fr_0}{2} \begin{bmatrix} (1 + \frac{1}{Fr_0}) & -1 \\ (1 - \frac{1}{Fr_0^2}) & -(1 - \frac{1}{Fr_0}) \end{bmatrix} = \begin{bmatrix} S_{11}^- & S_{12}^- \\ S_{21}^- & S_{22}^- \end{bmatrix}$$

Now the coefficients a_r and b_r, for r = 1 to 15 of Eq. 3.6 using balanced Godunov scheme are:

$a_1 + a_7 = -A_{11}^+ - \frac{3\beta\Delta\xi}{2} S_{12}^+;$

$a_2 + a_8 = A_{11}^+ - A_{11}^- - \frac{3\beta\Delta\xi}{2} S_{12}^+ - \frac{3\beta\Delta\xi}{2} S_{12}^-;$

$a_3 + a_9 = A_{11}^- - \frac{3\beta\Delta\xi}{2} S_{12}^-;$

$a_4 + a_{10} = -A_{12}^+ + \beta\Delta\xi S_{12}^+;$

$a_5 + a_{11} = A_{12}^+ - A_{12}^- + \beta\Delta\xi S_{12}^+ + \beta\Delta\xi S_{12}^-;$

$a_6 + a_{12} = A_{12}^- + \beta\Delta\xi S_{12}^-;$

$a_{13} = \frac{1}{Fr_0^2} S_{12}^+;$
$a_{14} = -\frac{1}{Fr_0^2} S_{12}^+ + \frac{1}{Fr_0^2} S_{12}^-;$
$a_{15} = -\frac{1}{Fr_0^2} S_{12}^-.$

$b_1 + b_7 = -A_{21}^+ - \frac{3\beta\Delta\xi}{2} S_{22}^+;$
$b_2 + b_8 = A_{21}^+ - A_{21}^- - \frac{3\beta\Delta\xi}{2} S_{22}^+ - \frac{3\beta\Delta\xi}{2} S_{22}^-;$
$b_3 + b_9 = A_{21}^- - \frac{3\beta\Delta\xi}{2} S_{22}^-;$
$b_4 + b_{10} = -A_{22}^+ + \beta\Delta\xi S_{22}^+;$
$b_5 + b_{11} = A_{22}^+ - A_{22}^- + \beta\Delta\xi S_{22}^+ + \beta\Delta\xi S_{22}^-;$
$b_6 + b_{12} = A_{22}^- + \beta\Delta\xi S_{22}^-;$
$b_{13} = \frac{1}{Fr_0^2} S_{22}^+;$
$b_{14} = -\frac{1}{Fr_0^2} S_{22}^+ + \frac{1}{Fr_0^2} S_{22}^-;$
$b_{15} = -\frac{1}{Fr_0^2} S_{22}^-.$

Appendix E

Coefficients of the One-sided Upwind-Downwind Finite Volume Scheme

The coefficients a_r and b_r, for r = 1 to 15 of Eq. 3.6 using one-sided upwind-downwind scheme are:

$a_1 + a_7 = 0;$

$a_2 + a_8 = 0;$

$a_3 + a_9 = 0;$

$a_4 + a_{10} = -1;$

$a_5 + a_{11} = 1;$

$a_6 + a_{12} = 0;$

$a_{13} = 0;$

$a_{14} = 0;$

$a_{15} = 0.$

$b_1 + b_7 = 0;$

$b_2 + b_8 = -\alpha - 3\beta\Delta\xi;$

$b_3 + b_9 = \alpha;$

$b_4 + b_{10} = -2;$

$b_5 + b_{11} = 2 + 2\beta\Delta\xi;$

$b_6 + b_{12} = 0;$

$b_{13} = 0;$

$b_{14} = \frac{1}{Fr_0^2};$

$b_{15} = -\frac{1}{Fr_0^2}.$